DOCTOR OF PHILOSOPHY

Outdoor stability studies in Organic Photovoltaics

Bristow, Noel

Award date:
2017

Awarding institution:
Bangor University

OUTDOOR STABILITY STUDIES IN ORGANIC PHOTOVOLTAICS

PRIFYSGOL
BANGOR
UNIVERSITY

Noel Bristow

School of Electronic Engineering

Bangor University

A thesis submitted in partial fulfilment for the degree of

Doctor of Philosophy

January 2017

"A day without learning is a day wasted.
There is so much to learn and so little time to learn it."
- Albert Einstein

DECLARATION OF AUTHORSHIP

This work has not previously been accepted in substance for any degree and is not being concurrently submitted in candidature for any degree.

Signed: Date:

Statement 1

This thesis is the result of my own investigations, except where otherwise stated. Throughout this thesis, Professor Frederik Krebs and his group at the Technology University of Denmark (DTU) supplied all of the freeOPV modules. The LBIC and tilted IV characterisations of the structured modules in Sections 6.2.1 and 6.2.3 were performed by DTU. The initial studies on LDS materials in Section 7.2.1 were performed in collaboration with Dr. Omar Moudam. The outdoor stability tests in Section 7.2.3 were performed in collaboration with DTU and Professor Eugene Katz of Ben Gurion University, Israel: DTU performed the IV characterisation before and after application of the LDS coatings and Ben Gurion University performed the outdoor measurements in Israel. The optical characterisation and stability tests of the LDS materials in Sections 7.3 and 7.4 were performed with the help of Ricardo Fernandes, an exchange student from Londrina State University, Brazil. Dr. Yanhua Hong assisted in AFM measurements. In all instances the analysis of the data was performed by the author. Other sources are acknowledged by giving explicit references.

Signed: Date:

Statement 2

I agree to deposit an electronic copy of my thesis (the Work) in the Bangor University (BU) Institutional Digital Repository, the British Library ETHOS system, and/or in any other repository authorised for use by Bangor University and where necessary have gained the required permissions for the use of third party material.

Signed: Date:

ABSTRACT

This thesis focuses on the outdoor monitoring of organic photovoltaics (OPVs) with the aim of improving the stability and performance of OPVs under real world conditions. This is important as in order for OPVs to become commercially viable they must make the transition from small laboratory cells to larger modules.

Over the course of several outdoor monitoring campaigns various types of OPV modules have been benchmarked against a number of other technologies: polycrystalline silicon, cadmium indium diselenide and dye sensitised solar cells. The principal performance parameters are examined in detail, analysing their dependence on irradiance and temperature. OPVs were shown to have positive temperature coefficients for efficiency, I_{SC} and fill factor and a negative temperature coefficient for V_{OC}. One of the main causes of degradation is ingress of water and oxygen into the module and subsequent photo-oxidation of the active layer and it was shown that UV filtering would improve stability.

To improve the yield of OPVs outdoors, modules were laminated to different corrugated substrates and subjected to indoor characterisation and outdoor monitoring. The corrugated modules were shown to have three advantages: the effective area of the module, allowing for curvature, is reduced which leads to an improvement in the power conversion efficiency per unit area; substantial enhancement at high angles of incidence led to increased output during early morning and evening; under diffuse irradiance performance improved by up to 25%. Outdoor measurements on larger module strips showed that corrugated strips outperformed flat strips by 7.5% with a 14.8% enhancement under diffuse conditions.

An alternative technique to improve the yield of OPVs is the use of luminescent down-shifting coatings which were investigated as alternatives to UV filters and have the added benefit of improving stability. The use of both discrete and multiple-dye blends dispersed in poly(methyl methacrylate) led to improvements in performance of up to 8% and a six-fold extension of operational lifetime. Dyes were systematically selected by examining their absorption and photoluminescence spectra and matching these to the spectral performance of P3HT:PC_{61}BM OPV devices. In doing so optimised multiple-dye blends were made possible.

ACKNOWLEDGEMENTS

First of all I would like to thank my supervisor, Dr. Jeff Kettle, for giving me this opportunity and for his support and guidance over the last four years.

I would like to thank the Wales Ireland Network for Innovative Photovoltaic Technologies (WINIPT), funded through INTERREG 4A, for financial support during this research.

I would like to thank Dr. Tracy Sweet at Cardiff School of Engineering for her support and the use of equipment in Cardiff, and Professor Igor Perepichka at the School of Chemistry (Bangor) for giving me full access to his optical characterisation equipment. I would like to thank Dr. Paul Sayers for his support and for providing a suitable working environment.

I would like to thank all of my colleagues at Bangor University for their camaraderie on this journey: Huw, Vasil, Omar, Ding, Dinesh, Eifion, Colin, Ricardo, Bruno, Roger, Dan, Iwan, David, Yvonne, Julie, Siân, Gaynor, Wendy, Saad, Professor Alan, Professor Martin and Professor Lewis.

I would like to thank Omar and Brian for taking the time and trouble to read through my thesis and for their feedback.

Last, but most definitely not least, I would like to thank my family for their love and support, especially Amanda for proof reading my thesis, and my children, Ffreuer and Efrog, for their patience.

PUBLICATIONS

Ricardo Fernandes, **Noel Bristow**, Vasil Stoichkov, Helder Anizelli, José Duarte, Edson Laureto, Jeff Kettle "Development of multidye UV filters for OPVs using luminescent materials." *Journal of Physics D: Applied Physics* 50 (2017) 025103

J. Kettle, **N. Bristow**, D.T. Gethin, Z. Tehrani, O. Moudam, B. Li, E.A. Katz, G.A. dos Reis Benatto, F.C. Krebs. "Luminescent down shifter for enhancing efficiency and stability of organic photovoltaics." *Solar Energy Materials and Solar Cells* 144 (2016): 481-487.

Jeff Kettle, **Noel Bristow**, Tracy Sweet, Nick Jenkins, Gisele A. dos Reis Benatto, Mikkel Jørgensen, Frederik C. Krebs. "Three dimension corrugated Organic Photovoltaics for building integration; improving the efficiency, oblique angle and diffuse performance of solar cells", *Energy & Environmental Science* 8.11 (2015): 3266-3273.

Omar Moudam, **Noel Bristow**, Shu-Wei Chang, Masaki Horie, Jeff Kettle. "Application of UV-absorbing silver (I) luminescent down shifter for PTB7 organic solar cells for enhanced efficiency and stability." *RSC Advances* 5.16 (2015): 12397-12402.

Noel Bristow, Jeff Kettle. "Outdoor performance of organic photovoltaics: Diurnal analysis, dependence on temperature, irradiance, and degradation." *Journal of Renewable and Sustainable Energy* 7.1 (2015): 013111.

L. Andrés, M. Menéndez, D. Gómez, A. Martínez, **N. Bristow**, J. Kettle, A. Menéndez, B. Ruiz. "Rapid synthesis of ultra-long silver nanowires for tailor-made transparent conductive electrodes: proof of concept in organic solar cells." *Nanotechnology* 26.26 (2015): 265201.

Huw Waters, **Noel Bristow**, Omar Moudam, Shu-Wei Chang, Chun-Jen Su, Wei-Ru Wu, U-Ser Jeng, Masaki Horie, and Jeff Kettle. "Effect of processing additive 1, 8-octanedithiol on the lifetime of PCPDTBT based Organic Photovoltaics." *Organic Electronics* 15.10 (2014): 2433-2438.

Peter Doggart, **Noel Bristow**, Jeff Kettle. "Optimisation of the material properties of indium tin oxide layers for use in organic photovoltaics." Journal of Applied Physics 116.10 (2014): 103103.

Morten Madsen, Suren Gevorgyan, R. Pacios, J. Ajuria, I. Etxebarria, Jeff Kettle, **Noel Bristow** et al. "Worldwide outdoor round robin study of organic photovoltaic devices and modules." *Solar Energy Materials and Solar Cells* 130 (2014): 281-290.

CONFERENCES

Noel Bristow, Jeff Kettle. "*Outdoor Organic Photovoltaic Monitoring*." 10th Photovoltaic Science Application and Technology (PVSAT), Loughborough University. April 2014 (oral)

Noel Bristow, Jeff Kettle. "*Outdoor Organic Photovoltaic Monitoring*." Royal Society of Chemistry Conference: "Next Generation Materials for Solar Photovoltaics." Jan 2014 (poster)

Huw Waters, **Noel Bristow**, Omar Moudam, Jeff Kettle. "*Lifetime studies on PCPDTBT:PCBM solar cells*." Royal Society of Chemistry Conference: "Next Generation Materials for Solar Photovoltaics." Jan 2014 (poster)

CONTENTS

Chapter 1. Introduction

Over the last two decades, concerns about climate change, peak oil and energy security have driven the growth of renewable energy. It is now generally accepted that the climate is warming due to exponential increases in CO_2 and other greenhouse gases in the atmosphere and that temperature rises of over 2°C are likely by the end of this century, with worse case scenarios predicting increases of up to 4.8°C [1]. It is predicted that global demand for electricity will increase by around 69% between 2012 and 2040 (growth rates based on the "IEO2016 Reference Case") (Figure 1.1) [2], [3].

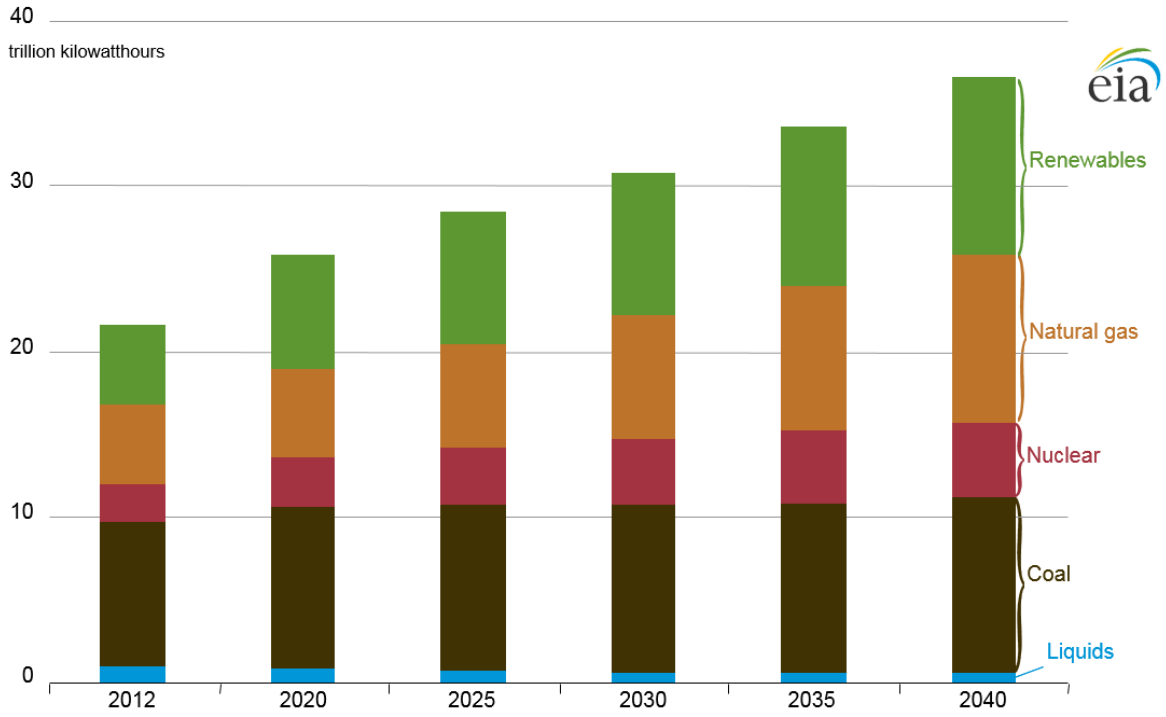

Figure 1.1: World net electricity generation by source, 2012-2040 [2].

In order to balance this increasing demand for energy with the need to combat climate change there must be a massive decarbonisation of global energy sources. In 2014 over 19% of global electricity generation was from renewable sources [4]. In 2015, 147 GW_P of renewable power capacity was added, the largest annual increase ever and the sixth consecutive year where net investment in renewable energy exceeded that for fossil fuels [4].

The main renewable energy resources are hydropower, wind, biomass, solar, tidal, wave and geothermal. Apart from geothermal, these are all ultimately powered by the sun which has a massive theoretical potential: in less than two hours the earth receives more energy from the sun (656 EJ) than total global primary energy supply for a whole year (2014 = 575 EJ) [5], [6].

In the UK recent government policies have led to ambitious targets of halving its greenhouse gas emissions between 1990 and 2027 and cutting them by a total of 80% by 2050 [7]. Since the mid to late nineties there has been a rapid and increasing growth in renewable energy and it produced 24.6% of the electricity generated in 2015 (Figure 1.2) [8]. This growth was initially in wind and biomass and more recently in solar following the introduction of feed-in tariffs in 2010.

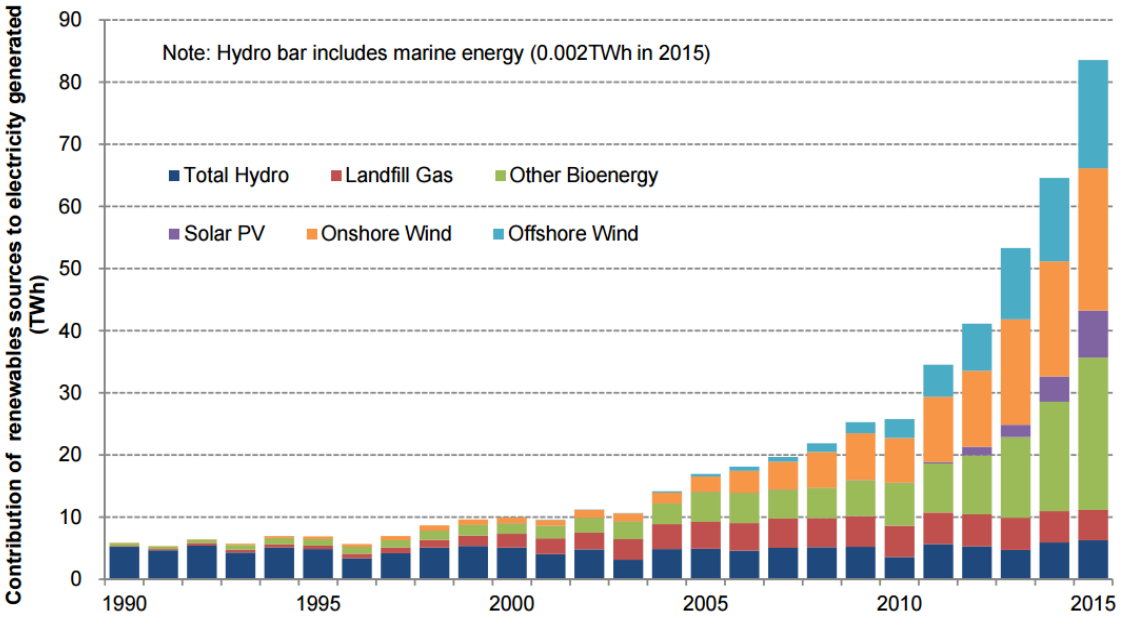

Figure 1.2: Electricity generated from renewable sources in the UK [8].

Globally, wind and solar are the fastest growing sources of electricity and are now technologically mature and affordable, with the cost of utility-scale solar PV dropping by two thirds between 2010 and 2015 [9]. The levelised cost of electricity (LCOE) for wind and solar have reduced significantly and are now approaching grid parity with other traditional sources of electricity [10]. As their contribution increases the problems of intermittency and integration must be addressed by improvements in energy storage and better site location so that the energy can be used locally [10]. The total global PV production in 2015 is estimated at 63.2 GW_P and brings the total installed capacity to about 227 GW_P, a growth of about 37% since 2014 [11], [12].

The first generation of solar PV is based on crystalline silicon wafers: monocrystalline (mono-Si) and polycrystalline (poly-Si). These accounted for about 93% of global PV production in 2015 (mono-Si: 24%, poly-Si: 69%) [12]. Second generation PV uses thin film technologies to reduce material usage and includes copper indium gallium selenide (CIGS), cadmium telluride (CdTe) and amorphous silicon (a-Si). Second generation PV accounts for the other 7% of global PV production in 2015 (CIGS: 1.7%, CdTe: 4.0%, a-Si: 0.9%) [12].

The third generation of PV covers a much broader range of technologies, from high efficiency multi-junction (tandem) cells and concentrated PV (CPV), through to the emerging technologies of organic, dye-sensitised solar cell (DSSC), perovskite and quantum dots [13], [14]. Tandem and CPV use high efficiency solar cells (> 30%), but are only suitable for specialist applications (e.g. space) and for areas of high direct irradiation. The emerging technologies are looking to reduce costs by using non-toxic, abundant materials and cheap processing methods. At present the majority of third generation technologies are still at the research and development stage and any commercial production is at very low levels.

It was not until the early 1980s that the first polymer based solar cells were developed [15], [16]. The first breakthrough was in 1986 when Tang produced a bilayer cell using two different dyes and obtained a power conversion efficiency (PCE) of 1% [17]. In 1992, Heeger et al. reported on photoinduced electron transfer from a polymer to a fullerene [18]. In 1995, the same group reported on the first bulk heterojunction (BHJ) polymer solar cell where the active layer was a blend of polymer and fullerene and had an efficiency of 2.9% [19]. This was a key discovery and led to a step change in OPV research, with an exponential growth in papers being published [20].

Efficiencies of best performing OPVs have exceeded 10% in recent years, with Mitsubishi reaching 11.1% in 2012 and Toshiba reaching 11.2% in 2015 [21]. Toshiba have also produced record breaking modules (8.7%, area: 802 cm^2) and mini-modules (9.7%, area: 26 cm^2) (see Figure 1.3) [21]. In early 2016, Heliatek achieved an efficiency of 13.2% for a multi-junction OPV device [22].

Research into organic photovoltaics (OPVs) has grown exponentially over the last decade but OPVs have not yet reached true commercial viability. The prospect is that OPVs will allow solar cells to be produced cheaply, based on solution processing, on flexible substrates, and at lower temperatures than silicon cells, reducing embodied

energy. At present OPVs lag far behind silicon based solar cells in terms of efficiency, cost (in terms of £/W_P) and lifetime. It is likely that initially the two technologies will complement each other with OPVs providing cheap consumer power sources whilst silicon based PV is used for energy production. In the long term it is feasible that OPVs will also be used in mainstream energy generation.

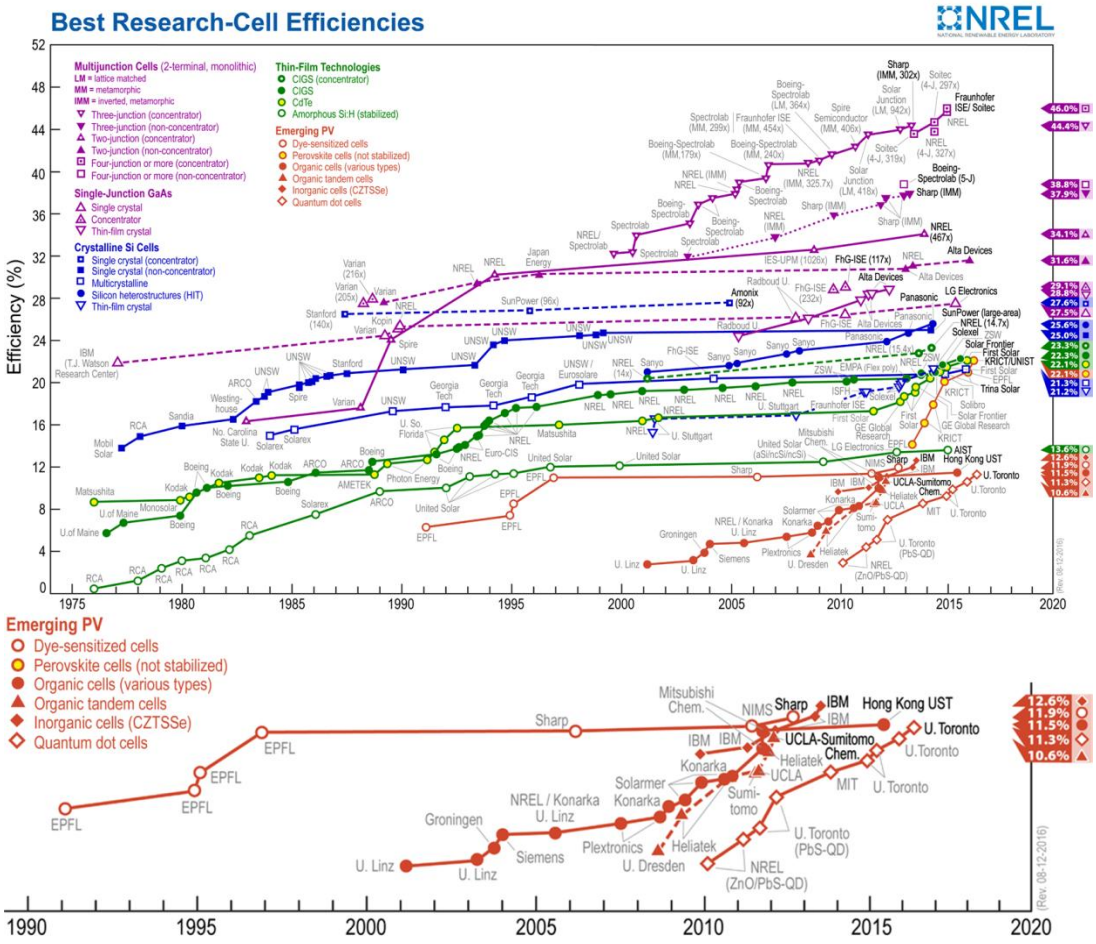

Figure 1.3: NREL regularly update this chart which shows the progress being made in various technologies by the world's leading laboratories. The progress of emerging PV is highlighted at the bottom. [21], [23].

One area where OPVs may have an advantage over traditional PV technologies is in building integrated photovoltaics (BIPV). The most common form of BIPV at present is silicon-based and it is usually applied as either wall cladding or roof tiles, as this suits its rigidity and opacity [24], [25]. Flexible thin film PV is also being used in BIPV, especially flexible amorphous silicon, as it is less sensitive to water and air than the other thin film technologies and can be semi-transparent [24], [25]. DSSCs and OPVs have a great potential in BIPV, as they offer cheap R2R manufacturing onto flexible lightweight substrates and offer a degree of transparency, so they could be used for clear

and tinted glazing [24]–[27]. OPVs have the advantages of ease of processing, low weight, flexibility, semi-transparency, and the ability to be coated onto substrates, compared to silicon-based PV, which is constrained to heavy, rectangular flat panels [24], [26], [28].

PolySolar in the UK are already providing a range of BIPV products including clear CdTe glazing, tinted a-Si glazing, mono-Si and poly-Si wall cladding and they are currently developing BIPV products based on OPVs [29]. Heliatek in Germany have developed a BIPV based on OPVs, HeliaFilm®, which is semi-transparent, flexible and lightweight, and has been installed on several demonstration projects in Europe and Asia [30]. At the Milan EXPO 2015, Belectric GmbH in conjunction with Merck Chemicals installed an OPV solar roof for the German pavilion, demonstrating the potential for OPVs in BIPV [31].

At present the increased cost and shorter lifetimes of BIPV products compared to standard building products are a deterrent [25]. Future regulations requiring buildings to be energy self-sufficient would increase the take-up of this technology. Financial incentives have been shown to stimulate the take-up of this technology in France and Italy [25].

OPVs still face the dilemma of balancing advances in efficiency, scalability, cost and lifetime and it is only once all of these are improved that OPVs will be ready for commercialisation [20].

1.1 Highlights and Structure of this Thesis

This thesis focuses on outdoor monitoring of OPVs, with the aim of improving the stability and performance of OPV cells and modules under real world conditions. This is important as in order for OPVs to become commercially viable they must make the transition from small laboratory cells towards larger modules that can be of real use.

The highlights of this research are:

- The first report on benchmarking of OPV modules against other PV technologies in outdoor test environment.
- Detailed analysis of OPV module performance as a function of temperature and irradiance under outdoor conditions.
- Demonstration of improved yield using three-dimensional structured OPV modules.

- Demonstration of improved performance, spectral response and stability of OPVs using luminescent downshifting (LDS) coatings consisting of both single and multiple-dye blends.

The structure of this thesis is as follows:

Chapter 2 provides a background of the science behind this research.

Chapter 3 discusses the current state of outdoor monitoring of OPVs, structuring of PV cells and modules, and the use of LDS materials with PV.

Chapter 4 discusses the experimental methods used including a full description of the outdoor monitoring setup on the roof at Bangor. The various characterisation and fabrication techniques are described.

Chapter 5 is the first of three results chapters and presents the results from various outdoor monitoring campaigns, including a comparison of the outdoor performance of different types of OPV modules and other PV technologies.

Chapter 6 presents the results from indoor characterisation and outdoor monitoring of four different corrugated OPV modules. Also presented are outdoor results from commercial OPV strips laminated onto a corrugated substrate.

Chapter 7 reports on detailed optical characterisations of a number of discrete and multiple-dye LDS blends, lifetime testing of OPV cells and modules coated with a selection of these dyes.

Chapter 8 summarises the main results from the thesis and discusses possible directions for further work.

Chapter 2.Scientific Background

2.1 Nature of Light

The sun emits radiation with a spectrum approximating a blackbody source at 5760 K and this is reasonably constant when it hits the upper atmosphere (solar constant: ~1.37 kW/m^2) [5]. As light passes through the atmosphere the radiation is attenuated by: Rayleigh scattering by molecules in the air (especially at shorter wavelengths); Mie scattering by aerosols and dust particles; absorption by atmospheric gases (especially ozone, oxygen, water and carbon dioxide) [32]. On a clear sunny day, with the sun directly overhead, ~18% of incoming irradiation will be absorbed, ~3% will be reflected back out into space, ~70% will reach the Earth's surface as direct radiation and ~7% will reach the Earth's surface as diffuse radiation [33]. Depending on the angle of incidence, it passes through different amounts of the atmosphere; this pathlength is called the air mass (AM) and affects the level of attenuation (Figure 2.1).

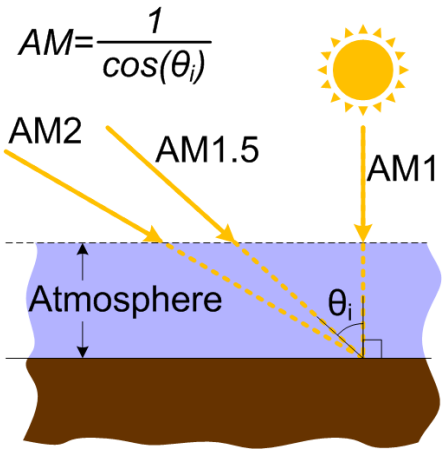

Figure 2.1: Definition of Air Mass.

As the incidence angle (θ_i) increases, the energy received at sea level reduces ($E \cong E_{AM1} \cos \theta_i$ [assuming a non-refractive atmosphere]) and the spectrum is shifted towards the infra red as more blue light is filtered out ("redder" at sunset/sunrise and "bluer" at noon) [34], [35]. Figure 2.2 shows the spectra of solar radiation received at

the top of the atmosphere (AM0) and the American Society for Testing and Materials (ASTM) reference at sea level (AM1.5G).

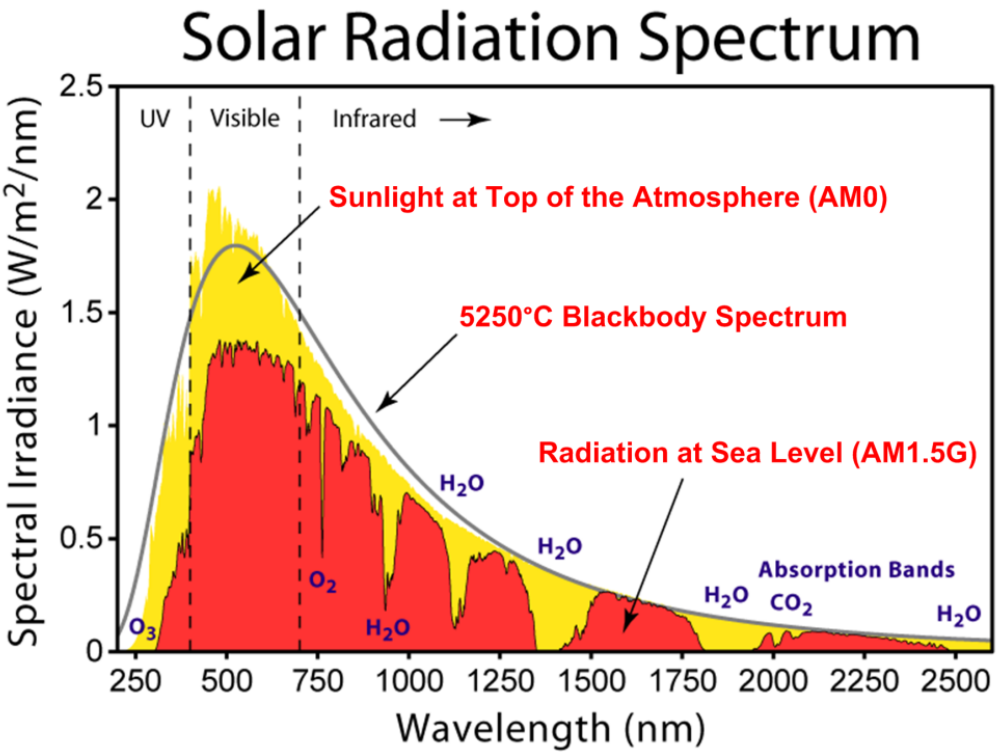

Figure 2.2: Solar radiation spectra (based on ASTM Terrestrial Reference Spectra) [36], [37].

The total irradiation received by a surface (global radiation) comes from various sources: direct normal irradiation (DNI) comprising beam and circumsolar radiation (bright disk within 2.5° from the centre of the sun); diffuse radiation; ground reflected (albedo) radiation which affects inclined surfaces (e.g. PV modules) (Figure 2.3a) [38], [39]. The albedo factor depends on the nature of the reflective ground surface. Under conditions of intermittent cloud on a sunny day there will be peaks of radiation as the sun passes an edge or gap in the clouds caused by edge of cloud lensing effects (Figure 2.3b) [40]. These cloud lensing events can cause irradiation to exceed normal direct irradiation by over 20% and with silicon PV can lead to even greater increases in yield, as the panels will be cooler having been previously exposed to diffuse sunlight [40].

To compare solar modules, a reference solar spectrum has been designed: the AM1.5 G173-03 (2012) spectrum is based on the average for the 48 contiguous states of the US, and has an integrated intensity of 963 W/m^2 which, via international consensus, is re-standardised to 1000 W/m^2 [36], [41].

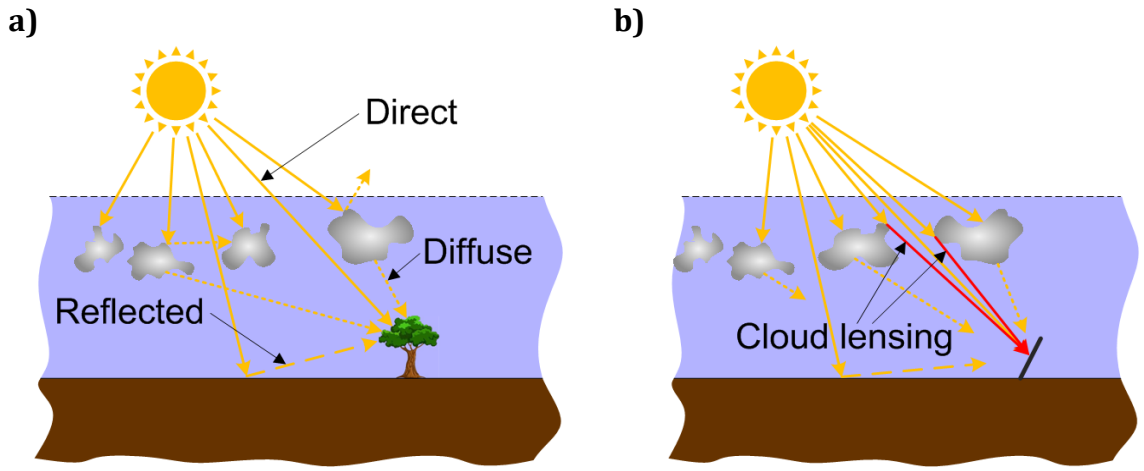

Figure 2.3: Solar radiation: a) direct, diffuse and reflected radiation; b) cloud lensing.

Several models have been proposed for calculating the three components of solar radiation incident on a tilted surface: direct, diffuse & ground reflected [42]. The calculation for direct radiation is based on the ratio of beam angle to solar zenith angle. The modelled values for ground reflected radiation have only a small contribution to the overall figure and are dependant mainly on direct radiation, with the influence from diffuse radiation often assumed as being isotropic. It is the calculations for diffuse radiation which show the biggest differences and are based on two different hypotheses. The early isotropic models proposed by Liu and Jordan assumed that the intensity of diffuse radiation is uniform across the whole sky [43]. Later models were based on the anisotropic principle where diffuse radiation is non-uniform and has multiple components: circumsolar, horizon brightening and isotropic radiation [44], [45]. For the purposes of global horizontal irradiance (GHI) calculations in this thesis, the isotropic clear sky model proposed by Bird and Hulstrom was utilised [46]. It is available as an Excel VBA program [47].

2.2 Solar Photovoltaic Characteristics

Electrical characterisation of a solar cell is performed by measuring its current-voltage (IV) curve (Figure 2.4). If the active area is known then the current density (J) can be calculated. From this curve the following parameters can be obtained: short circuit current (I_{SC} or J_{SC}); open circuit voltage (V_{OC}); maximum power point (MPP) and corresponding current (I_{MPP}) and voltage (V_{MPP}); fill factor (FF) (Equation 2.1).

$$FF = \frac{V_{MPP} \times I_{MPP}}{V_{OC} \times I_{SC}} \quad 2.1$$

If the irradiance is known then the power conversion efficiency (PCE) can be calculated (Equation 2.2).

$$PCE = \frac{Power_{Module}}{Power_{Irradiance}} = \frac{V_{OC} \times I_{SC} \times FF}{Irradiance \times Area_{Module}} \quad 2.2$$

It is important to accurately measure the active area of the cell and the power of the irradiance if the PCE and J_{SC} values are to be accurate [48].

Examination of the IV curve allows the series resistance (R_S) and shunt resistance (R_{SH}) to be assessed [49]. Once these parameters are known (the most important being I_{SC}, V_{OC}, FF and PCE) they can be used to compare different solar cells. To compare IV curves it is usual to perform these tests under standard test conditions (STC): Irradiance = 1000 W/m², Spectrum = AM1.5 G173-03 (2012), Module temperature = 25°C.

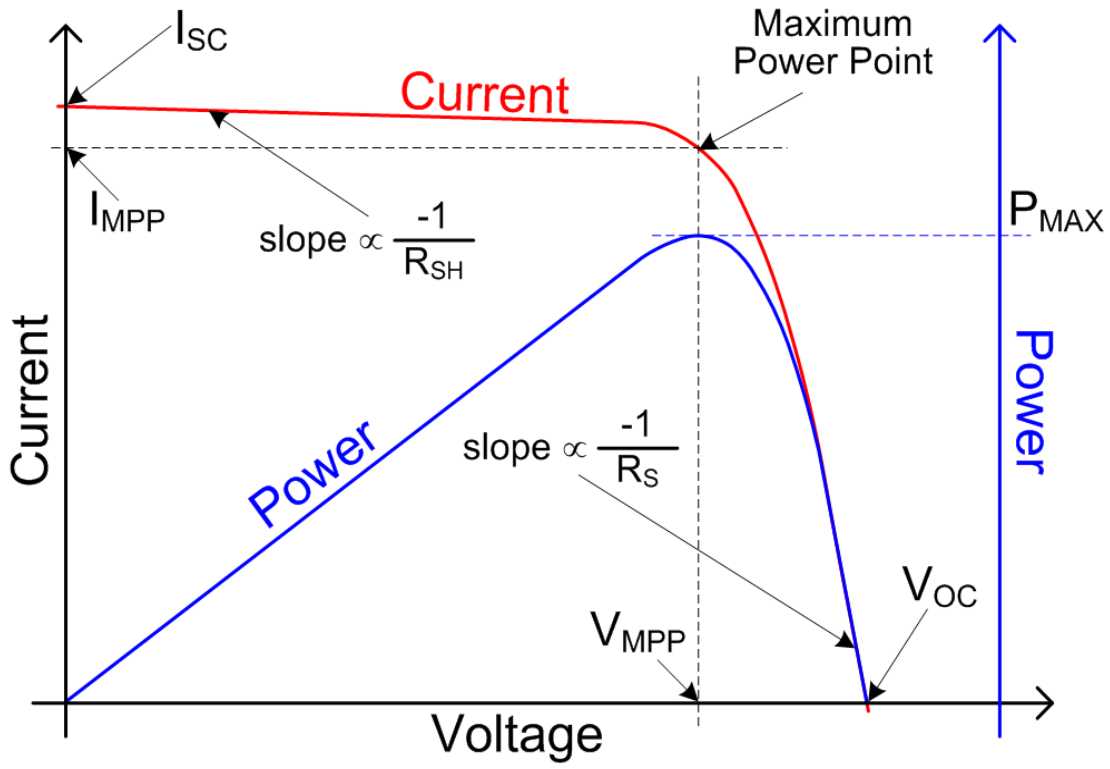

Figure 2.4: Current-voltage (IV) and power curves for a solar cell highlighting main parameters. The maximum power point (MPP) denotes the place on the I-V curve where power is at a maximum.

2.3 Equivalent Circuit Models

An ideal solar cell can be modelled as a current source in parallel with a diode (Figure 2.5a) [50]. Under dark conditions the IV behaviour will be that of a diode and under illumination this will be shifted by the photocurrent from the current generator (I_{PH}), which is directly proportional to the irradiance (Figure 2.5b) [50]. The current generated by an ideal solar cell is given by Equation 2.3 (derived from the Schockley diode equation), where I_L is the photocurrent, I_0 is the diode's reverse bias saturation current, n is the diode's ideality factor, q is the elementary charge, k is Boltzmann's constant and T is the cell temperature [50].

$$I = I_L - I_0\left[exp\left(\frac{qV}{nkT}\right) - 1\right] \qquad 2.3$$

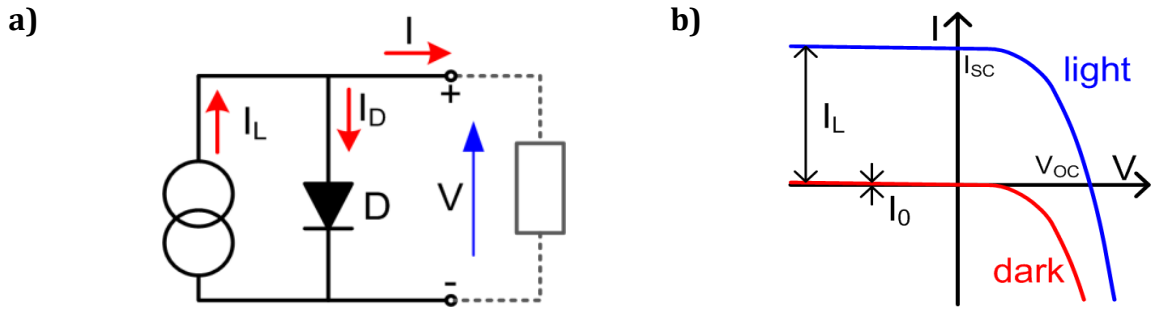

Figure 2.5: a) Equivalent circuit of an ideal solar cell. b) IV curves under dark and light conditions (I_{PH} is the photo-generated current and I_0 is the reverse bias saturation current of the diode).

In practice a solar cell will have parasitic resistances, known as shunt resistance (R_{SH}) and serial resistance (R_S), and these can be modelled by the equivalent circuit shown in Figure 2.6.

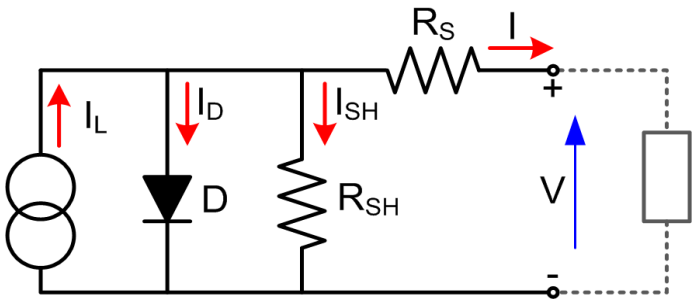

Figure 2.6: Equivalent circuit for a solar cell including parasitic resistances.

In an OPV device, low R_{SH} comes from problems in the active layer causing recombination (morphology, traps etc) as well as recombination further away from the

dissociation site (e.g. near the electrodes). High R_S comes from low charge mobilities and problems at the interfaces between layers and at the electrodes affecting conductivity.

Equation 2.4 shows the current in a solar cell allowing for the parasitic resistances and taking into account that $I_{SC} = I_L$ [50].

$$\boldsymbol{I = I_{SC} - I_0\left[exp\left(\frac{q(V + IR_S)}{nkT}\right) - 1\right] - \frac{V + IR_S}{R_{SH}}} \qquad 2.4$$

Equation 2.5 shows the derivation for V_{OC} based on the simple one-diode model:

$$\boldsymbol{V_{OC} = \frac{nkT}{q} ln\left(\frac{I_L}{I_0} + 1\right)} \qquad 2.5$$

2.4 Physics of Organic Photovoltaics

2.4.1 Organic Electronics

The physics of organic electronics have been studied for many years, conduction in polyaniline first being reported on in 1862, but it was not until 1989, with the discovery of organic light emitting diodes (OLEDs), that organic electronics became a heavily researched area [51], [52]. OLEDs are now widely used in active matrix displays, and organic electronics are being used for thin film sensors and transistors, e-paper displays and OPVs [52], [53].

Broadly speaking organic semiconductors are split into two main categories: small molecules (monomers and oligomers) and polymers. Alongside these are: fullerenes, nanotubes, graphene and other similar carbon-based structures; these have complimentary properties to small molecules and polymers [54].

Organic semiconductors share a common feature: a conjugated backbone, consisting of alternating single and double carbon-carbon bonds with a planar structure (see Figure 2.7a) [55]. The single bonds each consist of one σ bond and the double bonds consist of one σ and one π bond. The σ bonds are highly localised and are based on an sp^2 hybridisation, whereas the π bonds are based on the unhybridised p_z orbital, located perpendicular to the sp^2 plane, and allowing the π electrons to be delocalised along the backbone (see Figure 2.7b) [55]. The σ-σ* energy gap is much greater than the π-π* energy gap and therefore the π-π* energy bands form the basis for semiconducting properties of the polymer, as the π electrons allow charge transfer along the conjugated backbone (Figure 2.7c). The upper edge of the π band forms the valence band (VB) and

is called the highest occupied molecular orbital (HOMO). The conduction band (CB) is formed by the empty states of the π* orbitals and is called the lowest unoccupied molecular orbital (LUMO). The gap between the HOMO and LUMO defines the electrical band gap of the molecule (E_G). Charge transfer between different molecules occurs when the π orbitals on neighbouring molecules overlap, as conjugated molecules are usually planar. When an electron in the HOMO is excited with sufficient energy, either thermally or by an incoming photon, it will cross the band gap to the LUMO leaving behind a hole in the HOMO. These electron-hole pairs, known as excitons, are strongly bound by Coulombic attraction (0.3-1 eV) due to the low dielectric constant of the polymer and are not free to separate [56]. Excitons are neutral quasi-particles and therefore not influenced by external electric fields. Excitons travel by hopping between localised states, as HOMOs and LUMOs cannot form a continuous VB or CB. Normally, unless the electron and hole can dissociate into free charge carriers, they will recombine either radiatively or thermally.

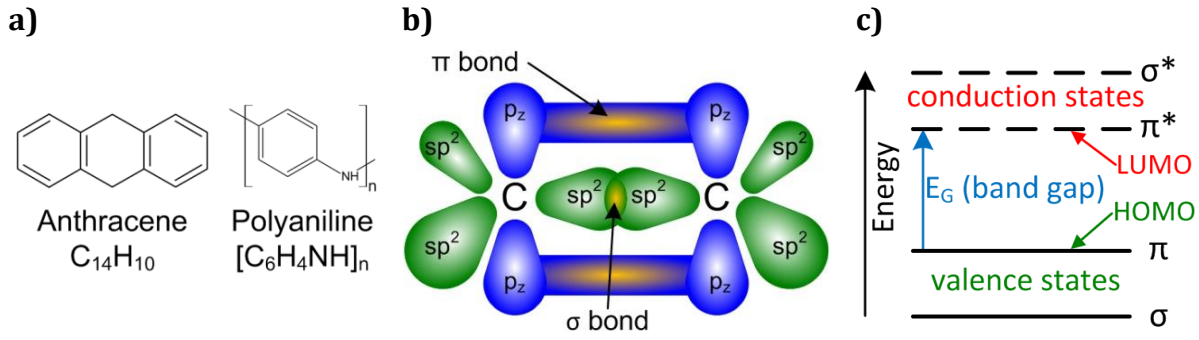

Figure 2.7: a) Examples of conjugated molecules. b) sp^2 and p_z orbitals and π- and σ-bonding (p_z orbitals perpendicular to sp^2 plane). c) Energy levels for σ-σ* and π-π* bands.

2.4.2 Organic Photovoltaics

All photovoltaic solar cells convert the energy of incident photons into electrical energy by the photovoltaic effect. Figure 2.8 shows a simplified energy diagram of an organic solar cell, consisting of donor and acceptor polymers sandwiched between two electrodes, and illustrates the principle processes: light is absorbed in the donor (analogous processes can happen with absorption in the acceptor) and generates an exciton (1); the exciton diffuses towards a donor-acceptor (D-A) interface (2); at the interface the exciton will rapidly dissociate into separate free charges, via the charge transfer (CT) state, due to the potential at the interface (3); the separated carriers are

free to migrate to the electrodes under the influence of a field created by the work function differences between the cathode and anode (4); the charges are collected by their respective electrodes (5).

There are several competing recombination processes which take place (Figure 2.8): geminate recombination by either exciton decay (6) or recombination through the charge transfer state (7); non-geminate recombination of free carriers (8) [55], [57], [58]. These recombination processes will either be radiative (if allowed) or thermal.

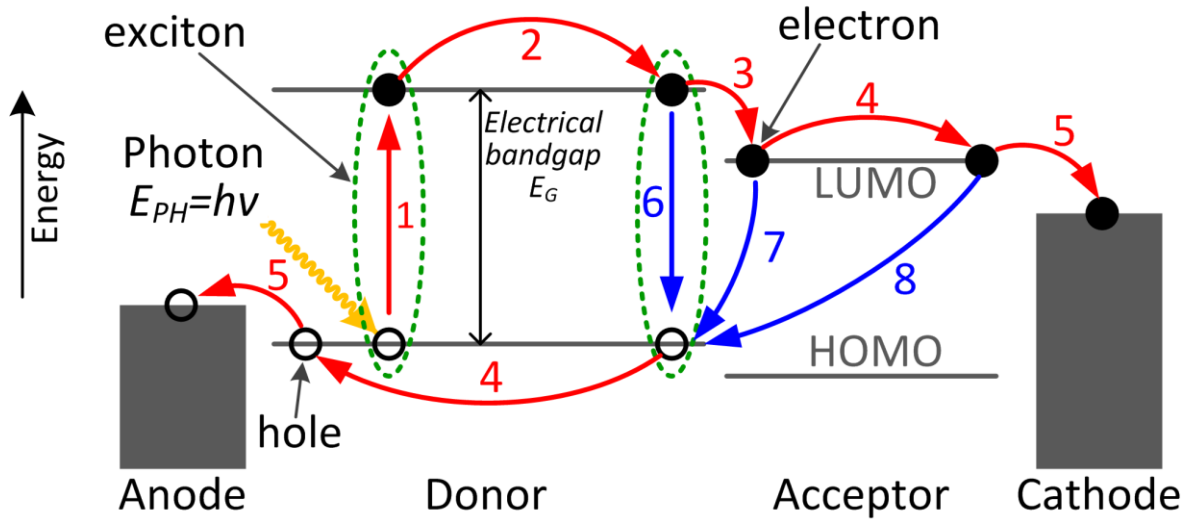

Figure 2.8: Photovoltaic processes within an organic solar cell.

The power conversion efficiency (PCE) of a solar cell is dependent on each of the following processes working at their maximum potential (Equation 2.6) [59].

$$PCE = \eta_{Opt} \times \eta_{Abs} \times \eta_{Diff} \times \eta_{Diss} \times \eta_{Trans} \times \eta_{Coll} \qquad 2.6$$

Optical (η_{Opt}): An incoming photon must reach the active layer. Reflection from the front surface (or subsequent interfaces) or absorption by the nominally transparent front substrate will reduce the number of available photons.

Absorption (η_{Abs}): An incoming photon with sufficient energy ($E_{PH} \geq E_G$) is absorbed by a semiconducting material and optically excites an electron which will be raised from the HOMO to the LUMO energy level forming an exciton. The efficiency of this process is determined by the ability of the material to absorb photons, based on the bandgap (E_G), optical absorption coefficient and thickness of the material. Organic semiconductors

have a relatively high optical absorption coefficient and complete absorption can be accomplished in film thicknesses of only a few hundred nanometres.

Diffusion (η_{Diff}): Excitons can travel along or between conjugated polymers via hopping and tunnelling. They have a short diffusion length (~10 nm) and lifetime (nanoseconds) compared to free carriers in inorganic semiconductors (100 μm and microseconds). The charge mobility in conjugated polymers is much lower (1-0.1 cm^2/Vs) compared to inorganic semiconductors (mono-Si: 300-900 cm^2/Vs, poly-Si: 50-100 cm^2/Vs) [60]. The exciton will diffuse through the donor material until it either recombines or dissociates. The efficiency of this process is determined by the lifetime and diffusion length of the exciton and by the density of defects where recombination can occur.

Dissociation (η_{Diss}): Exciton dissociation (charge separation) will normally only occur at a step change in the energy level, where the LUMO offset is greater than the exciton binding energy, and is a rapid process (femtoseconds) [18], [61]. This mainly occurs at interfaces between different polymer types (donor and acceptor), but can also occur at the electrodes and at defects in the lattice (e.g. absorbed oxygen or impurities). The electron will be transferred across to the acceptor leaving the hole in the donor. This forms a CT complex, which is bound by a much lower energy than the exciton, as the electron and hole are further apart [53].

Transport (η_{Trans}): The charges will be able to separate, under the influence of the electric field formed by the mismatch of the work functions of the two electrodes. The free carriers will be able to drift, via hopping processes, towards their respective electrodes (electrons → cathode, holes → anode). The efficiency of this process is determined by the electron and hole mobilities. Losses will occur if there are electrical shorts, high bulk resistance or traps (e.g. lattice defects). If the electron-hole pair recombine after charge separation this in non-geminate recombination [58].

Collection (η_{Coll}): Once they reach the electrodes the electrons and holes can be extracted to generate a photocurrent. The efficiency of this process is determined by the Fermi levels of the electrodes ($E_{Fcathode} < E_{LUMOacceptor}$ and $E_{Fanode} > E_{HOMOdonor}$) and should be very efficient [59].

2.4.3 OPV Device Structures

Most OPV devices consist of a transparent conducting window (front electrode), an active layer and a rear electrode layer, usually a metal. The front electrode is often

made from a transparent conducting electrode, such as indium tin oxide (ITO), coated onto a substrate, which can either be rigid (glass) or flexible. The active layer has evolved through four main variants. The simplest and earliest devices have a single organic material for the active layer (homojunction) and rely on the difference in work functions at the electrodes to separate the excitons. This is an inefficient mechanism, due to the short diffusion length of excitons and likelihood of recombination at the electrodes, and provides PCEs of less than 0.1% (Figure 2.9a) [62]. An improvement on this was the formation of a Schottky barrier at one contact (e.g. a donor polymer and a low work function electrode is commonly used), which provides a more efficient means of exciton dissociation and PCEs of up to 2% have been obtained (Figure 2.9b) [15], [62], [63]. The bilayer device proposed by Tang was a significant improvement and was based on two separate layers of organic material, one a donor and the other an acceptor (Figure 2.9c) [17]. The donor-acceptor (D-A) interface provides an efficient location for exciton dissociation, but only those excitons generated within a diffusion length of the interface are able to dissociate. The problem of the majority of excitons not reaching the junction before recombining, due to the short diffusion length, was overcome by mixing the donor and acceptor materials together before fabricating the device. The active layer forms a bulk heterojunction (BHJ), with a dispersed structure and a very large D-A interface area (Figure 2.9d) [62]. Subsequently wherever an exciton is generated it is within a short distance from a D-A interface and can more readily dissociate. The dispersed structure will allow the free carriers to reach the relevant electrode. As both donor and acceptor materials extend to each electrode it is necessary to add extra functional layers to select either holes or electrons, based on the work functions of the layers. It is possible for “islands” of donor or acceptor material to form, which are isolated from the electrodes, and these can limit charge transport and increase bimolecular recombination [64]. This type of device dominates present day solution processed OPV technology and research, and is the focus of the research in this thesis.

Improvements in morphology of the active layer are sought by improving a number of different factors: solvents, additives, donor/acceptor ratio, annealing time and annealing temperature [65]–[67]. These can all be tuned to improve performance. Ordered heterojunctions are another technique; a more regular organisation of the active layer can be achieved by nanoimprint lithography of the donor material before coating with the acceptor material (Figure 2.9e) [68]–[70]. So far this approach has yielded improved FF, but not an increase in PCE, as it is normally accompanied by a

reduced J_{SC}. Finally, molecular heterojunctions can be used to self-assemble donor and acceptor morphologies, with fullerene covalently bonded into a donor-acceptor backbone (known as double-cable polymers) [71]–[73].

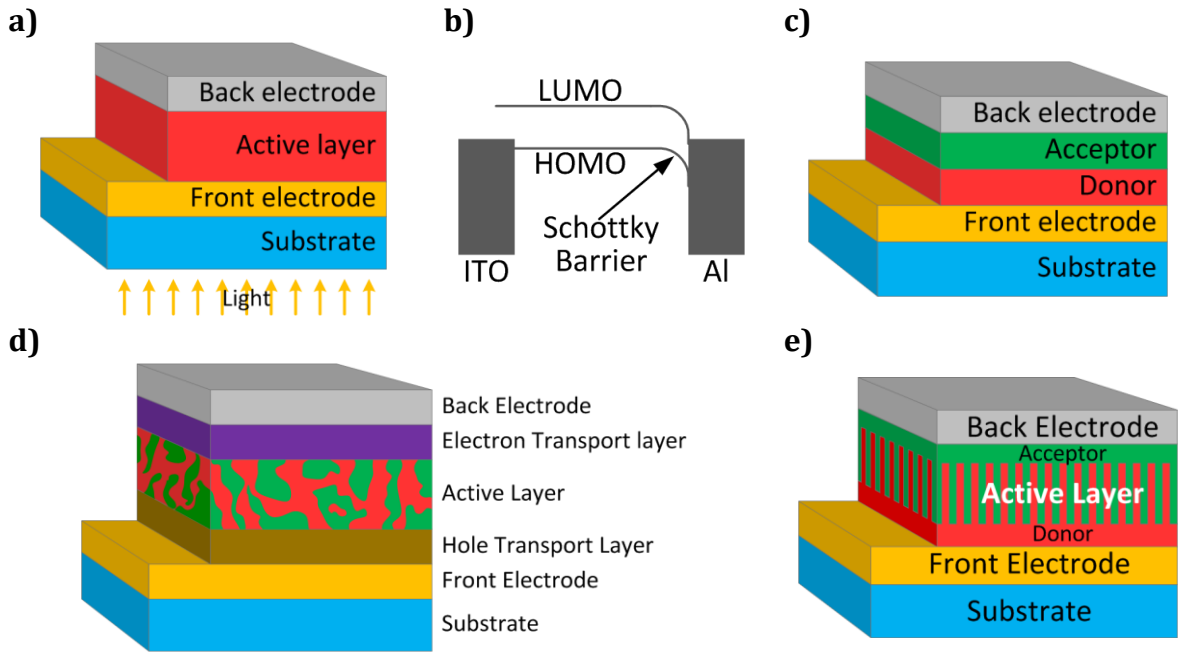

Figure 2.9: OPV device structures: a) Homojunction – cross section; b) Energy diagram showing Schottky barrier; c) Bi-layer device – cross section; d) Bulk heterojunction – cross section; and e) Ordered heterojunction – cross section.

2.4.4 OPV Materials

Active Layer: For solution processed OPVs, the active layer within BHJ devices commonly consists of a conjugated polymer as the donor and a fullerene derivative as the acceptor. Figure 2.10 shows the structure of materials commonly used in OPVs. The most commonly reported donor and acceptor materials are poly(3-hexylthiophene) (P3HT) and phenyl-C_{61}-butyric acid methyl ester ($PC_{61}BM$) respectively. A common variant of $PC_{61}BM$ is $PC_{71}BM$, based on C_{70}. C_{70} is ovoid in shape leading to better light absorption and $PC_{71}BM$ has a higher LUMO which increases V_{OC} [74]. P3HT is an excellent absorber and transporting material but having a band gap of 1.9 eV means that light of over 650 nm cannot be absorbed. In 2006, Scharber et al. published design rules for donors in BHJ devices using $PC_{61}BM$ as a common acceptor and showed that efficiencies above 10% were possible [75]. One area of research is to find active layer materials with lower bandgaps, which will allow light at longer wavelengths to be absorbed [75], [76]. One of these materials that has been extensively studied at Bangor is poly[2,6-(4,4-bis-(2-ethylhexyl)-4H-cyclopenta[2,1-b;3,4-b0]dithio-phene)-alt-4,7-

(2,1,3-benzothiadia-zole)] (PCPDTBT), which has a bandgap of ~1.5 eV extending absorption into the infrared region [67], [74], [77]–[79]. Most of these materials have sidechains, which are required to ensure the solubility of the polymers and fullerenes. This is particularly important in the fabrication of BHJs as the active layer is produced from a D-A blend in solution. Under optimised annealing conditions the active layer will phase segregate, such that the polymer becomes more crystalline, the PCBM will aggregate, and acceptor (donor) enrichment will occur at the cathode (anode) interfaces, leading to improved performance and FF [80]–[82]. Fullerene derivatives are the dominant acceptor material, but have the disadvantages of weak absorption and limited spectral breadth, so most research is focused on new oligomer and polymer acceptor materials [83].

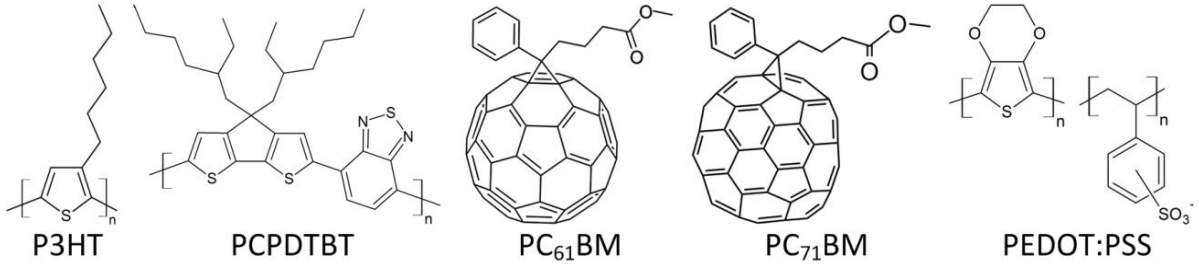

Figure 2.10: Common OPV materials: P3HT, PCPDTBT, $PC_{61}BM$, $PC_{71}BM$, and PEDOT:PSS.

Functional Layers and Electrodes: To minimise recombination, an electron transport layer (ETL) which has high electron mobility and acts as a hole blocker, and a hole transport layer (HTL) which has high hole mobility and acts as an electron blocker, are normally used in OPVs. Common HTLs are poly(3,4-ethylenedioxythiophene) polystyrene sulfonate (PEDOT:PSS) (Figure 2.10) and molybdenum trioxide. Common ETLs are zinc oxide and calcium. PEDOT:PSS and ZnO also improve the cell structure by forming a smooth, planarised surface for the active layer to be deposited on, which reduces pin hole defects (responsible for reduced shunt resistance and FF) [84].

Substrates: although the majority of laboratory test cells are fabricated on glass, as it is a rigid, stable material that is easily handled and readily available, one of the advantages of OPVs is that they can be fabricated onto flexible plastic substrates. A substrate must have low absorption over the desired range of wavelengths, compatibility with OPV materials and good barrier properties. Common plastic substrates are polyethylene terephthalate (PET) and polyethylene naphthalate (PEN). These are often assembled in

multi-layer structures with interfacial barrier layers of thin oxide films to improve resistance to transmission of oxygen and water [85].

Front Electrode: ITO is the most common transparent electrode used in OPVs, but indium is a rare element and other replacements are being investigated: silver nanowires (AgNW), ZnO doped with aluminium (AZO), silver grid with highly conductive PEDOT:PSS, carbon nanotubes and graphene [84], [86]–[90].

2.4.5 OPV Device Geometries

There are two different device geometries (see Figure 2.11): "Normal" geometry, which was used for all early devices, where the ITO acts as the anode; "Inverted" geometry where the ITO acts as the cathode.

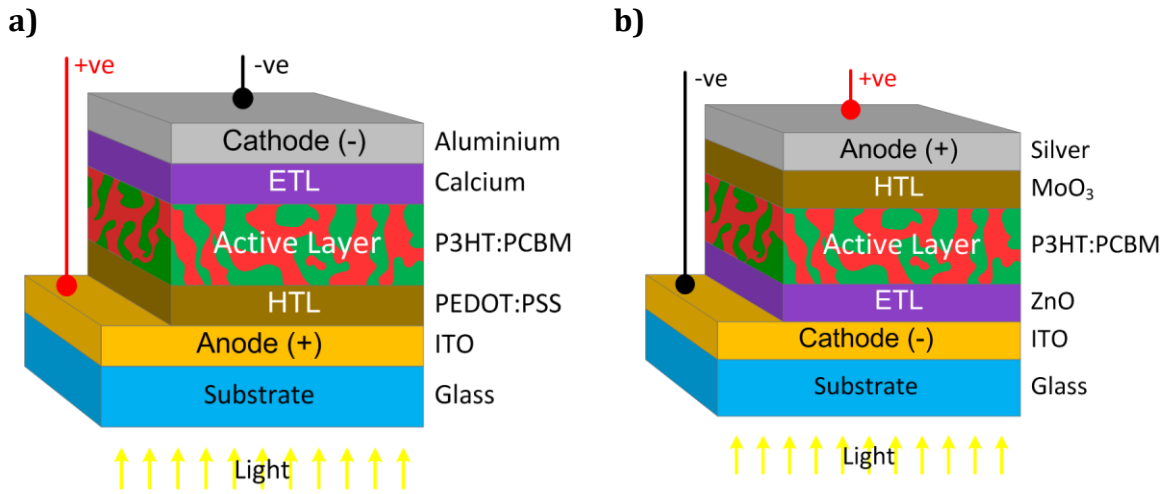

Figure 2.11: OPV device geometries: a) "Normal" geometry OPV device; and b) "Inverted" geometry OPV device.

The early ("normal") devices used PEDOT:PSS as the HTL and calcium as the ETL with aluminium for the cathode. Calcium and aluminium are easily oxidised and readily react with water. In addition, PEDOT:PSS is highly acidic and is usually deposited from an aqueous dispersion, with the device being heat treated to drive off the water before the active layer is applied. Consequently, these devices are particularly prone to degradation. Improvements were achieved using "inverted" geometry, with ZnO coated onto the ITO (either by sputtering or sol-gel deposition), followed by the active layer blend and then evaporation of MoO_3 followed by silver as the high work function back electrode. This has produced cells that are more resilient to degradation and it has the advantage that silver can be printed from liquid paste. Inverted devices have the

advantage that polymers tend to phase separate towards the top surface during deposition, due to their lower surface energy, leading to higher concentrations of acceptors near the cathode and donors near the anode [91].

2.4.6 OPV Stability and Causes of Degradation

Now that OPV cell efficiencies are exceeding 10%, an important area of research is looking at how to improve the stability of OPV cells and modules. High efficiency and longevity are key to enabling OPVs to become commercially viable [92].

Causes of degradation and instability can be separated into two broad categories:

Intrinsic degradation: Caused by internal changes involving the materials of the cell, morphology changes in the D-A blend and physical delamination of the layers [93].

Extrinsic degradation: Caused by external triggers such as light (especially UV), temperature, oxygen and humidity. This type of degradation is closely linked to the impermeability of the encapsulation [93].

There are many different factors which affect stability and degradation in OPVs:

Morphology: For efficient BHJ cells it is important to be able to control the structure of the active layer, as this determines the efficiency of charge generation, transport and collection. The architecture of this layer is not always thermodynamically stable and exposure to sunlight for long periods leads to macro phase separation which leads to distances beyond the exciton diffusion length [92]. Methods of controlling the morphology include modification of the chemical structure of the donor and acceptor materials, crosslinking to lock in the required structure and the addition of a stabiliser (called a compatibilizer) to reduce interfacial tension and thereby suppress phase separation [92].

Photo-oxidation of donor materials: The π bonds in conjugated polymers are susceptible to chemical degradation, particularly by oxidation and exposure to UV light, leading to reduced photovoltaic properties [92]. The mechanism of this oxidation involves the energy transfer from photo-excited polymer to adsorbed oxygen to form singlet oxygen which can then react with the polymer [94]. As this process is dependent on the presence of oxygen and water catalysed by UV it can be reduced by efficient encapsulation and UV filtering [95]. It has also been shown that reducing the number of sidechains on the polymer will reduce photo-oxidation, improving stability [96].

Interface and electrode degradation: A major cause of degradation in normal geometry devices are electro-chemical reactions at the ITO and aluminium electrodes. The cathode is commonly a thin layer of calcium with a thicker layer of aluminium on top. Both these metals are highly reactive due to their low work-function and are easily oxidised. This leads to a change in the work-function of the cathode which reduces its efficiency at electron collection, effectively increasing the series resistance of the device [92]. The metal oxides are insulating which reduces electron transport. A thin layer of lithium fluoride or Al_2O_3 between the polymer and metal electrode improves the lifetime and electrical characteristics of OPV devices. This is thought to be due to the change in electrical properties of the interface (the work-function is reduced and a dipole layer is formed) and because the interfacial layer protects the polymer from the hot aluminium during sputtering and therefore reduces any reaction between them [94].

At the anode the interface between PEDOT:PSS and ITO is also susceptible to degradation. The indium in ITO is known to diffuse through the whole device and this erosion of the ITO occurs faster under heat and humidity [94]. PEDOT:PSS is highly acidic and is normally spin-coated from a water solution/suspension, followed by heating to drive off the water. PEDOT:PSS is highly hygroscopic and any absorbed water increases its sheet resistance, as well as being a source of water for degradation of the ITO and polymer layers [92], [94]. The use of additives such as dimethylsulfoxide (DMSO) can improve the operational stability of the PEDOT:PSS [97].

Delamination: Delamination between the functional layers of a device will increase the series resistance of the cell, leading to a drop in FF and a loss of performance. Delamination can be caused by loss of physical contact between the layers due to chemical reactions (typically photo-oxidation), which can cause voids and insulating patches to form [93]. Delamination can be exacerbated by mechanical stresses.

S-shaped IV curve: A common failure mechanism is the development of an S-shaped IV curve which leads to reduced FF and short circuit current (I_{SC}) [98]. This is due to an insulating interface in the device affecting the mobilities and causing a space charge build up [99], [100]. This is often caused by band bending, leading to a Schottky barrier forming at the interface and can be prevented by utilising an interfacial layer to better match the energy bands of the two layers [101]. Degradation of an interfacial layer (e.g. Ca or PEDOT:PSS) can lead to the mismatch in work functions at the interface [101].

2.4.7 Encapsulation

OPV devices are susceptible to degradation caused by atmospheric oxygen and water and good encapsulation which prevents their ingress is essential for stable outdoor operation [102]–[104]. As well as providing protection from the elements an ideal encapsulant will also be optically clear, a good adhesive, stable to thermal and light degradation, and an insulator. In the laboratory this is often done with epoxies and glass cover slips, but these are not viable for the production of commercial cells [105], [106]. One encapsulant used with silicon PV is polydimethylsiloxane (PDMS), which has excellent UV and thermal stability, relatively low moisture absorption, and is optically clear down to 280 nm [107]–[109]. OPVs are much more susceptible to degradation due to water and oxygen ingress than silicon PV and for long term protection, barrier materials are required with a water vapour transmission rate (WVTR) less than 10^{-3} g/m^2/day [110]. Roll to Roll (R2R) manufacturing techniques are often used to fabricate OPVs and a pressure sensitive adhesive is normally applied onto the R2R sheet for encapsulation. These flexible modules are commonly based on PET or PEN, but these materials have high transmission rates for both water and oxygen, so barrier layers (e.g. SiOx) are being applied by techniques such as atomic layer deposition [94], [111], [112]. The join between the two flexible substrates is important; otherwise diffusion of oxygen and water can occur from the edges. One method is to laser cut the module once it has been completed which simultaneously seals the edges [112]. Other materials are being looked at; for example polyurethane, although deposition on a R2R line is challenging [113].

2.5 Spectral Response

An ideal solar cell would absorb all available photons across the whole spectrum. However, there is a cut-off based on the band gap of the semiconductor which prevents any photons with energy less than the band gap from creating an exciton. At the blue end of the spectrum (high energy photons) the response is reduced due to reflection, absorption by the substrate and front surface recombination. In the intermediate wavelengths there will be losses, due to incomplete absorption and recombination. External quantum efficiency (EQE), also known as incident photon conversion efficiency (IPCE), is an indicator of the spectral response of a solar cell.

2.6 Shockley Queisser Limit

In 1960 Shockley and Queisser determined the limit for the PCE of an ideal solar cell, depending on a balance between electron generation (from photon energy, band gap and spectrum losses) and radiative recombination, recently updated by Rühle to 33.7% (Figure 2.12b) [114], [115]. Many incoming photons are not absorbed ($E_{PH}<E_G$) and some of the energy of the photons that are absorbed is lost to thermalisation (Figure 2.12b). Janssen and Nelson examined this limit in view of OPVs and proposed a limit of 20-24%, allowing for a 0.3-0.5 eV energy offset at the D-A interface [116].

a)

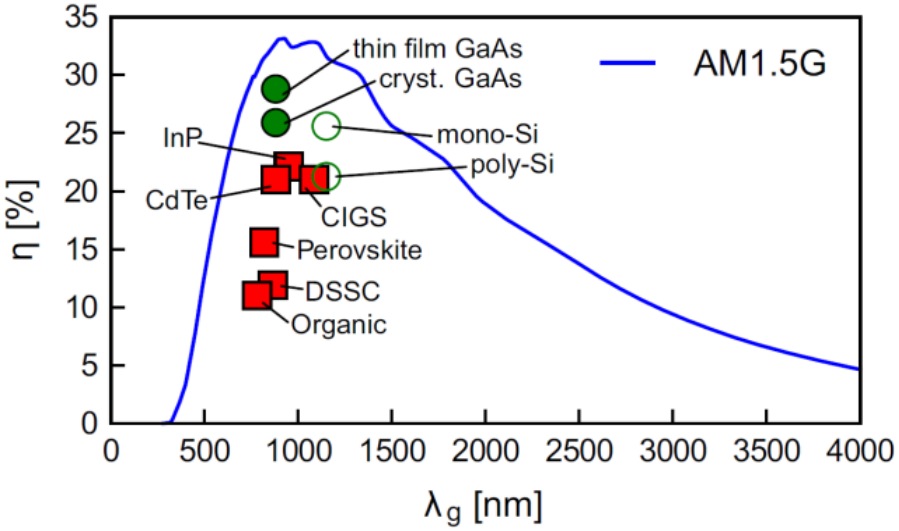

b)

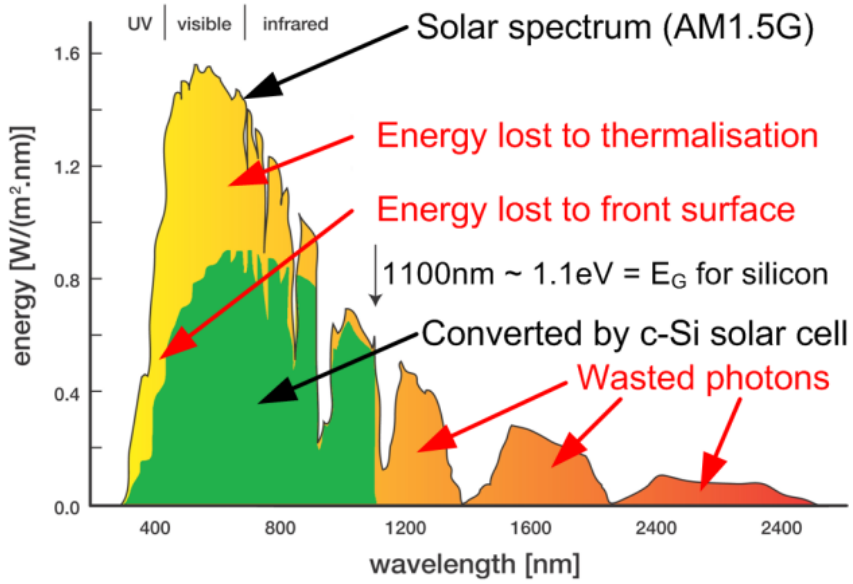

Figure 2.12: a) Record efficiencies of different PV technologies and SQ detailed balance limit plotted as a function of band gap wavelength [circles=homo-junctions, squares=hetero-junctions, filled=direct band gap, empty=indirect band gap] [115]. b) Spectral response for silicon [117].

Chapter 3. Literature Review

This chapter gives an overview of current research in the following areas: outdoor monitoring of OPVs; ISOS outdoor testing protocols; 3D structuring of OPVs; luminescent downshifting. Details of the criteria used to select suitable LDS materials are explained.

3.1 Outdoor Monitoring of OPVs

Research into OPVs has been beset by the problems of scalability. A meta analysis by Jørgensen et al. of about 9000 research papers on OPVs published before January 2012 provided some important insights into the current state of OPV research, including the fact that the vast majority of devices reported on were very small laboratory scale devices, 86% having an active area of 0.2 cm^2 or less (Figure 3.1) [20]. Scalability has problems because, as devices get larger, the higher sheet resistivity of ITO leads to drops in PCE [118]. Small devices are difficult to measure outdoors with any degree of accuracy, as the currents involved are small (nA), especially at lower irradiances, and require the use of specialist test equipment, and this has held back outdoor testing.

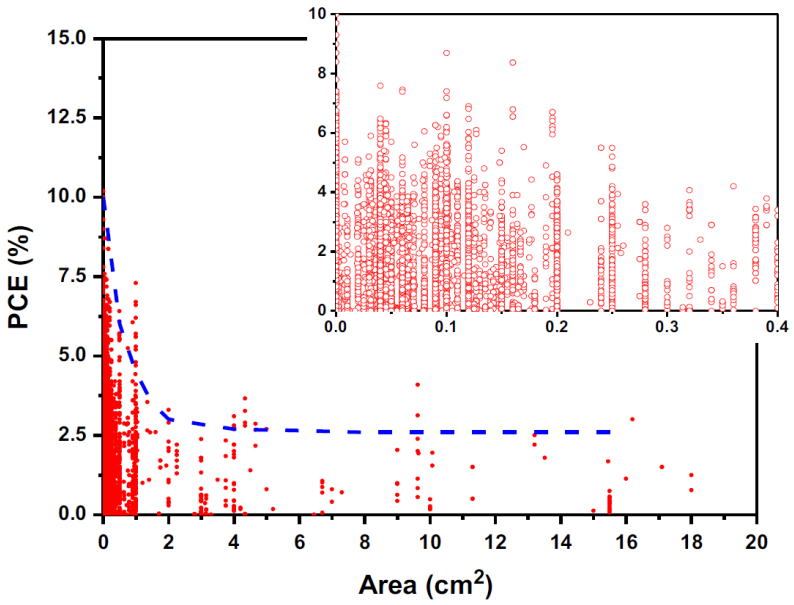

Figure 3.1: PCE vs. device active area in research papers up till 2012. This highlights the large number of very small scale laboratory devices and the lack of reported results from larger area devices [20].

3.1.1 ISOS Stability Test Protocols for Outdoor Testing

The International Summit on OPV Stability (ISOS) has published detailed protocols for measuring OPV devices, covering shelf life testing, outdoor monitoring, laboratory weathering and thermal cycling [119]. Each area has three levels of test protocols: basic (level 1), intermediate (level 2) and advanced (level 3). This allows laboratories with different capabilities to adhere to a standard set of protocols and improve the comparability of their results. The majority of laboratories would be expected to comply with level 2 and only a small number of certified testing centres would reach level 3. Table 3.1 shows the protocols which apply to outdoor testing and Table 3.2 shows the protocols which apply to indoor (laboratory weathering) testing.

Table 3.1: ISOS outdoor testing protocols [119]**.**

Test Type	ISOS-O-1 Outdoor	ISOS-O-2 Outdoor	ISOS-O-3 Outdoor
Light Source	Sunlight	Sunlight	Sunlight
Temperature	Ambient	Ambient	Ambient
Relative Humidity	Ambient	Ambient	Ambient
Environment	Ambient	Ambient	Ambient
Characterisation Light Source	Solar simulator	Sunlight	Sunlight and solar simulator
Load	MPP or open circuit	MPP or open circuit	MPP

Table 3.2: ISOS indoor (laboratory weathering) testing protocols [119]**.**

Test Type	ISOS-L-1 Laboratory weathering	ISOS-L-2 Laboratory weathering	ISOS-L-3 Laboratory weathering
Light Source	Simulator	Simulator	Simulator
Temperature	Ambient	65/85 °C	65/85 °C
Relative Humidity	Ambient	Ambient	Near 50%
Environment/setup	Light only	Light & Temperature	Light, Temperature & Relative Humidity
Characterisation Light Source	Solar simulator	Solar simulator	Solar simulator
Load	MPP or open circuit	MPP or open circuit	MPP

Devices being measured outdoors are exposed to a wide variety of conditions (e.g. temperature, humidity, wind, irradiance) which will influence the accuracy of the measurements. Irradiance is the most important and is ideally measured using a thermopile pyranometer which has a flat spectral response from 300 to 2800 nm [120]. The ISOS protocols also recommend measuring device temperature.

3.1.2 Stability and Lifetime Assessment

If a series of IV measurements are taken over time then it is possible to assess the stability and lifetime of the device by plotting the change in PCE, J_{SC}, V_{OC} or FF against time (Figure 3.2). The time for the monitored quantity to reduce to either 80% (T_{80}) or 50% (T_{50}) of its initial value is used as a measure of its lifetime. If there is an obvious change in device performance after an initial burn-in period then the stable and burn-in lifetimes may be given separately.

Silicon and thin film PV modules and systems are often assessed using specific yield (ratio of system yield to system size) or performance ratio (ratio of actual yield to potential yield), usually calculated on an annual basis [121]–[123]. However for the OPV cells and modules that are assessed in this thesis, the rate of degradation is too fast and therefore these metrics are of limited use.

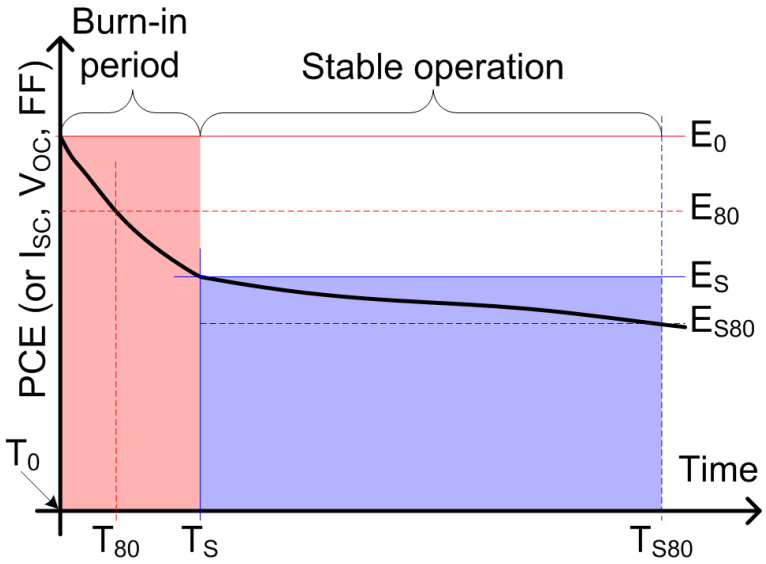

Figure 3.2: Stability and lifetime measurements. The time to drop to a percentage (usually 80% or 50%) of the initial value is used for lifetime comparisons [119].

3.1.3 Outdoor Monitoring Studies on OPVs

Few groups have developed facilities for conducting outdoor tests and therefore limited data exists on the outdoor performance of OPVs. The lack of suitable large area modules means that most research has concentrated on small laboratory scale devices. The perceived short lifetime of OPV devices, especially when exposed to real weather conditions, is also a disincentive. However, these are some of the most useful tests as they allow for performance of materials and systems to be understood in an

environment where the modules are likely to be used. Despite these challenges there have been some comprehensive studies.

A number of papers have emerged from the group at the Technical University of Denmark (DTU) lead by Professor Frederik Krebs. Few laboratories have the facilities to fabricate large area flexible OPV devices and DTU are leading the way in the development of R2R techniques using environmentally friendly materials and methods [124]–[127]. They provide large numbers of OPV modules to the research community, both through inter-laboratory partnerships, round-robins and through their freeOPV programme [112].

One of the earliest studies, in 2006, on long-term evaluation of OPV performance outdoors was by Katz et al. at Ben Gurion University, Israel. They published a study of outdoor degradation based on OPVs encapsulated with glass and aluminium with different semiconductors in the active layer (BHJ of MEH-PPV:$PC_{61}BM$, BHJ of P3HT:$PC_{61}BM$, bilayer P3CT:C_{60}), all with an active area of 10 cm^2 (Figure 3.3a) [128]. They found that the main degradation losses were due to I_{SC} and FF, whereas V_{OC} remained relatively stable. I_{SC} and V_{OC} were seen to degrade during the day and recover overnight (Figure 3.3b). This recovery effect was also observed if the cells were shaded for 30 minutes during the day. They suggested that non-reversible photochemical degradation occurred in parallel with reversible degradation from photo-induced generation of charge traps. FF showed a steady decline over the course of the monitoring. Overall the cells were relatively unstable and the best cell (P3CT:C_{60}) showed a 50% drop in PCE within 90 hours of sunlight exposure.

a) **b)**

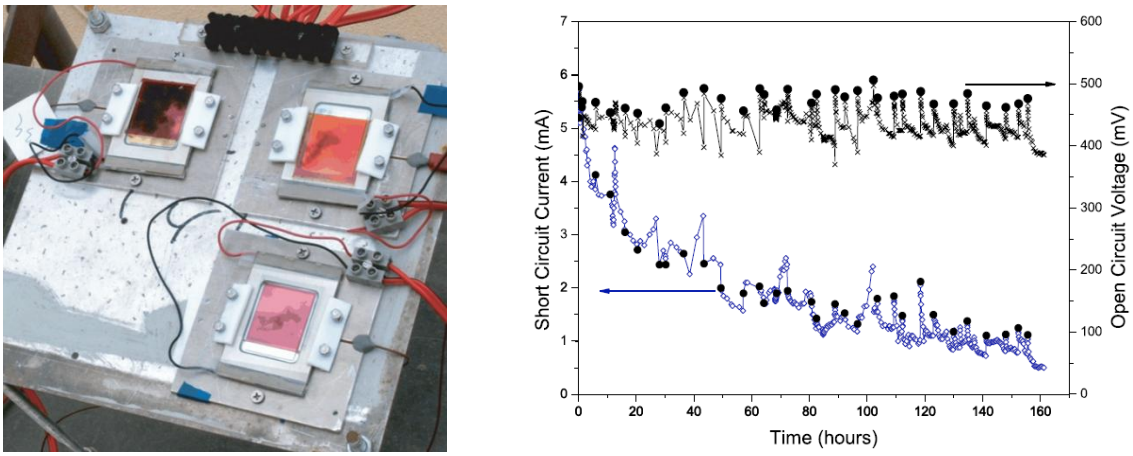

Figure 3.3: Outdoor testing in Israel: a) three different cells mounted for outdoor testing; b) evolution of I_{SC} and V_{OC} for P3HT:$PC_{61}BM$ cell [128].

In 2008 Hauch et al. at Konarka Technologies (Lowell, MA, USA) reported on eight flexible modules monitored outdoors based on P3HT:$PC_{61}BM$ which showed that after one year outdoors P_{MPP} had only dropped to 80% of its initial value (Figure 3.4) [129]. For the first six months, after an initial jump in P_{MPP} performance of about 40%, the performance correlates to the ambient temperature and subsequently the modules show a linear degradation. After 14 months of outdoor testing the modules were retested under the solar simulator and there was found to be an 11% increase in FF, 3.3% increase in PCE, 7% drop in V_{OC} and no change in J_{SC}. When the modules were first placed on the roof they were loaded with a fixed resistor at their MPP. As the performance of the modules changed, due to degradation and changes in irradiance and temperature, the MPP changed. Every 60 seconds the voltage drop across the resistor was logged and the output power was derived from this. This highlights the importance of taking IV curves, from which the performance parameters can be derived, as their outdoor results are severely affected by the non-optimal loading.

a) **b)**

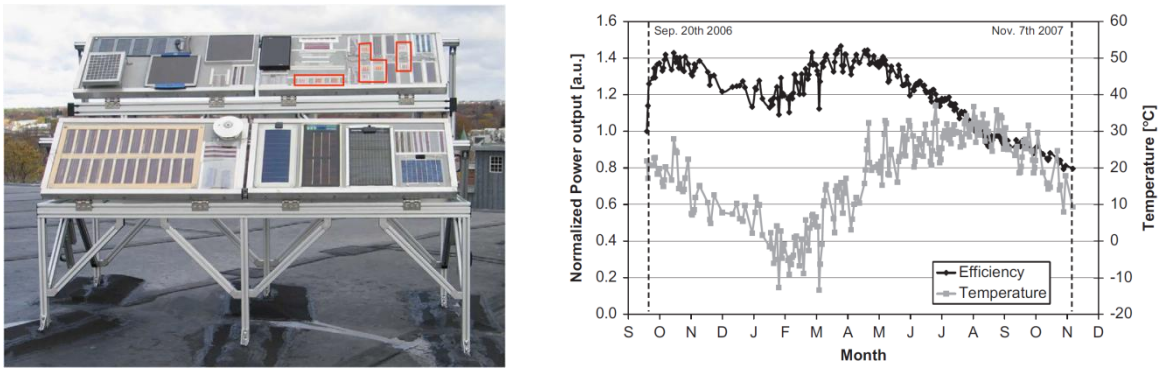

Figure 3.4: Outdoor testing at Konarka: a) outdoor testing rack; b) evolution of PCE (normalised) over the course of a year [129].

Angmo et al. (DTU) have published several reports into long term (one and two years) outdoor studies of OPV devices. A one year study was performed on two different batches of ITO-free P3HT:PCBM modules (active area: 70-100 cm^2), encapsulated with low-cost plastic barrier material, under different climatic conditions (Denmark, Holland and India) [130]. The second batch was fabricated with improved edge sealing. All of the modules in the first batch failed, whereas the best of the second batch of modules retained 95% of their initial performance after 1 year of outdoor testing. Degradation for all of these modules was through failures in edge sealing and at the contacts. Another outdoor stability study in Denmark and India, using similar modules to the first batch,

showed maximum T_{80} lifetimes of 1500 hours and little variation in performance between the modules in India and Denmark, despite the higher temperature and humidity levels in India [131]. Another study looked at large area (100 cm^2) ITO-free modules, with the improved edge sealing, over the course of two years under both outdoor and dark-storage conditions in Denmark [132]. These modules showed reasonably stable outdoor performance and all maintained an MPP performance above 80% of initial performance over the course of the two years. The degradation that was observed was attributed to oxygen permeation through the barrier layers.

DTU have coordinated several inter-laboratory and round robin studies with the aim of assessing and improving the ISOS standards (both indoors and outdoors) [119], [133]–[136]. One study looked at the reproducibility of outdoor measurements and involved 46 different laboratories worldwide [134]. Suitcase samples, consisting of three OPV modules and a silicon reference cell, were sent between laboratories for V_{OC}, I_{SC} and IV testing at noon on a clear day, by whatever means each laboratory had available. Comparison of the results from each laboratory revealed a standard deviation of about 5%, which indicates a high level of consistency and confirms the validity of these multi-laboratory studies. For effective research it is important for results between laboratories to be consistent and therefore comparable.

An inter-laboratory study by Søndergaard et al. (DTU) in 2012 reported on outdoor testing in eight countries of OPV modules encapsulated in polyurethane sandwiched between two plates (one glass and the other polycarbonate) [113]. Although the average degradation trends were similar across all locations it was noted that 13% of modules at seaside locations experienced catastrophic failure compared to only 5% of modules at inland sites. This was attributed to the higher concentration of salt in the air and corrosion of the external copper electrodes was observed. Lifetimes increased by a factor of over three when compared to similar modules with only front and back barrier foil for encapsulation.

In 2013 Gevorgyan et al. (DTU) reported on an inter-laboratory outdoor stability study involving six laboratories and lasting over 17 months [137]. The modules (P3HT:$PC_{61}BM$) were fabricated at DTU and included an extra layer of UV-filter/barrier encapsulation. Two modules were distributed to each of the participating laboratories. The results showed that T_{80} lifetime varied between a few hundred to over 10,000 hours, and the primary source of degradation was deterioration of the sealing at the

contact terminals, which allowed water and oxygen to diffuse into the cells. This caused progressive cell degradation, with the cells nearest the contacts showing the largest drop in performance, which was attributed to the absorption of moisture by PEDOT:PSS (which is strongly hygroscopic) leading to oxidation of the Ag/PEDOT:PSS interface (Figure 3.5).

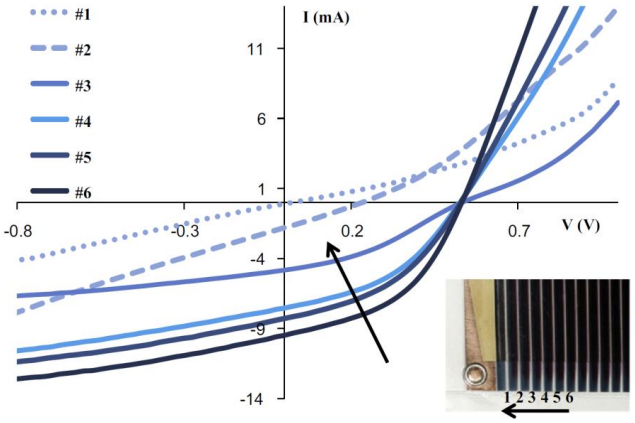

Figure 3.5: IV curves of individual cells in a module, highlighting the failure of cells close to the terminals [137].

Another inter-laboratory study by Gevorgyan et al. (DTU) compared ISOS-O-1 and ISOS-O-2 measurements at 16 different laboratories [138]. It was found that ISOS-O-1 tests (characterisation performed indoors under calibrated light) were inherently more unreliable and led to greater failure rates than ISOS-O-2 tests (characterisation performed outdoors) due to the minimal handling required for ISOS-O-2 tests. The performance results for these tests showed that V_{OC} was fairly stable and degradation of PCE was due to drops in FF and I_{SC}, in agreement with the earlier results from Katz [128].

Several studies have looked at how indoor accelerated lifetime testing (ALT) can be used to predict outdoor lifetimes. Haillant used Atlas solar simulators for testing OPV degradation as a function of irradiance and temperature [139]. Existing ISOS test procedures were used and the results indicated that degradation in OPVs does not correlate linearly with increasing irradiance, but according to a power law. In addition, increasing temperature can significantly alter the nature of the degradation process, as outdoor degradation is mainly photo-oxidative in nature, whereas increasing temperature affects the rate of photo-chemical reactions; increasing humidity can lead

to swelling due to absorption of water, which can lead to abnormal mechanical stresses in the module resulting in cracking.

A study by Corazza et al. (DTU) tested different OPV modules outdoors for one year in order to compare the results to several complimentary indoor studies and establish a method of predicting outdoor lifetime based on indoor accelerated tests [140]. They found a correlation between lifetimes under accelerated indoor testing, under damp heat and light soaking (ISOS-D-3 and ISOS-L-2), and lifetime outdoors.

An inter-laboratory study by Owens et al. was performed at Pomona College (Claremont USA) involving 8 different laboratories [141]. Each laboratory supplied their best OPV modules for indoor and outdoor testing under standardised conditions. Normalised PCE results (Figure 3.6) show the huge disparity in lifetimes between the different modules/cells, with some cells showing linear decay, whilst others show rapid exponential decay.

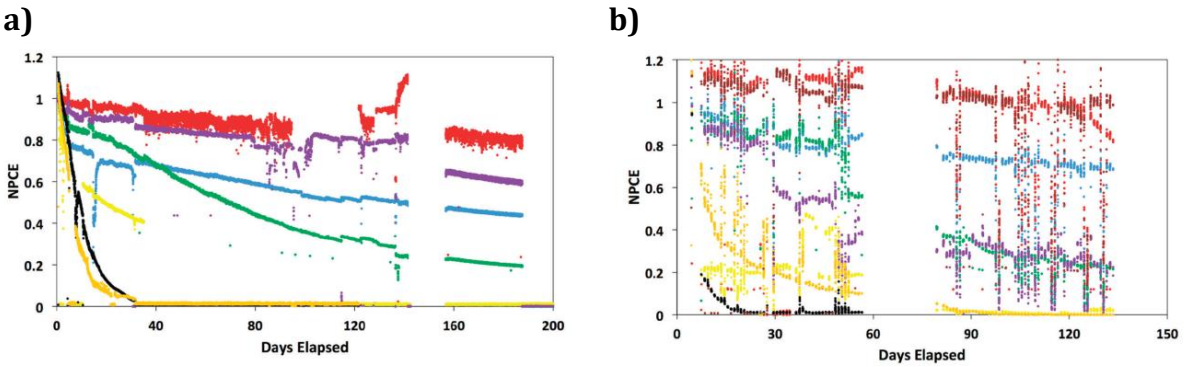

Figure 3.6: Comparative testing results of different OPV module types: a) indoor; and b) outdoor [141].

Weerasinghe et al. conducted research into flexible barrier layers and encapsulation techniques with large area OPVs [142]. They tested three different levels of encapsulation, all based on 3M™ Ultra Barrier Solar Film (Figure 3.7). The first two levels used adhesive transfer tape to laminate the barrier film to the front and back of the modules: on one the film on the rear did not completely cover the module, allowing access to the electrodes ("partial"); on the other both the films were both oversize and overlapped the module all round, with electrical connection via copper tape accessed through two small perforations in the rear film ("perforated"). The third encapsulation method ("complete") used ethylene vinyl acetate (EVA) to laminate oversized barrier film to the module, along with moisture barrier tape to seal all round the edges and the

copper tape where it exited. Modules with the "complete" level of encapsulation showed no evidence of degradation after 13 months outdoors and they projected a potential T_{80} lifetime of at least 3 years, assuming similar degradation modes as the "partial" modules and no catastrophic failures.

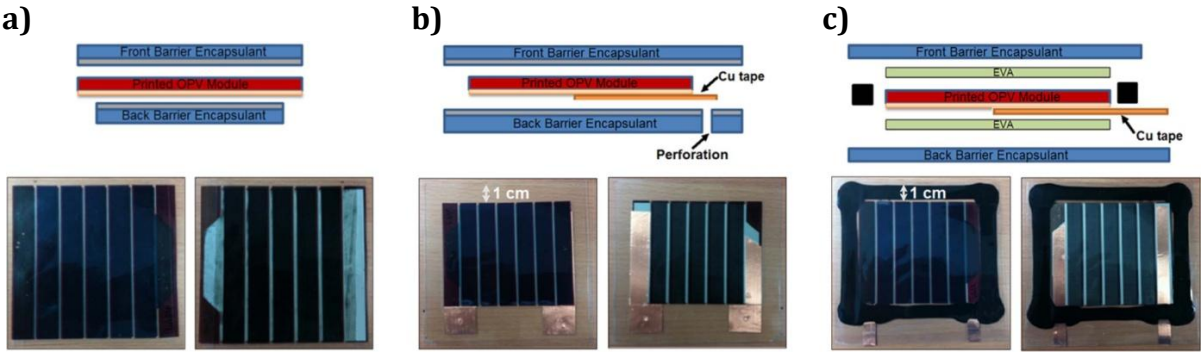

Figure 3.7: Exploded cross sections and photographs of encapsulation test modules: a) "partial"; b) "perforated"; and c) "complete" [142].

A recent field trial by Emmott et al. of fourteen large area (1200 cm^2) OPV modules in rural Rwanda were used to test OPV degradation at high levels of irradiance (spectral air mass ≈ AM1.0), high temperatures and heavy rainfall [143]. This resulted in early degradation of the modules, due to delamination caused by the failure of the non-UV stable encapsulation. The modules exhibited lifetimes of between 2½ and 5 months; 5 to 6 times shorter than the lifetimes of control modules kept indoors in the dark.

In 2010 Medford et al. (DTU) tested a set of OPV panels with active areas up to 9180 cm^2 and power levels up to 8 W [144]. The panels were fabricated by taking a number of R2R fabricated OPV modules and connecting them together, as if they were cells in a standard silicon module, with a glass front, EVA encapsulation and tetlar foil backplane (Figure 3.8a). Each panel was encapsulated differently and tested outdoors (Figure 3.8b). The best panel (T_{80}=1 month, T_{50}=6 months) had been fabricated with an additional thin protective foil layer at the back, which further reduced oxygen and water diffusion. No difference was found between those panels with or without UV filtering, and this is attributed to the UV filtering caused by the tempered glass at the front.

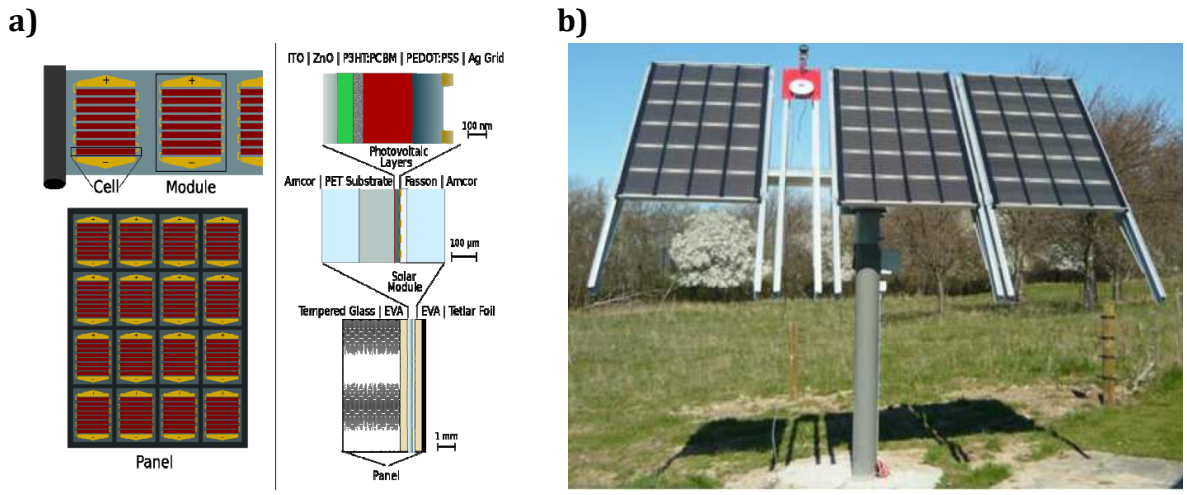

Figure 3.8: Large area OPV panels: a) fabrication; b) testing outdoors [144].

The latest development from DTU is the production of continuous R2R OPV modules, with serially connected module stacks (so called infinity cells) [145], [146]. These foils can be up to 100m long and at that length will have a V_{OC} of about 10kV and power rating of over 220 W_P. To demonstrate the potential of these new module foils a solar park has been setup with 4 inclined racks, each with six rows of infinity-PV foil. The energy payback time for these grid connected systems is 277 days in Denmark, and just 180 days in southern Spain[1].

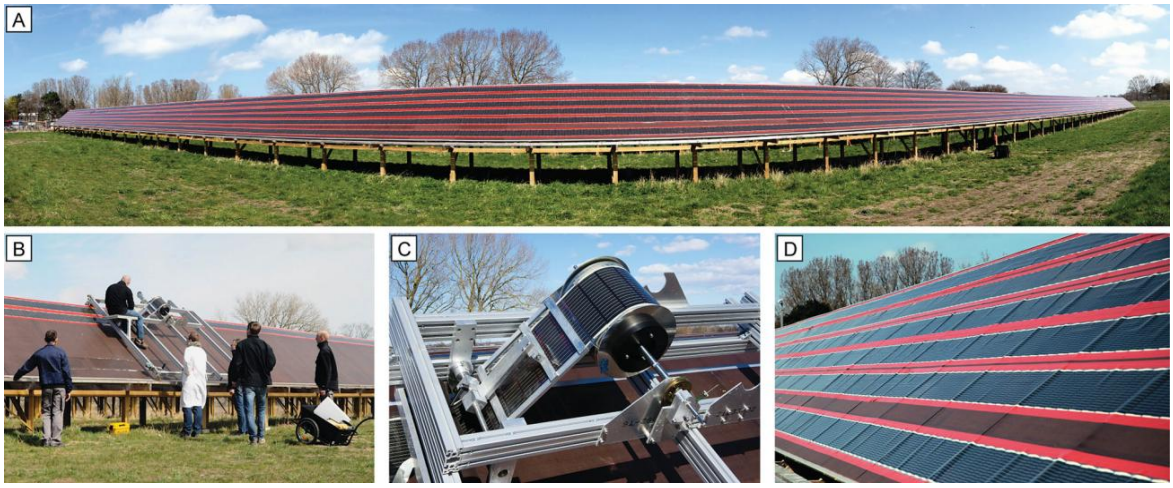

Figure 3.9: DTU Solar Park using infinity-PV foil [145].

The importance of edge sealing was highlighted by Tanenbaum et al. who compared matched pairs of R2R modules, one of which had exposed cut edges and the other was re-laminated with extra adhesive sealing around the cut edges (edge sealing

[1] The energy payback time is the time required for the solar PV system to generate the equivalent amount of energy that is consumed in the construction and decommissioning phases of the system.

rim: 10 mm) [147]. Tests, including indoor stability studies and imaging, showed that in both cases degradation was caused by the ingress of atmospheric reactants from the edges. The edge sealed devices showed significantly reduced levels of degradation and improved stability, with fast non-linear degradation eliminated.

Overall these results all highlight the variability of outdoor performance depending on location and module type, and that ingress of oxygen and water through the edges and contacts provide the primary source of initial degradation. Efficiency and material lifetimes, which are affected by intrinsic degradation, are being addressed indoors in the laboratory, but it is only by taking OPV modules outdoors that they can be properly tested against extrinsic sources of degradation. OPV devices now have lifetimes that significantly exceed their energy payback time, which is the first hurdle towards cost effective commercialisation [145], [148]. The next hurdle is to improve LCOE, by continuing improvements in efficiency and lifetime, and by reducing costs [149], [150].

3.1.4 Temperature and Irradiance Dependence

Experiments by Katz et al. on OPVs fabricated from polyphenylene-vinelyne (PPV) and $PC_{61}BM$ show that they possess positive temperature dependence for PCE, I_{SC} and FF and negative temperature dependence for V_{OC} (Figure 3.10) [151]. I_{SC} and FF saturated at about 50°C which led to a drop in PCE above this temperature.

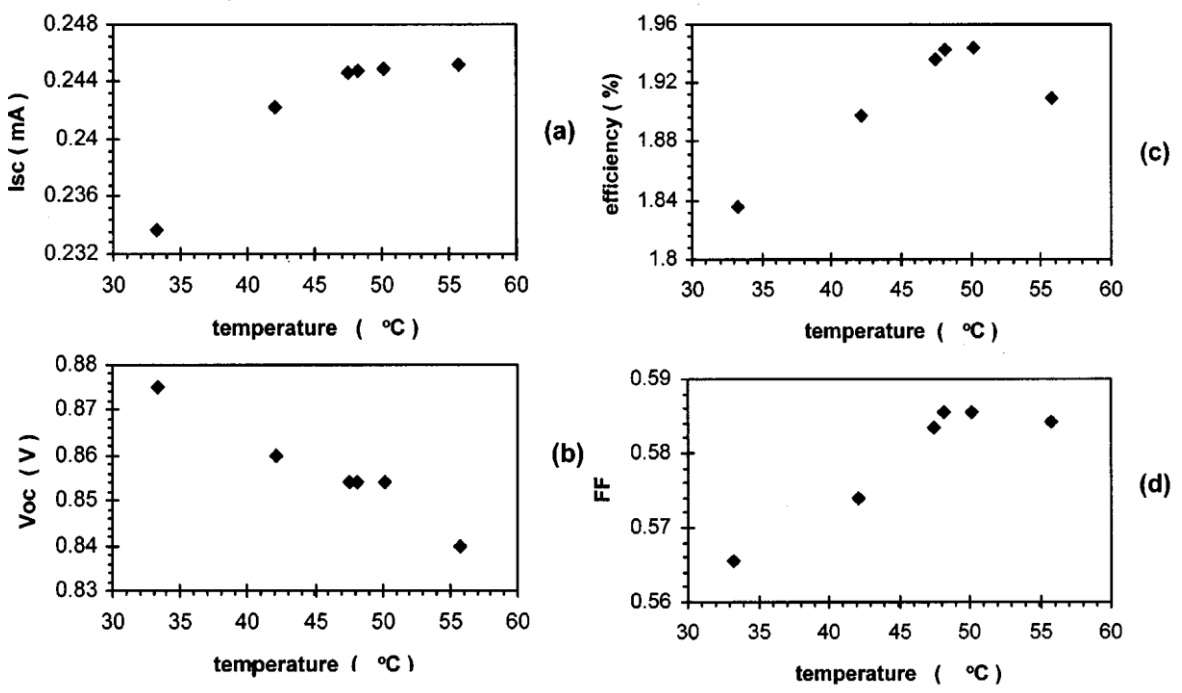

Figure 3.10: Temperature dependence for OPVs derived from outdoor measurements by Katz et al.: a) I_{SC}; b) V_{OC}; c) PCE; and d) FF [151].

Riedel et al. looked at the IV characteristics of PPV:$PC_{61}BM$ devices as a function of temperature (125-320 K) and irradiance (0.03-100 mW/cm²) [152]. For temperature dependence they had similar results to Katz: PCE, I_{SC} and FF had a positive dependence and V_{OC} had a negative dependence (Figure 3.11a). Against irradiance I_{SC} was observed to have a linear dependence and V_{OC} a logarithmic dependence. However PCE and FF were observed to have a weak negative dependence on irradiance. Their investigation of R_S and R_{SH} (Figure 3.11b) found R_S to be unaffected by irradiance, but negatively dependent on temperature, as R_S is primarily due to the ohmic resistance of the absorber material. R_{SH}, caused by recombination, was unaffected by temperature but had a strong negative dependence on irradiance, leading to the drop in FF at higher light intensities.

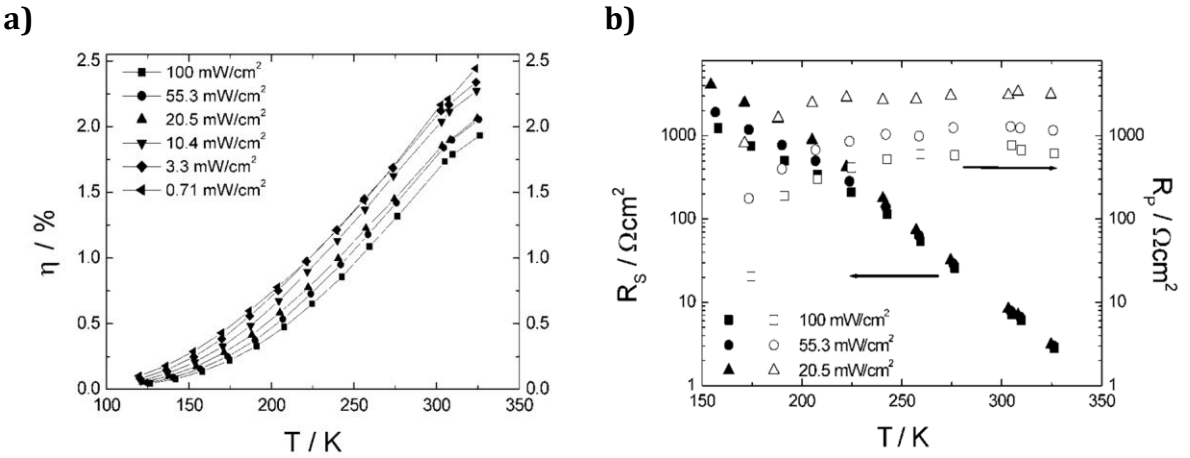

Figure 3.11: Temperature and irradiance dependencies: a) PCE; b) serial resistance (R_S, full symbols) and shunt resistance (R_P, open symbols) [152].

Tromholt et al. investigated the effect of concentrated sunlight on OPVs and found that PCE increased slowly, until saturation at 0.5-2 suns, followed by a strong reduction with further increases in irradiance (Figure 3.12) [153]. At irradiances below 10 suns, I_{SC} was linearly dependent on irradiance, but at higher levels the rate reduced. V_{OC} had a logarithmic dependence on both irradiance and I_{SC}. V_{OC} peaked at about 10 suns and reduced at higher irradiances. FF and PCE peaked at about 1 sun and reduced thereafter.

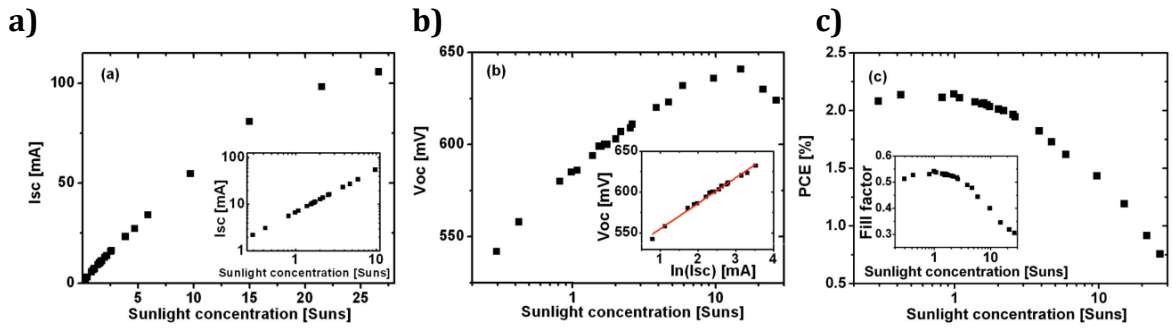

Figure 3.12: Effect of concentrated sunlight on OPVs: a) I_{SC}; b) V_{OC}; c) PCE [153].

3.2 Use of 3D Structuring to Increase Yield in PV Devices

Microscopic and macroscopic approaches to 3D structuring have been used to improve PV device yield. In silicon PV, microscopic surface texturing and/or anti-reflection coatings have been used to reduce optical losses for many years. Anti-reflection coatings often work by adding thin dielectric films which change the refractive properties of the surface and use destructive interference to reduce reflections at normal incidence [154], [155]. Surface texturing reduces reflective losses as incident light will undergo multiple reflections which will increase light trapping. One of the early methods was to create microscopic pyramids by chemical etching along the faces of the crystal planes (Figure 3.13a) [156]. An alternative method is nanoimprinting the texture (either pyramids or moth-eye structures) onto the surface [157]–[160]. Moth-eye structures are a dense periodic array of sub-wavelength pillars which reduce Fresnel reflection of light at an abrupt optical interface by forming the equivalent of a graded refractive index layer [161]. Patterning can also be applied to a polymer film which is then applied as a protective layer to the solar cells [162].

Similar anti-reflection coatings and processes have been used on OPVs, although there are fewer reports. Haque et al. have proposed triangular textured OPVs; modelling showed an 11-13% improvement in absorption, leading to PCE improvements of 15-20% [163]. Several groups have investigated the use of moth-eye structures fabricated by nanoimprint lithography on OPV cells to improve light capture. Chuang et al. observed an improvement in light capture at high angles of incidence (Figure 3.13b) [164]. Similar results were found by Forberich et al. [165]. Kettle et al. added anti-reflective structures to the PET substrate of an OPV cell using thermal nanoimprint lithography, leading to a 4% relative increase in PCE with light at normal incidence and 32% at oblique angles of incidence (80°) [166]. OPVs have low carrier mobility and

therefore the active layer needs to be relatively thin (50-300 nm) in order to maximise the capabilities of the device and minimise recombination losses. There have been various light trapping schemes which use buried nano-electrodes, gratings, plasmons and scattering grids to increase the light absorption in thin film OPVs [167]–[172].

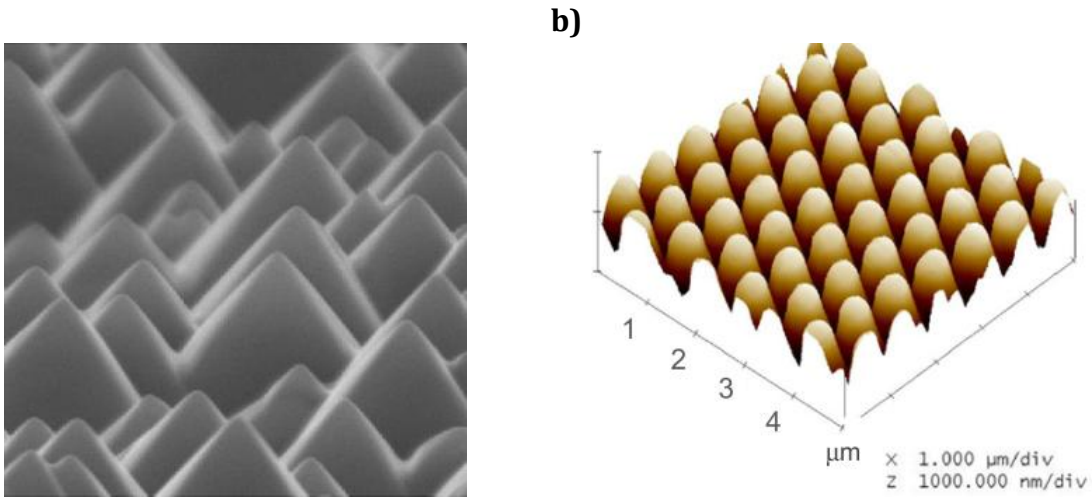

Figure 3.13: Surface texturing: a) textured silicon [173]; b) AFM image of moth-eye structure on an organic solar cell [164].

At the macroscopic scale, 3D structuring of solar cells is used to improve light capture at oblique angles of incidence, leading to improved performance in the morning and evening and improved total diurnal yield. Bernardi, Grossman et al. at Massachusetts Institute of Technology studied the use of 3D structures built from silicon cells and their ability to improve yield (Figure 3.14a) [174]. The use of 3D structures increased the energy density (energy per base area) by a factor of 2-20 compared to a fixed inclined flat panel and by a factor of 1.3-1.8 compared to a flat panel with dual-axis sun tracking. These structures could double the number of peak power generation hours and reduce seasonal, latitude and weather variations compared to stationary flat panels. However the area of solar panels required increased by up to a factor of 1.5-4 (based on solar cell area per kWh generated). Their designs utilised reflection from one surface onto another cell in order to capture more light and they used both computer modelling and outdoor monitoring. They also examined combining mirrors and solar panels in 3D structures.

In 2010 Myers (in collaboration with Bernardi and Grossman) used computer simulations to examine 3D structures based on various algorithms [175]. They were trying to improve the yield from a given footprint area and found that the increase in yield correlated linearly with the height of the array. The designs depended on inter-cell

reflections, sometimes from multiple surfaces, and allowed for loss at each reflection. The ideal design, involving 64 individual triangular panel sections (see Figure 3.14b), would not be easily realised in practice and required nine times as much active material compared to a flat panel. However it did have an increase in yield of x2.38 and provided fairly even power throughout the day.

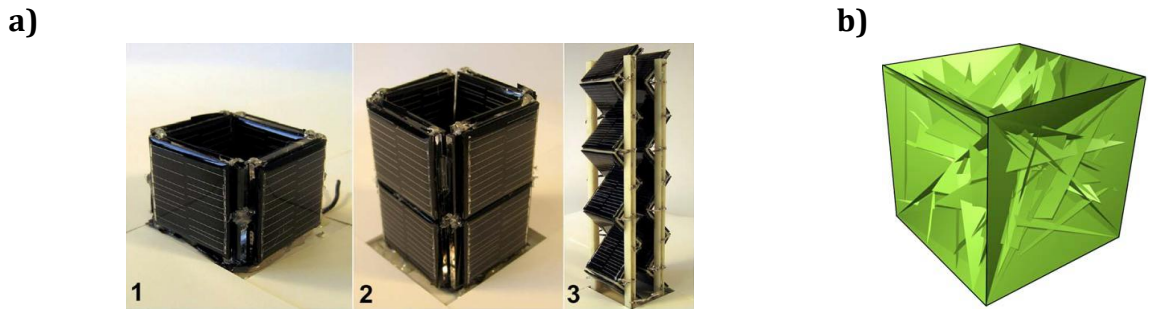

Figure 3.14: a) 3D structures fabricated from silicon cells (Bernardi et al.) [174]. b) Optimal theoretical 3D PV design from Myers et al. [175].

In 2014 Zardetto et al. investigated the performance of curved metal/plastic dye cells (Figure 3.15a) [176]. Under a solar simulator they compared energy density for various curvature radii (R_{CURVE}) against a flat module. Low curvature modules had an improved energy density (e.g. at R_{CURVE} = 13.5 cm → +9.4%) due to an increase in FF; at higher curvatures there was no improvement. Outdoor results showed that at low curvature (R_{CURVE} = 13.5 cm) there was an increase in diurnal yield (+7.9%), with higher energy density at noon, but no improvements in the morning or evening (Figure 3.15b). The high curvature module (R_{CURVE} = 5.5 cm) showed a 9.1% increase in diurnal yield, with improvements during the morning and evening and slightly lower energy density at noon (Figure 3.15c).

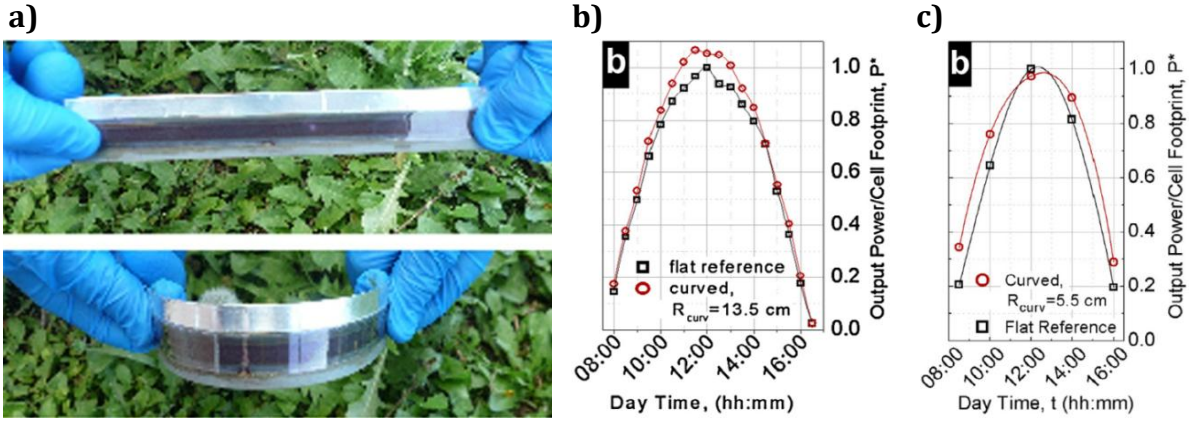

Figure 3.15: Effect of curvature on curved DSSC modules: a) flat and curved modules; Diurnal results: b) R_{CURVE} = 13.5 cm, and c) R_{CURVE} = 5.5 cm [176].

There has only been one report of macroscopic structuring on OPVs, by Chuang et al. who investigated how P3HT:$PC_{61}BM$ cells respond to light when the cells are curved or the light is at a high angle of incidence and they found that the EQE decreased significantly in both cases [164]. They looked at the difference between polarised light in transverse electric (TE) and transverse magnetic (TM) modes incident on a flat P3HT:$PC_{61}BM$ cell and on a curved P3HT:$PC_{61}BM$ film (Figure 3.16). Absorption of TM-polarised light was significantly reduced at higher angles of incidence or increased curvature, whereas TE-polarised light was largely unaffected.

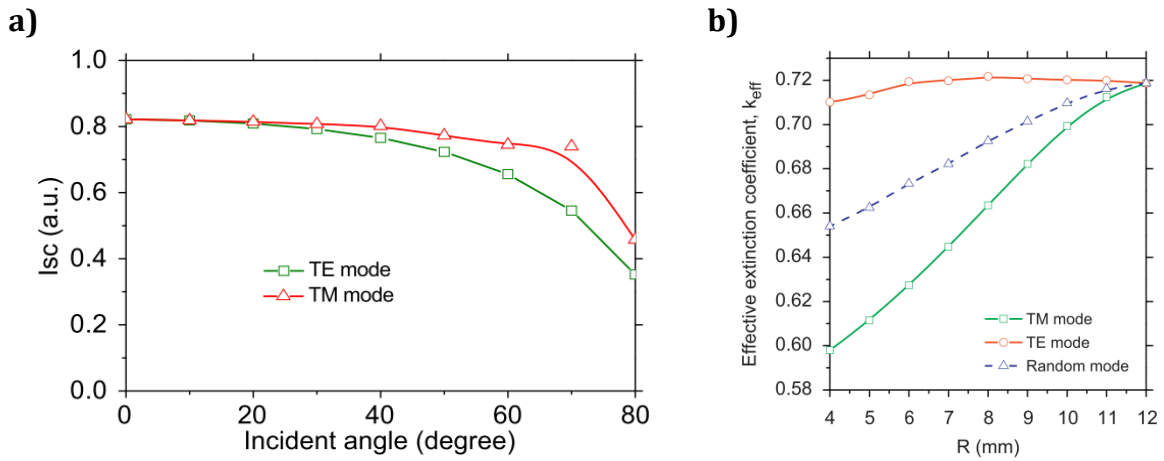

Figure 3.16: Effect of polarised light: a) I_{SC} vs. angle of incidence for a flat OPV cell; b) Extinction coefficient vs. radius of curvature (R) for a P3HT:PCBM film on polycarbonate substrate [164].

Various groups have shown an improvement in light trapping using V-shaped geometries (Figure 3.17a). Peumans et al. at Stanford demonstrated an improvement in J_{SC} of 29% with an interior angle of 30° in one paper and in another paper reported a relative improvement in PCE of 52% with an interior angle of 35° using a device with an active layer thickness of 170 nm [177], [178].

Tvingstedt et al. proposed a V-fold tandem device with different active layer materials on each side of the device, so that unabsorbed light could be reflected onto the opposite side, where it could be absorbed (Figure 3.17b) [179]. The optimum folding angle was 70°, leading to x1.8 enhancement in PCE.

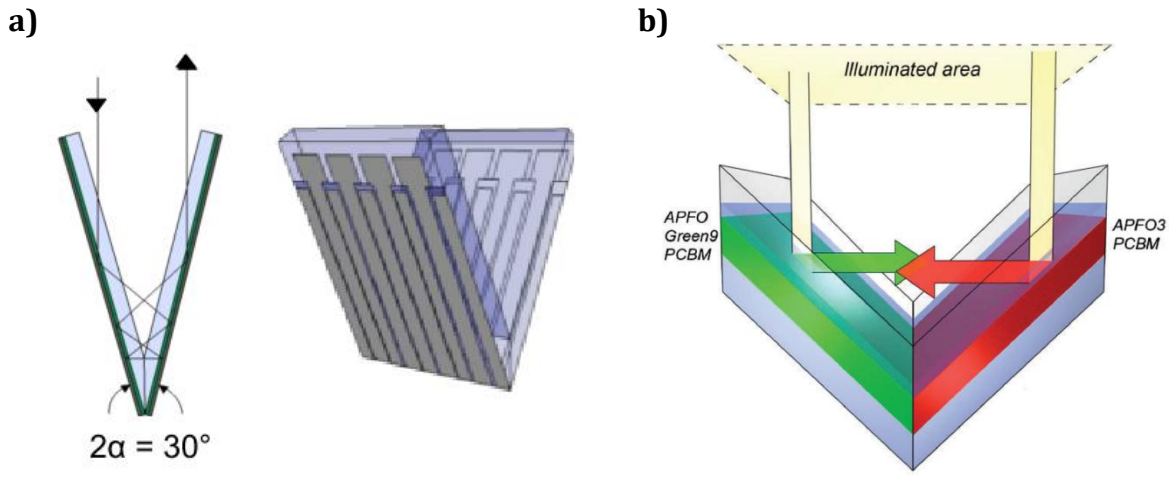

Figure 3.17: V-fold light trapping techniques: a) V-shaped groove light trapping [178]; b) V-fold tandem device [180].

There have been studies by Dennler et al. who investigated the dependence of EQE in OPV cells on incidence angle and found that the peaks were blue-shifted with increasing angles of incidence (Figure 3.18) [181]. J_{SC} was found to increase up to a maximum at 50°, but to drop at higher angles of incidence. Cells with thin (170 nm) active layers had enhanced absorption under oblique incident radiation when compared to cells with thick (880 nm) active layers.

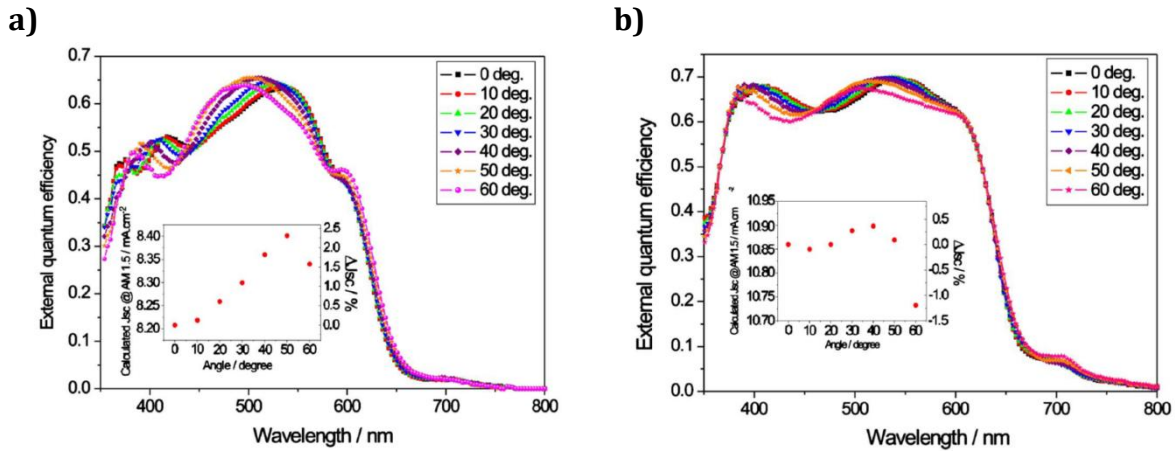

Figure 3.18: Effect of incidence angle on EQE & J_{SC} for P3HT:$PC_{61}BM$ OPVs with different active layer thicknesses: a) 170nm; b) 880nm [181].

3.3 Luminescent Downshifting to Increase Yield

In solar cells there is an uneven absorption profile across the UV, visible and infrared (IR) spectrum, especially for higher energy photons (UV and blue light) where there are additional losses due to absorption by the optical window layer, front surface

recombination and other mechanisms. One approach to improve efficiencies at short wavelengths is to use luminescent down shifting (LDS) of the incident spectrum: short wavelength photons are absorbed by a coating and re-emitted at higher wavelengths where they match the absorption profile of the solar cell better. This allows energy to be shifted from wavelengths outside the optimum spectral response of the solar cell towards wavelengths where the solar cell has higher efficiency. In the case of OPVs it also has an added benefit as it allows UV wavelengths to be filtered out, reducing the potential for photo-oxidation and other degradation mechanisms.

LDS is one of three spectral conversion mechanisms: downshifting (LDS) – one high energy photon is absorbed and re-emitted as a lower energy photon; down conversion (DC) – one high energy photon is absorbed and two (or more) lower energy photons are emitted; up conversion (UC) – two (or more) low energy photons are absorbed and one higher energy photon is emitted [182]–[186].

3.3.1 Physics of Photoluminescence

Photoluminescence (PL) is the emission of light from a material after the absorption of photons (photoexcitation) and Figure 3.19 illustrates the physics behind these processes. When photons with an energy level greater than or equal to the energy gap are absorbed, an electron is raised from the ground electronic state, S_0, to a higher excited state, S_1, or above (1). Excited electrons will decay back to the bottom of S_1 by relaxation (2). Electrons which have been raised to a higher excited state (e.g. S_2) will return to S_1 by internal conversion (3). From the S_1 state some electrons will return back to the S_0 ground state without emitting a photon (quenching) (4). Some electrons will emit a photon (fluorescence) as they drop back to the ground state, which is normally a fast process (typically 0.5 to 20 ns) (5). Some electrons will transfer to a triplet state (T_1) via a process known as intersystem crossing (6), from where they can emit a photon (phosphorescence) as they drop back to the ground state, which happens relatively slowly (milliseconds to hours) (7).

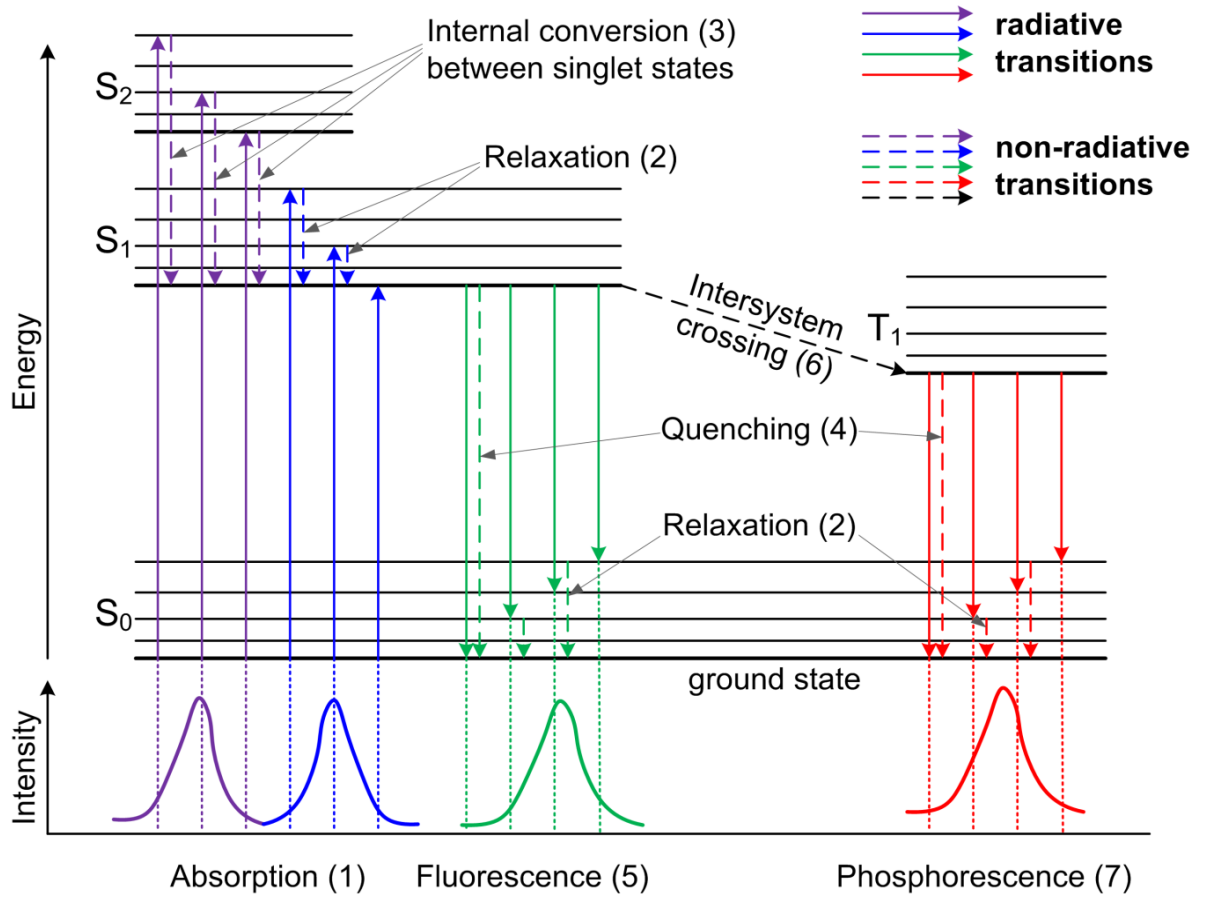

Figure 3.19: Jablonski energy band diagram showing possible transitions. The spectra of the processes are shown below to illustrate that these usually occur across a range of wavelengths.

The absorption and emission spectra are spread across a range of wavelengths due to relaxation and internal conversion. In dyes where the principle PL mechanism is fluorescence this can lead to symmetry between the absorption and emission spectra. The difference between the absorption and emission peaks is called the Stokes' shift (Figure 3.20a) [187]. This shift occurs because absorbed light usually loses some energy through relaxation, before it is re-emitted through fluorescence or phosphorescence at a lower wavelength.

Figure 3.20b shows the main processes that occur when light is incident on an LDS layer on top of a solar cell. Incident light will either be absorbed by a dye molecule if its wavelength matches the absorption spectrum of the dye (1) or will pass straight through the LDS layer (2). The majority of the light that is absorbed by the dye molecule will be re-emitted isotropically and a proportion of it will reach the solar cell: directly (3); after total internal reflection at the front surface (4); after absorption (5) and re-emission by another dye molecule (6). Some of the light will escape through the edges of the LDS layer (7) and some of the light will escape from the front surface (8) if its

incident angle is within the escape cone ($\theta_i<\theta_C$). Light which is incident at an angle above the critical angle will be reflected at the front surface (9). Reflection at the interface between the solar cell and the LDS layer is less as their refractive indices will be similar.

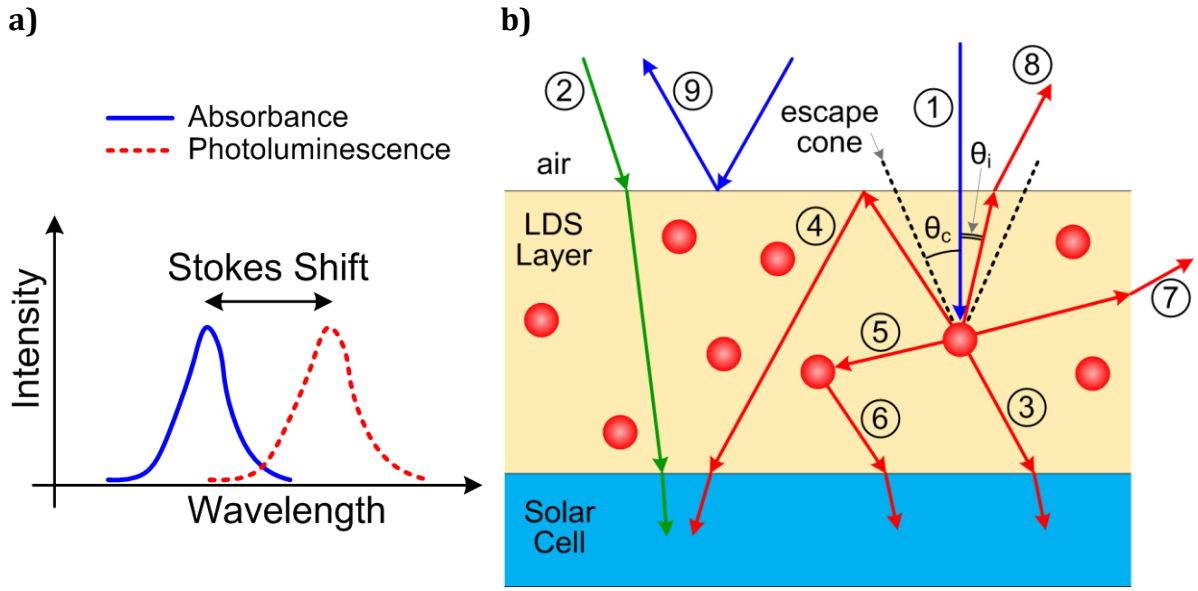

Figure 3.20: a) Stokes' Shift. b) Schematic of LDS layer on a solar cell showing the various processes.

3.3.2 Simplified Optical Efficiency Model for LDS on Solar Cell

The application of an LDS layer will modify the incident spectrum due to losses and the down shifting of light. For the overall effect to be beneficial the losses need to be less than the increase in PCE of the solar cell. These losses are wavelength dependent and Equation 3.1 shows how the optical efficiency (η_{LDS}) is calculated [188] (equivalent to η_{Opt} in Equation 2.6).

$$\boldsymbol{\eta_{LDS} = T \times PLQY(1 - L_{esc})(1 - L_{host})(1 - L_{reabs})(1 - L_{other})} \qquad 3.1$$

Reflective Losses at the Front Surface (T): The amount of transmitted light (T) is given by the simplified Fresnel's relation, Equation 3.2, for normally incident light, where n_0 and n_1 are the refractive indices and R is the reflected light [189] (Figure 3.20b(9)).

$$\boldsymbol{T = 1 - R = 1 - \left(\frac{n_0 - n_1}{n_0 + n_1}\right)^2} \qquad 3.2$$

For a device in air (n_0=1) the front surface reflection (R) for glass (n_1=1.5) is 4% and decreases slightly to 3.87% with a PMMA coating (n_1=1.49), giving a value for T for PMMA of ~96%.

Photoluminescent Quantum Yield (PLQY): if PLQY is less than 100% it leads to a reduction in the number of down shifted photons.

Escape Cone Losses (L_{esc}): If the incidence angle (θ_i) of a re-emitted photon on a surface is less than the critical angle (θ_c) then the photon will not be reflected back but will escape out of the surface (Figure 3.20b(8)). The probability of this (L_{esc}) is given by Equation 3.3, where n_0 and n_1 are the refractive indices for the LDS layer and air respectively [190], [191].

$$\boldsymbol{L_{esc} = \frac{1 - \sqrt{1 - (n_0/n_1)^2}}{2}} \qquad 3.3$$

For PMMA in air (n_1=1.49, n_0=1) L_{esc} is ~12.9%, assuming isotropic emission [182].

Parasitic absorption by the host material (L_{host}): any absorption by the host material will reduce the number of photons that are available for either absorption by the LDS material or transmission directly through to the solar cell underneath. This is dependent on thickness and the absorption properties of the host material. A 1mm thick layer of PMMA will absorb ~1% of the incident light [182].

Re-absorption Losses (L_{reabs}): When a photon is re-absorbed (due to the overlap between absorption and PL spectra), the PLQY, escape-cone and edge losses will be re-applied to this photon, leading to further losses.

Edge Losses etc. (L_{other}): Losses from the edge will occur through the same mechanism as escape cone losses (Figure 3.20b(7)). These losses are dependent on film thickness and area: thicker, smaller area films will have higher losses and this will adversely affect small scale laboratory devices. An LDS film 1 mm thick with an area of 1 cm^2 will lose 4.3%, compared to 1.8% for an area of 9 cm^2 and just 0.1% at 7200 cm^2 [182]. There will also be reflective losses at the LDS layer/solar cell interface.

Apart from minimising losses in the LDS layer itself, there must also be a match between the absorption and emission spectra of the LDS material and the EQE curve of the solar cell (Figure 3.21). The absorption and PL spectra must not overlap, otherwise this leads to re-absorption. There must be a good absorption match with the EQE of the solar cell, such that the LDS material will absorb photons in regions of the spectrum where the solar cell does not absorb (low EQE) and not absorb in regions where the solar cell works well (high EQE). The photons which would have been wasted are utilised and the solar cell is not shaded by the LDS material. The LDS material will be

absorbing in the blue region (short wavelengths) and transparent in the green/red region (longer wavelengths). The PL peak must be near the peak of the EQE curve, where the solar cell is working at its maximum efficiency. And for an OPV device there needs to be high absorption over the UV range, in order to reduce photo-oxidation in the device.

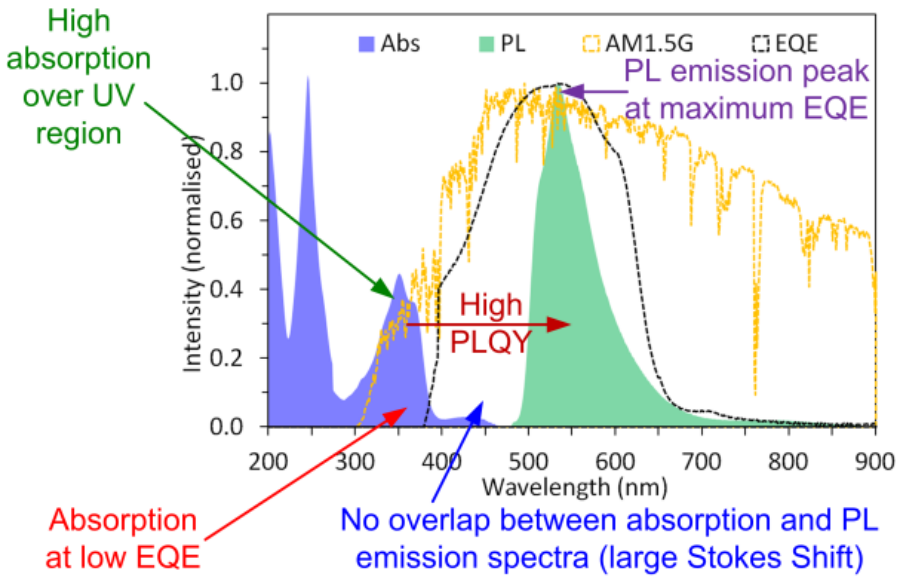

Figure 3.21: Optical properties for an ideal LDS material on a solar cell.

3.3.3 Review of Existing Studies of LDS with Different PV Technologies

There are few reports of LDS coatings on OPVs, but LDS coatings have been used with most of the mainstream PV technologies, and the materials applied could be of relevance to this thesis.

The first reports of LDS was in the late seventies, when Hovel et al. started using LDS layers to enhance the output of solar cells, reporting efficiency improvements of up to 2% using PMMA doped with organic dyes [192]. They used several different materials: PMMA doped with various organic dyes such as Coumarin 540 and Rhodamine 6G, leading to an increase in PCE from 11.5% to 13.5%; rubrene dissolved in polystyrene, which led to a relative increase in PCE of 16%; ruby crystals, which were polished and applied using an optical matching liquid.

Klampaftis, Richards et al. at Heriot-Watt University, Edinburgh, report on several different studies on poly-Si and thin film (CdTe, CIGS) cells and mini-modules and showed the effect of LDS layers on the EQE curve below 400 nm [193]–[197]. In some cases the EQE between 400 nm and 600 nm was lower after the LDS coating had

been applied, due to the absorption of the dye in that region. They experimented with several different organic dyes and a europium based complex, all being incorporated into either the EVA encapsulation layer or in a top sheet of PMMA. Alongside extensive experimental work they used ray tracing to model performance; in most cases there was a slight increase in PCE.

Examination of the effect of LDS coatings on the EQE response of mono-Si cells by McIntosh et al. showed an increase below 400 nm from 0% to 40% after the addition of the LDS layer, leading to a relative gain in PCE of ~1% [198].

The Ephocell project, which ran from 2009 till 2013 and was funded by the European Union, investigated combining down-shifting and up-conversion to increase the efficiency of solar cells. Whereas down-shifting is a known and efficient process with high PLQYs commonplace, up-conversion is considerably more difficult and PLQYs are much lower. The project was aimed at commercial PV technologies as well as OPVs. As part of this project Kennedy et al. used europium complexes to provide active UV-blocking layers for DSSCs, which were predicted to increase energy production outdoors by 3-5% [199]. Kennedy, Ahmed et al. characterised europium and terbium complexes and Lumogen organic dyes and observed that high PLQYs were easily attainable when the dyes were dissolved in solvent, but when the dyes were used in thin films of PMMA or epoxy much lower PLQYs were obtained, down to 50% [200]. Aubouy et al. looked at the role of ray-tracing to predict the resulting spectrum that would be transmitted through an LDS layer and then used that to predict the output from different PV technologies [201]. Turshatov et al. were able to obtain a PLQY of 11% using an up-converter [202].

The use of LDS materials in conjunction with DSSCs has been studied by Zahedifar et al. and Hosseini et al. [203]–[206]. Zahedifar et al. used lanthanide orthovanadate doped with dysprosium ($LaVO_4:Dy^{3+}$) and showed that J_{SC} could be improved by 6.7% [203]. Hosseini et al. used a europium based phosphor and compared using a front LDS layer (transmissive mode) against putting the LDS layer at the bottom of the cell with a reflective layer underneath [204]. This reduced the losses and led to an improvement in PCE at 500nm of 200% and an overall improvement of ~50% for J_{SC}.

There have been a few trials of LDS on OPVs. Ma et al. looked at adding an LDS layer (based on AlQ_3) on an OPV (P3HT:PC_{61}BM) leading to a 15% relative improvement in PCE [207]. Das et al. looked for ways to maintain PCE as module area increased [208].

Instead of creating large single cells they fabricated cells consisting of a number of small pixels. To increase the light harvesting they doped the polycarbonate framework surrounding the pixels with LDS material and integrated this with an OPV (PCPDTBT:$PC_{71}BM$) pre-fabricated module. The dye was optimised to absorb in the 500-600 nm range (where PCPDTBT shows a drop in EQE) and PL emission was at 600-800 nm. They showed an improvement in PCE from 1.91% for 1 cm^2 unpatterned cells to 3.65% for 1 cm^2 cells consisting of 25x 0.01 cm^2 pixels. There was also a threefold reduction in R_S, which is one of the major loss mechanisms as OPV cells are scaled up.

As part of studies into fabricating ITO free OPV cells Prosa et al. added silk fibroin protein and used it as an interfacial layer between the front substrate (glass or PET) and the high conducting PEDOT:PSS layer [209]. They compared devices with and without Stilbene (an LDS material) doping of the silk fibroin and found that thin layers with doping led to an increase in EQE at low wavelengths whereas thick layers with doping had a drop in EQE due to high levels of absorption. This highlights the importance of optimising the absorbance of the LDS layer. The devices with Stilbene doping had the longest lifetimes.

Several groups have used UV absorbing layers to reduce photodegradation in OPV devices, but this has always led to a drop in performance [210]–[214]. Ryu et al. reported a drop in PCE from 4.3% to 3.6% on application of a 4 μm thick UV absorbing coating, but over a fivefold increase in stability [213]. An improvement in this was the use by Xu et al. of an LDS coating on a P3HT film [210]. They used phosphors, based on yttrium vanadate doped with europium ($YVO_4:Eu^{3+}$) sensitised by bismuth, which absorb UV light and have a sharp emission peak at 619 nm and these led to a threefold increase in stability of a P3HT film. Turkovic et al. looked at reducing photodegradation in OPV devices by using commercially available UV absorbers and observed that although there was a significant drop in photocurrent there was an overall three-fold increase in long-term energy production [214]. Engmann et al. looked at reducing this loss in performance by using an LDS layer (anthracene in epoxy) as the UV filter on OPV devices [215]. They found that the loss of photocurrent from UV wavelengths was compensated for by the photocurrent from the down shifted photons from the LDS layer and they observed an increase in PCE from 1.57% to 1.79% by the addition of the LDS layer.

Apart from the simple use of LDS films coated directly onto PV devices there is another class of device that uses LDS materials, the luminescent solar concentrator (LSC), which consists of a collector, fabricated from transparent plastic doped with fluorescent dyes, with a solar cell on one edge [216], [217].

3.3.4 LDS Materials

Although there have been few studies using LDS materials on OPV cells it is necessary to select dyes for this research. The selection of LDS materials depends on the EQE of the solar cell that they are being matched to. It is important that LDS absorption occurs where EQE is low and that PL emission occurs at or near to the highest EQE.

Based upon studies, thirteen dyes were selected from the literature, based on their suitability for use with OPVs, specifically P3HT:$PC_{61}BM$ (Table 3.3). Many of these dyes have already been shown to be effective LDS materials when used with 1st and 2nd generation PVs, DSSCs and in LSCs [197], [198], [218]–[224]. Coumarin, perylene, alizarin and rhodamine have all been used as photosensitisers in DSSCs [225]–[228].

Table 3.3: List of LDS dyes that were used for initial screening.

LDS Dye	Colour	Chemical Family
Europium	Red	Lanthanide complex
Coumarin 7	Orange/yellow	Coumarin dye
Coumarin 153	Yellow	Coumarin dye
Kremer blue (94736)	Blue	Naphthalimide dye
Kremer green (94737)	Green	Perylene dye
Kremer orange (94700)	Orange	Perylene dye
Lumogen F red 300	Red	Perylene dye
Lumogen F orange 240	Orange	Perylene dye
Alizarin	Purple	Anthraquinone dye
Disperse Blue 3	Blue	Anthraquinone dye
AlQ_3	Green	Metal/organic complex
DCM	Red	Organic dye
Rhodamine B	Pink	Rhodamine dye

Figure 3.22 shows the basic chemical structures for these dyes. They are all based around aromatic organic compounds with a conjugated structure; it is this structure along with its delocalised π electrons which allows the ready absorption of photons, similar to absorption and photo-generation of excitons in OPVs [229].

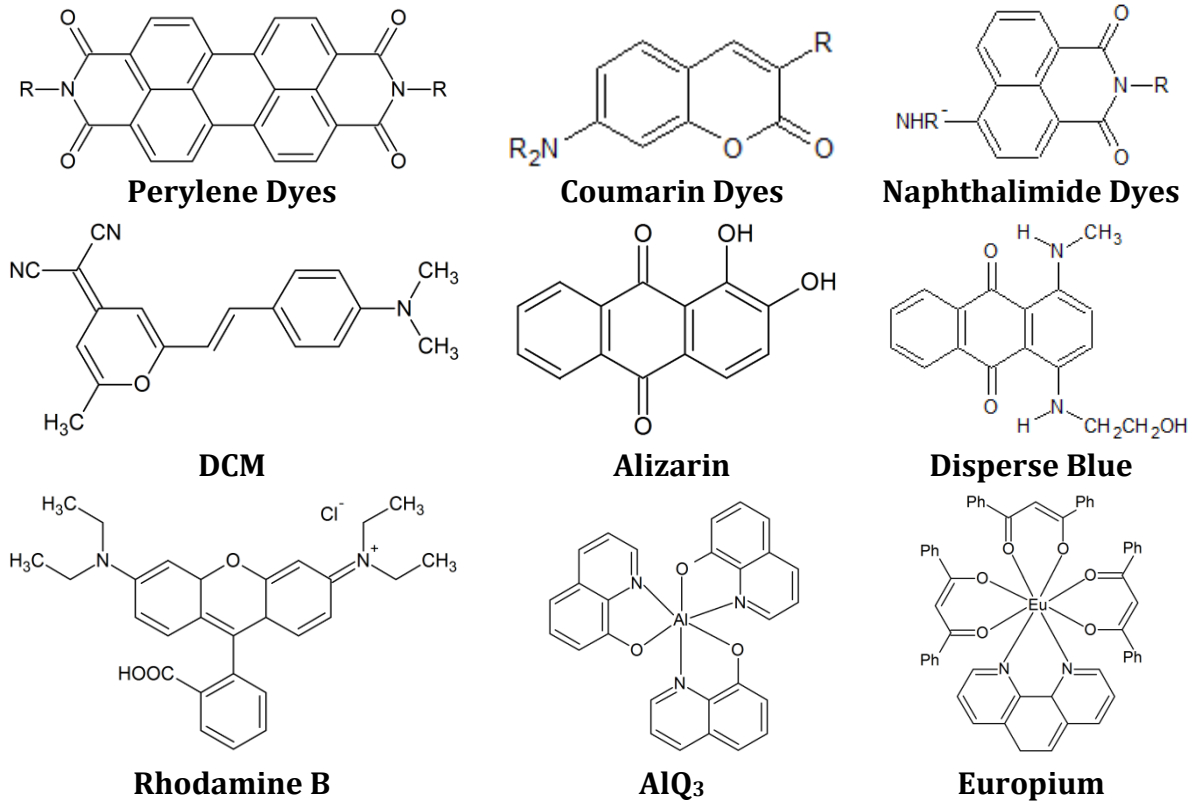

Figure 3.22: Chemical structures of the LDS materials used. AlQ_3 and europium are organo-metallic dyes and the rest are organic. All these dyes are based around aromatic ring structures.

Europium Complex: Europium is a lanthanide and these complexes have been studied comprehensively, as they are known to have good luminescent characteristics, with intense narrow emission spectra, large Stokes' shifts (>150 nm) and long luminescent lifetimes of up to a millisecond [222], [230], [231]. The absorption of lanthanides is not very high, and they rely upon the organic ligands of the complex to absorb the incident photons, the energy of which is then transferred to the lanthanide ion which re-emits at a lower energy ("antenna effect") [232]. For this work the europium complex used was europium(III) tris(1,3-diphenyl-1,3-propanedionato) mono(1,10-phenanthroline) [sym.: $Eu(dbm)_3(phen)$], supplied by Sigma Aldrich (#538965). Europium complexes have been researched as LDS coatings for DSSCs, CdTe PV cells and in LSCs.

Tris (8-hydroxyquinolinato) aluminium (AlQ_3): AlQ_3 has been widely used in the active layer of green organic light emitting diodes (OLEDs) [233], [234]. It has been successfully used as an LDS with polymer solar cells [207].

Napthalimide and Perylene Dyes: These two chemical groups are similar, as perylene is a molecule consisting of two naphthalene molecules joined together. Dyes from these

two chemical groups have been used extensively in LDS and LSC applications and as sensitisers in DSSCs [219], [228], [235]–[238]. Two manufacturers of these dyes are Kremer Pigments and BASF (Lumogen®) and a representative selection of their dyes was used for the research in this thesis, based on their absorbance and PL spectra, and previous reports of their use.

Lumogen Dyes: Lumogen red (F300) and Lumogen orange (F240) are both perylenes. These dyes have been shown to improve the performance of multicrystalline silicon PV by being included as a dopant in the EVA encapsulant [193].

Kremer Dyes: Kremer blue (94736) (naphthalimide); Kremer Orange (97400) and Kremer Green (94737) (both perylenes) [239].

Coumarin Dyes: Coumarin dyes have been used in DSSCs as sensitizers and in LSCs [225], [240]–[243]. Two dyes were selected, based on their absorbance and PL spectra: Coumarin7 and Coumarin153.

Alizarin & Disperse Blue 3: Both alizarin and disperse blue 3 are anthraquinone dyes (alizarin is purple). Alizarin was used as the sensitiser in early work on DSSCs [244]. Neither is known to have been used in previous studies on LDS on PVs.

DCM [4-(Dicyanomethylene)-2-methyl-6-(4-dimethylaminostyryl)-4H-pyran]: DCM has been used as an LDS with LSCs and on CdTe devices [219], [245]. DCM has been blended with AlQ_3 and used as an LDS material on ZnPc:C_{60} OPVs, showing an increase in efficiency of more than 10% [246].

Rhodamine B: Rhodamine B is a pink dye that has traditionally been used as a standard for relative PLQY measurements [247], [248]. It has been used as a sensitiser in DSCs and as an LDS in LSCs [226], [249], [250].

3.3.5 LDS Host Materials

Although LDS materials can be applied directly onto the surface of solar cells (e.g. by sublimation [251]) it is more usual to dissolve the LDS dye in a host material. As this is applied to the front of a solar cell it must have low haze (scattering) and high transmittance across all of the relevant wavelengths for both the dye (absorption spectrum) and the solar cell (EQE). It will need to be compatible with the LDS material and the solvent used to dissolve the LDS material. If it is the final layer on the front surface it needs to be weatherproof, with good UV stability. Solar modules can reach temperatures in excess of 40°C, so both host and LDS materials must have good thermal

stability. It must have a lifetime that matches or exceeds that of the solar cell (over 25 years for silicon), remaining stable and transparent. It must have a suitable refractive index to complement the solar cell and any other layers which it touches. Crucially it must have good mechanical adhesion and be compatible with the fabrication techniques being used.

A common host material is poly(methyl methacrylate) (PMMA), which is also known as acrylic or by various trade-names (e.g. Perspex). It is a hard, clear polymer which is soluble in a large range of solvents. It is transparent down to below 300 nm, relatively UV stable with good weatherability and has good miscibility with most LDS dyes. It has a long history of being used as the bulk material for LSCs [252]. Other host materials which have been used are: polyvinyl acetate (PVA), EVA, polyurethane, and epoxy resin [195], [200], [220], [253]. All of these materials have been used previously as encapsulants so their suitability for use with PV is known and they have the advantage that LDS materials can be utilised without having to add extra fabrication steps.

3.3.6 Comparison using Figures of Merit of LDS Layers

To analyse and compare different LDS materials, a number of figures of merit have been used. These build upon the work of Alonso-Álvarez et al. and have been extended by the author to include "UV Coverage", as this is of particular importance to OPVs [224]. The first three are based solely on the optical characteristics of the LDS material (transmittance, PL and PLQY). Transmittance ($T(\lambda)$) is used as it defines the actual amount of light passing through the layer according to the Beer-Lambert Law (see Equation 3.4, where λ is wavelength).

$$\boldsymbol{T(\lambda) = 10^{-Absorbance(\lambda)}} \quad 3.4$$

Radiative Overlap (RO): A measure of the overlap between the absorption and PL spectra (Figure 3.23a & Equation 3.5). RO is the proportion of emitted light which will be reabsorbed by the dye itself and ideally will be 0%.

$$\boldsymbol{RO = \frac{\int [1 - T(\lambda)] PL(\lambda) d\lambda}{\int PL(\lambda) d\lambda}} \quad 3.5$$

UV Coverage (UVC): Defined as the fraction of incident light within the UV region (300-400 nm), which is absorbed by the LDS layer and prevented from reaching the solar cell (Figure 3.23b & Equation 3.6). Ideally this figure will be high providing the cell with

good UV filtering as, although this does not affect the actual performance of the solar cell, it will have a serious impact on the degradation of a solar cell (due to photo-oxidation) and therefore its lifetime.

$$\boldsymbol{UV = \frac{\int_{400}^{300}[1 - T(\lambda)]AM1.5G(\lambda)d\lambda}{\int_{400}^{300} AM1.5G(\lambda)d\lambda}} \quad 3.6$$

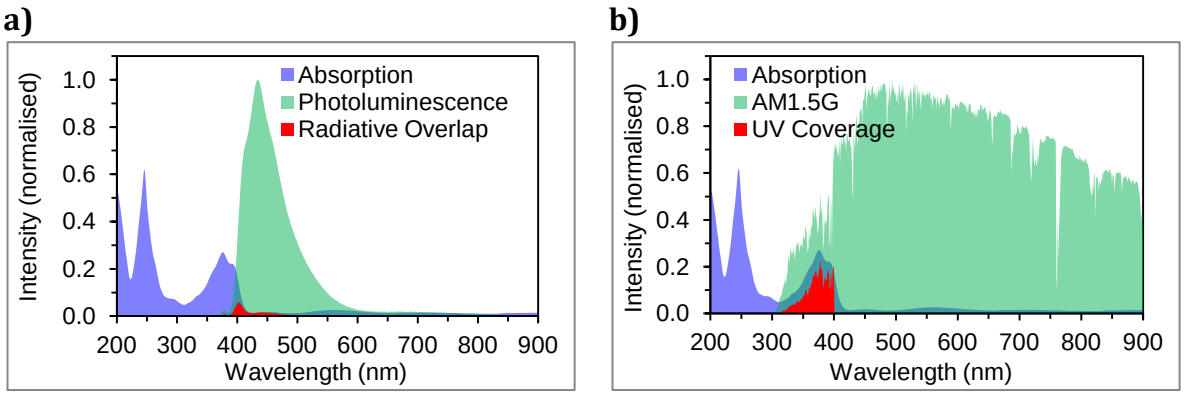

Figure 3.23: Figures of Merit: a) Radiative Overlap; b) UV Coverage.

Photoluminescent Quantum Yield (PLQY): this is the probability that an absorbed photon will be re-emitted:

$$\boldsymbol{PLQY = \frac{No\ of\ emitted\ photons}{No\ of\ absorbed\ photons} \times 100\%} \quad 3.7$$

The following figures of merit are also based on spectrum of the incident light (AM1.5G) and on the EQE of the active layer of the OPV:

Absorption Spectral Matching (ASM): A measure of how well the LDS layer absorbs photons which are not utilised by the solar cell (Figure 3.24a). Equation 3.8 defines *Φ(λ)*, the spectral distribution of the wasted photons which cannot be utilised by the solar cell, and Equation 3.9 defines the fraction of the wasted photons which are absorbed. Ideally this will be 100%.

$$\boldsymbol{\Phi(\lambda) = AM1.5G(\lambda)[1 - EQE(\lambda)]} \quad 3.8$$

$$\boldsymbol{ASM = \frac{\int[1 - T(\lambda)]\Phi(\lambda)d\lambda}{\int \Phi(\lambda)d\lambda}} \quad 3.9$$

Parasitic absorption (PA): A measure of the absorption in the region where the solar cell performs well (Figure 3.24b). Ideally this will be 0%. Equation 3.10 defines *Θ(λ)*, the spectral distribution of the photons which are absorbed by the solar cell. Equation 3.11

defines parasitic absorption, the fraction of the photons absorbed by the dye which would otherwise have been absorbed by the solar cell.

$$\boldsymbol{\Theta(\lambda) = AM1.5G(\lambda)EQE(\lambda)} \quad 3.10$$

$$\boldsymbol{PA = \frac{\int [1 - T(\lambda)]\Theta(\lambda)d\lambda}{\int \Theta(\lambda)d\lambda}} \quad 3.11$$

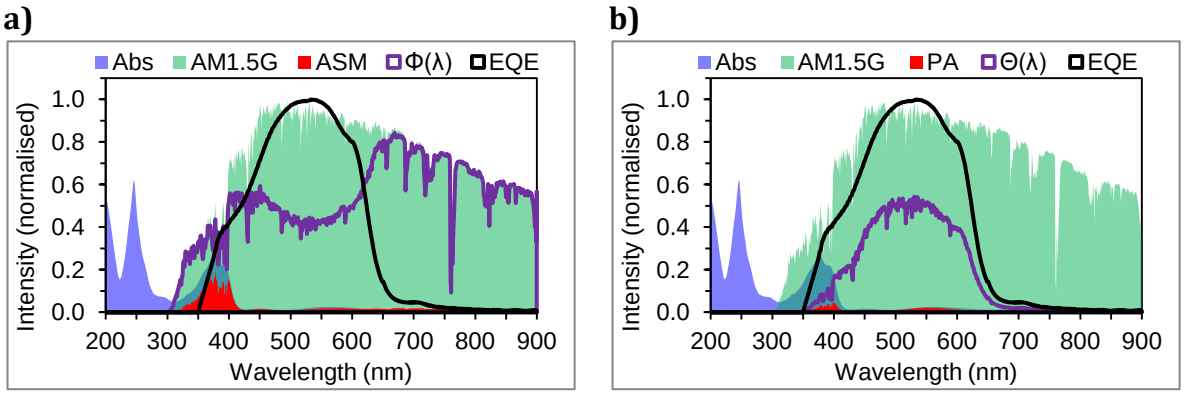

Figure 3.24: Figures of Merit: a) Absorption Spectral Matching; b) Parasitic Absorption. [Based on Kremer Blue and P3HT:$PC_{61}BM$].

Emission Spectral Matching (ESM): A measure of how well the PL of the LDS material matches with the solar cell (Figure 3.25 & Equation 3.12). Ideally this will be 100%.

$$\boldsymbol{ESM = \frac{\int PL(\lambda)EQE(\lambda)d\lambda}{max(EQE)\int PL(\lambda)d\lambda}} \quad 3.12$$

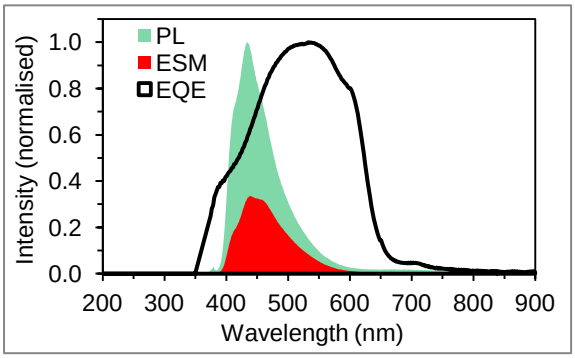

Figure 3.25: Figures of Merit: Emission Spectral Matching. [Based on Kremer Blue and P3HT:$PC_{61}BM$].

Chapter 4. Experimental Methods

This chapter details the experimental methods used during this research. A full description of the outdoor measurement system is given, followed by details of the methods used to analyse the outdoor data. The different OPV modules supplied by DTU are described. Details of the in-house OPV test cells are given, along with the fabrication methods employed. Laboratory characterisation of cells and modules is very important as it allows testing under controlled conditions, which facilitates comparisons between different materials and designs. The various techniques are described, including optophysical characterisations used with LDS coatings and the setting up of an EQE system. One phase of research involved the use of structured modules to improve the outdoor performance of OPVs and details are provided of how these were fabricated and tested. The final chapter of this thesis investigates how the application of luminescent downshifting layers could improve the performance and stability of OPV devices. Details of application methods and sample preparation are provided.

4.1 Outdoor Measurement System at Bangor

The majority of the outdoor monitoring took place on the roof of the School of Electronic Engineering, Dean St., Bangor, Gwynedd (53.23°N 4.13°W), which has an altitude of 40 m above sea level and is located 250 m from the Menai Strait. The UK is classified as Oceanic (Cfb) under the Köppen-Geiger climate classification [254]. Long term climatic averages[2] are 14°C during summer and 4.7°C during the winter. The humidity levels are similar all year, with an average mean of 79%, an average maximum of 90%, and an average minimum of 61% in summer and 65% in winter. UV indices are very different, with an average mean of 1.07 in the summer (average maximum of 5.45) and 0.43 in the winter (average maximum of 2.38). Appendix B.1 shows climatic averages experienced during the course of the research. The location is a flat roof with brick parapets to 1.3 m all round. Bangor Mountain is to the South and causes shading in

[2] Long term climate data was sourced from the Meteorological Office for RAF Valley on Anglesey (~20 miles away).

the winter in early morning and late afternoon. There is a brick shed where the monitoring equipment and computer hardware are installed.

4.1.1 Outdoor Monitoring – Hardware

A complete outdoor measurement system for this research was designed and installed by the author on the roof at Dean Street (see Figure 4.1 and Figure 4.2). The measurement system conforms to ISOS-O-2 outdoor measuring protocol [119]. It comprises two OPV module mounting racks, each of which can be independently adjusted for inclination. OPV modules are attached on raised studs to allow free air flow behind the modules. Two 8-channel multiplexers are each connected to a separate source measure unit (SMU) (supplied by Botest Systems GmbH), allowing two sets of up to eight modules to be monitored synchronously. Two silicon irradiance sensors (supplied by IMT Solar) are used to measure irradiance. One is mounted horizontally and the other in-plane-of-array with one of the inclined OPV racks.

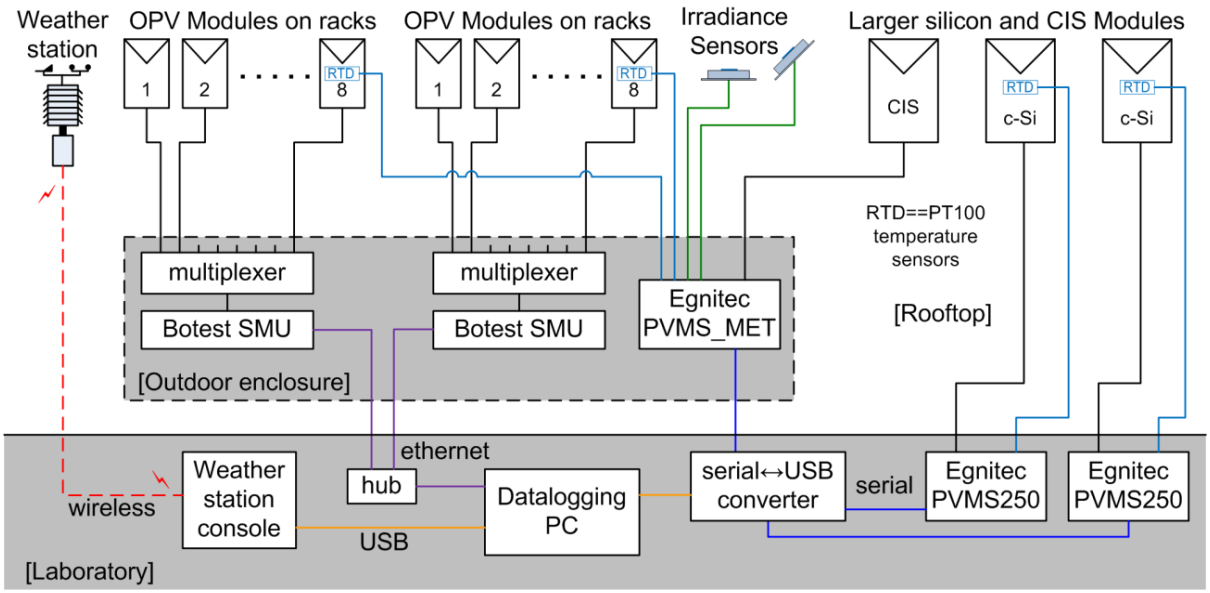

Figure 4.1: System schematic of the outdoor monitoring system on the roof of the School of Electronic Engineering at Dean Street, Bangor.

Table 4.1 has details of the non-OPV modules tested during this research. There are two PWSQM-48 polycrystalline silicon modules on the roof, one mounted horizontally and the other inclined at 35° and facing due south. These are monitored by two PVMS-250 measurement systems, supplied by Egnitec Ltd. Each silicon module has a PT100 temperature sensor, attached to its backplane, also monitored by the Egnitec PVMS units. There is an ST36 copper indium diselenide (CIS) module, inclined at 35° and

facing due south [255]. This is connected to an Egnitec PVMS-250(MET) measurement system, which also monitors the two irradiance sensors and the two OPV PT100 sensors. During the research a dye sensitised solar cell (DSSC) was also monitored on the OPV rack, but its model number, rated power and nominal efficiency are unknown.

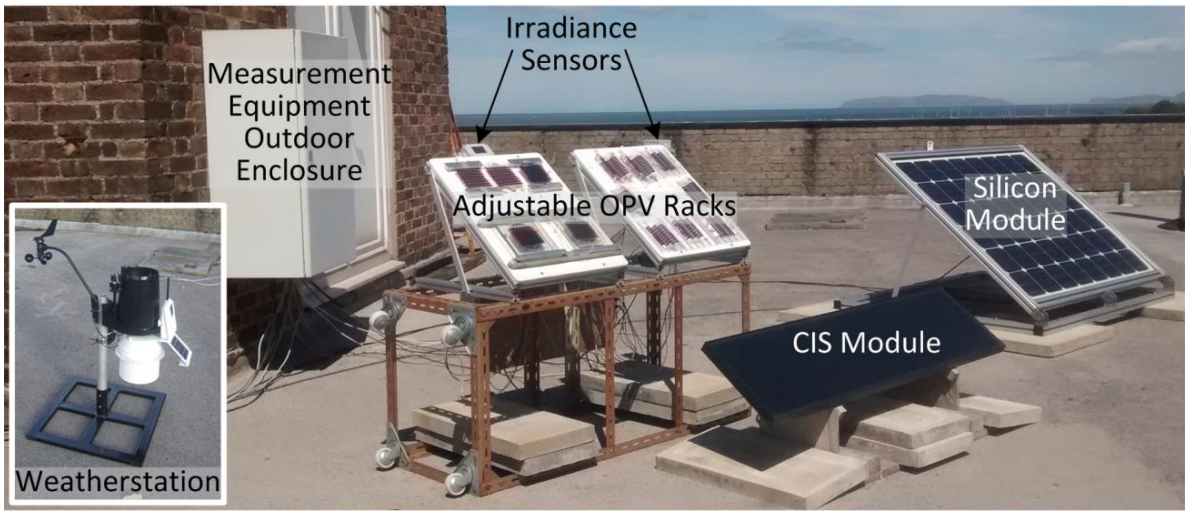

Figure 4.2: Photograph of the outdoor monitoring system on the roof of the School of Electronic Engineering at Dean Street, Bangor.

Table 4.1: Details of PV modules tested during this research.

Type & Model Number	Manufacturer	Dimensions (cm x cm)	Rated Power	Nominal Efficiency
Poly-Si: PWSQM-48 polycrystalline silicon	Pure Wafer Solar Ltd.	132.7 x 99.9	185 W_P	14.0%
CIS: ST36 Copper indium diselenide	Shell Ltd.	129.3 x 32.8	36 W_P	8.5%
DSSC: Dye sensitised solar cell	SolarPrint (Dublin)	7.3 x 7.5	N/A	N/A

4.1.2 Outdoor Monitoring – Weather Station

A Davis Vantage Pro 2 weather station is used to collect meteorological data including temperature, humidity, wind speed and direction, solar radiation, UV, rainfall, and air pressure [256]. The solar powered integrated sensor suite is mounted on the roof and communicates wirelessly to a console indoors (see inset in Figure 4.2). The console is connected to the main datalogging PC and periodically downloads its data to the PC. The weather station has its own internal clock and therefore the weather data is not synchronised to the PC. In order to maintain reasonable synchronisation between the weather data and the datalogger measurements on the PC, it was necessary to regularly reset the weather station clock to match the PC's internal clock. As the weather

data is stored as minute by minute averages, a slight discrepancy (<30 seconds) between the two clocks is not a significant problem.

4.1.3 Outdoor Monitoring – Software

The Botest SMUs and the Egnitec measurement units both have dedicated datalogger software which runs on the same PC, ensuring that the measurement timestamps are synchronised. The Botest software was controlled by an autoclicker[3], which starts a new measurement cycle every 10 minutes. The measurement cycle runs a full IV sweep on each module connected to the multiplexers in turn. The two Botest SMUs run their measurements simultaneously. Each IV sweep takes between 10 and 30 seconds to complete depending on start and end points, step size and preset delay. Between IV sweeps the OPV modules are kept at V_{OC}.

The Egnitec datalogger software controls all of the PVMS units simultaneously. Each PV module was kept at maximum power point (MPP). The software was configured to measure current and voltage (I_{MPP}, V_{MPP}), irradiances (horizontal and in-plane) and PT100 temperature sensors once every 15 seconds. Once a minute an IV sweep was performed on each module, taking about 3-5 seconds to complete, before returning the module to MPP.

4.1.4 Outdoor Monitoring – Data Analysis

The data from each source (weather station, Botest and Egnitec) are stored in different format text files and have different measurement frequencies. An Access database was designed, which incorporated import routines to process these different datafiles, including extracting the performance parameters (I_{SC}, V_{OC}, FF, I_{MPP} and V_{MPP}) from the IV curves. Once the data was imported a series of programs to synchronise the data from the different sources were run. This was necessary as, in order to calculate module efficiency, the irradiance at the time of each measurement is required. The result of this synchronisation was that every module measurement was linked to the nearest irradiance and weather measurement. The data from each measurement campaign was kept in its own database in order to speed up queries on the data.

A separate MS Access database frontend was written, which can connect to each of the campaign databases individually. This frontend has a large number of queries

[3] Autoclicker software replicates the clicking of a mouse at predetermined intervals.

which have been developed over the course of the research and are used to extract the required results from the measurement data.

4.2 OPV Devices

Two different types of OPV modules were used for this research: freeOPV modules from DTU; small six-pixel test cells, fabricated in-house at Bangor, for indoor characterisation and lifetime testing.

4.2.1 DTU freeOPV Modules

OPV modules were fabricated and supplied by Professor Frederic Krebs' group at Technical University of Denmark (DTU) as part of their freeOPV programme [112]. The freeOPV modules are fabricated using a R2R process under ambient conditions with screen and flexographic printing, slot die coating and spray coating of the various layers (see Figure 4.3a) [131], [257].

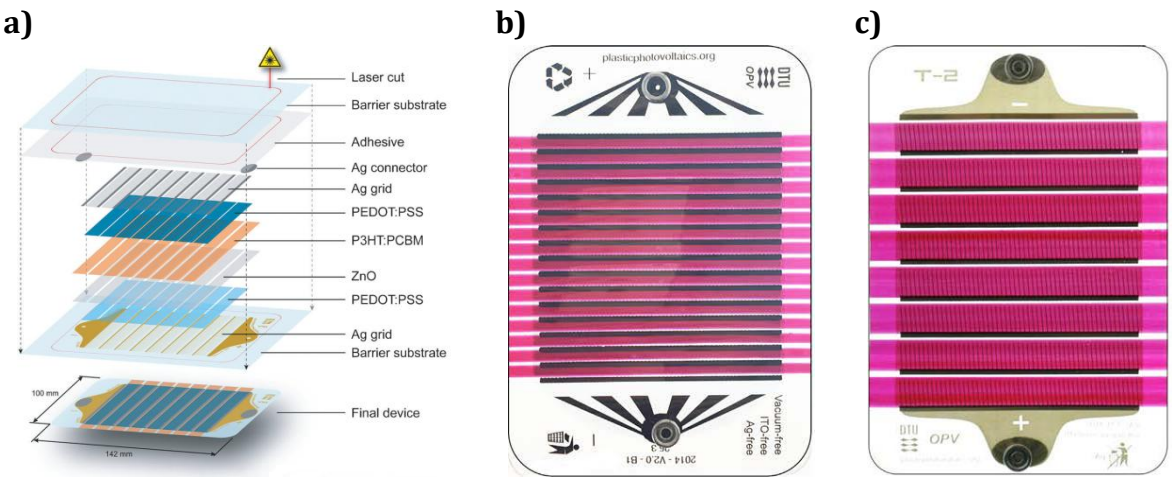

Figure 4.3: DTU freeOPV modules: a) outline of the multilayer structure in first generation freeOPV module; b) freeOPV module with graphite busbars; and c) freeOPV module with silver nanowire front electrode [112], [258]**.**

The following freeOPV module types were used, selected as availability allowed (see Figure 4.3):

DTU(AgGrid): These were the first modules supplied under the freeOPV programme and are based on an inverted geometry with 8 serially connected cells [112]. The modules are fabricated on an ITO-free "Flextrode" PET substrate, consisting of an Ag grid coated with PEDOT:PSS and then ZnO (acting as an electron transport layer) [257].

The active layer is slot die coated on top of the Flextrode, followed by PEDOT:PSS (acting as a hole transport layer) and finally an Ag grid. The top substrate is PET with SiOx barrier layers, which encapsulates the module using pressure sensitive adhesive. Finally the modules are laser cut from the foil which seals the edges. Active area: 64.8 cm^2.

DTU(Carbon): These modules replace the front Ag grid with highly conductive PEDOT:PSS and carbon (graphite) busbars between the cells, and the back Ag grid with PEDOT:PSS and ZnO. The module consists of 16 serially connected cells [97], [258], [259]. Active area: 30 cm^2.

DTU(AgNW): These modules are similar to the DTU(AgGrid) modules, but the front Ag grid is replaced by a hybrid AgNW/ZnO layer [260], [261]. Active area: 64.8 cm^2.

4.2.2 OPV Device Fabrication at Bangor

All the devices were fabricated in a category 1000 cleanroom and nitrogen atmosphere glovebox. The glovebox was maintained at levels down to <1 ppm for O_2 and <100 ppm for H_2O and was fitted with a solvent scrubber. The small six-pixel test cells were fabricated using pre-patterned ITO on glass substrates (see Figure 4.4), with the ITO having a sheet resistance of 16 Ω/square. Each pixel had an active area of 7 mm^2 defined by the overlap between the top electrode and the ITO.

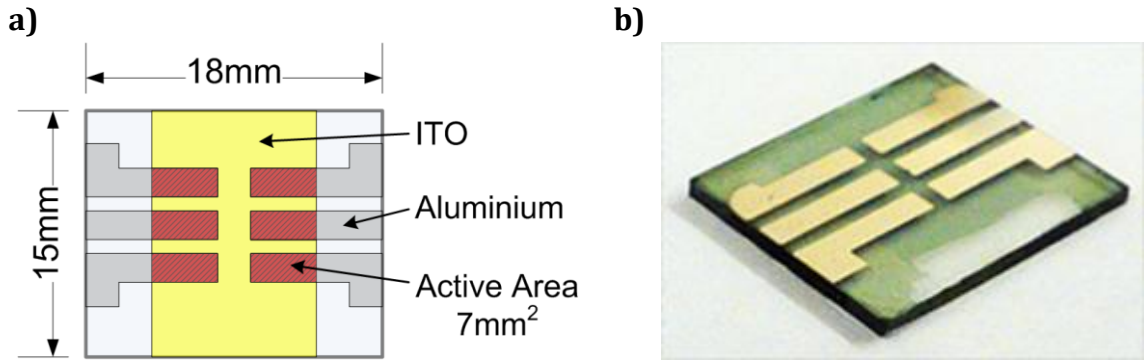

Figure 4.4: Small six-pixel test cells: a) design; b) photo of PCPDTBT OPV device.

Fabrication of Normal Geometry OPV Devices

Normal (non-inverted) geometry OPV device fabrication followed the following procedures:

Active Layer Blend Preparation: Prior to fabrication of the devices the blend had to be prepared and allowed to completely dissolve. The majority of devices were fabricated

using P3HT:$PC_{61}BM$ as the active layer, deposited from solution. P3HT (supplied by Sigma Aldrich) and $PC_{61}BM$ (supplied by Nano-C Inc.) were prepared with weight ratios of 1:0.8 and dissolved in anhydrous chlorobenzene to give a solution with a concentration of 30 mg/ml. After preparing the blend in the cleanroom it was transferred to the glovebox in a sealed vial. This was placed on a hot plate with a magnetic stirrer at 50°C for 48 hours to ensure solids were completely dissolved.

The order of processing is as follows:

Substrate Cleaning: The standard small area test cells were fabricated on glass substrates with pre-patterned ITO electrodes. These were jet washed with deionised water, followed by acetone and finally isopropyl alcohol, then dried using nitrogen gas. This was followed by 5 minutes of O_2 plasma etch which removes any residual organic compounds and alters the surface energy of the ITO in preparation for coating with PEDOT:PSS.

PEDOT:PSS Deposition: The substrates were spin coated with PEDOT:PSS (Heraeus Clevios™ AI 4083 supplied by Ossila) at 5000 rpm for 30 seconds to give a thickness of ~45 nm, then moved into the glovebox and baked on a hotplate at 120°C for 20 minutes to anneal and dry the PEDOT:PSS layer. All subsequent processing was performed in the glovebox.

Active Layer Deposition: The active layer was applied by spin coating from a 60°C blend at 1500 rpm for 60 seconds, giving a thickness of ~100 nm. The active layer was then annealed at 140°C for 1 hour.

Thermal Evaporation of Top Electrode: Thermal evaporation of the cathode was performed though a shadow mask to define the electrode pattern and consisted of 8 nm of calcium and 100 nm of aluminium.

Encapsulation: For some devices an optional encapsulation step was performed before the devices were removed from the glovebox. A drop of UV-curable epoxy resin (supplied by Ossila) was placed on top of the device and a glass coverslip was applied, being careful to remove any air pockets. This was cured under a UV lamp until the epoxy had set (about 3-4 minutes). The active layer was protected from UV irradiation by the aluminium electrode.

Fabrication of Inverted Geometry OPV Devices

Inverted devices were processed in a similar manner to the normal geometry devices with the following steps:

Substrate Cleaning: as above.

Zinc Oxide Deposition: A film of ZnO was sputter coated at room temperature onto the ITO/glass substrate to give a thickness of 20-30 nm. The substrates were transferred to the glove box and annealed on a hotplate at 200°C for 30 minutes. An alternative method for depositing the ZnO layer was the sol-gel process. Zinc acetate dihydrate (109 mg) was dissolved in a solution of 2-methoxyethanol (1 ml) and ethanolamine (0.03 ml) and stirred for 1 hour at room temperature. This was then spin coated onto the substrate at 2000 rpm for 60 seconds and then baked at 150°C for 1 hour in atmospheric oxygen [262]. This allowed the zinc acetate to calcinate into zinc oxide, forming a layer of ZnO ~30 nm thick.

Active Layer Deposition: as above.

Thermal Evaporation of Top Electrode: Thermal evaporation of the anode was performed though a shadow mask to define the electrode pattern and consisted of 10 nm of molybdenum trioxide and 100 nm of silver.

Encapsulation: optional – as above.

4.3 Encapsulation of DTU Modules

The first OPV modules monitored outdoors showed fast degradation rates and this highlighted the importance of encapsulation to prevent ingress of water and oxygen. The DTU modules have PET barrier foil from Amcor used as front and back substrates, but are susceptible at the edges and where the contacts pierce the foil [147], [263]. Although PDMS is not suitable for long term encapsulation, as it has a relatively high WVTR, for short term testing it is ideal, providing an easy to use encapsulant with excellent optical properties. The PDMS used was Sylgard 184, supplied by Dow Corning. After preparing the required quantity of PDMS it was degassed under vacuum before being poured onto a module, pre-prepared with wires soldered to the contacts, within a PTFE former taped to a glass backing sheet. The assembly was then heated to 40°C (low enough to prevent degradation of the OPV modules) and allowed to cure for 24 hours (Figure 4.5).

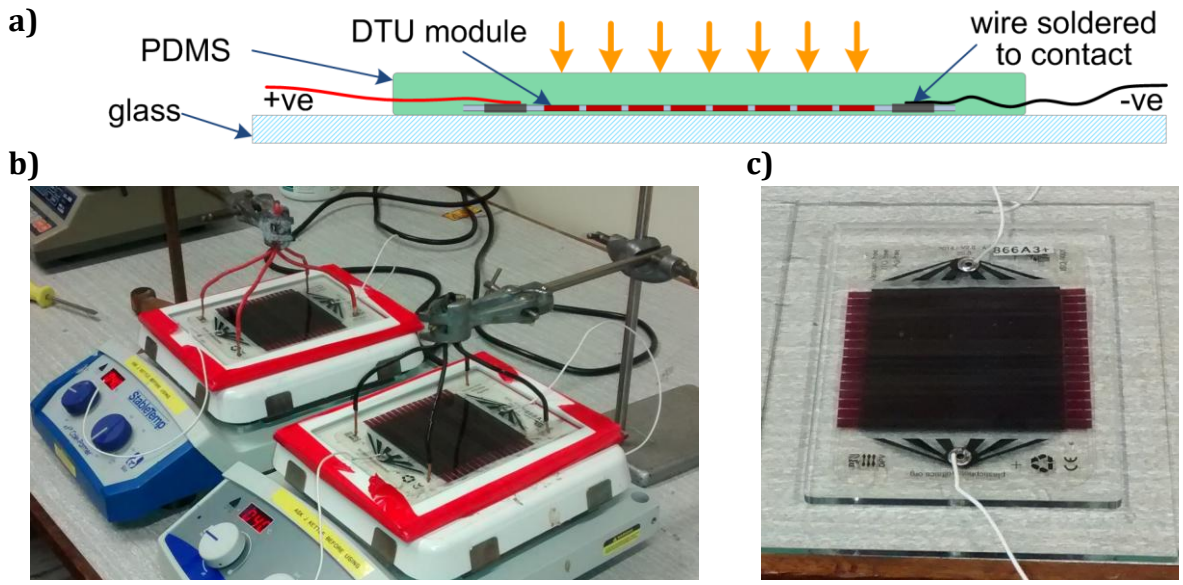

Figure 4.5: PDMS encapsulation of OPV modules: a) cross section of PDMS on glass; b) curing on hotplate at 40°C; and c) OPV module encapsulated in PDMS on a glass backing sheet ready for outdoor testing.

4.4 Characterisation Techniques

4.4.1 IV Characterisation and Lifetime Testing

A solar cell's performance parameters (V_{OC}, I_{SC}, FF, and PCE) can be evaluated from on an I-V curve measured under a source at a known irradiance. These measurements were performed using a Newport Oriel™ Sol1A class ABB solar simulator (Figure 4.6a). It has a xenon bulb with additional filtering which provides irradiance at 100 mW/cm^2 and a spectrum of AM1.5G. This simulator has a reasonably even light profile across an area of 10 cm x 10 cm which is large enough for measuring the performance of the freeOPV modules from DTU. The IV curve was measured using an SMU supplied by Botest Systems GmbH. This was supplied with a multiplexer allowing up to eight channels to be measured sequentially. This was used along with a bespoke cell holder for lifetime testing of up to four small test cells (Figure 4.6b). For lifetime stability tests the cells were placed under the solar simulator and regular IV curves taken (normally once every 30 minutes). In between measurements the cells were kept at V_{OC}. The lifetime setup conforms to ISOS-L-1 indoor measurement protocol [119].

a) b)

Figure 4.6: a) IV characterisation under the Newport Oriel™ Sol1A class ABB solar simulator at Bangor. Photograph shows a 3D module being measured. b) Lifetime testing of small six-pixel test cells was performed using a bespoke cell holder kept under constant illumination under the solar simulator.

4.4.2 Angular IV Characterisation.

The IV characterisations described in Section 4.4.1 were performed with the modules perpendicular to the irradiance. For the structured modules in Chapter 6 it was necessary to ascertain the effect that modifying the angle of incidence had on the performance parameters. This was measured on the Lucas Nuelle solar simulator at Cardiff School of Engineering (Figure 4.7).

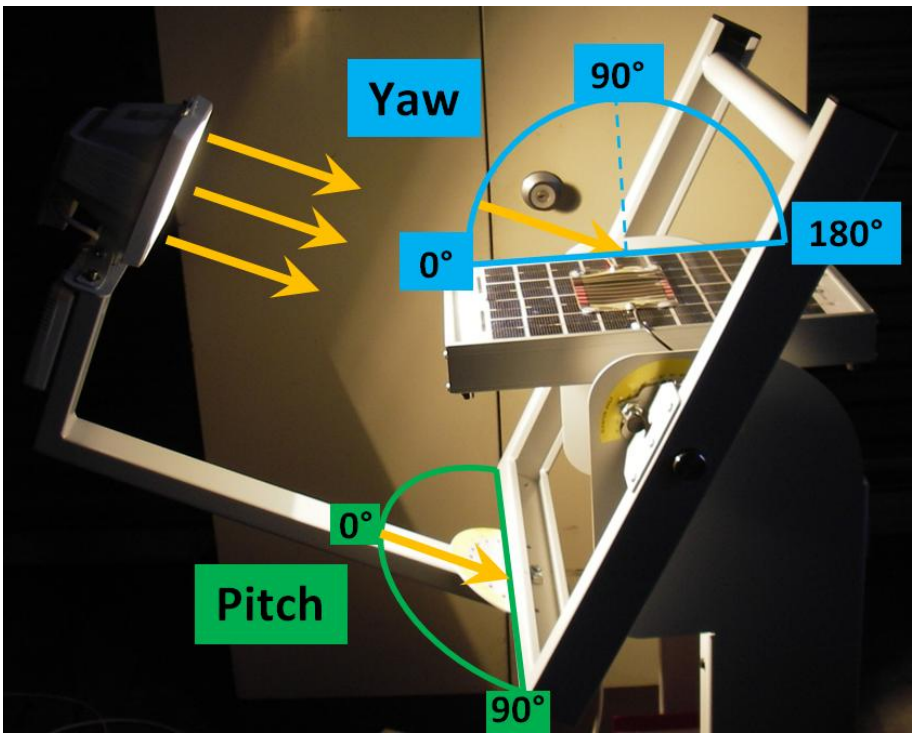

Figure 4.7: Lucas Nuelle solar simulator at Cardiff School of Engineering.

The light source is a linear halogen bulb, adjustable from 0 to 500 W, and can be tilted to allow measurements at various angles of yaw and pitch to simulate the path of the sun at different times of the day and of the year (Figure 4.8). The equipment provides solar simulation of the sun's elevation angle (pitch) in 15° increments with a total 120° sweep angle. The passage of the sun during the day (yaw) can be set in 10° increments with a 180° range. The module measurements were taken using a Botest SMU to obtain an IV curve from which the performance parameters could be derived.

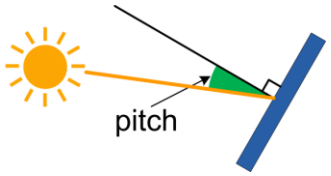

PITCH is the angle of the "sun" away from normal incidence and simulates the vertical tilt of the panel.
(0° = panel directly facing the sun)

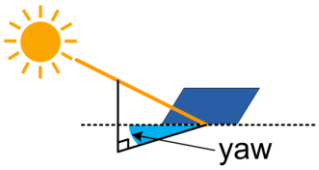

YAW is the angle of the "sun" in the horizontal plane and simulates the diurnal passage of the sun.
(90° = panel directly facing the sun).

Figure 4.8: Definition of pitch and yaw.

Light Spectra Mismatch

Figure 4.9 shows the normalised spectra of the AM1.5G standard [264], the solar simulator at Bangor (xenon bulb with filtering) and the Lucas Nuelle simulator at Cardiff (linear halogen bulb). It also shows the EQE curve for P3HT:$PC_{61}BM$.

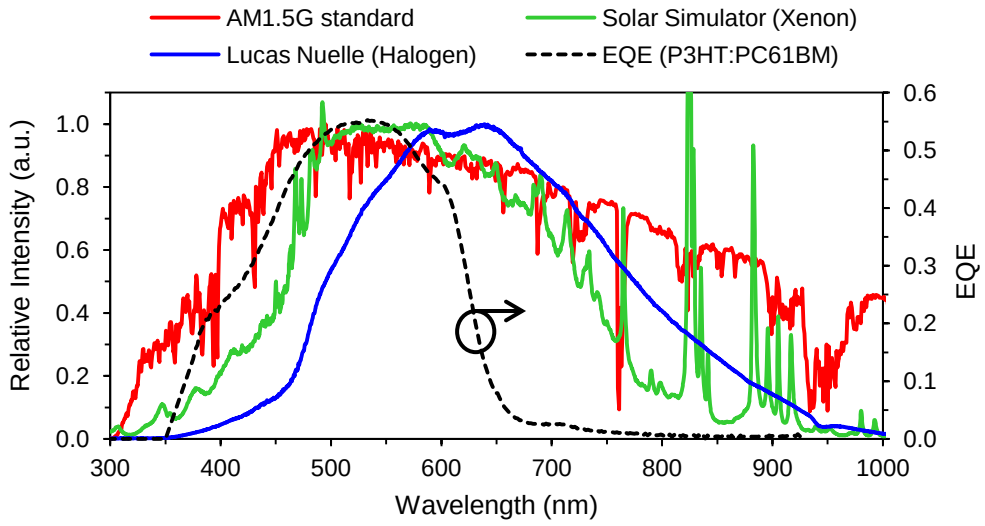

Figure 4.9: Spectral Mismatch. The standard light spectra for AM1.5G, the Newport solar simulator at Bangor (xenon bulb with filtering), and the Lucas Nuelle solar simulator at Cardiff (linear halogen bulb). The EQE of P3HT:$PC_{61}BM$ is also shown.

Although there is fairly a close match between the AM1.5G standard spectrum and the xenon bulb, there is a large spectral mismatch between the xenon and halogen bulbs. This leads to a lower calculated efficiency from the Lucas Nuelle results, as the spectrum of the halogen bulb has relatively low intensity in the region where P3HT:$PC_{61}BM$ is most efficient (400-600 nm) in comparison to the xenon bulb. Therefore the efficiency measurements obtained from the Lucas Nuelle need to be adjusted by a multiplier, known as the spectral mismatch factor.

The IEC standard IEC60904-7 defines how the mismatch factor (MMF) should be calculated [265]. Equation 4.1 shows how the *MMF* is calculated from the spectral responses of the reference cell ($S_R(\lambda)$) and test cell ($S_T(\lambda)$) and the output spectrums from the reference cell ($E_R(\lambda)$) and the solar simulator ($E_S(\lambda)$) [48], [265]–[267].

$$\boldsymbol{MMF} = \frac{\int \boldsymbol{E_R(\lambda) S_R(\lambda) d\lambda}}{\int \boldsymbol{E_S(\lambda) S_R(\lambda) d\lambda}} \times \frac{\int \boldsymbol{E_S(\lambda) S_T(\lambda) d\lambda}}{\int \boldsymbol{E_R(\lambda) S_T(\lambda) d\lambda}} \qquad 4.1$$

The mismatch factor obtained was 2.67 and has been applied to all the PCE measurements made on the Lucas Nuelle equipment (similarly for J_{SC}) [268]:

$$\boldsymbol{PCE_{AM1.5G}} = \frac{\boldsymbol{P_{out}}}{\boldsymbol{P_{in}}} \times \boldsymbol{MMF} \qquad 4.2$$

4.4.3 External Quantum Efficiency Measurements

EQE is measured by exposing a solar cell to a narrow bandwidth of light at a known power and measuring the short circuit current. EQE is the ratio between incident photons (Equation 4.4) and number of generated electrons (Equation 4.5), where *P* is the power, λ is the wavelength of the incident light and *I* is the generated current:

$$\boldsymbol{EQE} = \frac{\boldsymbol{\#electrons}}{\boldsymbol{\#photons}} \qquad 4.3$$

$$\frac{\boldsymbol{\#\,photons}}{\boldsymbol{s}} = \frac{\boldsymbol{P}}{\boldsymbol{hf}} = \frac{\boldsymbol{P\lambda}}{\boldsymbol{hc}} \qquad 4.4$$

$$\frac{\boldsymbol{\#\,electrons}}{\boldsymbol{s}} = \frac{\boldsymbol{I}}{\boldsymbol{q}} \qquad 4.5$$

The EQE estimated AM1.5G short circuit current can be calculated from EQE measurements by integrating [Number of Photons x Fraction Converted to Electrons x Elementary Charge] across all relevant wavelengths:

$$I_{sc}^{EQE} = \int_{\lambda} (n_p)_{\lambda} (EQE)_{\lambda} q \, d\lambda \qquad 4.6$$

EQE provides a significant indication of PV performance, providing both spectral as well as J_{SC} information. A fully featured EQE measurement system is very expensive and therefore the author designed and built a system that would provide the whole OPV group at Bangor with a long term solution for EQE measurements on small test cells.

Figure 4.10 and Figure 4.11 show a photograph and system schematic of the EQE measurement system at Bangor. The quartz tungsten halogen light source has a usable range of 350-2500 nm and is driven by a stabilised power supply. This is coupled into a monochromator (Bentham M300), which has a servo-controlled diffraction grating to provide a beam of light with a bandwidth of 1 nm and a wavelength range of 375-925 nm. The output from the monochromator passes through an optical chopper, a filter and a lens which focuses the light onto the target which is positioned on an XYZ stage. The very low current output from the target is measured on a Stanford Research Systems SR830 lock-in amplifier, which is synchronised with the optical chopper in order to maximise the signal to noise ratio. A feature of diffraction gratings is the existence of overlapping spectra within the output, based on harmonics of the selected wavelength [269]. These harmonics are removed using different bandpass filters.

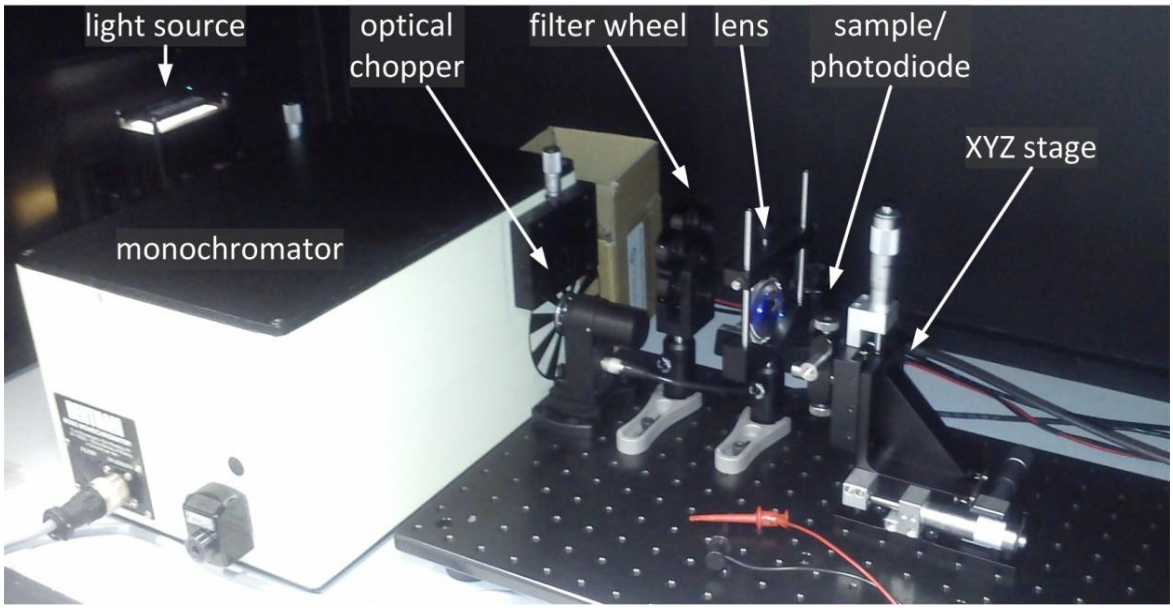

Figure 4.10: Photograph of the EQE measurement system at Bangor. The optical equipment is kept in a black enclosure to prevent stray light affecting the measurements.

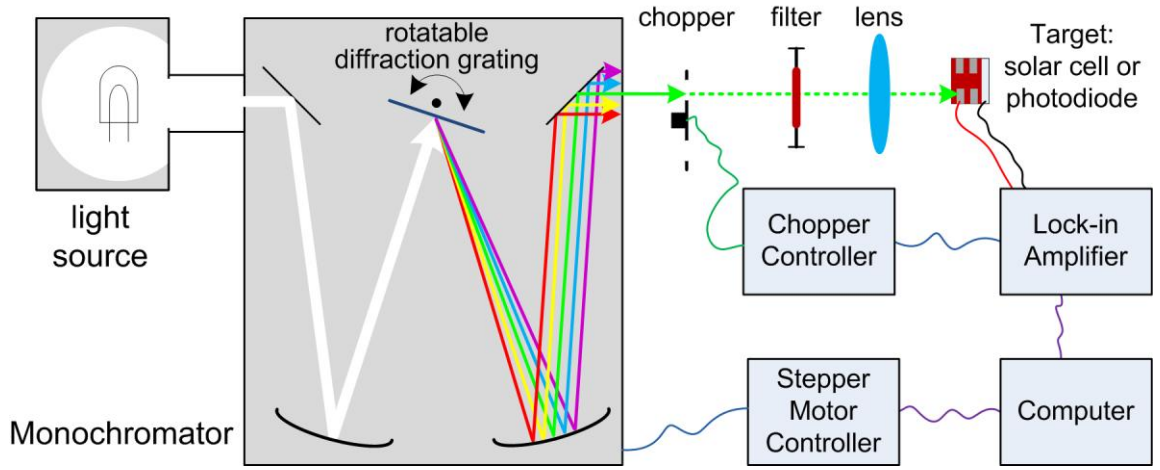

Figure 4.11: System schematic of EQE measurement system.

The hardware is controlled by a LabVIEW program (Figure 4.12a), which controls the measurement process. Two sweeps are performed, one using a calibrated photodiode (Thorlabs SM1PD1A) to measure the photon flux and the second measuring the output from the sample to measure the electron flux. Before each sweep the XYZ stage is adjusted to give maximum output. The photodiode has a mask in front to reduce its active area to the same size as the sample cells being tested. The data is then processed on a macro-enabled spreadsheet to give a graph of the EQE (Figure 4.12b).

a) **b)**

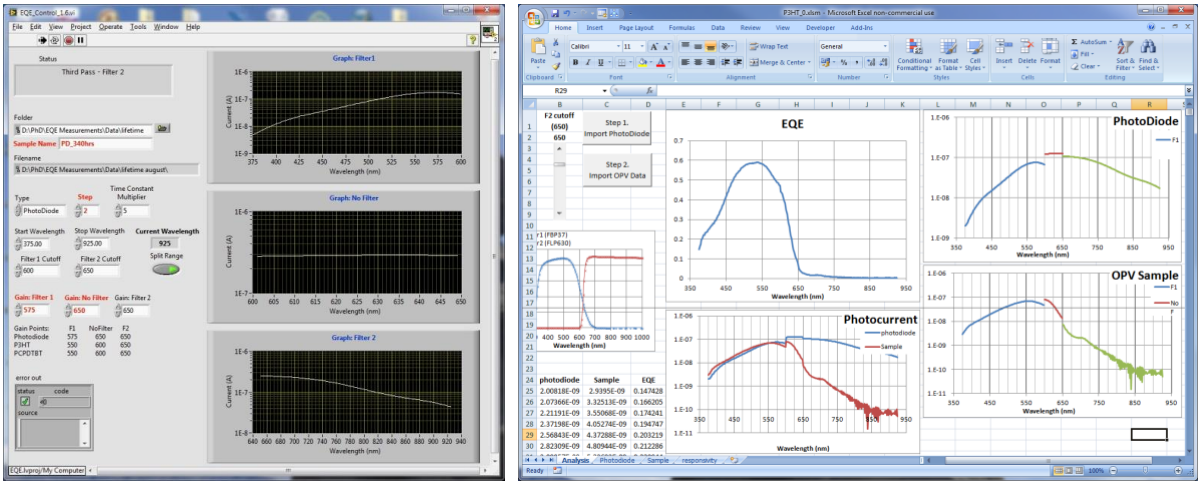

Figure 4.12: EQE Processing on the PC: a) screenshot of the LabVIEW program that controls the measurement process; and b) a screenshot of the macro enabled spreadsheet used to semi-automate the production of the EQE graphs.

4.4.4 Laser Beam Induced Current

All of the LBIC measurements in this thesis were performed by DTU. A laser beam (405 nm, 65 W/m^2, <100 μm spot size) is scanned over the surface of the module while the short circuit current is measured using a Keithley 2400 SMU [125], [270]. The data is used to construct a map where the colour gradient (blue to yellow) represents lowest to highest solar cell output. The images show the current profile of the device and can pinpoint areas with elevated or reduced performance. The colour gradient between blue (minimum current) and yellow (maximum current) is qualitative and therefore not comparable between different LBIC images [270].

4.4.5 Atomic Force Microscopy

Atomic force microscopy (AFM) was used to measure film thicknesses by scanning across a scratch made in the layer. AFM was also used to measure average surface roughness (R_A). These measurements were performed using a Digital Instruments Nanoman V running in tapping mode.

4.4.6 Optical Characterisation

Absorption spectra, photoluminescent emission spectra and PLQY measurements were used to characterise the optical properties of the LDS materials. Absorption measurements were made using a Shimadzu UV-3600 spectrophotometer. This has three detectors, a resolution of 0.1 nm and can measure across a wavelength range of 185-3300 nm. It is a dual beam instrument allowing samples to be compared against a reference (usually air). Photoluminescent emission spectra and PLQY were both measured using a Horiba Scientific Fluoromax-4 spectrofluorometer. Once the absorption peak for a sample had been identified, using UV-Vis spectroscopy, the sample was excited at this wavelength and the photoluminescent spectrum was obtained. To measure PLQY, an integrating sphere was fitted to the spectrofluorometer and a series of measurements were taken (both with and without the sample present in the chamber). These measurements were analysed by software to calculate absolute PLQY, based on the technique proposed by de Mello et al. [271].

4.5 Structured OPV Modules

One element of the research was to investigate how structured OPV modules perform compared to flat modules. OPVs have the benefit of being flexible which gives

them an advantage over traditional PV, which is flat and inflexible. In order to examine the potential performance benefits of structured solar panels, a choice has to be made as to what shape to test. The simplest way of structuring a flat flexible sheet is to form corrugations.

Two different substrates were chosen from the Corolux™ range of corrugated PVC roofing available from Ariel Plastics, Chesterfield, UK. One had a large corrugated profile (Figure 4.13a), which closely matched the size of the freeOPV modules, allowing one module to occupy a single section of the corrugated profile. The other substrate had a smaller sized corrugation (Figure 4.13b) which allowed one freeOPV module to span several corrugations. The different sizes of corrugation allowed different mechanical and optical properties to be examined.

The freeOPV modules were attached to the corrugated substrates using a double-sided adhesive tape with a foam core (0.7 mm thick) (Unibond™ exterior mounting tape). One batch of modules was attached using a thin (90 μm) double-sided adhesive tape with a polypropylene core (Tesa™ 64261 double-sided tape) but this was found to have too little give and caused sharp edged crinkles to form in the module. This was most noticeable on the modules mounted on the small corrugation with the tighter bend radius.

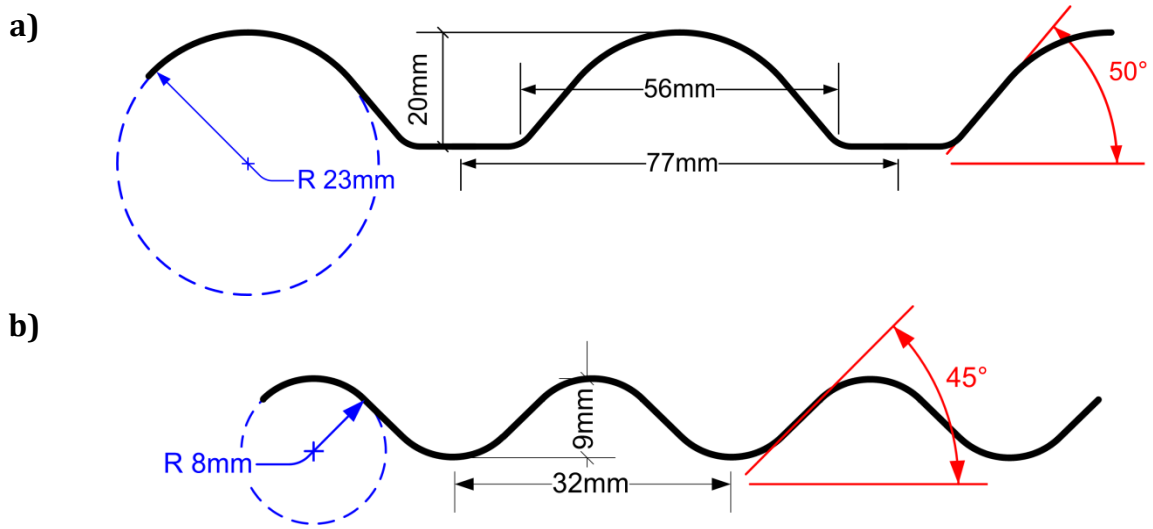

Figure 4.13: Cross sectional dimensions of corrugated substrates, showing depth, width, radius and sidewall angle. a) Large corrugation (Corolux™ 77/20 Profile), b) small corrugation (Corolux™ Miniature Profile).

The 3D modules were fabricated to four different patterns (and are shown in Figure 4.14):

A. **Single Concave:** the module is laminated on the inside of one section of the large corrugated substrate, forming a U-shaped bowl.

B. **Single Convex:** the module is laminated on the outside of one section of the large corrugated substrate to form an inverted U-shape.

C. **Small Inline:** the module is laminated onto the small corrugated substrate with the cells in-line with the corrugations. This tests how the module performs as the angle of incidence reduces and some cells become shaded whilst some cells remain fully illuminated.

D. **Small Transverse:** the module is laminated onto the small corrugated substrate with the cells across the corrugations. This tests how the module performs as the angle of incidence increases and parts of each and every cell become shaded whilst other parts of the same cells remain fully illuminated.

All of the results in Chapter 6 were obtained using DTU(AgNW) modules. Two sets of each 3D structured module plus two flat reference modules were used. The monitoring was performed during summer 2015. In Appendix C the results from two earlier sets of structured modules, based on DTU(AgGrid) modules, are presented: one set was monitored outdoors in summer 2014 and the other set was monitored outdoors during winter 2013, both having first been characterised indoors under the Lucas Nuelle solar simulator (Section 4.4.2).

4.5.1 Indoor Characterisation of Structured Modules

The experiments in Chapter 6 were performed in collaboration with Professor Frederic Krebs at DTU. After fabrication at DTU the flat modules were tested (characterised under AM1.5G and LBIC imaging) before being sent to Bangor. At Bangor they were laminated onto corrugated substrates; two sets of each 3D module type. After lamination one set of modules were taken to Cardiff for angular characterisation by the author and the other set were sent back to DTU for post-lamination characterisation under AM1.5G and LBIC imaging, before being sent back to Bangor for outdoor monitoring.

4.5.2 Outdoor Performance Monitoring of Structured Modules

For these measurements the 3D modules were attached to the inclined panels of the outdoor OPV rack on the roof of the School of Electronic Engineering at Bangor University (Figure 4.14). Both racks were inclined at 35° to horizontal and facing south.

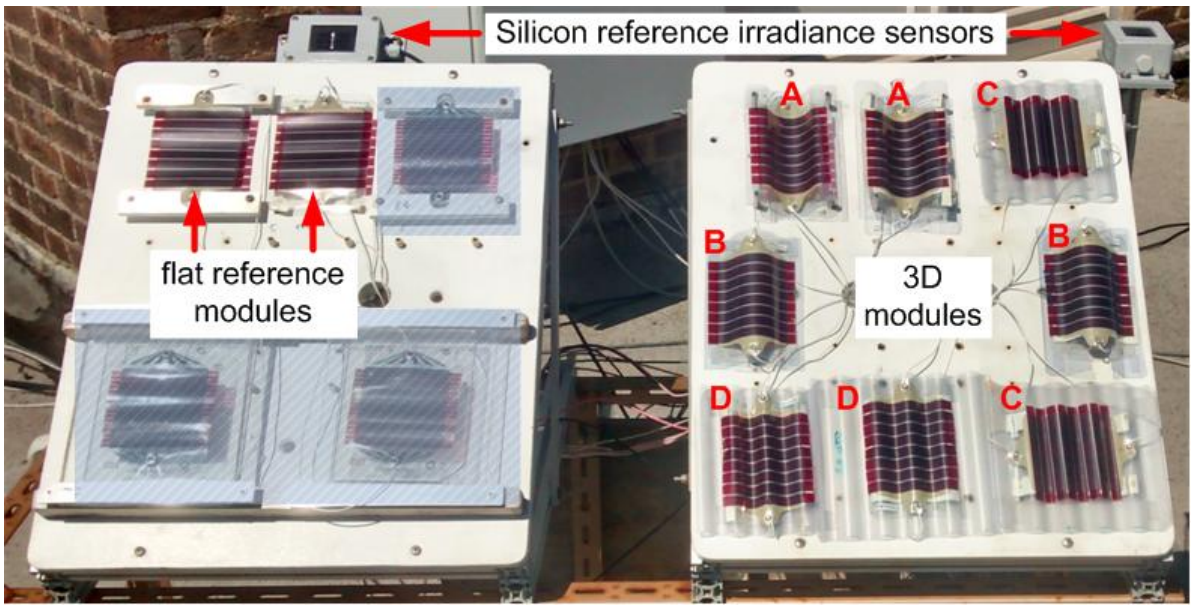

Figure 4.14: Outdoor monitoring system at Bangor, showing flat reference and 3D modules mounted on the inclined OPV racks, and horizontal and in-plane silicon reference irradiance sensors.

4.5.3 Multiple Module Strips on Large Corrugations

The final outdoor monitoring experiment used a new type of module supplied by InfinityPV, a company founded in 2014 by Professor Frederik Krebs of DTU to commercialise their research [272]. The modules are fabricated on a roll-to-roll plant, as a continuous series of module stacks connected together (Figure 4.15). The foil can be cut to length as required, having a voltage output of up to 60 V/m, which will give a voltage of several kilovolts over the full 100 m length [145], [146]. The active material is undisclosed, but is assumed to be a low band gap polymer, based on its appearance which is similar to PCPDTBT.

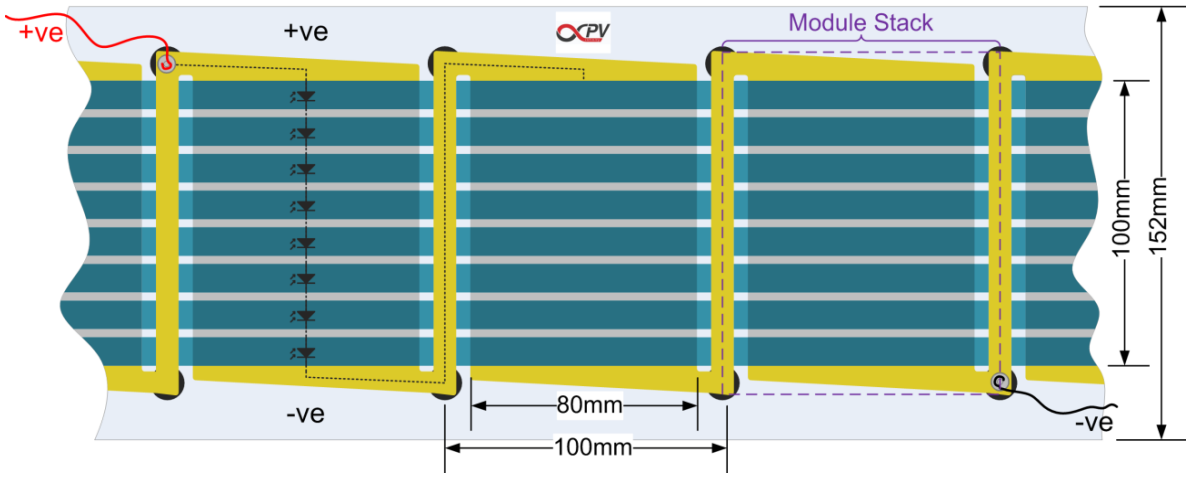

Figure 4.15: Dimensions of infinityPV foil. The foil consists of serially connected module stacks, the cells of which are horizontally aligned. The foil can be cut to length as required and contacts are snap fasteners, which are press fitted through the foil and then have connecting wires soldered to them (in the figure three module stacks are shown wired up).

For this experiment the module strips were prepared as four module stacks in series. A large corrugated substrate was chosen from the Corolux™ range of corrugated PVC roofing (Figure 4.16).

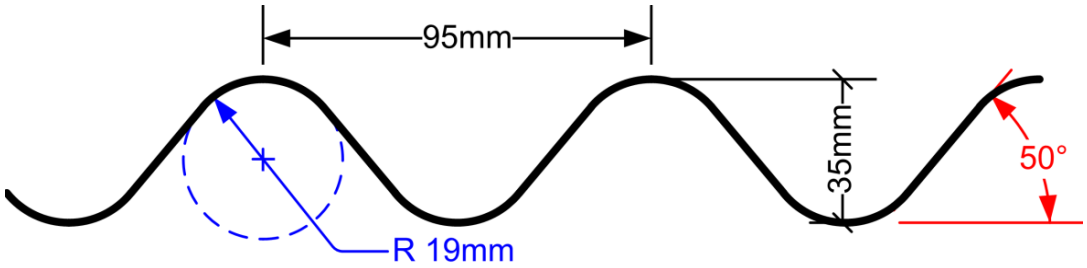

Figure 4.16: Cross section of large corrugations (Corolux™) used for multiple module experiment. Each set of four modules covered about 3 corrugations.

Two of the module strips were laminated to this corrugated substrate, with about 4 module stacks spread across 3 corrugations. Due to their size it is not possible to characterise these under the solar simulator. The flat strips had a total module footprint of 400 cm^2 and for the corrugated strips this was reduced to 320 cm^2.

Two of the corrugated module strips were mounted on the outdoor measurement rack, along with two flat module strips (all inclined at 35° and facing due south) (Figure 4.17). They were monitored outdoors for two months during the autumn of 2015, connected to the multiplexed Botest SMU.

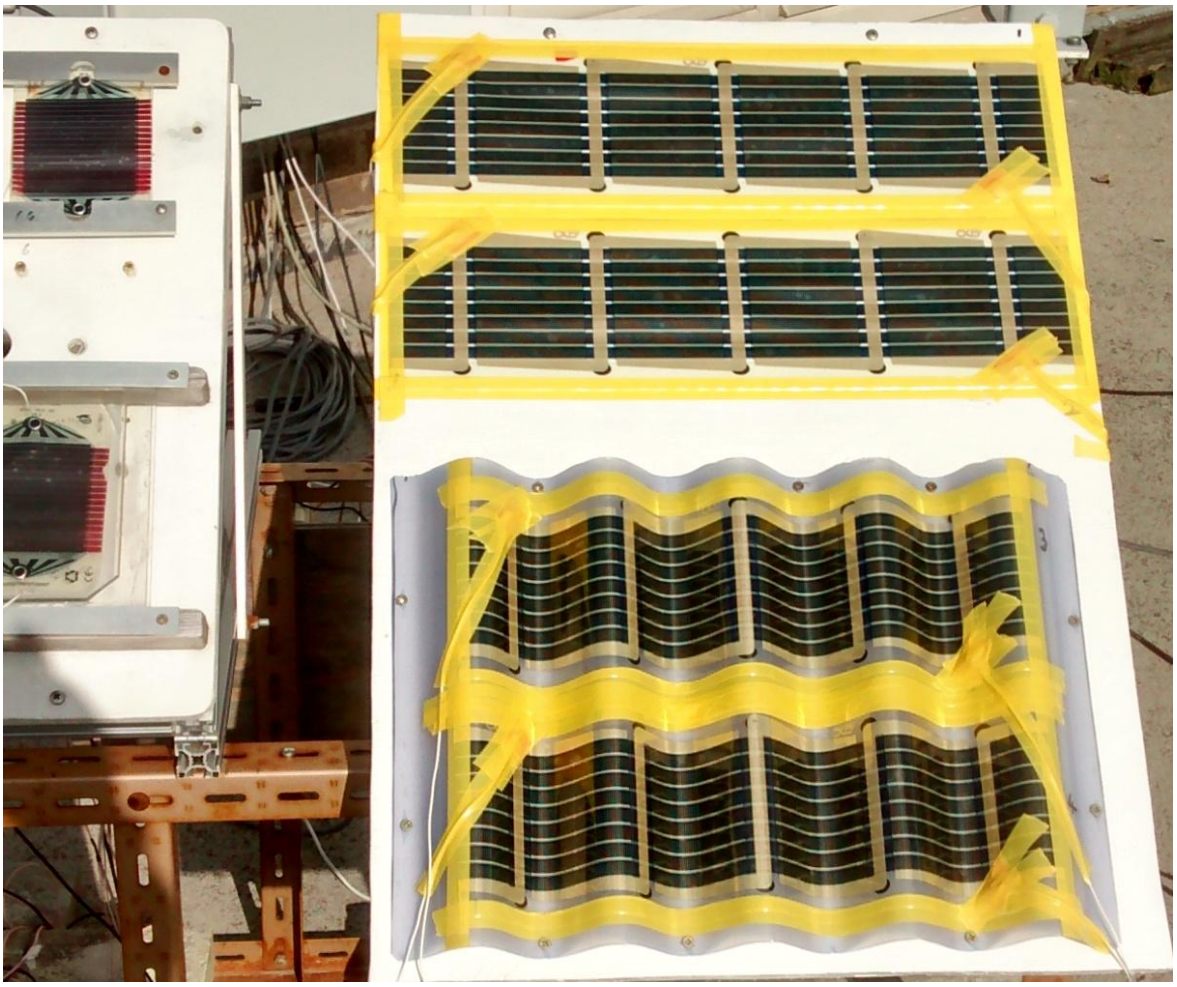

Figure 4.17: Foil modules mounted on outdoor rack for testing. The top pair are mounted flat and the bottom pair are laminated onto large corrugated PVC (Corolux™). The edges were taped to provide an extra level of protection against moisture ingress.

4.5.4 Indoor Characterisation of Various 3D Profiles

In order to provide insight into how curvature affects the performance parameters of the structured modules, further tests were undertaken using a set of curved substrates. A range of profiles were printed on a Velleman K8200 3D printer to compare the performance of OPV modules laminated on curved profiles with different sidewall angles (Figure 4.18). The profiles were all based on a parabola, with the sidewall angle of the module edge ranging from 15° to 80°. A DTU(Carbon) module was measured flat under the solar simulator and then attached to each 3D profile and re-measured (Figure 4.18c).

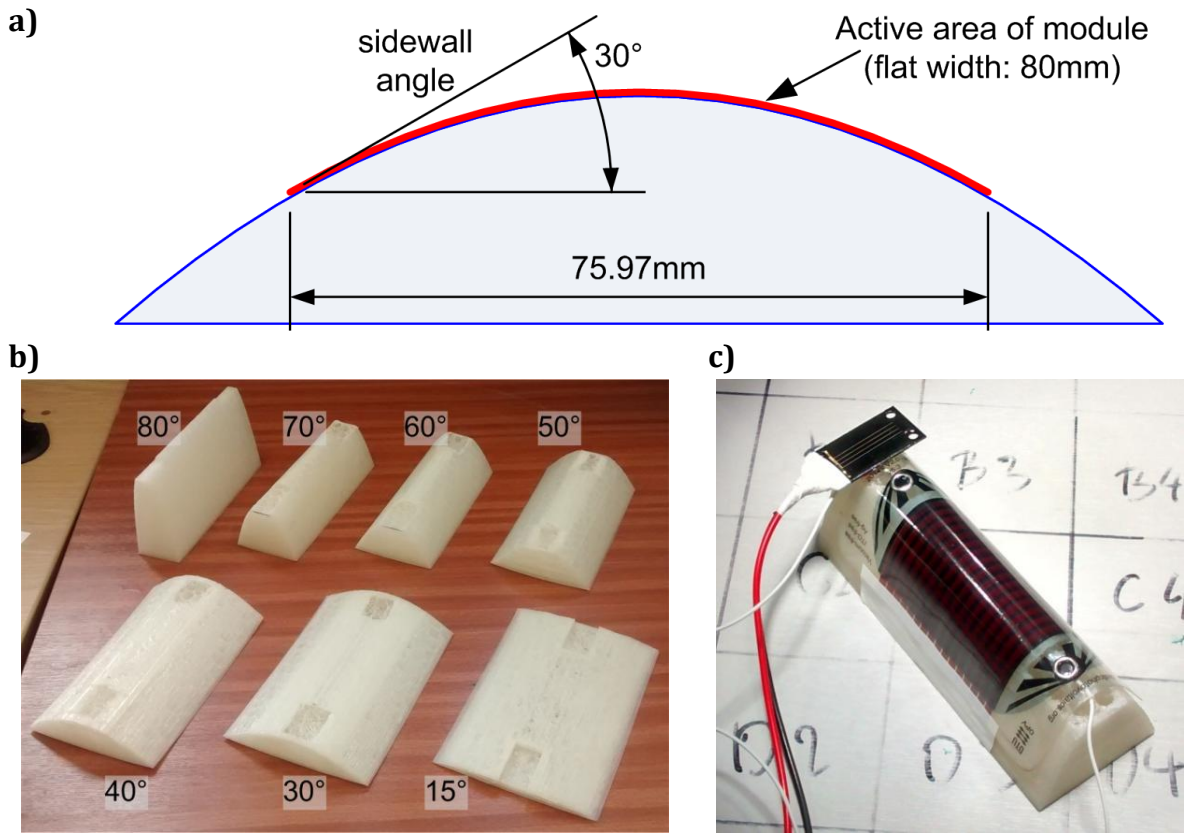

Figure 4.18: 3D parabolic profiles: a) cross section of 30° profile (showing where sidewall angle is measured at edge of module active area); b) photograph of the 3D profiles; and c) photograph of a module mounted onto a 3D profile.

4.5.5 Computer Simulation on PVsyst

A series of simulations were run on PVsyst PV simulation software to compare the output from a number of different configurations of 3D structured PV modules [273]. Although it is normally used to simulate and assess real life PV installations it was capable of simulating different 3D structures, as it allows multiple PV arrays to be arranged at different angles of tilt and direction. Unfortunately the simulation was not able to directly model the performance of corrugated structures as, although it is able to calculate shading by nearby structures/arrays, it is not able to simulate any enhancement due to reflection. However it is useful for insight into how 3D modules can affect PV yield.

In order to simulate different corrugated profiles a set of three strings of PV modules was used, each string being oriented differently and at varying angles (Figure 4.19). Although using flat panels is a simplification, the software gave very good results and allowed a comparison of different profiles to be made. One of the advantages of the software is that it has very good shading algorithms built in.

The software includes meteorological data covering a typical meteorological year (TMY) for Preston in Lancashire, which is at a similar latitude to Bangor. Analysis of this data allowed four days to be selected covering winter diffuse, winter sunny, summer diffuse and summer sunny. This allows system performances to be compared under different weather conditions at different times of the year. The software uses the simplified clear sky model proposed by Bird et al. to simulate global direct and diffuse radiation [46]. The validity of the PVsyst algorithms has been confirmed by several authors, including an assessment of the shading simulation [274]–[277].

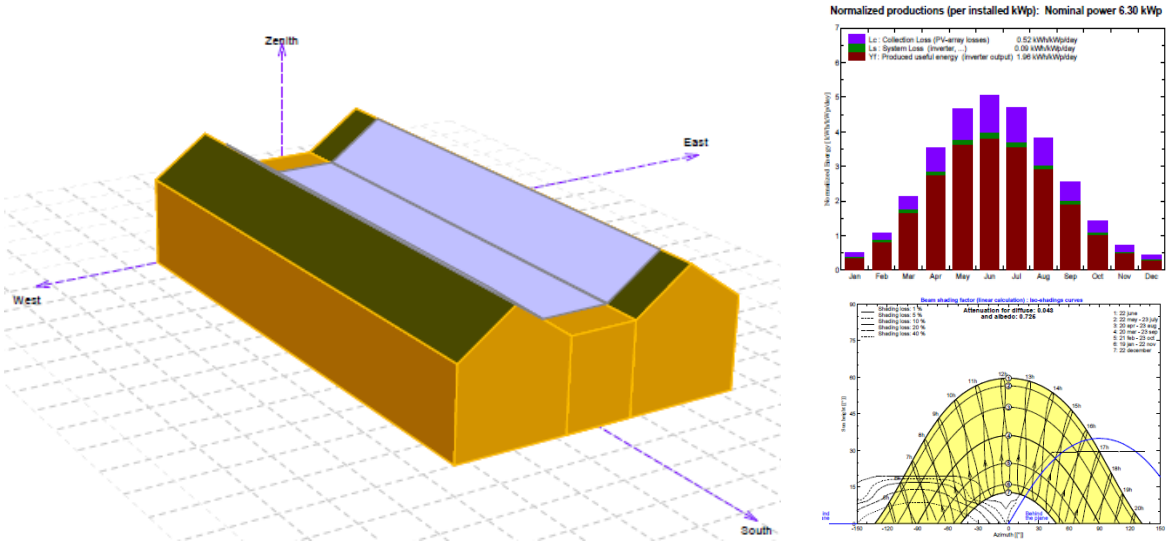

Figure 4.19: PVsyst software was used to simulate various simple profiles. In this case three strings of silicon panels are being used to simulate a corrugated structure with sidewalls at 35° to the horizontal. The software will provide hourly, monthly (top right) and annual performance figures, as well as doing shading calculations (bottom right).

4.5.6 Module Footprint for Efficiency Calculations

When calculating a single cell's performance it is usual to measure the total area of the cell (typically length x width) and use that in the efficiency calculation:

$$Efficiency = \frac{Output\ Power}{Irradiance \times Area} \tag{4.7}$$

Once multiple cells are combined together to form a module there is a choice of which module area measurement to use (Figure 4.20).

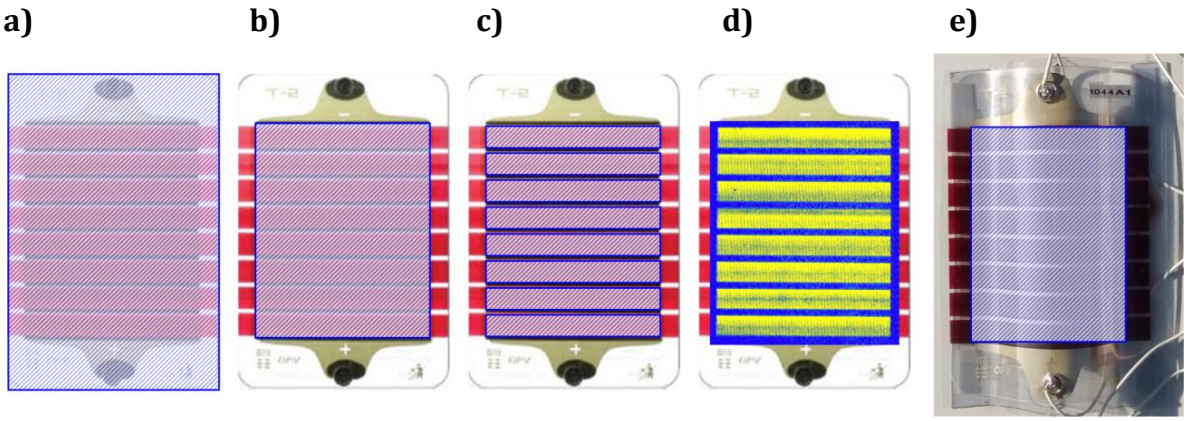

Figure 4.20: Module area definitions: a) total module area; b) nominal active area; c) real active area; d) LBIC defined active area (bright yellow shows areas of current extraction); and e) 3D footprint area, which is based on the nominal active area, but the width is reduced due to the curvature of the module leading to reduced effective area (figure shows type B module).

Total module area: this is the size of the whole module, including the border. If multiple modules were being deployed then this is the physical area that each module would occupy.

Nominal active area: this is the area taken up by the active cells, but includes the space between cells (interconnects and separation distance).

Real active area: this is the total active area occupied by each cell. Cell interconnects and separation space is ignored. When flat modules are being characterised indoors or outdoors the real active area is normally used.

LBIC defined active area: every cell in a module will potentially have an active area slightly smaller than the real active area, due to the presence of busbars and variations in the fabrication process (leading to slight variations in the actual active area), and the LBIC image allows this to be accurately measured. This is the most accurate measurement of active area. When LBIC data is available this gives a more accurate measurement of the active area and is used in preference to the real active area.

3D footprint area: this only applies to 3D structured modules and is the total area that the active layer covers when viewed perpendicular to the plane of array and is calculated from the reduced width of the curved module multiplied by its length. This is less than the nominal module area, due to the reduction in the width caused by the curvature of the module.

For the structured modules in Chapter 6 the 3D footprint area was used for all the flat and structured modules, as this allows the total energy generated per unit area to be calculated. The assumption is that the cost of structured modules would not be dramatically greater than that of the equivalent flat module and that this would lead to a more cost effective use of the space available for a PV system.

4.5.7 Incidence Angle Modifier

Figure 4.21 shows the effect that varying the angle of incidence (AOI) has on irradiation. Based on the change in effective area the irradiance changes according to the cosine of the AOI, see Equation 4.8, where A_0 is the area at normal incidence, A_θ is the area and θ is the AOI (Figure 4.21a) [38].

$$\boldsymbol{A_\theta = A_0 cos\theta} \tag{4.8}$$

As the AOI increases, losses due to reflections at the surface and between layers also increase, and the irradiance reduces by a factor known as the incidence angle modifier[38]. There are various models for the incidence angle modifier, F_{IAM}; Equation 4.9 was proposed by Souka and Safwat, where b_0 is the incidence angle modifier coefficient and for silicon is often set at 0.05 [38], [278]. The application of the incidence angle modifier to irradiance is shown in Equation 4.10, where I_0 is the irradiance of the lamp measured at normal incidence, and I_θ is the irradiance experienced by a module with light incident at an angle of θ.

$$\boldsymbol{F_{IAM} = 1 - b_0\left(\frac{1}{cos\,\theta} - 1\right)} \tag{4.9}$$

$$\boldsymbol{I_\theta = F_{IAM} I_0\, cos\,\theta} \tag{4.10}$$

Figure 4.21b shows curves for both the simple cosine and IAM adjusted cosine models, as well as real data taken from a silicon reference cell and a flat DTU module, measured on the Lucas Nuelle equipment at various angles of yaw. The silicon reference cell follows a similar curve to the IAM adjusted model, but the flat DTU module has much higher efficiencies. This is because the silicon reference cell has a very small area (width ≈1 cm), whereas the DTU module has a much larger area (width ≈8 cm). The lamp on the Lucas Nuelle equipment is relatively close to the modules (~50 cm) and does not provide a collinear light source. As the larger module is tilted half of the module will be closer to the lamp and will benefit from higher levels of irradiance. This leads to a higher output from the larger module, as seen in Figure 4.21b. For the purposes of the angular

characterisation the cosine model has been used to provide figures for irradiance (used to calculate efficiency), as only the flat modules present their surfaces at a single angle of incidence.

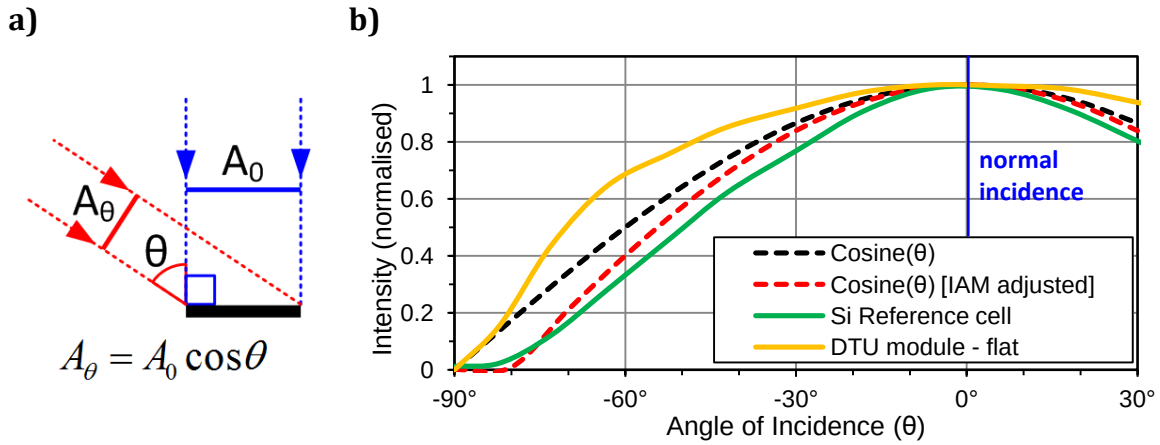

Figure 4.21: Effect of change in angle of incidence on irradiance: a) change in angle of incidence away from perpendicular reduces the effective area that is illuminated; b) curves from cosine and cosine adjusted by incidence angle modifier models plotted alongside measured irradiance from silicon reference cell and flat OPV module.

4.6 Application of Luminescent Downshifting Layers on OPVs

The last phase of research investigated the use of LDS coatings to improve the stability and performance of OPV devices. This work involved material and device characterisation and both indoor and outdoor stability tests.

The substrate used for all of the optical characterisations was UV fused silica (Spectrosil®) supplied by UQG Optics Ltd, Cambridge. This is high quality glass of exceptional purity and is designed for deep UV applications (>92% transmission from 300 nm to 2000 nm). The substrates were supplied as 12.5 mm round, 1 mm thick, glass windows.

4.6.1 Coating Techniques for LDS Materials

LDS Preparation: although it is possible to apply LDS materials directly onto surfaces (e.g. by sublimation [251]) most LDS samples were prepared in a host material. LDS solutions for coating were prepared by weighing out the LDS material and PMMA into a vial (both as dry powders) and then adding the requisite volume of solvent. For the early part of this work PMMA was dissolved at a concentration of 20 mg in 1 ml of solvent.

After trials the optimum solvent was found to be 25% anisole mixed with 75% chloroform. During the second stage of the work commercially available PMMA dissolved in anisole was used (#A8 supplied by MicroChem), at a concentration of 8% by weight [279]. This was added to the dry LDS materials. In all cases the solutions were left overnight on a heated magnetic stirrer at 60° to ensure solids were completely dissolved.

Various coating techniques were utilised:

Spin Coating: the most commonly used technique for the small test samples was spin coating. For the host material MicroChem A8 was used, which is a readymade solution of PMMA dissolved in anisole at a concentration of 8% solids. Spin coating at 2000 rpm for 60 seconds, followed by annealing at 50° for 30 minutes produced a film with very consistent thickness (830±5 nm), low roughness (R_A: ~1 nm). This was found to be the ideal coating method for small samples and could also be used for coating OPVs, as the low annealing temperature does not cause any degradation to the active layer.

Screen Printing: for coating larger samples (e.g. DTU freeOPV modules) screen printing was adopted. This printing work was carried out by Welsh Coating and Printing Centre (WCPC) at Swansea University under the supervision of the author. They optimised an ink blend for screen printing PMMA onto PET. The LDS material was dissolved in PMMA (10 mg/ml) with 4% by weight polyethylene glycol 400 acting as a binder. Printing directly onto the modules entailed first removing the contacts so that the modules would pass through the printer, followed by refitting the contacts. Although this would have been the preferred method it was found that there was quite a high failure rate after refitting the contacts. An alternative was to print the LDS material directly onto a PET substrate and laminate the PET onto the OPV module using PDMS as an adhesive. These inks were used to print 8.5 cm x 10 cm rectangles on 125 μm thick PET (supplied by DuPont Teijin Films) using a DEK 248 silkscreen printer. As the printed thickness was 10 μm, this minimised wave-guiding to the edges and losses are estimated at < 1% of optical losses. The surface was very smooth and the surface roughness was measured at R_A = 3 nm.

4.6.2 Outdoor Stability Testing of LDS Materials at Bangor University

The first outdoor lifetime tests were conducted at Bangor using DTU(AgGrid) modules. Three configurations were prepared (see Figure 4.22):

A. **Control**: PMMA (with no LDS) printed onto PET and laminated onto the module using PDMS.

B. **LDS (on PET)**: LDS (Kremer Blue) printed onto PET and laminated onto the module using PDMS.

C. **LDS (printed)**: LDS (Kremer Blue) printed directly onto the module.

The modules were tested outdoors on the inclined OPV rack for 10 weeks from 01/07/2014 till 09/09/2014 (Figure 4.22b).

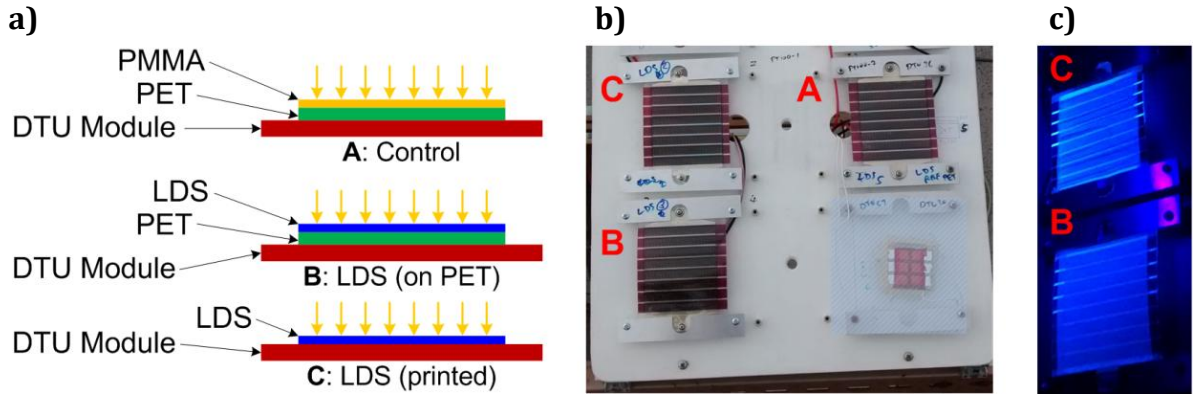

Figure 4.22: LDS modules tested outdoors at Bangor: a) module configurations; b) modules on outdoor OPV rack; and c) LDS modules photoluminescing under exposure to UV light.

4.6.3 Outdoor Stability Testing of LDS Materials at Ben Gurion University

Collaboration was sought with Professor Eugene Katz at Ben Gurion University, Israel. This meant that outdoor stability studies of LDS materials could be conducted at Jacob Blaustein Institutes for Desert Research in the Negev Desert, under much higher levels of UV irradiation. Four of each of the following configurations were prepared (see Figure 4.23), based on DTU(Carbon) modules:

A. **Reference**: uncoated module.

B. **Europium Complex**: LDS (Europium complex) printed on PET and laminated onto a module.

C. **Kremer Blue**: LDS (Kremer Blue) printed on PET and laminated onto a module.

D. **PMMA Only**: PMMA (with no LDS) printed on PET and laminated onto a module.

E. **UV Filter**: a commercial self-adhesive UV filter (Solaronix SA #49132) was applied to a module.

To improve the long term stability of the modules they were all encapsulated in PDMS and mounted on a glass backing sheet (see Section 4.3).

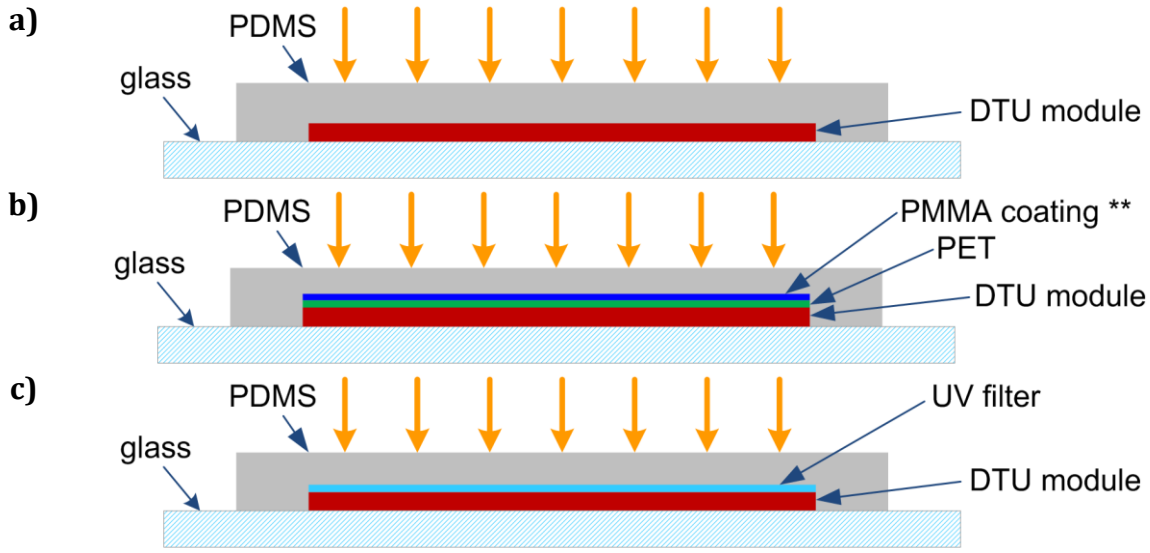

Figure 4.23: Cross sections of LDS modules tested outdoors at Ben Gurion University: a) DTU modules with just PDMS (type A); b) DTU modules with coated PET layer [PMMA coating was prepared in 3 different formulations: type B: PMMA with Europium complex; type C: PMMA with Kremer Blue dye; type D: Pure PMMA]; and c) DTU modules with UV filter (type E)**

Figure 4.24 shows two of the modules with LDS coating under exposure by UV light ($\lambda_{EXCITATION}$ = 365 nm): the Europium Complex photoluminescing with a red light and the Kremer Blue dye with a blue light. These photographs show that the screen printing has produced a very even coating. They also show the photoluminescence of the PET barrier layers [280].

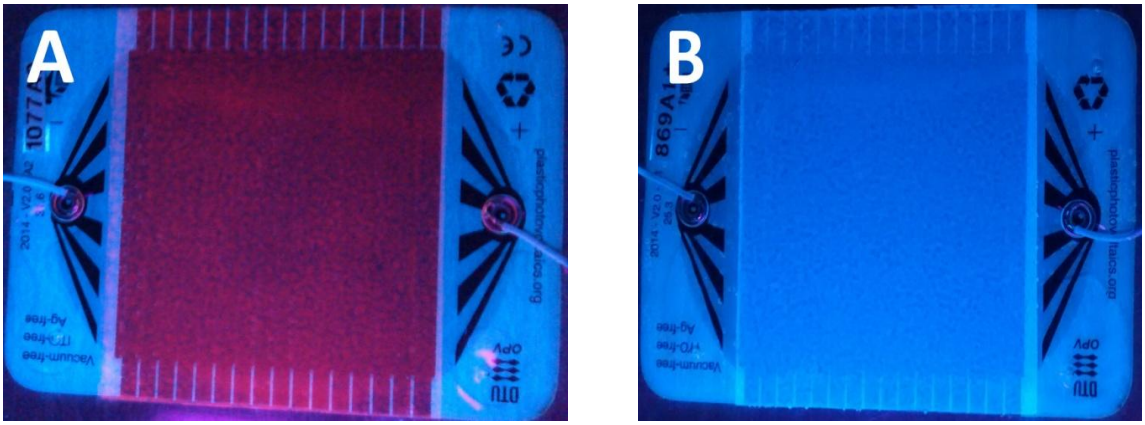

Figure 4.24: DTU modules photoluminescing under exposure to UV light ($\lambda_{EXCITATION}$ =365 nm). A: Europium and B: Kremer Blue.

After fabrication the modules were sent to DTU for further characterisation, before being shipped to Israel for the outdoor testing. They were mounted on inclined outdoor racks (at 30°) facing south and tested over a period of 80 days (see Figure 4.25).

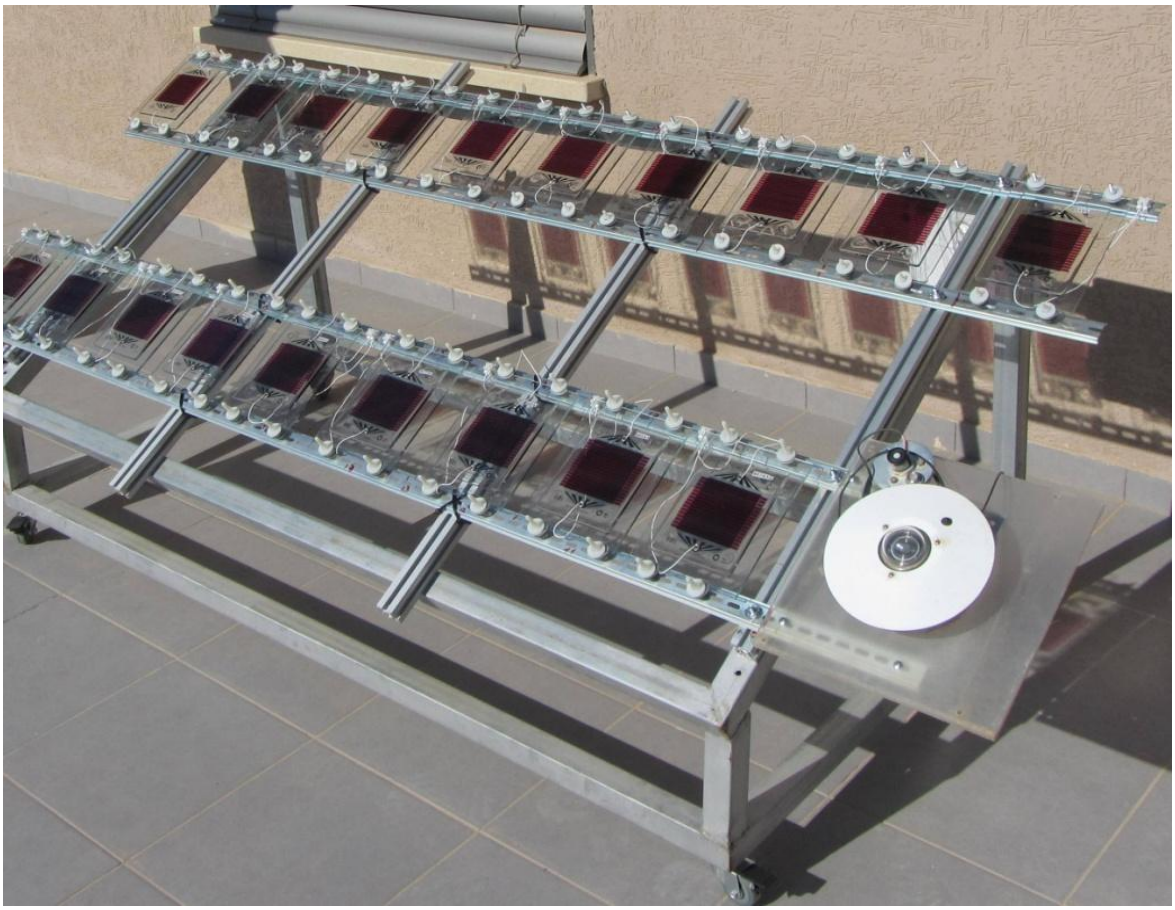

Figure 4.25: Outdoor OPV rack at Jacob Blaustein Institutes for Desert Research, in the Negev Desert.

4.6.4 Testing of Discrete and Multiple-Dye LDS Layers

For all subsequent tests the LDS materials were dissolved in MicroChem A8 (8% by weight PMMA in anisole) and spin coated onto the substrates (see Section 4.6.1). A series of tests on discrete LDS materials were conducted, followed by testing on blends of LDS materials. The final tests were performed using inverted geometry P3HT:$PC_{61}BM$ devices (Section 4.2.2): IV characterisation and indoor lifetime tests were performed.

Chapter 5. Outdoor Monitoring of Organic Photovoltaics

The bulk of the research for this thesis involves outdoor monitoring of OPV modules. This chapter examines in detail the various analysis methods used based around a series of outdoor monitoring campaigns. Over the course of several campaigns various OPV mini modules are benchmarked against a number of other technologies: polycrystalline silicon (poly-Si), cadmium indium diselenide (CIS), and dye sensitised solar cells (DSSC). The principal performance parameters (PCE, I_{SC}, V_{OC} and FF) are examined in detail, analysing their dependence on irradiance and temperature. The early OPV modules are shown to have high rates of degradation and two degradation paths were identified. One of the main paths for degradation is ingress of water and oxygen into the cell, leading to electrode/interface failure and photo-oxidation of the active layer. The use of UV filtering to reduce photo-oxidation of the active layer is investigated.

5.1 Comparison of OPV Outdoor Performance against Silicon

Eight DTU(AgGrid) modules were monitored outdoors over a period of twelve weeks during the summer of 2013 (start date: 09/07/2013). Four modules were mounted on a rack inclined at 35° and facing due south (S1-S4) and four were mounted on a horizontal rack (S5-S8). The initial efficiencies of these modules were 0.77±0.09%, which indicates the close tolerances obtained in the R2R processing of this batch of modules. One module on each rack had a PT100 temperature sensor attached to the back (S2 & S5).

5.1.1 Comparison of Performance under Different Climatic Conditions

Data from two contrasting days are used to compare relative OPV performance with that of the poly-Si (see Figure 5.1). On the cloudy day (05/08/2013) the horizontal and in-plane irradiances are closely matching, as the irradiance is predominantly diffuse (until 18:00 when the cloud begins to disperse). On the sunny day (03/08/2013) there is a distinct difference between the horizontal and in-plane irradiance, with the in-plane exceeding the horizontal at local noon by about 25%, indicating that the irradiance is

dominated by direct normal irradiation (DNI). After 15:00 in the afternoon intermittent full sun was observed leading to cloud lensing effects [40], [281]. The days were selected to be close together so that the effects of degradation on the OPV modules were not significant. As the OPV modules degraded relatively quickly it was not possible to find two completely contrasting days that were close together and with a full set of data (OPV data on 05/08/2013 was missing before 09:00).

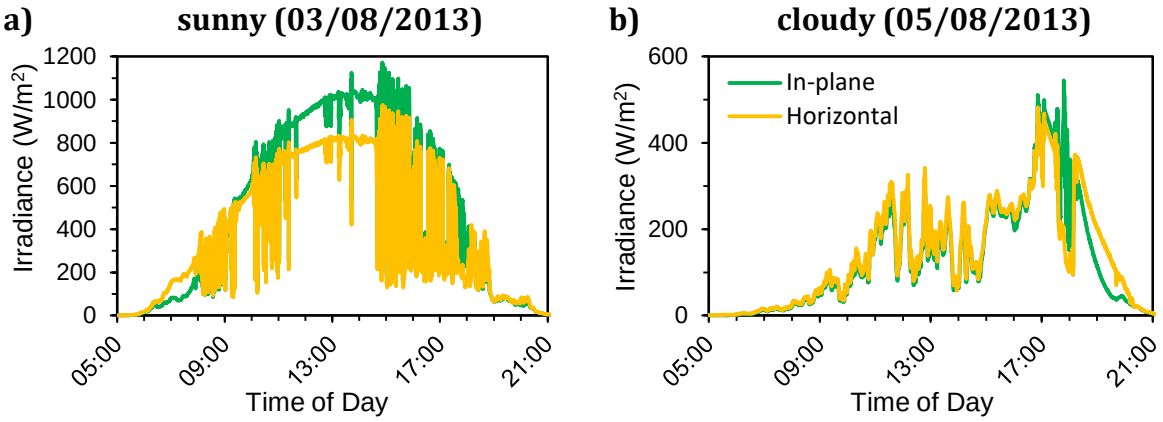

Figure 5.1: Irradiance on two contrasting days: sunny (a) and cloudy (b).

The graphs in Figure 5.2 show PCE, I_{SC}, V_{OC} and FF plotted for an OPV module (S2) and a poly-Si module for both days (both inclined). On the sunny day some large spikes are evident in the PCE and FF data which are caused by temporal mismatching of the fast changing irradiance levels during cloud lensing. This cloud lensing mismatch is less evident for the OPV module, as the IV sweep takes much longer (~10 s) than it does for the poly-Si module (~1 s). For both modules I_{SC} closely tracks the changing irradiance over the course of the day, apart from a brief period of shading on the poly-Si module before 08:00. However for PCE, V_{OC} and FF there is a difference between the two module types. The parameters for poly-Si rise quite quickly at sunrise to their limiting values which are maintained until early evening when they drop back to zero at sunset. The parameters for the OPV module start their rise slightly later and rise more slowly before reaching their limiting values which are maintained until late afternoon after which they steadily return to zero. Both modules show a slight drop in PCE in the early afternoon.

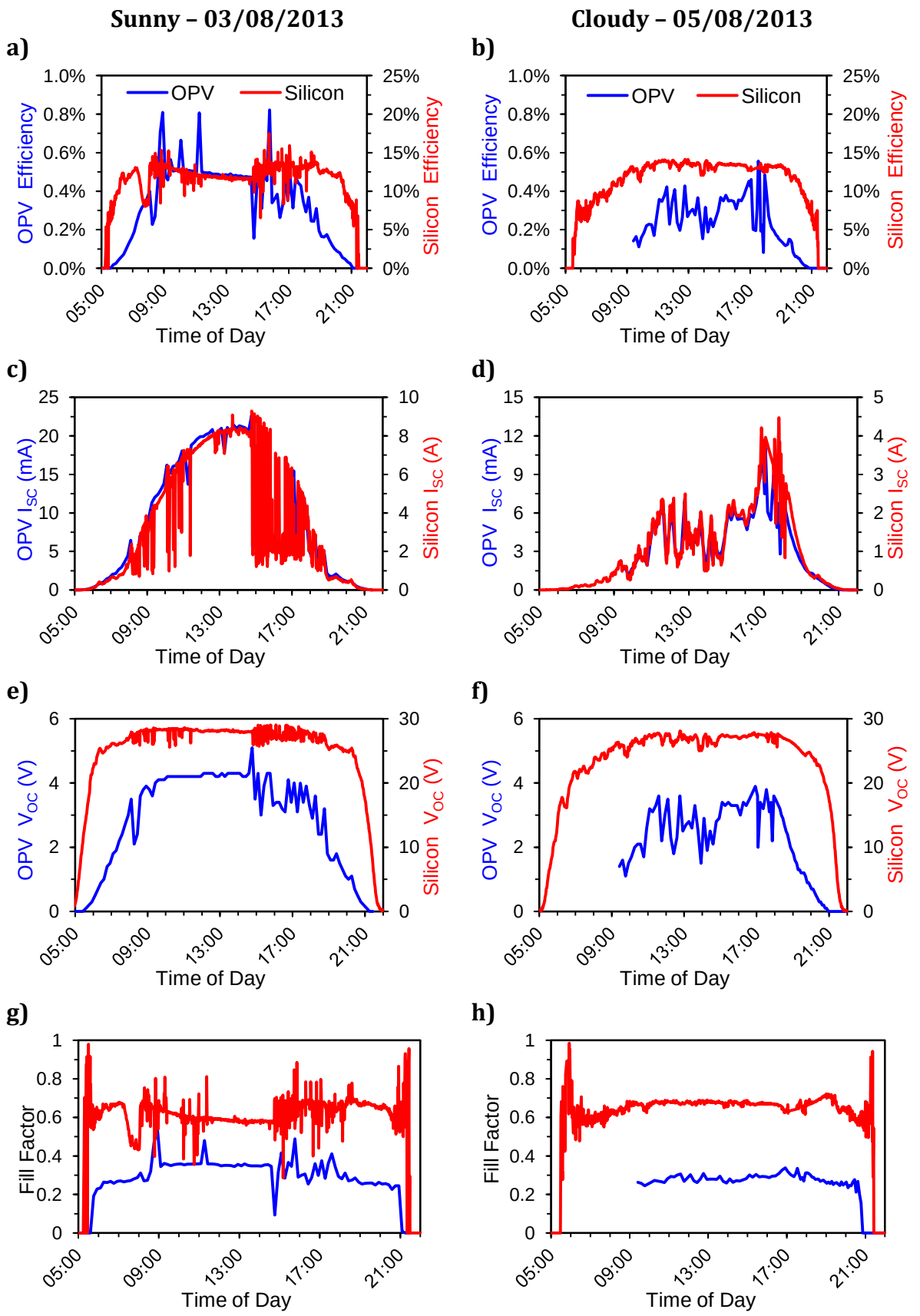

Figure 5.2: Comparison of diurnal performance of OPV (S2) and poly-Si modules on two contrasting days (sunny: left column, cloudy: right column): a) & b) PCE; c) & d) I_{SC}; e) & f) V_{OC}; and g) & h) Fill Factor.

On the cloudy day I_{SC} for both modules track irradiance very closely. The shading effects on the poly-Si module that were seen on the sunny day are not present due to the higher proportion of diffuse light. PCE, V_{OC} and FF for the poly-Si module show similar trends as seen on the sunny day, rising to their maximum values early in the morning and staying reasonably constant until early evening before dropping back to zero. The drops seen in PCE and FF in early afternoon are not present. The maximum values for PCE (13%), V_{OC} (28 V) and FF (0.65) are similar to those seen on the sunny day. However the OPV module is much more unresponsive on the cloudy day as, although early morning data is missing until 09:00 (due to hardware problems), it is still apparent that the module is not reaching such high and steady values as were seen on the sunny day.

The morning, evening and cloudy results show that PCE for the OPV device is more affected by low irradiances than it is for the poly-Si module, which leads to the lower increase in PCE with increasing irradiance.

5.1.2 OPV Degradation

All of the OPV modules were seen to degrade relatively quickly over the course of the outdoor monitoring. Two sets of graphs are presented: one set shows the change in the performance parameters vs. irradiance on a weekly basis for one module (Figure 5.3); the other set shows the performance parameters (calculated as a daily average) vs. time for a representative number of modules (Figure 5.4).

In order to examine the change in the performance parameters vs. irradiance plotted against time, each parameter was averaged on a weekly basis, binned at 25 W/m^2 intervals so that the effect of changing irradiance is still clear. To declutter the graphs, only the data from every other week was plotted.

Figure 5.3 plots the main performance parameters against irradiance for the best performing inclined OPV module (S2). I_{SC} maintains a linear trend throughout, remaining relatively stable for the first 5-6 weeks before steadily degrading. V_{OC} maintains a logarithmic trend for the first 6 weeks, although the irradiance level where it attains 90% of maximum V_{OC} drops from 300 W/m^2 in week 2, to 525 W/m^2 in week 6. Maximum V_{OC} drops from 4.3 V in weeks 2 and 4 down to 4.0 V by week 6, after which it degrades rapidly with the trend becoming linear. FF shows a steady degradation over the first 8 weeks, dropping from a maximum of 0.4 in week 2 to 0.25 in week 8, after

which it does not change. A FF of 0.25 is indicative of a straight line IV curve and is normally the minimum that would be expected. PCE rapidly degrades from a maximum of 0.6% in week 2 down to 0.1% by week 8.

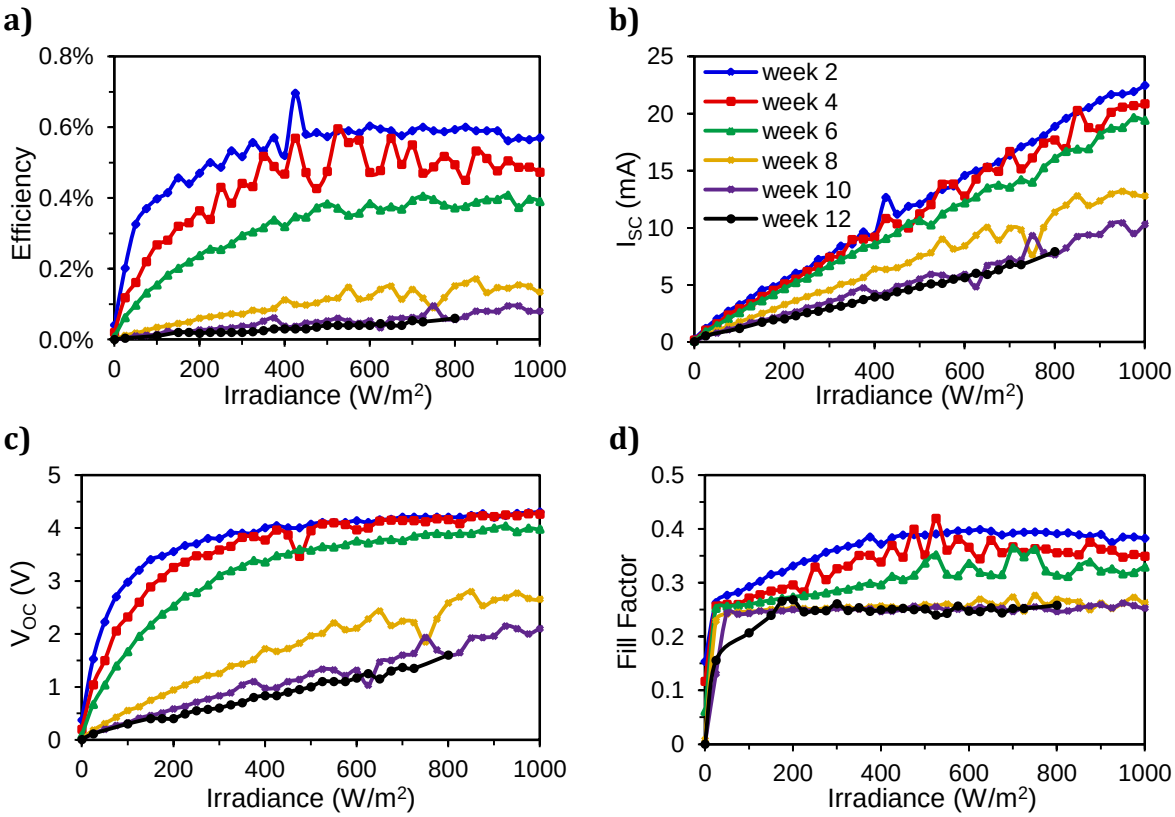

Figure 5.3: Degradation of performance parameters for module S2 (best performing inclined OPV module): a) PCE, b) I_{SC}, c) V_{OC} and d) Fill Factor. Each data point is a weekly average for irradiance binned in 25 W/m² intervals.

To analyse the degradation of these modules against time it was necessary to separate the decline in the performance parameters due to degradation from the diurnal variation due to changes in irradiation, especially at the lower irradiances. This was achieved by averaging data where the irradiance was within a narrow band, as this removed the effect changing irradiation had on the performance parameters. After investigation an irradiance band of 600±15 W/m² was selected, as this filtered out data from diffuse conditions where performance was reduced. Choosing a higher irradiance would have limited the number of available data points to only those from very sunny conditions, which would also be more likely to be affected by cloud lensing. The novel approaches to degradation analysis seen in Figure 5.3 and Figure 5.4 have not been seen in the literature before.

Figure 5.4 shows the evolution of PCE, I_{SC}, V_{OC} and FF for four modules over the course of the monitoring. The modules selected are the best and worst performing from the inclined (I) and horizontal (H) racks: best: S2(I) & S7(H); worst: S1(I) & S8(H). The PCE data shows that all of the modules have degraded within 6-8 weeks. There are two different degradation patterns. In the first pattern, seen in S1(I) and S8(H), I_{SC} and V_{OC} show a steady decrease over time, reaching a minimum at 8 weeks. In addition the FF reaches a minimum at 4-5 weeks. These combine to give a very fast decay in PCE, reaching a minimum after about 6 weeks. In the second pattern, seen in S2(I) and S7(H), I_{SC}, FF and PCE hold relatively steady for the first 2 weeks, after which they steadily decline, reaching a low at about 8 weeks. V_{OC} holds steady for the first 4-5 weeks, before dropping relatively quickly and also reaching a low value at about 8 weeks. The modules split equally between the two degradation patterns and those in the second group showed better stability than the first group. Degradation affecting I_{SC} is usually associated with chemical degradation of the photoactive layer (PAL), as well as degradation of the PAL/electrode interface, whereas degradation in V_{OC} and FF are normally caused by problems in the PAL/electrode interface [92], [93].

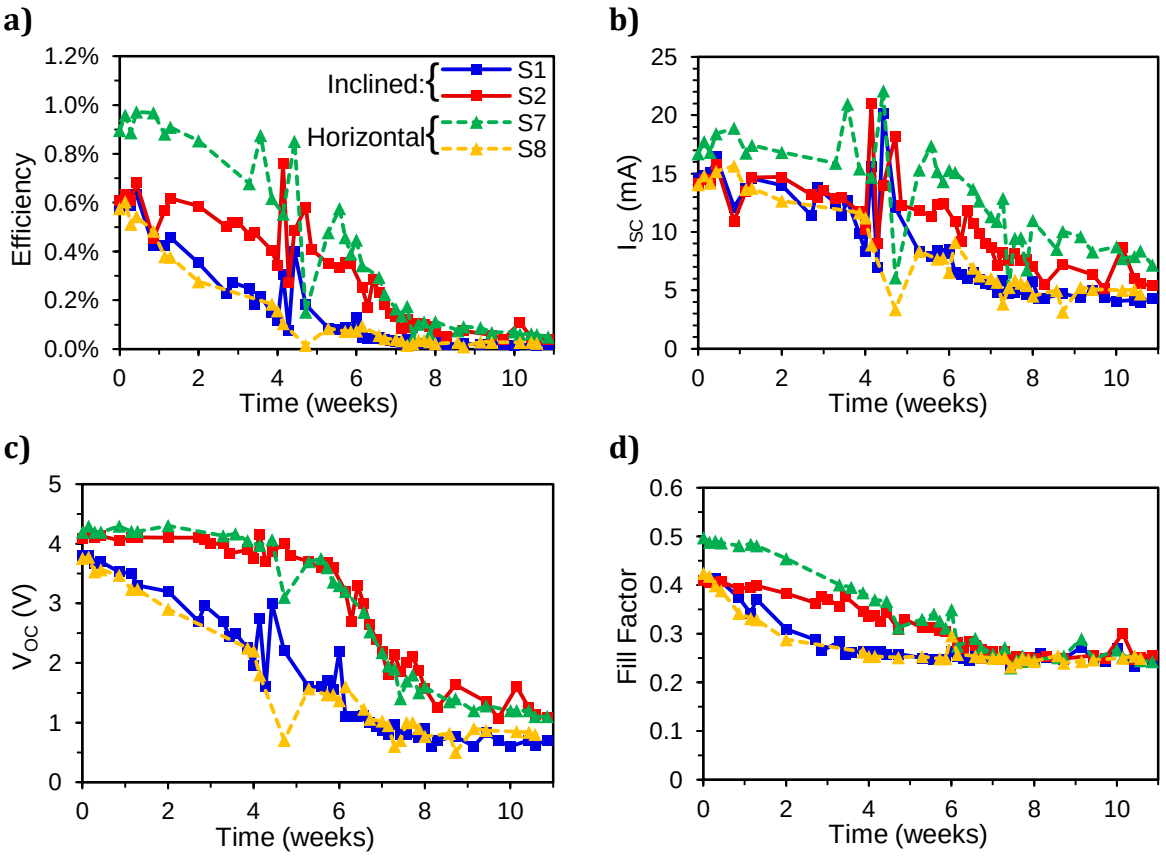

Figure 5.4: Degradation of OPV modules (Summer 2013): a) PCE; b) I_{SC}; c) V_{OC}; and d) FF. Two modules from each rack: inclined (solid lines); horizontal (dashed lines). Data is diurnal average where irradiance was 600±15 W/m².

Table 5.1 shows the T_{80} and T_{50} lifetimes for all of the modules. The best two performing modules, S2 (inclined) and S7 (horizontal), had similar lifetimes (S2: T_{80} = 22 days, T_{50} = 42 days; S7:T_{80} = 21 days, T_{50} = 42 days). The worst performing module was S8 (horizontal): T_{80} = 6 days, T_{50} = 14 days. The worst five modules had average lifetimes of T_{80} = 6.6 days and T_{50} = 14.8 days, which highlights the fast degradation rates of these modules.

No significant differences were observed between the horizontal and inclined modules, either in performance or rates of degradation. All subsequent testing was performed with the racks inclined at 35° to horizontal and facing south.

Table 5.1: T_{80} and T_{50} lifetimes (Summer 2013). Data based on diurnal average PCE where irradiance was 600±15 W/m².

Rack	Sample	T_{80} Lifetime (days)	T_{50} Lifetime (days)
Inclined	S1	6	17
	S2	22	42
	S3	10	26
	S4	6	11
	Average	11	24
Horizontal	S5	8	18
	S6	7	14
	S7	21	42
	S8	6	14
	Average	10.5	22

One major source of degradation is at the edges of the modules, where the active layer has been rapidly degraded by the ingress of water and oxygen (see Figure 5.5). This shows that water and oxygen can penetrate sideways through the device, leading to chemical degradation of the active layer, interfacial layers and electrodes. This is not surprising as a pressure sensitive adhesive is used to laminate the backside PET and could be the source of initial degradation. Although laser cutting has been used to separate the modules from the R2R foil, this would suggest that it is not an effective method for edge sealing.

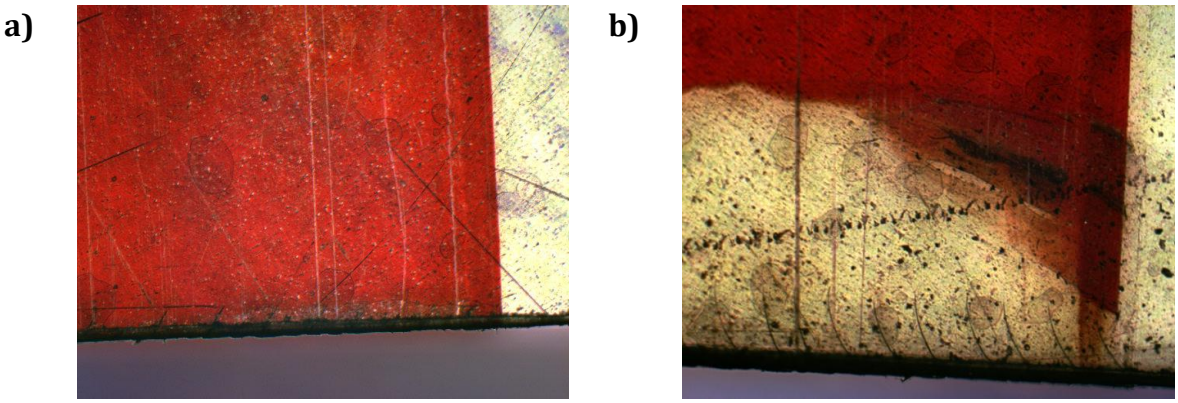

Figure 5.5: Microscope photographs (magnification x2.5) showing the edge of an OPV module (a) before and (b) after outdoor performance monitoring, demonstrating degradation at the module edges. Laser cutting is used to separate the modules from the R2R foil, giving rise to the burnt edges.

5.1.3 Effect of Irradiance on OPVs and Comparison with Silicon PV

Figure 5.6 shows PCE, I_{SC}, V_{OC} and FF plotted against irradiance for the poly-Si and OPV modules on the sunny and cloudy days. The effect of partial shading on PCE and FF in the early morning can be seen in the poly-Si data for the sunny day and this has been highlighted. Otherwise there is very little difference between the sunny and cloudy characteristics for each module type.

I_{SC} has a linear relationship to irradiance for both module types and the rate of change of I_{SC} as a function of irradiance is the same on both days. Likewise V_{OC} shows the expected behaviour with a logarithmic relationship to irradiance for both module types and on both days. However 90% of maximum V_{OC} is reached at ~80 W/m^2 for the poly-Si compared to ~250 W/m^2 for the OPV, which explains why V_{OC} for the OPV module is variable at low irradiances.

The FF data shows both OPV and poly-Si reaching steady values very quickly (poly-Si=0.6, OPV=0.2). The poly-Si then rises slightly to 0.7 (at 100 W/m^2) before steadily dropping off with increasing irradiance to 0.6 at 1000 W/m^2. In comparison FF for the OPV module continues to rise with increasing irradiance, reaching 0.35 at 800 W/m^2, after which it remains constant.

The PCE curve for poly-Si shows it reaching maximum efficiency (13.5%) at 200 W/m^2, after which the efficiency steadily reduces down to 11.5% at 1000 W/m^2. The OPV module has PCE showing a more logarithmic trend, rising to a maximum of 0.5% at 500 W/m^2 and then remaining constant for higher irradiances.

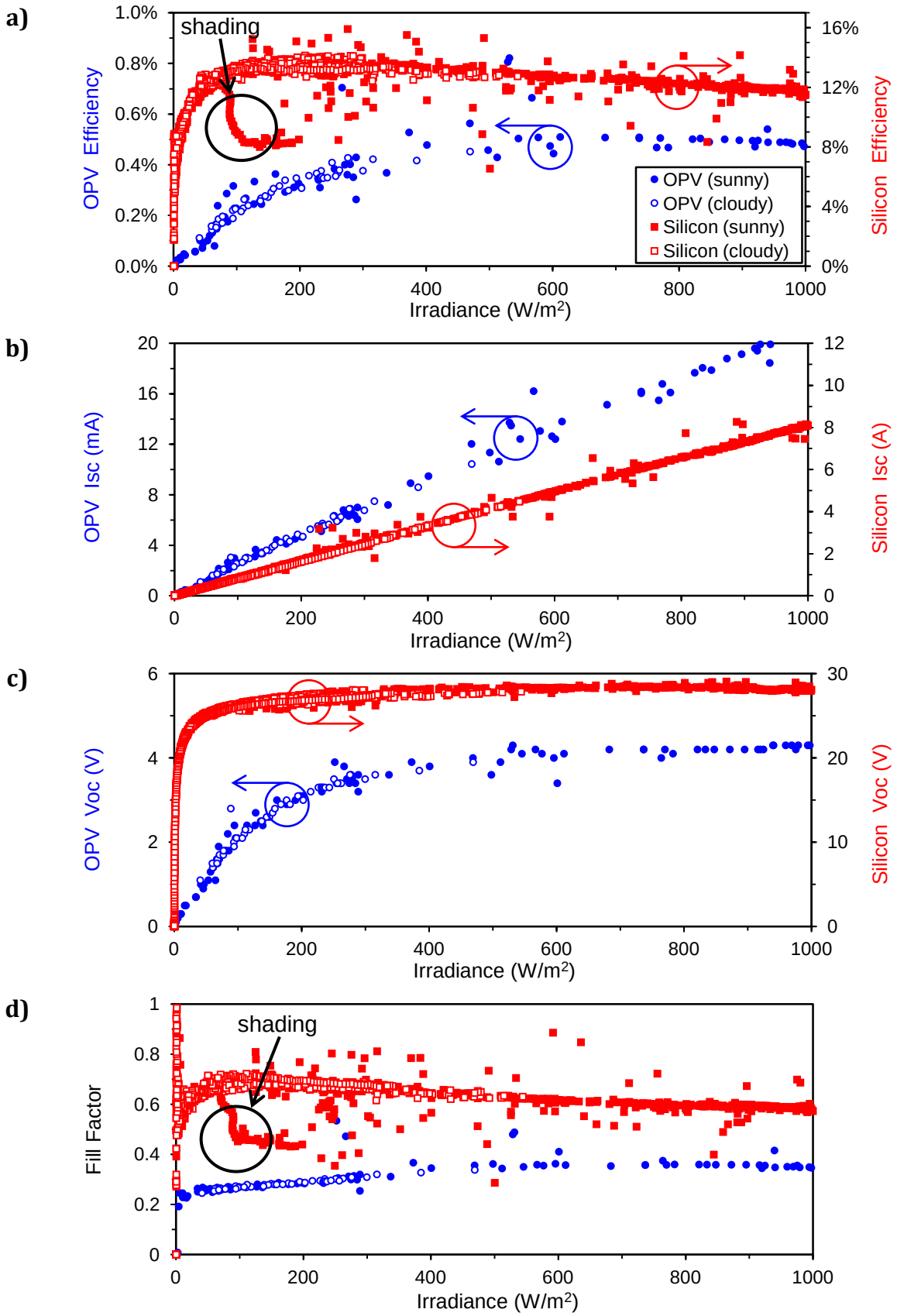

Figure 5.6: The effect of irradiance on a) PCE, b) I_{SC}, c) V_{OC} and d) Fill Factor for OPV and poly-Si modules on 03/08/2013 (sunny) and 05/08/2013 (cloudy). The effects on PCE and FF of partial shading for the poly-Si module are highlighted.

5.1.4 Module Temperature Analysis

Two contrasting days (sunny: 03/08/2013 and cloudy: 17/08/2013) were selected and the irradiances are shown in Figure 5.7a&b. Figure 5.7c&d shows the module temperatures of OPV and poly-Si modules over the course of the two days. On both days the cooling effect of the wind is similar, with the wind speed rising from 2 m/s in the morning to 4 m/s at noon before dropping back to 2 m/s in the evening, and on the cloudy day there are two periods of rain (see Figure 5.8a).

On the cloudy day all of the modules follow a similar temperature profile, with module temperature differences above ambient (T_{DELTA}) rising and falling in line with irradiance. The maximum values for T_{DELTA} are +3.5°C for the inclined poly-Si, +4.2°C for the horizontal poly-Si, +3.3°C for the inclined OPV and +3.2°C for the horizontal OPV. There are two sharp drops in T_{DELTA}, at 11:30 and 14:00, which are caused by the cooling effect of the rain.

On the sunny day there is a marked difference between the OPV and poly-Si modules, and between the horizontal and inclined modules of each type. The maximum temperatures reached are 38.7°C (T_{DELTA}=+17.7°C) for the inclined poly-Si module, 32.8°C (T_{DELTA}=+11.8°C) for the horizontal poly-Si module, 32.4°C (T_{DELTA}=+11.5°C) for the inclined OPV module, and 29.9°C (T_{DELTA}=+8.9°C) for the horizontal OPV module. The horizontal modules follow a similar temperature profile as the inclined modules but at lower levels as the angle of incidence of the sun is closer to perpendicular for the inclined modules. Figure 5.8b shows the linear relationship between T_{DELTA} and irradiance for the inclined modules on the sunny day, defined by Equation 5.1, where G is irradiance and k is the slope, known as the Ross coefficient [282], [283].

$$\boldsymbol{T_{DELTA} = T_{module} - T_{ambient} = kG} \qquad 5.1$$

The values obtained for the Ross coefficient are: OPV=0.0101 K.m^2/W and poly-Si=0.0154 K.m^2/W. Expected values for freestanding poly-Si are slightly higher (~0.02 K.m^2/W), the difference being due to cooling by the wind [282]. The temperature rises are closely linked to irradiance and to the ability of the modules to absorb infrared radiation [284]. The poly-Si modules get hotter, as silicon can absorb at wavelengths up to 1100 nm, compared to 650 nm for the OPV modules (P3HT:$PC_{61}BM$) [285], [286].

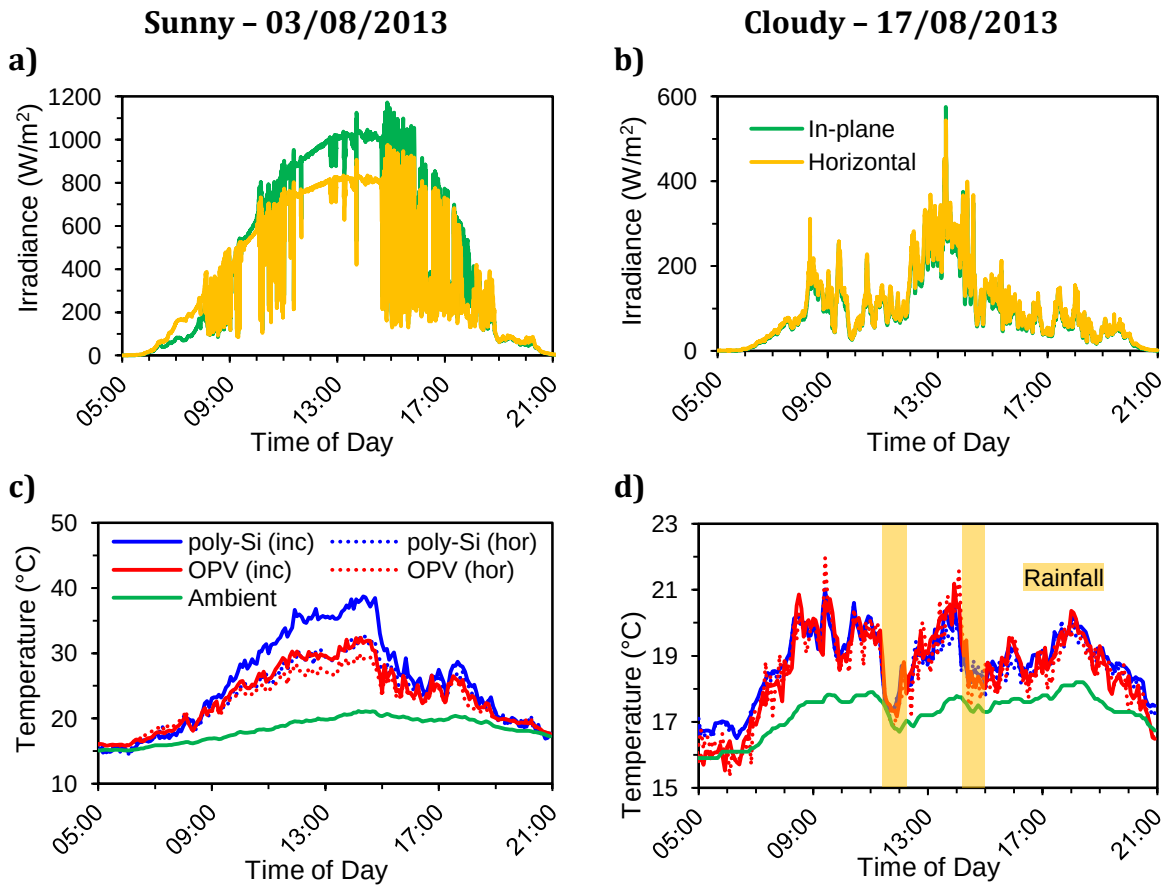

Figure 5.7: Temperature analysis of OPV and PV modules on two contrasting days (sunny: 03/08/2013 & cloudy: 17/08/2013): a) & b) horizontal and in-plane irradiance; and c) & d) module and ambient temperatures. The sharp drops in module temperature during rainfall can be seen in d).

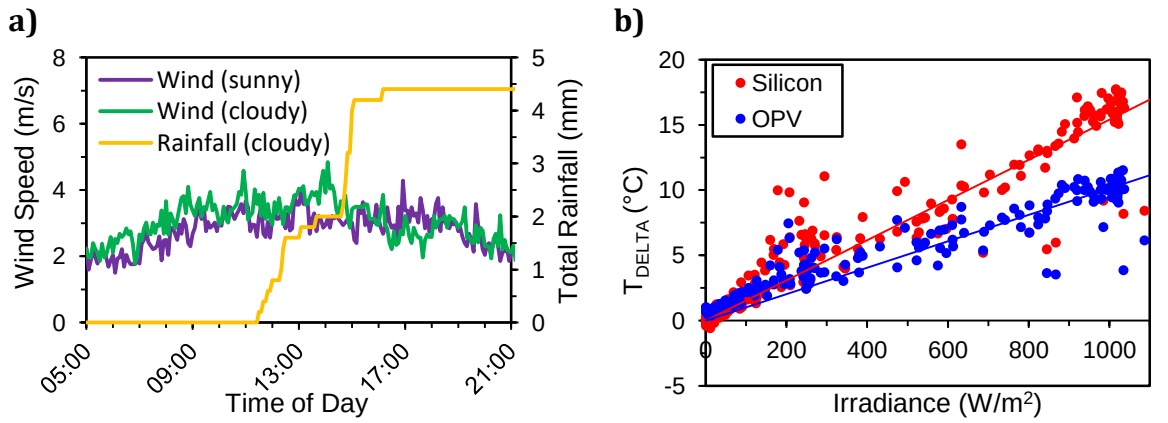

Figure 5.8: (a): Wind speed and total rainfall on the two days. [NB there was no rainfall on the sunny day]. (b): Temperature rise above ambient (T_{DELTA}) plotted against irradiance with linear trend lines.

5.1.5 Effect of Temperature on OPV Performance

A common method for measuring temperature coefficients (TCs) is to shade the module and lower its temperature to ambient. The module is then uncovered and allowed to heat up whilst several IV curves are taken at different temperatures [34], [287], [288]. This is impractical for OPV modules at this location, as the temperature variation over the course of a day is relatively low and therefore would require specialised equipment. However the TCs can also be obtained through performance monitoring. To obtain the TCs data was fitted to the following equation for efficiency [288]–[290]:

$$\boldsymbol{\eta(T) = \eta_{ref}\left[1 + \beta(T - 25°C) + \gamma Log\frac{G}{1000\ W/m^2}\right]} \qquad 5.2$$

where T is the module temperature and G is irradiance, $\eta(T)$ is efficiency at temperature T, η_{ref} is the efficiency at STC, and γ is the solar irradiance coefficient and β is the temperature coefficient. The solar irradiance coefficient, γ, is usually taken as zero which reduces it to a simple linear expression [291]. This equation can also be used to calculate the TC for V_{OC}. Equation 5.3 is used to calculate the TC for I_{SC}:

$$\boldsymbol{I_{SC}(T) = I_{SC_{ref}}[1 + \alpha(T - 25°C)]\frac{G}{1000\ W/m^2}} \qquad 5.3$$

where $I_{SC}(T)$ is I_{SC} at temperature T, I_{SCref} is I_{SC} at STC, and α is the TC for I_{SC}. To remove the effect of solar radiation on the TCs the outdoor data was filtered for fixed irradiance ranges of 600±20 W/m^2 and 1000±20 W/m^2. This also ensures that: diffuse conditions are excluded and therefore the majority of the irradiance is DNI; and that the measurements are from near noon ±3 hours when spectral conditions will be closer to AM1.5G. Data was analysed for a 14 day period in order to reduce the effect of degradation of the OPV modules.

The results for the OPV module are shown in Figure 5.9 along with trend lines and Table 5.2 has the calculated TCs, fitted by the least squares method.

Table 5.2: Calculated temperature coefficients for OPV module.

Irradiance Range	PCE (%/K)	I_{SC} (mA/K)	V_{OC} (mV/K)	FF (K^{-1})
600±20 W/m^2	0.0047	0.0774	-0.80	0.0015
1000±20 W/m^2	0.0080	0.1126	-0.86	0.0038
Average	0.0063	0.0950	-0.83	0.0027

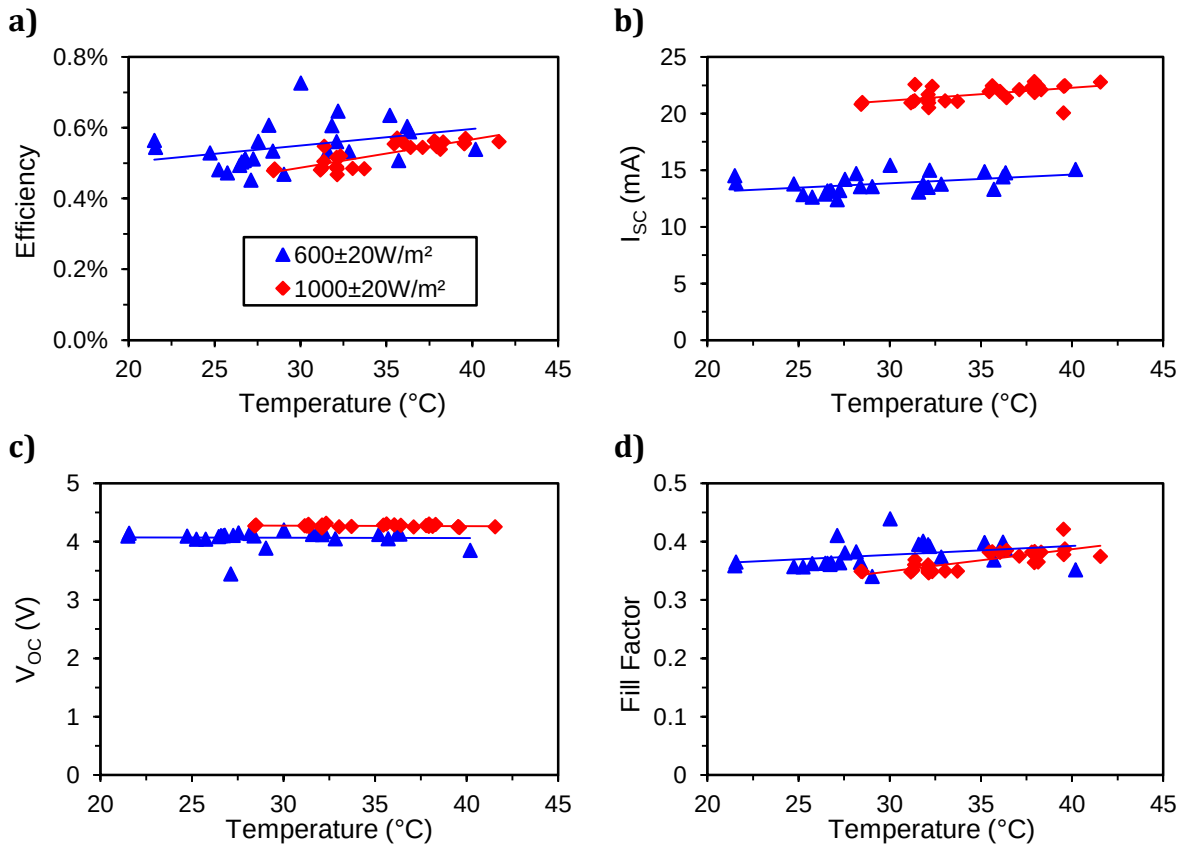

Figure 5.9: Temperature dependence of a) PCE, b) I_{SC}, c) V_{OC}, and d) FF. Measurements were filtered for irradiances of 600±20W/m² and 1000±20W/m² over a 10 day period.

V_{OC} shows the least variation against temperature with an average TC of -0.83 mV/K, which is -0.1 mV/K/cell (8 cells in the OPV module). V_{OC} at STC is 4.3 V which gives a value for β_{Voc} of -0.0002 K^{-1}. As temperature increases there will be a drop in the energy difference between the HOMO in the donor and the LUMO in the acceptor, leading to a drop in V_{OC} [151]. All of the other performance parameters show positive TCs. I_{SC} shows a TC of 0.095 mA/K (α=0.0046 K^{-1}). In OPVs, charge carrier transport in polymers is governed by carrier hopping and is therefore thermally assisted, which means that mobility and charge-carrier transport should improve with increasing temperature [292], [293]. In addition, temperature increases will also lead to more efficient dissociation of electrons and holes [294]. The FF has a positive TC (0.0027 K^{-1}) and this has been attributed to a decrease in the series resistance, whereas shunt resistance remains relatively unchanged by temperature [152]. Overall the strongly temperature-dependant coefficients for I_{SC} and FF combined with the weakly temperature-dependent coefficient for V_{OC} leads to a positive TC for efficiency of

0.0063%/K (β=0.0092 K^{-1}). These results also show higher TCs under conditions of higher irradiance, as reported previously[295].

5.1.6 Effect of Temperature on poly-Si Performance Parameters

Temperature analysis on the outdoor results was also performed for the poly-Si modules and the results are shown in Figure 5.10 and Table 5.3. These were taken over a 30 day period, as degradation was not an issue, and over tighter irradiance ranges (±5 W/m²).

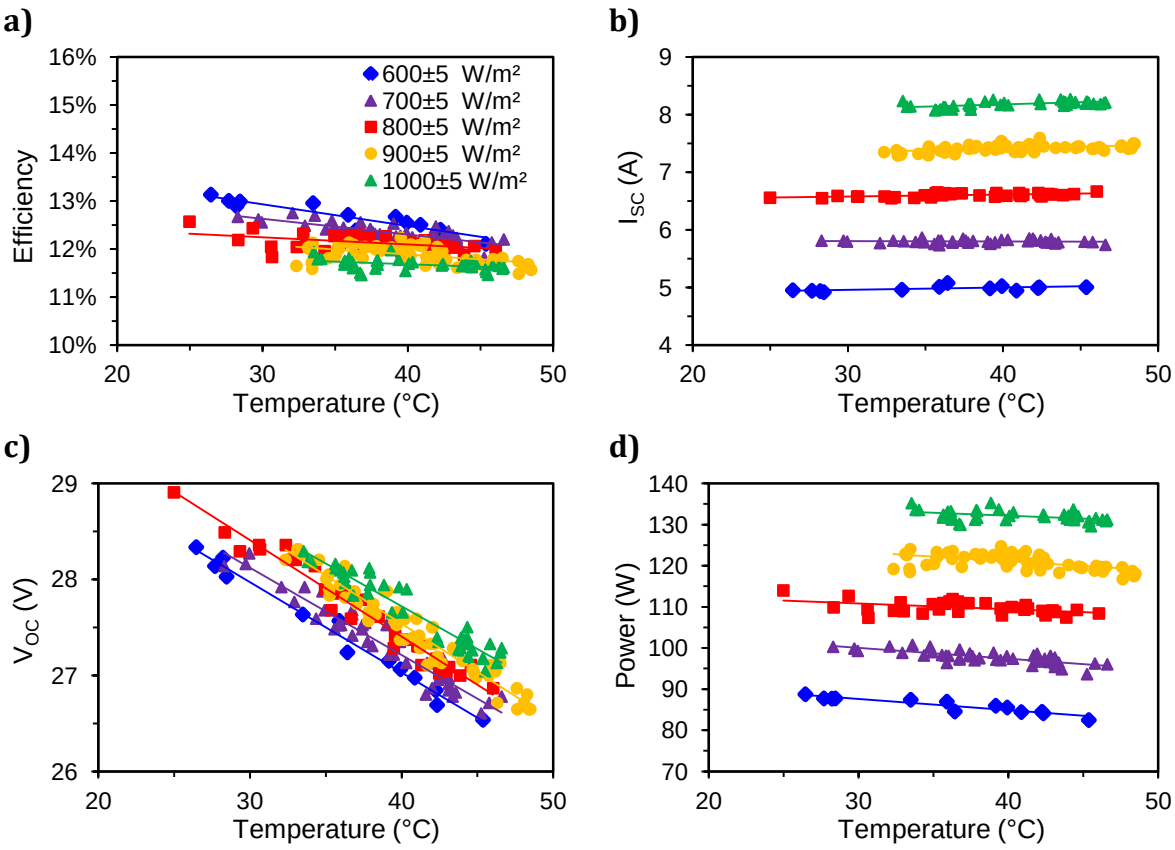

Figure 5.10: Temperature dependence of a) PCE, b) I_{SC}, c) V_{OC}, and d) Power (at MPP). Measurements were filtered for various irradiance ranges over a 30 day period.

Table 5.3: Calculated temperature coefficients for poly-Si module.

Irradiance Range	PCE (%/K)	I_{SC} (mA/K)	V_{OC} (mV/K)	FF (K^{-1})	Power (W/K)	Power (%/K)
600±5 W/m²	-0.0451	3.87	-94.2	-0.00032	-0.271	-0.315
700±5 W/m²	-0.0273	1.51	-95.5	0.00058	-0.223	-0.228
800±5 W/m²	-0.0151	3.59	-100.4	0.00108	-0.140	-0.128
900±5 W/m²	-0.0206	6.75	-100.6	0.00050	-0.229	-0.189
1000±5 W/m²	-0.0108	7.57	-89.2	0.00073	-0.139	-0.105
Average	-0.0238	4.66	-96.0	0.00051	-0.200	-0.193

V_{OC} was very consistent for all irradiance ranges, giving an average value of -96.0 mV/K, which is -2.0 mV/K/cell (poly-Si module has 48 cells). V_{OC} at STC is 28.5 V which gives a value for β_{Voc} of -0.0034 K^{-1}. V_{OC} has a negative TC due to a narrowing of the semiconductor's bandgap and increase in the saturation current [290]. I_{SC} shows a positive TC with an average value of 4.66 mA/K, which gives a value for α of 0.009 K^{-1} at 1000 W/m^2. The positive TC for I_{SC} is mainly due to thermally excited intrinsic charge carriers and narrowing of the semiconductor's bandgap with increasing temperature [289]. Despite a positive TC for I_{SC} the poly-Si has a negative TC for power and PCE, as the negative TC for V_{OC} is more significant.

Table 5.4 shows a comparison of measured and reported temperature coefficients. The calculated TC for efficiency for poly-Si (-0.292%/K) compares well with reported values obtained using a similar method (-0.4%/K). This gives confidence in the values obtained for OPVs. In comparison to other PV technologies, OPVs appear to be one of the few that have positive temperature coefficients for efficiency.

Table 5.4: Comparison of measured and reported temperature coefficients.

Type	η (PCE) (%/K)	η (PCE) [a] (K^{-1})	α I_{SC} [b] (K^{-1})	V_{OC} [c] (mV/K/cell)	β V_{OC} [d] (K^{-1})
OPV (Bangor)	0.0063	0.0092	0.0046	-0.10	-0.0002
poly-Si (Bangor)	-0.292	-0.024	-0.0009	-2.0	-0.0034
poly-Si [288], [290]	-0.4	-0.031	-0.0005	-2.0	-0.0044
CIGS [288], [290]	-0.484		-0.0003		-0.006
CdTe [288]	-0.25		-0.0004		-0.0036
a-Si [288]	-0.165		-0.0018		-0.0031

[a] Normalised to PCE at STC: (OPV=0.69%, poly-Si=12.39%)
[b] Normalised to I_{SC} at STC (OPV=20.6 mA, poly-Si=8.07 A)
[c] V_{OC} data is adjusted to cell values (Bangor: OPV=8 cells; poly-Si=48 cells)
[d] Normalised to V_{OC} at STC (OPV=4.3 V, poly-Si=28.5 V)

5.2 OPV Performance under Winter Conditions

Three DTU(AgGrid) modules (W1-W3) were monitored, over a fourteen week period, mounted on the inclined rack at 35°. These modules had a large variation in PCE, indicating that this batch was not as uniform as the modules from summer 2013. One module (W3) was protected by a UV filter (Solaronix #49132) in order to test whether this would improve stability.

5.2.1 OPV Degradation under Winter Conditions

Figure 5.11 and Table 5.5 show the degradation of the modules over winter. The module with the UV filter (W3) has not degraded over the period of monitoring; in fact it has shown a very slight increase in PCE (102% of its initial value), I_{SC} and FF. One of the modules (W2) showed rapid degradation, V_{OC} and PCE dropping steadily from the start (T_{80} = 28 days, T_{50} = 51 days). The other module (W1) showed a slight drop in V_{OC} and FF after 6 weeks and a slight drop in I_{SC} at 8 weeks, leading to a decrease in PCE between weeks 6 to 8, followed by a stabilisation (T_{80} = 44 days).

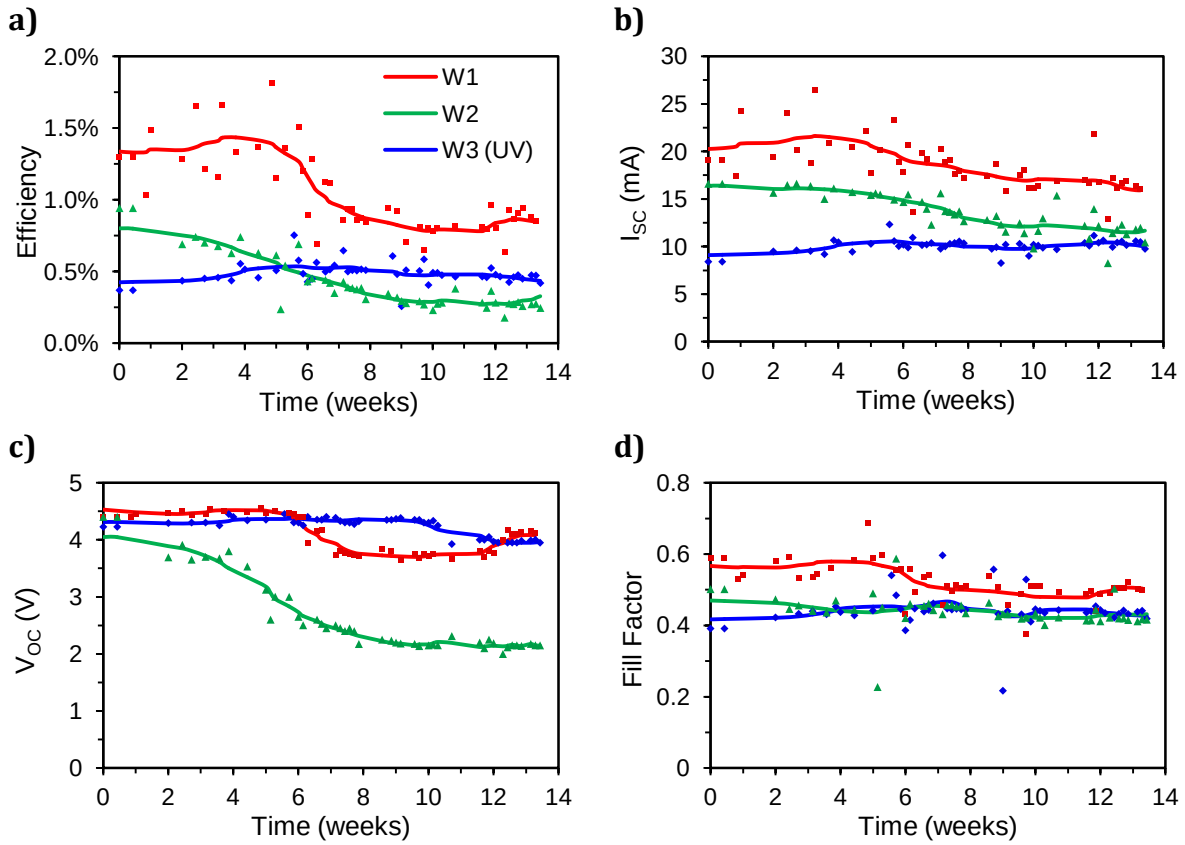

Figure 5.11: Degradation of DTU modules (Winter 2013/14): a) PCE; b) I_{SC}; c) V_{OC}; and d) FF. Measurements were selected at irradiances of 600±15 W/m².

Table 5.5: T_{80} and T_{50} lifetimes (Winter 2013/14). Data based on diurnal average PCE where irradiance was 600±15 W/m².

Sample	T_{80} Lifetime (days)	T_{50} Lifetime (days)	Normalised final PCE (at 95 days)
W1	44	-	64%
W2	28	51	40%
W3 (UV)	-	-	102%

5.2.2 Comparison with Summer Results

From analysis of how the modules from each group degraded over time it was apparent that the summer modules degraded much quicker than the winter ones. In order to compare the two datasets it was necessary to consider cumulative insolation received by the modules, as most degradation is caused by photo-oxidation and therefore will proceed much more slowly in winter than in summer. Comparison of the two datasets for V_{OC} indicated that degradation was dependent on time rather than insolation, which would mean that it is a physical rather photo-oxidative process that is causing it. Figure 5.12 shows a comparison of the summer and winter modules: PCE, I_{SC} and FF are plotted against cumulative insolation and V_{OC} is plotted against time. When plotted against these different x-axes the degradation rates are seen to be comparable.

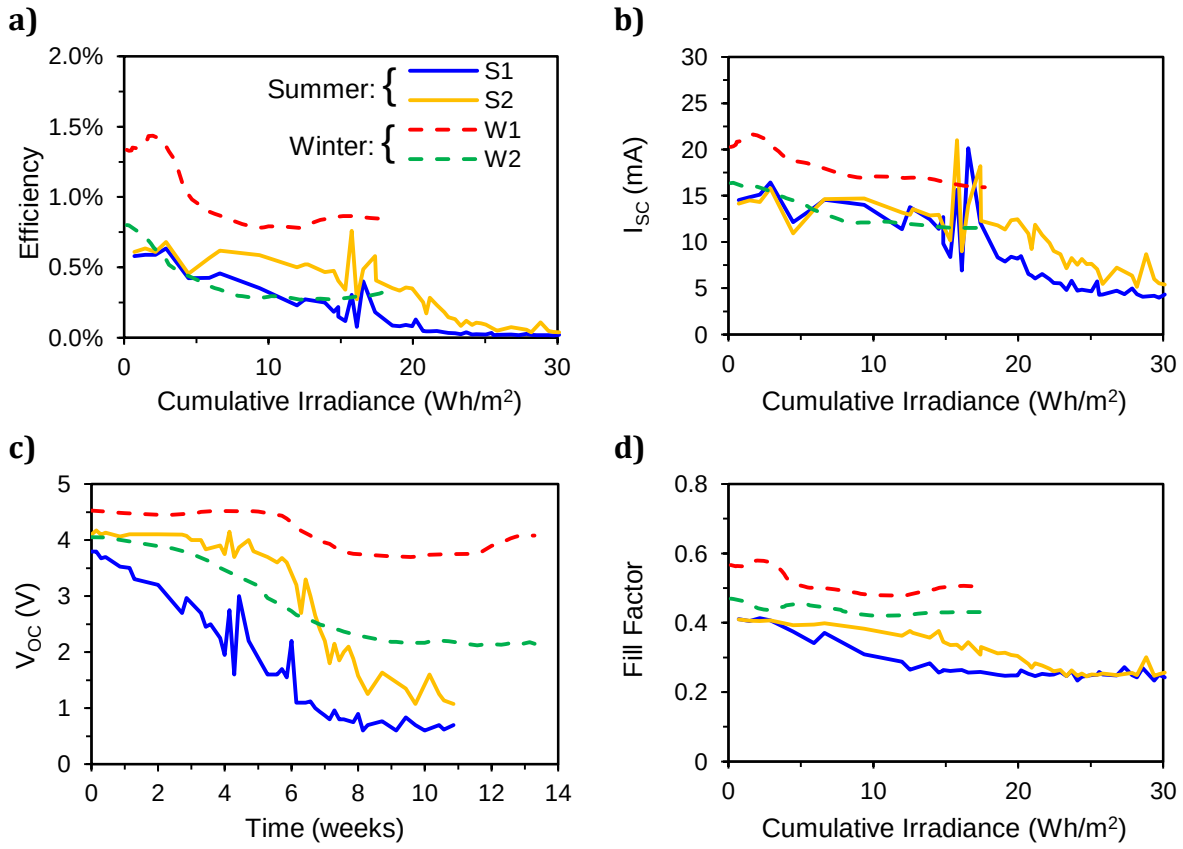

Figure 5.12: Comparison of degradation between summer 2013 and winter 2013/14: a) PCE; b) I_{SC}; c) V_{OC}; and d) FF. Measurements were selected at irradiances of 600±15 W/m². Measurements are plotted against cumulative insolation, apart from V_{OC} which is plotted against time. [Summer modules: S1 & S2, Winter modules: W1 & W2; All modules are on inclined racks].

Table 5.6 shows the average T_{80} and T_{50} lifetimes for the all the modules from each measurement campaign. The modules in summer degraded much faster ($T_{80(AVG)}$ =

11±7 days, $T_{50(AVG)}$ = 23±13 days) than the modules in winter ($T_{80(AVG)}$ = 36±11 days) and one of the winter modules only dropped to 64% of its initial PCE by the end of the monitoring (95 days). The high standard deviations (winter: ±11, summer: ±7 & ±13) are indicative of the wide variation in lifetimes of these modules.

Table 5.6: Comparison of summer 2013 and winter 2013/14: Average T_{80} and T_{50} lifetimes.

Sample	Module Count	T_{80} Lifetime (days)	T_{50} Lifetime (days)
Summer 2013	8	11±7	23±13
Winter 2013/14	2	36±11	51 †

† Only one module reached T_{50}, the other module only dropped to 64% of initial PCE by the end of the testing (95 days).

5.2.3 Assessment of UV Filtering

One module (W3) had been protected by a UV filter in order to test whether this would improve its stability. Figure 5.13 shows the cumulative yields of the three modules over the monitoring period. As the modules all started the monitoring with different PCEs the data has been normalised to module W1, based on their initial PCEs.

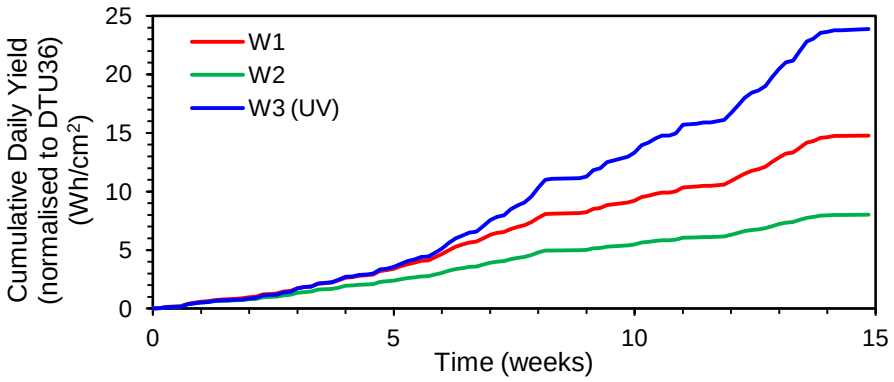

Figure 5.13: Comparison of cumulative yields of modules with and without UV filters. (Data has been normalised to initial PCE of W2).

The modules all showed similar yields for the first 5 weeks, but then the UV module (W3) started to show increasingly better performance over the other two modules. The module with the UV filter (W3) has exceeded both of the other modules, showing an improvement over module W1 of 33% at 8 weeks, increasing to 62% by week 15. This is because it has shown very little degradation over the course of the monitoring. Without normalisation module W1 showed the better performance, as the

module with the UV filter has a very low performance. However the long term benefits of the UV filter (very slow degradation rates) outweigh the lower initial performance levels. These results confirm that degradation during the summer could be due to UV.

5.3 Improving Stability using Silver Nanowire Front Electrodes

The first two monitoring campaigns used DTU(AgGrid) modules and these degraded relatively quickly. It was shown that even under winter conditions the application of a UV filter could improve stability. Here we examine data for one DTU(AgNW) module, which was monitored outdoors from 16/04/2015 till 17/07/2015. The primary difference between this module and those examined in Sections 5.1 and 5.2 is that the front electrode has been changed; a composite electrode of AgNW and ZnO has been used in the DTU(AgNW) modules. The ZnO thickness has to be increased for optimal processing and therefore absorbs more UV irradiation [296]. The purpose of this outdoor monitoring campaign is to examine whether these modules have improved stability.

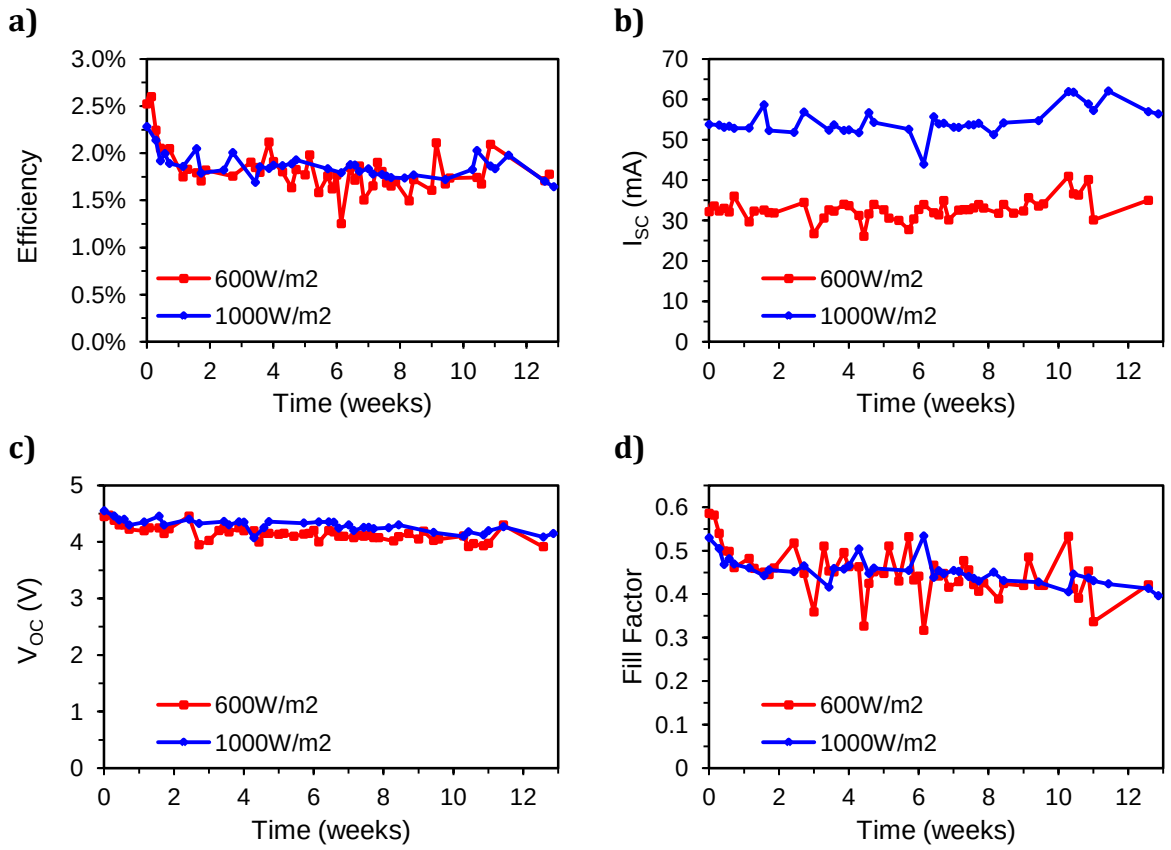

Figure 5.14: Degradation of DTU modules with silver nanowire front electrodes: a) PCE; b) I_{SC}; c) V_{OC}; and d) FF. Measurements were selected at two different irradiances: 600±15 W/m² and 1000±15 W/m².

Figure 5.14 shows the degradation of the performance parameters selected at irradiances of 600±15 W/m² and 1000±15 W/m². The efficiency curves show a rapid deterioration during burn-in over the first week or so, dropping from 2.5% to just below 2% (T_{80} = 6 days). This loss of efficiency mainly comes from a drop in fill factor as well as a very slight drop in V_{OC}. Once the module reaches stabilisation it is followed by a much slower degradation for the remainder of the outdoor monitoring; characteristic behaviour for these types of modules [297]. PCE stabilises at about 1.8% and maintains this for the rest of the monitoring period and I_{SC} increases very slightly over the course of the monitoring. FF and V_{OC} degrade very slowly over the same period. It is clear that using the AgNW/ZnO composite electrode greatly enhances the stability in an outdoor environment.

5.3.1 Reversible Degradation Pattern of DTU(AgNW) Modules

It was observed that when PCE was plotted against irradiance for a sunny day it followed a different pattern in the morning than in the afternoon (Figure 5.15). As it was a clear sunny day irradiance followed a predictable curve, climbing steadily until midday and then dropping down again. This morning/afternoon split affected all four performance parameters, especially PCE, I_{SC} and FF.

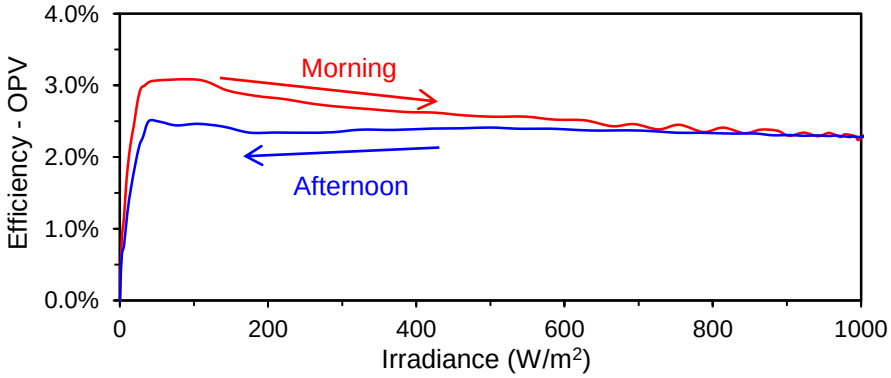

Figure 5.15: PCE plotted against irradiance on a sunny day near the beginning of the monitoring (18/04/2015), highlighting the different pattern in the morning and afternoon.

Closer examination of IV curves at similar irradiances, one from the morning and one from the afternoon (see Figure 5.16), show that the morning IV characteristic has better performance parameters than the afternoon curve: ΔPCE(relative)=25%; ΔI_{SC}=+14%; ΔFF=+9%; and ΔV_{OC}=+2%. I_{SC} and FF are the parameters with the most change and V_{OC} is virtually unaffected. This indicates that there is some reversible

degradation occurring in the active layer, which is either temperature or irradiance induced [298]. Examination of data later in the monitoring period showed that this morning/afternoon split no longer occurred.

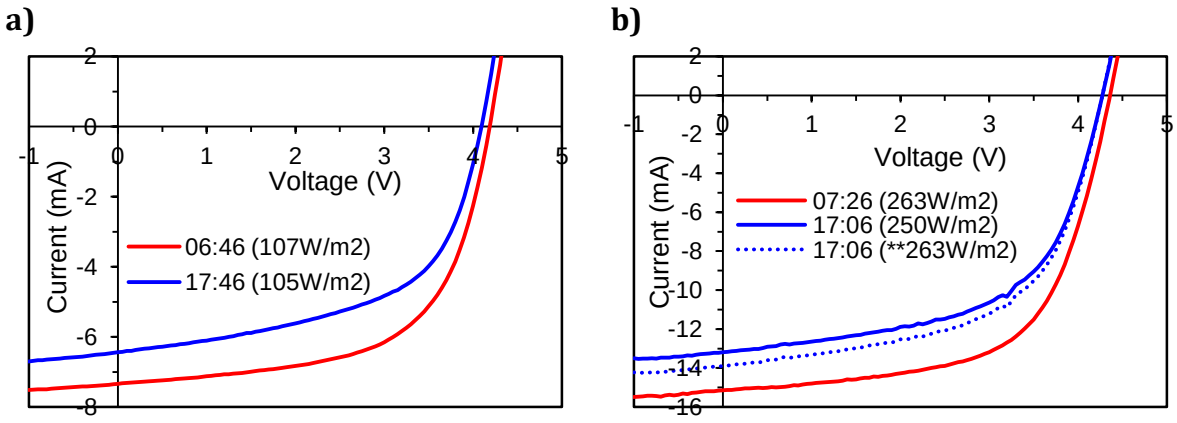

Figure 5.16: Comparison of morning (red) and afternoon (blue) IV curves on 18/04/2015 (2 days after monitoring commenced) at two similar irradiance levels: a) 105 & 107 W/m² and b) 250 & 263 W/m². The morning curves show higher current and voltage and better fill factor than the afternoon curves. [dotted line: current linearly adjusted to match irradiance of other curve]**

5.4 Summary of PV Benchmarks

Figure 5.17 shows a comparison of the performance parameters for poly-Si, CIS[4], DSSC[5], DTU(AgGrid) and DTU(AgNW) modules. In order to allow a better comparison between the very different module types, J_{SC} and V_{OC}/cell have been plotted. All data was sourced from clear sunny days, with high levels of direct normal irradiance, and all modules were inclined at 35° to the horizontal and facing south.

Apart from the DSSC module all of the modules display a linear trend for J_{SC}. They all display logarithmic V_{OC}, with DSSC having a V_{OC} of ~0.8 V/cell, poly-Si having a V_{OC} of ~0.6 V/cell and all the others having a V_{OC} of ~0.5 V/cell. However the rate of rise to maximum V_{OC} is very different, with DSSC, poly-Si and CIS reaching maximum V_{OC} at low irradiances, whereas the OPV modules have a much slower response, with DTU(AgGrid) being the slowest.

[4] A cadmium indium diselenide (CIS) module was installed on the roof in early 2014, inclined at 35°.

[5] A dye sensitised solar cell (DSSC), supplied by SolarPrint (Dublin), was monitored outdoors from 03/03/2014 till 07/05/2014 in order to provide a comparison of OPVs to other third generation modules. SolarPrint specialised in DSSCs fabricated using an electrolyte paste composed of carbon nanotubes [320].

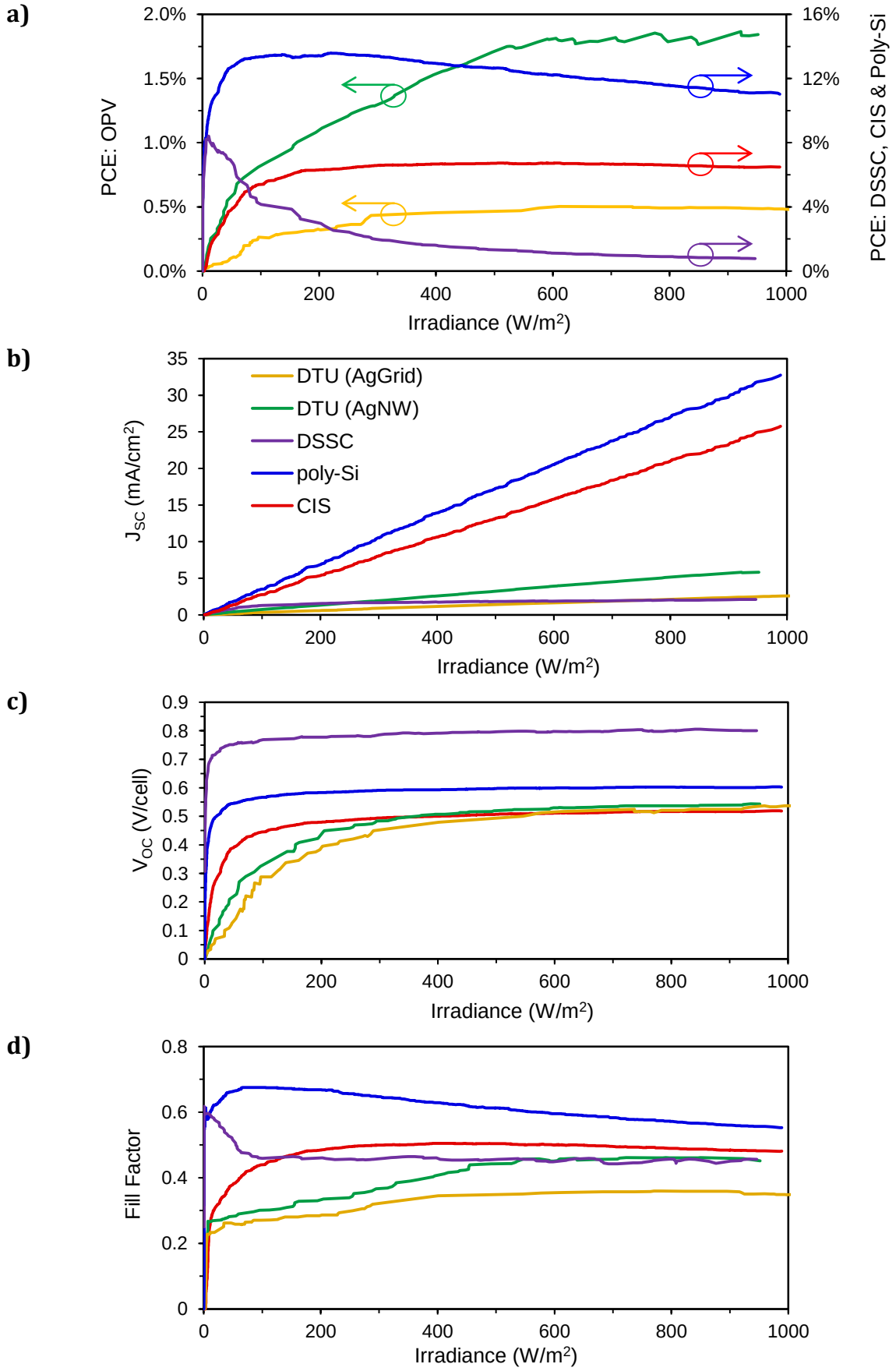

Figure 5.17: Comparison of performance parameters for poly-Si, CIS, DSSC and two OPV mini-modules from DTU: a) PCE; b) J_{SC}; c) V_{OC}/cell; and d) FF.

Poly-Si shows a similar profile for both PCE and FF, both reaching maximum levels at low irradiances (100-200 W/m^2) and then reducing with further increases in irradiance. The PCE and FF profiles for CIS are slightly different, reaching maximums at slightly higher irradiance levels (~400 W/m^2), and then reducing only very slightly with higher irradiance. The OPVs show very different profiles: for PCE they reach their maxima at much higher irradiances (600-800 W/m^2) and then stay relatively constant, whereas FF starts at low values (~0.25) and steadily increases with increasing irradiance. Of the two OPV modules DTU(AgNW) has the best overall performance.

The DSSC module has very different PCE and I_{SC} characteristics when compared to the other modules. PCE peaks at very low levels of irradiance, reaching 10% at 12 W/m^2, before dropping logarithmically to reach a steady PCE of ~1%; J_{SC} has the expected linear trend up to irradiance levels of ~100 W/m^2, after which it remains linear but with a much lower rate of growth. This current limiting effect is related to the low concentration of iodine in the electrolyte, as at higher irradiances the cell is current limited by the rate of migration of I_3^- (triiodide) ions through the electrolyte and subsequent triiodide reduction rate at the counter electrode [299]–[302]. Similar results have been seen in DSSCs monitored outdoors in Abu Dhabi [303] and Japan [302] and these results confirm that DSSCs perform better under low light conditions.

5.5 Summary

Over the course of several outdoor monitoring campaigns it has been possible to investigate several different properties of OPV modules. The first campaign was performed over summer using DTU(AgGrid) modules from DTU. These were shown to degrade very quickly, displaying two different degradation patterns. Detailed module temperature analysis was performed on both OPV and polycrystalline silicon modules, showing that both have a linear relationship between irradiance and module temperature above ambient, giving a Ross coefficient of 0.01 K.m^2/W for the OPV module. Further analysis was performed on the relationship between module temperature and PCE, I_{SC}, V_{OC} and FF for OPV modules. It was shown that V_{OC} has a negative temperature coefficient, but that I_{SC}, PCE and FF have positive temperature coefficients.

A second outdoor campaign looked at similar OPV modules over winter, one of which had a commercial UV filter applied. In comparison with the summer results all of these modules degraded much more slowly due to the lower levels of irradiance and UV

experienced. The module with the UV filter was shown to be particularly stable and outperformed the best control module by 62% (based on normalised yields). Comparison of the degradation rates of the summer and winter modules indicated that whereas I_{SC} and FF degradation was based on cumulative insolation, V_{OC} was time based. This suggests that I_{SC} and FF degradation is due to photo-oxidation, whereas V_{OC} degradation is a physical process.

A third monitoring campaign looked at DTU(AgNW) modules under summer conditions. These were found to degrade much more slowly than the DTU(AgGrid) modules and this is attributed to the UV filtering effect of the ZnO in the composite AgNW/ZnO electrode. The DTU(AgNW) module was found to undergo temporary reversible degradation when exposed to higher levels of irradiance and UV.

Over the course of this research several different PV technologies were compared to examine the effect of irradiance on PCE, I_{SC}, V_{OC} and FF. These included polycrystalline silicon (poly-Si), cadmium indium diselenide (CIS), dye sensitised solar cells (DSSC), and two different types of freeOPV module: DTU(AgGrid) and DTU(AgNW).

Overall these results showed that OPV modules perform well under high levels of irradiance, aided by positive temperature coefficients. It was also shown that degradation was driven by photo-oxidation and physical ingress of water. It was shown that UV filtering slowed these degradation rates. UV filtering will be looked at again in more detail in Chapter 7.

Chapter 6. Development of OPVs onto Structured Corrugated Substrates

This chapter examines how the performance of OPVs can be improved by laminating them to corrugated substrates in order to improve their light capture capability in outdoor conditions. OPVs are ideal candidates for lamination onto curved substrates as they are flexible. This chapter specifically looks at the performance of OPVs laminated onto curved substrates, but the results will be applicable to both laminated and printed modules.

These 3D structures are particularly relevant for use in building integrated PV (BIPV) applications and this is an area where OPVs could compete directly with mainstream PV technologies [304]*. OPVs have the advantage of ease of free form design that flexibility, printing and lamination offer over traditional rigid PV technologies* [27]*.*

6.1 3D Structured Module Preparation

Four different configurations of structured OPV modules were fabricated, based on DTU(AgNW) modules and were laminated onto two different corrugated PVC roofing substrates supplied by Ariel Plastics Ltd. (see Section 4.5 and Figure 4.13) [112]. The 3D modules were fabricated to four different patterns:

A. **Single Concave**: the module is laminated on the inside of one section of the large substrate forming a U-shape.

B. **Single Convex**: the module is laminated on the outside of one section of the large substrate to form an inverted U-shape.

C. **Small Inline**: the module is laminated onto the small corrugated substrate with the cells parallel to the corrugations.

D. **Small Transverse**: the module is laminated onto the small corrugated substrate with the cells across the corrugations.

In all four cases the footprint area of the flat module is reduced (by up to 18%) when the module is laminated over the curved substrate (Table 6.1). Laser beam

induced current (LBIC) imaging has been used to define real active areas, as this has an impact on the effective efficiency of the modules (see Section 4.5.6).

Table 6.1: Active area footprints of flat and 3D modules. The nominal active area is based on the length and width of the total active area and includes "dead" areas between cells, whereas the real active area is measured by LBIC. The percentages in brackets show the active area of the 3D modules compared to the original flat module.

Module Type	Nominal Active Area (cm^2)	Real Active Area (LBIC defined) (cm^2)	
Flat	73.47	56.70	(100%)
A	61.38	47.37	(84%)
B	60.45	46.65	(82%)
C	64.78	49.99	(88%)
D	66.96	51.68	(91%)

6.2 Single Module Tests

The testing was carried out with four experiments: characterisation under AM1.5G conditions; LBIC; indoor angular characterisation; and outdoor monitoring.

6.2.1 Characterisation under AM1.5G

All of the modules were first characterised at DTU using an AM1.5G source prior to lamination onto the corrugated substrates by the author at Bangor. After lamination the 3D modules were retested at DTU, first with the module positioned normal to the incident light and then at various angles of tilt to simulate changes in angle of incidence (AOI).

Table 6.2 shows the performance figures at AM1.5G for modules before and after lamination under irradiation at normal incidence. Prior to lamination the modules showed very little variation in PCE across the batch (2.13±0.05%). After lamination both the single convex and the single concave modules showed an increase in PCE, with type A showing a relative enhancement of 5.3% and type B of 10.6%. These improvements in PCE are primarily due to gains in J_{SC}, with type A increasing by 5.3% and type B by 13.4%. Neither of the modules on the small corrugations performed very well. Type D showed relative losses of -13.5% in PCE and -14.8% in J_{SC}. The worst performing module was type C, with relative drops of -39.9% in PCE and -39.5% in J_{SC}.

By comparison there was very little variation in V_{OC} across all of the modules, measured at 4.27±0.02 V before lamination and 4.33±0.03 V after lamination. Similarly for fill factor, going from 53.0±0.2% before lamination to 52.0±0.8% after lamination. This indicates that lamination onto 3D structures causes PCE changes that are primarily due to variations in J_{SC}.

Table 6.2: Performance of modules before and after lamination onto corrugated substrates (averaged across two sets of modules).

Before lamination Effective area: 56.7 cm²			After Lamination				
Type	**PCE (%)**	**J_{SC} (mA/cm²)**	**Effective Area (cm²)**	**Effective PCE (%)**	**J_{SC} (mA/cm²)**	**PCE gain**	**J_{SC} Gain**
A	2.10	0.92	47.37	2.17	0.97	3.2%	5.3%
B	2.17	0.96	46.65	2.40	1.09	10.6%	13.4%
C	2.18	0.96	49.99	1.31	0.58	-39.9%	-39.5%
D	2.06	0.91	51.68	1.78	0.78	-13.5%	-14.8%
Flat	2.15	0.94	-	-	-	-	-

Table 6.3 and Table 6.4 have the performance results for the flat and structured modules tilted at 20° and 45° in both orientations (definitions shown in Figure 6.1). Relative gains in PCE and J_{SC} relative to the flat module at the same angle of tilt have been calculated in order to compare the performance of the 3D modules against a flat module.

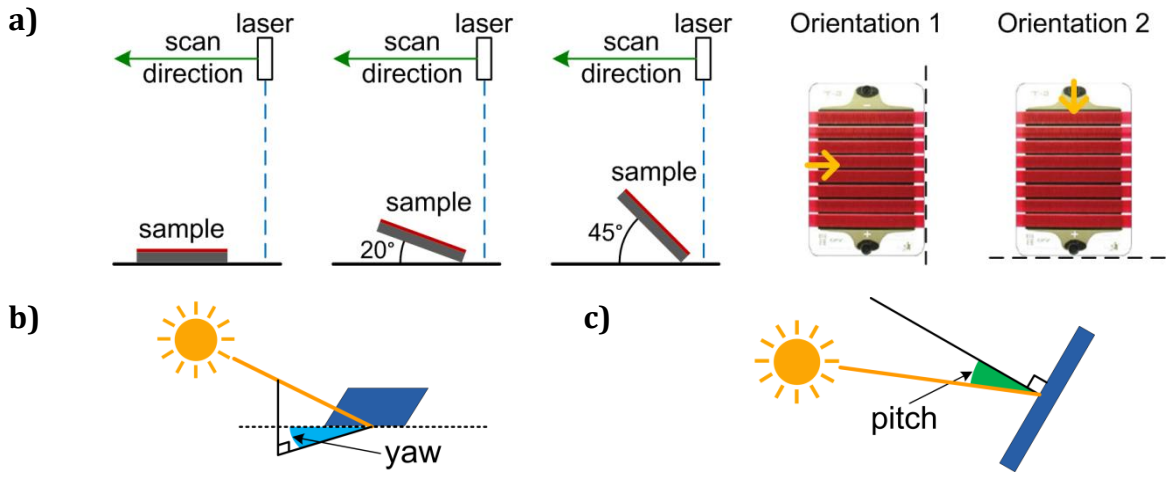

Figure 6.1: a) Definition of tilt angles and module orientations for LBIC testing and AM1.5G characterisation measurements at DTU. Tilting in Orientation 1 represents changes in yaw (b) and in Orientation 2 represents changes in pitch (c).

In both orientations and at both tilt angles type B showed the best overall increase in performance when compared to the flat module. In orientation 1 (changing yaw angle) it showed relative PCE enhancements of 5.6% (at 20°) and 19.4% (at 45°). In orientation 2 (varying pitch) it showed relative PCE enhancements of 14.2% (at 20°) and 10.6% (at 45°). Type A also outperforms the flat module at 20° with relative enhancements of 2.3% (orientation 1) and 1.2% (orientation 2). However at 45° it only outperforms the flat module in orientation 2 with a PCE enhancement of 2.9%, whereas in orientation 1 it does not perform as well as the flat module with a relative drop in PCE of -10.8%.

Neither of the smaller corrugated modules (types C & D) performed as well as the flat module. As will be seen later there are reasons why these two modules have performed so badly, but it is interesting to note that the module with the cells parallel to the corrugations (type C) was outperformed by the module with the cells perpendicular to the corrugations (type D) and that when the modules were tilted at 45° they both performed better when the light was coming from a direction parallel with the direction of the corrugations (varying pitch) and worse when it was perpendicular to the corrugations (varying yaw).

Table 6.3: Performance of modules at 20° of tilt and comparison of structured modules against flat module at 20°.

Orient-ation	Type	Module tilted at 20°			cf. to flat module at 20°	
		Effective Area (cm^2)	Effective PCE (%)	J_{SC} (mA/cm^2)	PCE gain	J_{SC} gain
1	A	44.51	2.32	1.04	2.3%	-4.5%
1	B	43.84	2.39	1.18	5.6%	8.1%
1	C	46.98	1.45	0.64	-36.1%	-41.1%
1	D	48.56	1.88	0.86	-17.1%	-21.3%
1	Flat	53.28	2.27	1.09	-	-
2	A	44.51	2.31	1.02	1.2%	-3.8%
2	B	43.84	2.60	1.18	14.2%	10.5%
2	C	46.98	0.84	0.37	-62.9%	-65.0%
2	D	48.56	1.87	0.80	-18.0%	-24.8%
2	Flat	53.28	2.28	1.07	-	-

Table 6.4: Performance of modules at 45° of tilt and comparison of structured modules against flat module at 45°.

Orient-ation	Type	Module tilted at 45°			cf. to flat module at 45°	
		Effective Area (cm^2)	Effective PCE (%)	J_{SC} (mA/cm^2)	PCE gain	J_{SC} gain
1	A	33.50	2.13	0.98	-10.8%	-11.4%
1	B	32.99	2.85	1.33	19.4%	20.3%
1	C	35.35	1.56	0.73	-34.9%	-34.3%
1	D	36.54	1.71	0.89	-28.6%	-19.3%
1	Flat	40.09	2.39	1.11	-	-
2	A	33.50	2.59	1.13	2.9%	-2.6%
2	B	32.99	2.78	1.18	10.6%	2.1%
2	C	35.35	0.50	0.24	-80.2%	-79.2%
2	D	36.54	1.95	0.88	-22.3%	-23.8%
2	Flat	40.09	2.52	1.16	-	-

6.2.2 Angular Characterisation

Indoor angular characterisation measurements were performed on the Lucas Nuelle solar simulator which allows variation of both yaw and pitch of the light source. By varying the yaw the response to the diurnal passage of the sun can be evaluated. Variation of the pitch allows for seasonal variation, latitude or tilt of the module to be simulated. The efficiency figures have been multiplied by a spectral mismatch multiplier of x2.67 in order to bring them into line with the IV characterisation measurements made at DTU, as the light source on the Lucas Nuelle is a halogen bulb (Section 4.4.2).

Figure 6.2a shows the irradiance used for all efficiency calculations, calculated from the cosine of the AOI (Section 4.5.7). Figure 6.2b shows the angular characterisation for the flat module. As expected the highest efficiency is when the light source is normal to the module (PCE = 1.90%). As the position of the light source is varied by altering the pitch and yaw the PCE drops off as a function of the AOI (approximately *cosine(AOI)*). These efficiency measurements for the flat module are used for comparison with the 3D modules in order to assess relative performance.

Figure 6.3 shows the angular characterisation for the structured modules. The trends in PCE as pitch and yaw are varied are significantly different to those obtained for the flat module (Figure 6.2c). Figure 6.4 shows the relative enhancement in effective PCE for each of the structured modules when compared to the flat module.

The two modules laminated onto the larger corrugated substrate (types A & B) have higher PCE than the flat module at normal incidence ($PCE_{0°}$(A) = 2.16%, $PCE_{0°}$(B) = 2.24%). As pitch and yaw are increased effective PCE for both modules initially

decreases at a similar rate to the flat module. However, as yaw reaches 70°-80° away from normal incidence there is a dramatic rise in the performance, with type B actually increasing its PCE to nearly 4%. This can be seen more clearly in Figure 6.4, with an enhancement in PCE of nearly x15 for type B and of x6 for type A. The modules on the smaller corrugated substrate (types C & D) have slightly lower PCE than the flat module at normal incidence ($PCE_{0°}$(C) = 1.50%, $PCE_{0°}$(D) = 1.21%). As pitch and yaw are increased these modules also exhibit effective PCE decreasing at a similar rate to the flat module. For type C there is a trough in relative PCE enhancement at high angles of yaw (>70° away from normal), as PCE reaches almost zero. This is due to whole cells becoming shaded resulting in the reverse biasing of individual cells in the module which leads to a large drop in module performance. Variations in pitch do not have the same dramatic changes as are seen for yaw.

Further data confirming the reproducibility of these results is in Appendix C.3.

a)

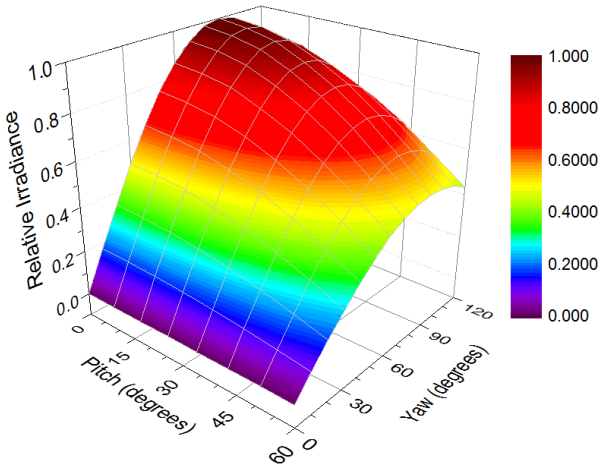

b)

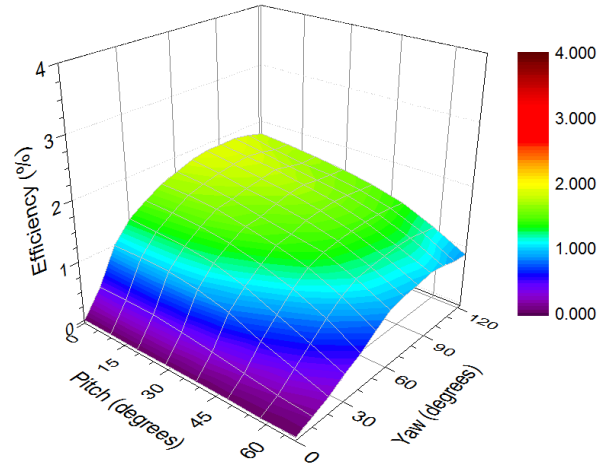

Figure 6.2: 3D Angular characterisation: a) calculated relative irradiance [=Irr_0 x cos*(AOI)*, where Irr_0 is irradiance at normal incidence and *AOI* is the angle of incidence], used for calculating module efficiency; and b) measured efficiency of flat reference cell, with the maximum efficiency at normal incidence.

a)

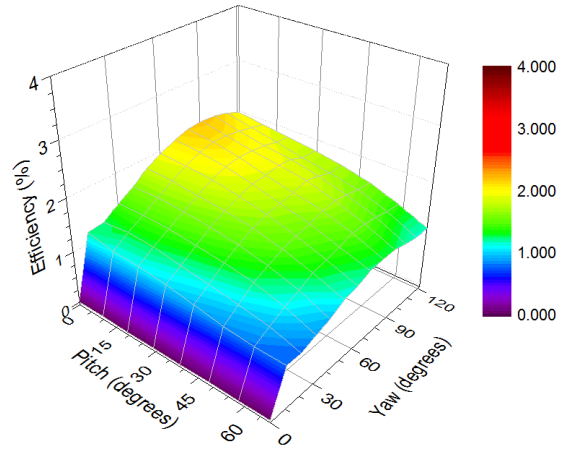

b)

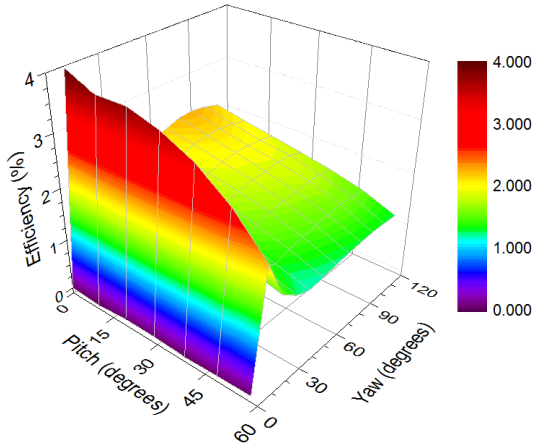

c)

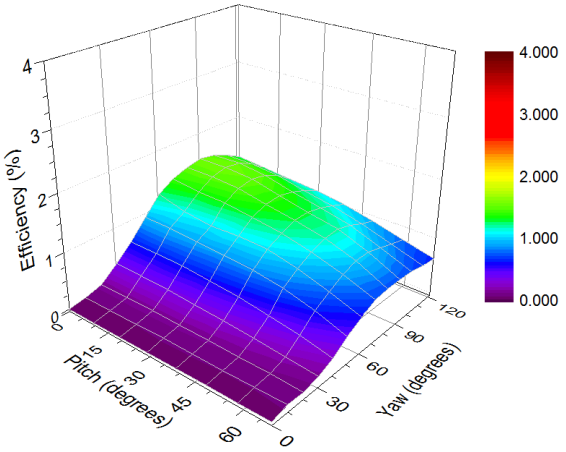

d)

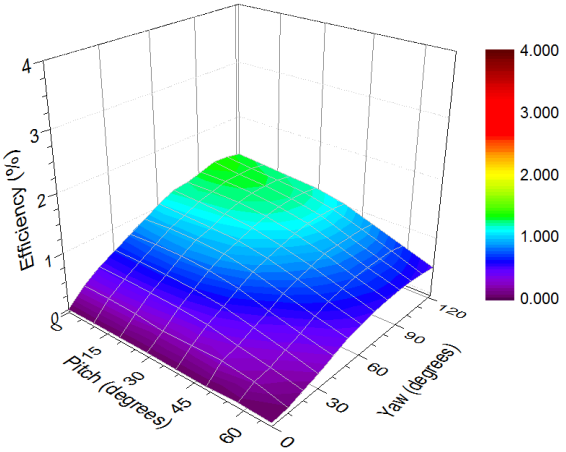

Figure 6.3: 3D angular characterisation – module efficiency: a) type A; b) type B; c) type C; and d) type D.

a)

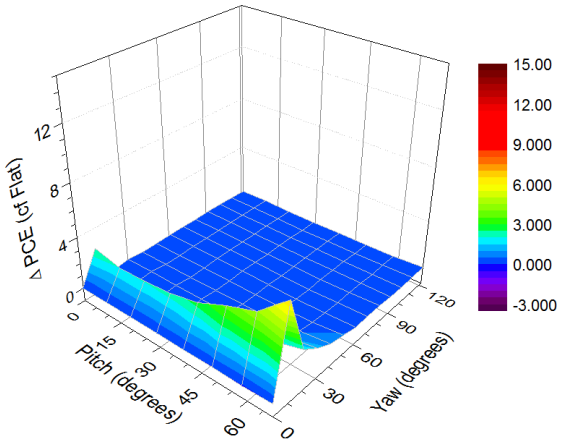

b)

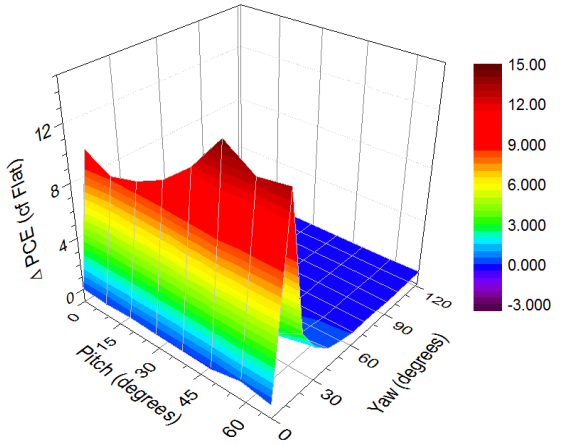

c)

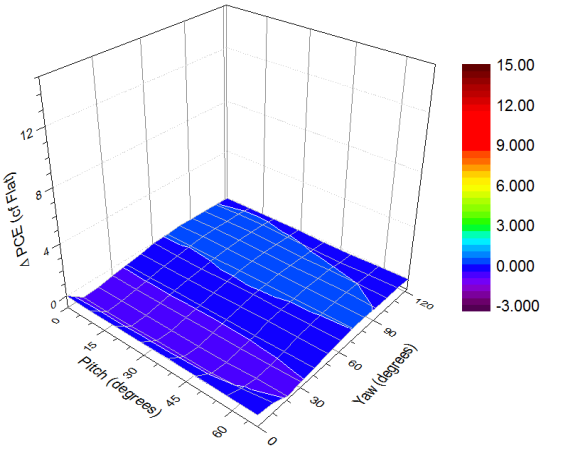

d)

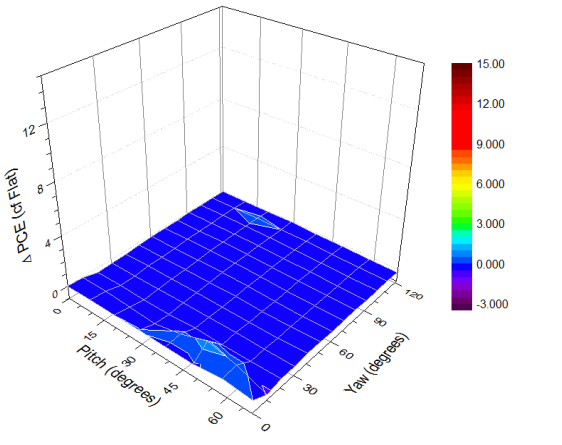

Figure 6.4: 3D angular characterisation – relative enhancement in PCE when compared to flat reference module: a) type A; b) type B; c) type C; and d) type D .

6.2.3 Laser Beam Induced Current Imaging

LBIC imaging was performed at DTU on all of the flat modules before they were laminated [270]. After the modules were laminated, one set were sent back to DTU for further LBIC imaging, initially with the modules positioned normal to the laser beam and then at various angles of tilt to simulate changes in pitch and yaw (Figure 6.1). The full set of images is in Appendix C.1 and the important findings are discussed below.

All the flat modules showed generally uniform current extraction between all the cells with very few imperfections, although there was some horizontal banding caused by slight variations in the R2R printing [145] and vertical slanted striping caused by the Ag grid of the back electrode (Figure 6.5a&b). Figure 6.5 shows that after lamination the LBIC images indicate two different phenomena: stripes of higher current generation (indicated by red arrows) and delamination defects (circled in white). Type A shows distinct bands of elevated photocurrent generation along the areas corresponding to the steepest curvature of the module (Figure 6.5c). This would indicate that whilst some of the laser beam is coupling into the module in these areas, a proportion is also being reflected off and coupling in at the bottom of the corrugation leading to an enhanced photocurrent being measured at the point of reflection. This light trapping effect only occurs where the module surface is at its steepest (~50° to normal) and the high AOI leads to maximum reflection towards another photoactive area of the module. This could be thought of as a reflective in-coupling effect. This effect can also be clearly seen in type D (Figure 6.5f). The effect is seen to a much lesser extent in type C (Figure 6.5e). Although this could be due to the severe delamination defects (discussed below), it is more likely that this is because any enhancement or reduction affects whole cells and therefore reduces the total current flow through the whole module as it is limited to the current flow of the worse performing cells. This will have the effect of reducing the visibility of the reflective in-coupling effect. LBIC images taken at different angles of pitch and yaw (Figure B.1) show that the reflective in-coupling effect also occurs as the module is tilted. Type B showed the most uniform current generation across the photoactive areas, which indicates that there is little variation due to reflective losses or gain.

The modules laminated onto the smaller corrugated profiles (types C & D) have significant areas of defects where there is no photocurrent generation (Figure 6.5e&f). These areas of defects explain the lower efficiencies found in these modules (see Section 6.2.1). Close visual examination of the modules shows crinkling at the edges of these

areas. This would indicate that severe delamination has occurred, either when they were being laminated onto the corrugated substrates or at some time afterwards. They are mounted onto the smaller corrugated profile, which leads to greater bend stresses due to the smaller bend radius (8 mm). These faults are not observed on module types A and B, which were fabricated on the larger corrugated profile (23 mm bend radius), even after outdoor testing for over two months. Results of cyclic bend testing conducted on these types of modules with Ag-nanowire electrodes show that they are stable even after 500 cycles [260]. This would indicate that it is the long term static stress that these modules have been subjected to that has caused these defects to appear. Repeat LBIC imaging on freshly laminated modules showed less severe delamination on these modules confirming that the delamination is exacerbated by prolonged static stress (see Appendix C.2) [260]. This indicates that both cyclic and static bending tests should be considered when testing flexibility of modules for their compliance to non planar surfaces.

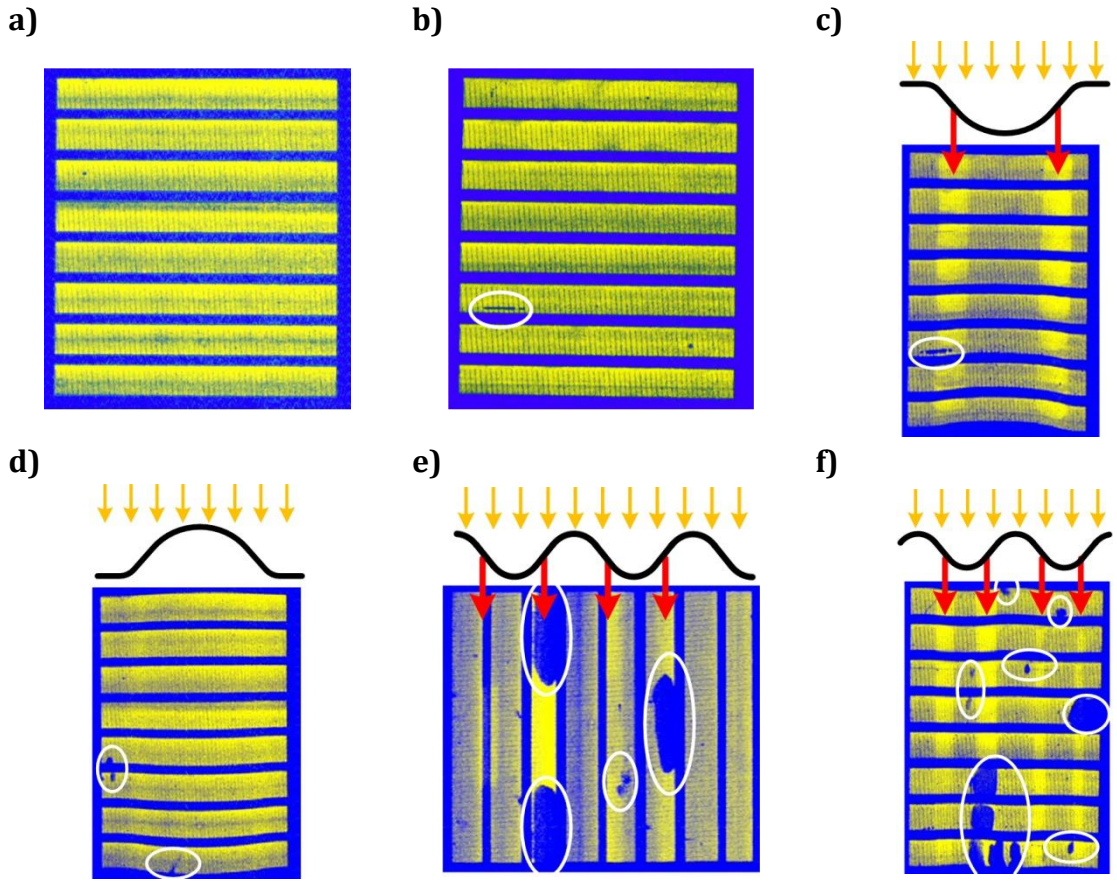

Figure 6.5: LBIC images of 3D structured modules: a) & b) Flat (before lamination; c) Type A; d) Type B; e) Type C; and f) type D. The corrugated profile of each structured module is indicated. Defects caused by delamination and R2R printing problems are highlighted in white. Strips of higher current generation caused by internal reflection are highlighted in red.

6.2.4 Outdoor Performance Monitoring

Outdoor measurements were taken at Bangor under both summer and winter conditions. In all cases the modules were mounted on racks inclined at 35° to the horizontal and facing due south. Regular IV and irradiance measurements were taken and from these the main performance parameters (V_{OC}, I_{SC}, FF and PCE) were derived.

The system yields were analysed to compare overall performance on days with different climatic ratings, based on comparing the measured daily global horizontal irradiation (GHI) against the nominal GHI[6]: "Sunny" (daily irradiation >80% of nominal GHI), "Diffuse" (daily irradiation <40% of nominal GHI), and "Intermediate". This allows the performance of the different module types to be compared under different irradiance conditions. From each set of data a pair of contrasting days was also selected to provide diurnal comparisons between sunny (high levels of direct normal irradiance) and cloudy (mainly diffuse irradiance) conditions.

The tests reported below were performed between 13/05/2015 and 18/06/2015 and used structured modules laminated using DTU(AgNW) modules. Figure 6.6 shows the irradiance and diurnal efficiencies for the modules on a sunny day (10/06/2015) and a cloudy day (22/05/2015).

Considering the sunny day: the total irradiation was 8.1kWh/m^2 and maximum horizontal irradiance reached 890W/m^2; average and maximum ambient temperatures were 14.3°C and 17.2°C respectively. The flat module exhibits typical diurnal performance for an OPV module, staying relatively constant over the majority of the day with a gentle rise in the morning and a gentle fall during the evening. Examination of I_{SC}, V_{OC} and FF over the course of the day (Appendix C.4) shows that I_{SC} is linearly dependent on irradiance and therefore PCE is dependent on variations in V_{OC} and FF. As V_{OC} and FF are constant across the majority of the day, the effective PCE is also almost constant from 08:00 till 16:00.

In contrast the type B module shows significantly improved efficiency under oblique angles of incidence which occur in the early morning and evening. In the morning it reaches a maximum efficiency of 4.7%, which is a fourfold improvement on the flat module. Considering the times of day and angles of the sun relative to the module, these increases are consistent with the indoor results in Section 6.2.2. This

[6] Nominal GHI: GHI on a clear day derived from the model proposed by Bird et al. [46].

improvement is primarily due to increased I_{SC} which is related to improved light capture. Whilst this improvement is substantial it is lower than that predicted from the indoor results. This could be attributed to several reasons including the different spectral characteristics in early morning/late evening and the effect of local shading from structures on the roof and nearby mountains. One other likely reason is that the light source used for the indoor tests is not collinear as the lamp is quite close to the module under test. Type A also shows a diurnal trend in performance similar to type B, but the relative enhancements are not as great.

Considering the performance of the two smaller corrugated modules, they have not performed as well as the single convex and single concave modules. Type C shows its highest performance at midday, but performance is not stable over the course of the morning and afternoon and drops off significantly at the ends of the day. By comparison type D has a relatively steady performance over the course of the day, although at a much lower efficiency than the flat module.

Now considering the data for the cloudy day, where the irradiation levels are much lower (total irradiation of 2.4kWh/m^2 and maximum irradiance of 631W/m^2) and mainly diffuse (as shown by the close overlap of in-plane and horizontal irradiance) (Figure 6.6b). Ambient temperatures are much lower with an average of 13.4°C and a maximum of 15.0°C. As OPVs possess a positive temperature coefficient the potential effective PCE over the course of the day is reduced. PCE is also dependent on irradiance at levels below 500W/m^2; above this level of irradiance the efficiency becomes constant (Figure B.5d in Appendix C.4). This can be seen in Figure 6.6d, with effective PCE following changes in irradiance. Comparing the different module types, type B is the best performing, followed by the flat reference and type A modules which both have similar performances. Finally the modules on smaller corrugations (types C & D) have performed the worst but with closely matching results. Type B does not show the substantial early morning/evening enhancements seen on the sunny day as the light is predominantly diffuse with very little or no direct irradiation.

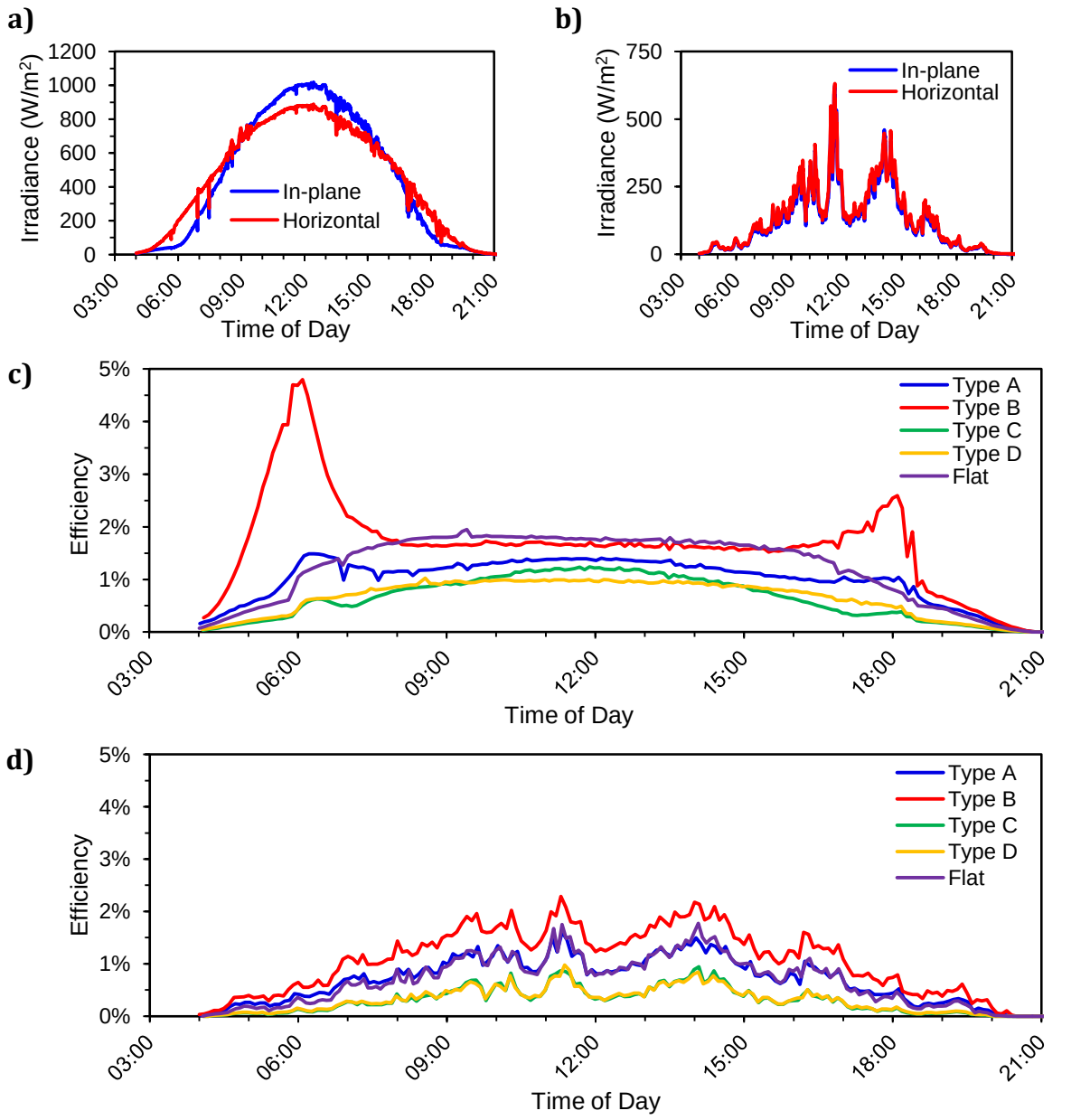

Figure 6.6: Outdoor monitoring: summer 2015. Diurnal irradiance: a) sunny day (10/06/15); b) cloudy day (22/05/15). Diurnal Efficiency: c) sunny day; d) cloudy day. [sunrise: 04:20, sunset: 20:05]

Analysis of average diurnal yields for the different module types and under different irradiance conditions allows a better understanding of the potential for the different module types (Table 6.5). Type B outperforms the flat module by 17% overall, with the best gain (25%) being seen under diffuse conditions compared to just 11% under sunny conditions. This is of significance to countries like the UK where cloudy conditions are predominant. Type A does not perform as well as the flat module under any conditions and shows the least loss (cf. flat module) under cloudy conditions. The smaller corrugated modules do not show much variance between different days.

Table 6.5: Analysis of average daily yields from outdoor performance monitoring over a five week period (start: 13/05/2015) under different climatic conditions. Gain is the percentage improvement shown by the 3D modules when compared to the flat reference module.

Module Type	Sunny		Intermediate		Cloudy		Total	
	Average Daily Yield (mWh/cm²)	Gain (cf. Flat)	Average Daily Yield (mWh/cm²)	Gain (cf. Flat)	Average Daily Yield (mWh/cm²)	Gain (cf. Flat)	Average Daily Yield (mWh/cm²)	Gain (cf. Flat)
Flat	11.72	-	6.30	-	2.35	-	7.42	-
A	8.50	-27%	5.16	-18%	2.13	-9%	5.76	-22%
B	13.05	11%	7.68	22%	2.94	25%	8.65	17%
C	6.42	-45%	3.78	-40%	1.32	-44%	4.23	-43%
D	5.89	-50%	3.42	-46%	1.15	-51%	3.85	-48%

One of the apparent benefits of the 3D modules is their increased performance in the early morning and evening. This is potentially of great benefit in countries where electricity demand peaks at these times, especially in the late afternoon/evening, which is often associated with higher electricity prices. In the UK these diurnal fluctuations in demand peak between 16:30 and 19:30 [305]. Further analysis of the system yield between 16:30 and 19:30 is presented in Table 6.6. This shows that for type B there is an average performance gain of 70% under sunny conditions, rising to 74% under intermediate conditions and dropping to 37% under diffuse conditions, and averaging 70% overall. This highlights the benefits that could be obtained with 3D modules by increasing output at times of high demand and reducing the need for fossil fuel back up on the grid [306].

Table 6.6: Analysis of peak hour yields (between 16:30 and 19:30) from outdoor performance monitoring over a 5 week period (start: 13/05/2015) under different climatic conditions. Gain is the percentage improvement shown by the 3D modules when compared to the flat reference module.

Module Type	Sunny		Intermediate		Cloudy		Total	
	Average Daily Yield (mWh/cm²)	Gain (cf. Flat)	Average Daily Yield (mWh/cm²)	Gain (cf. Flat)	Average Daily Yield (mWh/cm²)	Gain (cf. Flat)	Average Daily Yield (mWh/cm²)	Gain (cf. Flat)
Flat	0.62	-	0.44	-	0.24	-	0.48	-
A	0.51	-17%	0.38	-13%	0.21	-11%	0.41	-15%
B	1.05	70%	0.77	74%	0.33	37%	0.81	70%
C	0.23	-63%	0.17	-61%	0.11	-54%	0.18	-62%
D	0.28	-54%	0.20	-54%	0.12	-50%	0.22	-54%

Additional outdoor tests were conducted under summer conditions between 23/06/2014 and 30/06/2014 and gave broadly similar results (see Appendix C.5). Outdoor monitoring under winter conditions was performed between 26/11/2013 and 04/12/2013 (see Appendix C.6). These results showed no early morning or evening enhancements. This is due to the short day lengths and the fact that the maximum AOI is ~50° away from normal incidence. In the indoor angular characterisation (Section 6.2.2) the enhancements were seen at AOIs of ~80°.

6.3 Effect of Corrugation Sidewall Angle on Module Performance

In the indoor characterisation and outdoor monitoring, module type B showed the best results, based on a non-optimised geometry. To provide insight into how curvature affects the performance parameters of the structured modules, further tests were undertaken using a set of curved substrates printed on a 3D printer. The substrates were based on parabolic profiles with different sidewall angles (from 15° to 80°) (see Section 4.5.4).

Figure 6.7 shows how the performance parameters change as a function of sidewall angle (Figure 4.18a). Effective PCE increases with increasing sidewall angle, so to obtain best performance a high sidewall angle is desired. In practice a high sidewall angle is likely to lead to delamination effects, so a trade off exists between best performance and long term stability. The effective J_{SC} increases with increasing sidewall angle but this is entirely due to reduced footprint. I_{SC} itself reduces with increasing sidewall angle due to higher reflection at higher angles of incidence. This leads to a reduced in-coupling of light but this is offset by the reduction in footprint leading to an increase in J_{SC}. V_{OC} reduces as the sidewall angle increases due to a reduced in-coupling of light. Finally FF increases very slightly with sidewall angle from 38% to 41%.

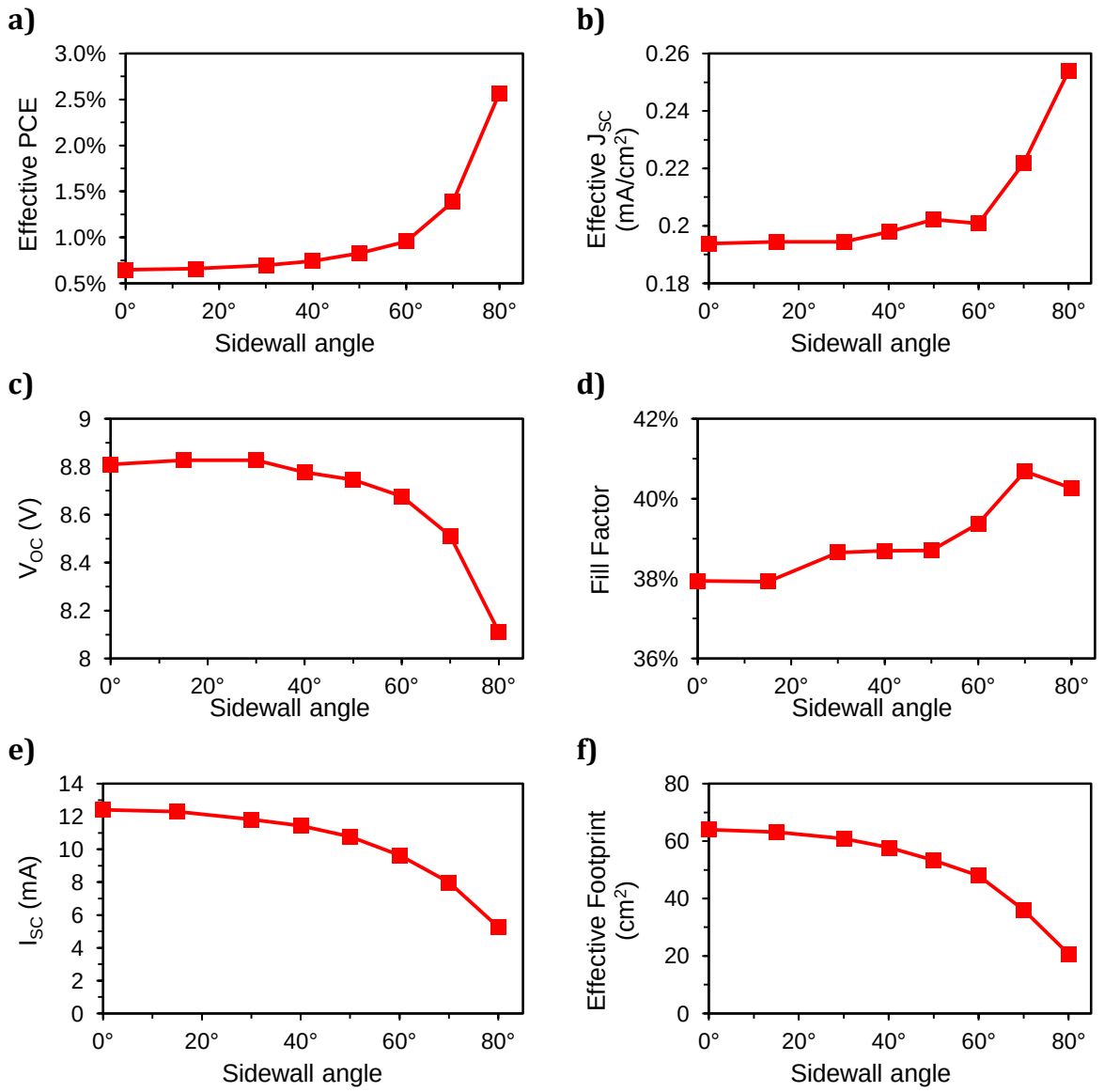

Figure 6.7: Effect of sidewall angle on performance parameters: a) effective PCE; b) effective J_{SC}; c)V_{OC}; d) Fill Factor; e) I_{SC}; and f) effective footprint.

6.4 Larger Module Tests on Corrugated Substrates

The tests in Section 6.2 focused on individual corrugated modules and showed that type B was the best performing geometry. The next set of tests looked at how a practical corrugated structure would work, with multiple corrugations causing shading at higher angles of incidence. The final set of outdoor measurements were conducted using multiple module strips (supplied by infinityPV, Denmark) [146]. Four strips were prepared, each 40 cm long and having four serially connected modules. Two strips were mounted flat and two were laminated to a large corrugated PVC substrate (Section 4.5.3). The strips were mounted onto the outdoor rack at Bangor, inclined at 35° and facing due south, and monitored for two months (from 29/09/2015 till 30/11/2015).

Figure 6.8 shows the diurnal performance of the strips under different irradiances (averaged for each type). Under sunny conditions the flat strips have a fairly constant efficiency throughout the day, whereas the corrugated strips have a parabolic profile that peaks at local noon and exceeds the flat modules between 10:00 and 14:00. Under diffuse conditions the corrugated strips outperform the flat strips throughout the day.

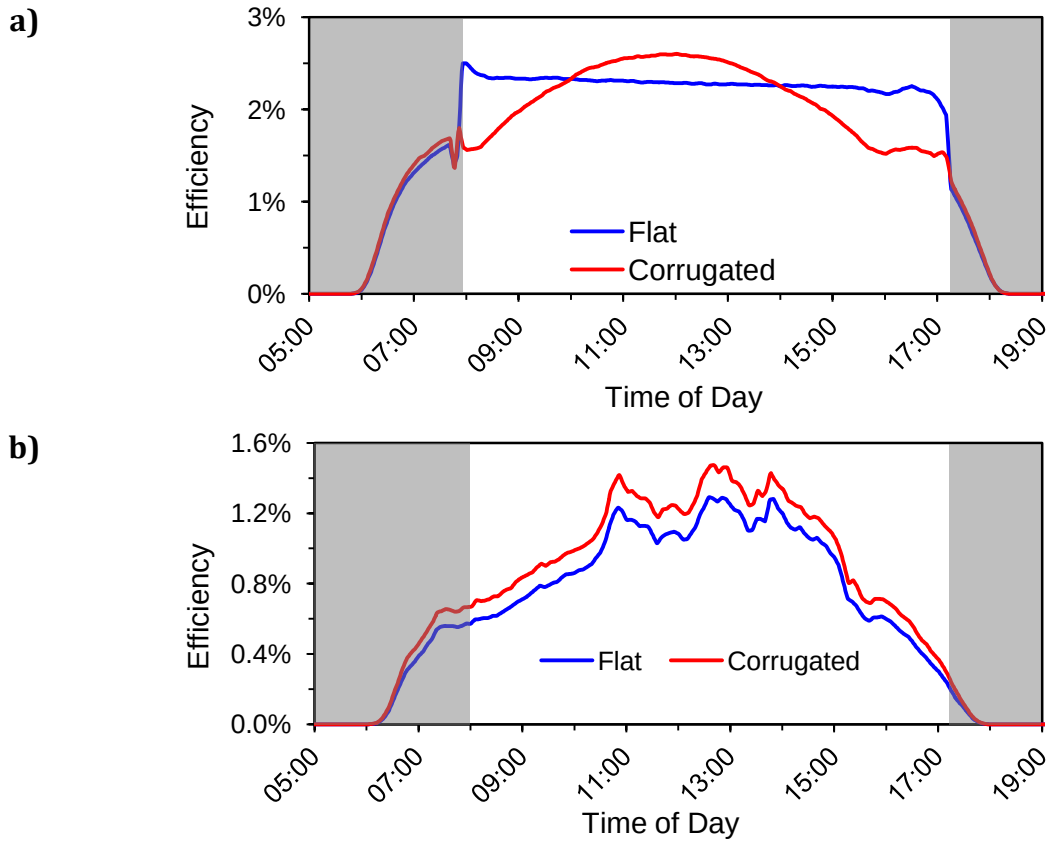

Figure 6.8: Diurnal performance of multiple module strips under different irradiance conditions: a) sunny (01/10/2015); b) diffuse (09/10/2015). The greyed out areas are when the module strips were subject to shading from the adjacent racks and roof structures.

Figure 6.9 shows the cumulative daily yield for the four module strips (averaged for each type); the corrugated strips outperformed the flat strips. Comparison of average daily yields under diffuse, intermediate and sunny conditions shows that under sunny conditions the corrugated strips perform 2.6% better than the flat strips (Table 6.7). Under diffuse conditions this rises to a gain of 14.8% for the corrugated strips and overall the average gain is 7.5%.

These results corroborate the earlier findings that corrugated modules perform better than flat modules, especially under cloudy conditions, but the benefits are not as

great as were seen with the individual modules on the larger corrugated substrate (types A & B), due to the shading of serially connected modules in the multiple module strips.

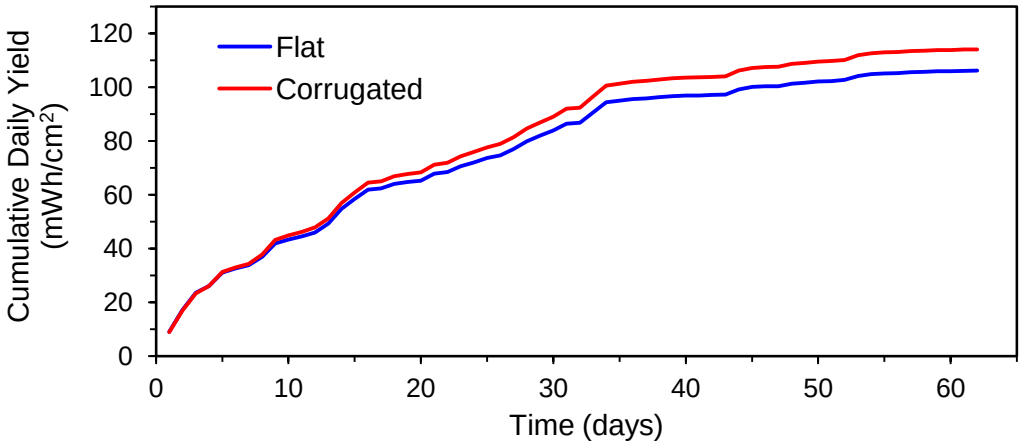

Figure 6.9: Average cumulative daily yield per active area for module strips.

Table 6.7: Analysis of daily yields for the multiple module strips under different irradiance conditions[7]. Gain is the percentage improvement shown by the corrugated (3D) strips when compared to the flat strips.

Strip Type	Sunny		Intermediate		Cloudy		Total	
	Average Daily Yield (mWh/cm²)	Gain (cf. Flat)	Average Daily Yield (mWh/cm²)	Gain (cf. Flat)	Average Daily Yield (mWh/cm²)	Gain (cf. Flat)	Average Daily Yield (mWh/cm²)	Gain (cf. Flat)
Flat	5.19	-	1.96	-	0.31	-	1.68	-
3D	5.33	2.6%	2.17	10.7%	0.35	14.8%	1.81	7.5%

6.5 Modelling of Optimal Geometry for 3D Profile

A series of simulations were run on PVsyst, a PV simulation, design and analysis package, to investigate various 3D configurations (Section 4.5.5) [273]. Multiple simulations were run for the configurations shown in Figure 6.10 with the sidewall angle (θ) varied between 0° and 45°. The relative annual yield for each configuration compared to the flat array is shown in Figure 6.11. This shows that configuration T (Inverted U) offers the largest increase in annual output per unit area (10% improvement at 35° sidewall angle) and that for the concave configurations the best performing configuration is P (No Infill), with over 4% gain at 45° sidewall angle.

[7] Irradiance ratings are based on daily irradiation figures by comparing measured irradiation against theoretical maximum GHI (based on Bird model[46]): Sunny: >80% of maximum GHI irradiation, Diffuse: <40% of maximum GHI irradiation, otherwise Intermediate.

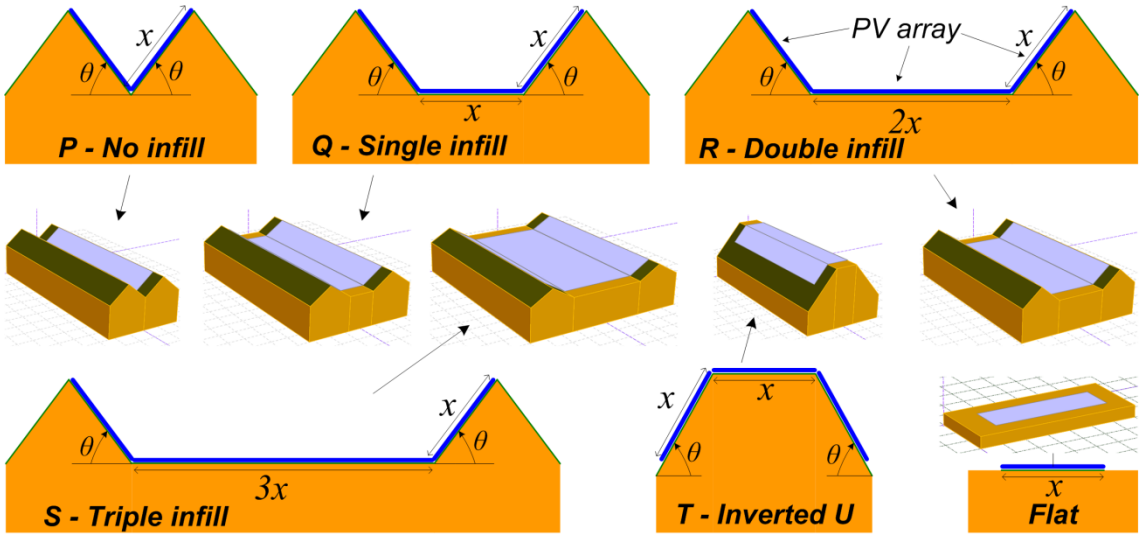

Figure 6.10: Various PV array configurations used for PVsyst simulations. Sidewall angle (θ) is varied for separate simulation runs.

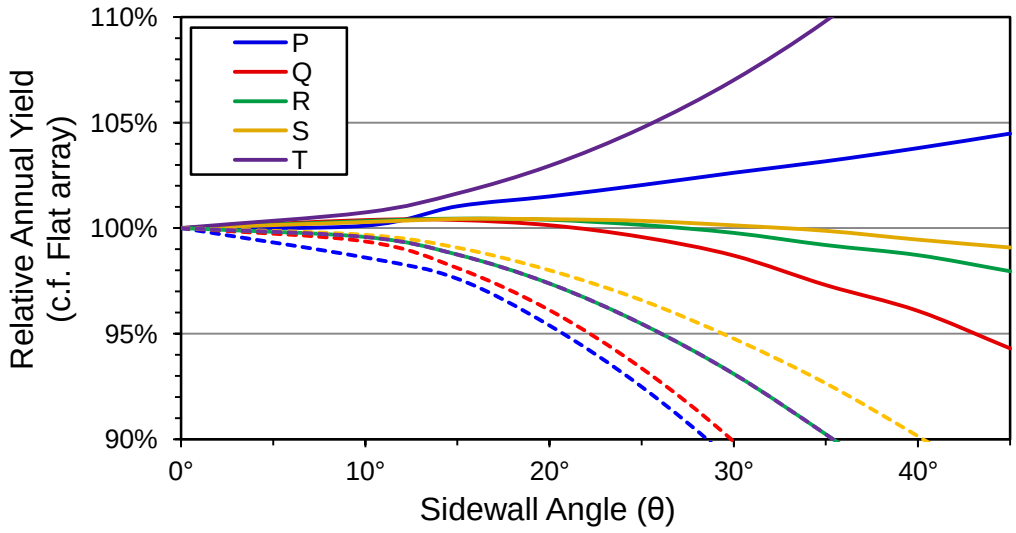

Figure 6.11: PVsyst simulation results: relative annual yield (c.f. horizontal flat array) The dashed lines are actual array output, whereas the solid lines show yield/unit area (adjusted for reducing footprint as the sidewall angle increases).

Figure 6.12 shows simulation diurnal efficiency results under different irradiance conditions, based on horizontal global irradiance and footprint area of the arrays. Configurations T and P, both with sidewall angles of 45°, show distinct efficiency improvements in the morning and evening for sunny conditions. Configuration T also shows higher efficiency throughout the day under cloudy conditions. This configuration shows the greatest geometric overlap to the 3D module type B from Section 6.2 and corroborates the experimental data from the outdoor monitoring.

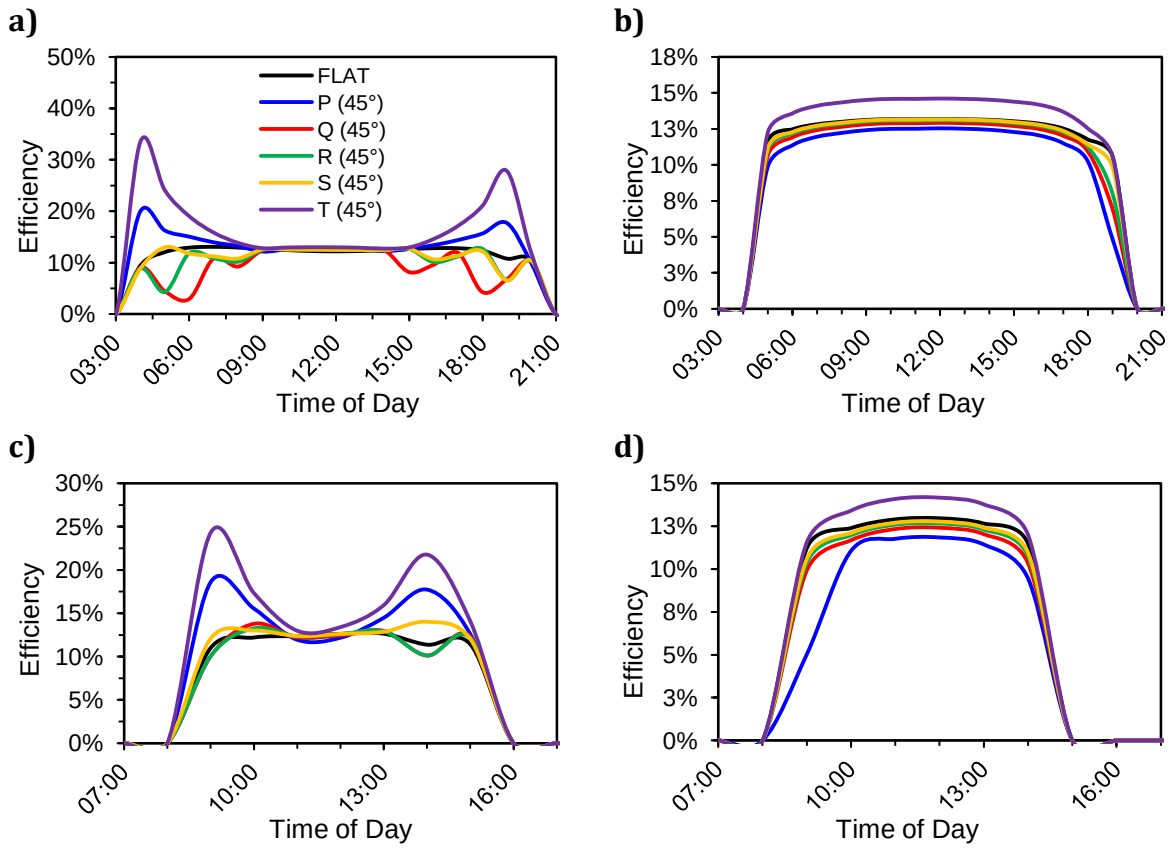

Figure 6.12: Simulation results for diurnal efficiency comparing different panel configurations: a) summer, sunny (24/06/1990); b) summer, cloudy (25/06/90); c) winter, sunny (15/12/90); and d) winter, cloudy (07/12/90).

6.6 Discussions on Improvements in Performance

The photocurrent generation characteristics under oblique angles for the flat modules are consistent with other reports [164], [166], [307]. At high angles of incidence, Fresnel reflection losses become significant as a result of the mismatch between the refractive indices of PET and air [189], [308]. As the AOI increases from 0° to 85° the reflection losses increase from 5% to 38% (at wavelength λ = 550 nm). This limits the in-coupling of light and subsequent photo-generation. When the modules are laminated onto corrugated substrates these reflection losses are reduced as a much higher proportion of light is at normal incidence to the active area of the module particularly under sunny conditions when there is a higher level of direct irradiation. The curved modules have the advantage that part of the surface will be close to normal incidence for much of the day, leading to high light absorption, whereas for the flat module this would only be true near midday. Before and after midday the absorbed irradiance on a flat surface will drop off by a function of the cosine of the AOI, leading to a corresponding drop in photo-generation (ignoring reflective and refractive losses at

oblique angles). In addition, when considering diffuse conditions where the radiation is equally distributed throughout the sky (isotropic model proposed by Liu and Jordan [309]), the 3D modules have the advantage over the flat module that a greater proportion of light will hit part of the active surface at or close to normal incidence.

Comparing the different designs on the larger corrugated substrate there is a difference between type A and type B modules under irradiation at moderately oblique angles. Figure 6.13b shows irradiation of the type B structure with some areas receiving light normal to the surface, some areas receiving light at high angles of incidence leading to light being lost by reflection and some areas being completely shaded. Once the angle of incidence exceeds the sidewall angle there will be some shading. Figure 6.13a shows how a type A structure has similar effects, but with the addition of some light being reflected back onto another part of the active area of the module. This in-coupling reflective effect was clearly seen during the LBIC tests (Section 6.2.3) with type A acting as a pseudo lens. As the angle of incidence increases beyond 45° the type A module will become increasingly shaded whereas one half of the type B module will remain fully illuminated, even as AOI reaches 90°. On a repeating corrugated structure this would only apply to the end corrugation nearest to the source of irradiance.

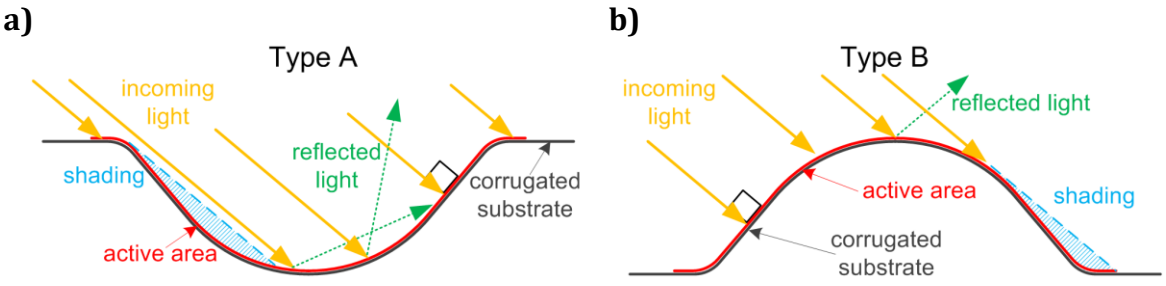

Figure 6.13: Irradiation of corrugated structures: a) type A; b) type B. Highlighted are areas where the irradiation is perpendicular (and current generation is at a maximum), irradiation is oblique (leading to reflection) and areas where there is shading (leading to zero current generation).

Figure 6.14 shows the effect of oblique angle irradiation on the two module designs on the smaller corrugated substrate. The cells in the DTU modules are connected in series with no bypass diodes, so the module current is limited to the current carrying capability of the worst performing cell. As a cell becomes increasingly shaded its current carrying capacity reduces until at 100% shading, even if other cells are fully illuminated, the module current reduces to zero as the shaded cell is reverse biased. The type D module has the cells aligned across the corrugations, so shading is

applied equally to portions of each cell as the angle of yaw increases away from normal. Therefore all of the cells maintain equal current generating/carrying potential and there is no mismatch between individual cells in the module (Figure 6.14b). This means that although the efficiency of the module will reduce as the AOI increases the efficiency will not approach zero until the AOI reaches 90°. In the type C module changes in yaw will cause some cells to become increasingly shaded, whilst others are still fully illuminated (Figure 6.14a). As the AOI approaches the sidewall angle deep shading occurs on certain cells, leading to a sharp drop in performance. As the AOI continues to increase, eventually a cell will become fully shaded and the performance of the module will reduce. The DTU modules are not particularly good diodes when in reverse bias (indicated by poor fill factor), so the current, although reduced, will not actually go to zero [145], [310].

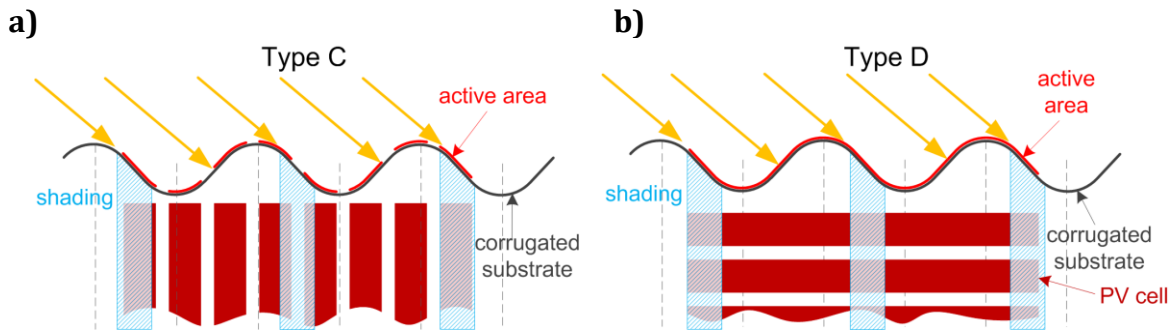

Figure 6.14: Comparison of effects of shading on multiple cell modules: a) type C vs. b) type D cell configurations. As the angle of incidence increases the shading on the type C configuration causes unequal shading, whereas for the type D configuration the shading affects all the cells within the module equally.

6.7 Summary

These experiments have looked at the performance of OPV modules laminated onto corrugated roofing. It has been shown that corrugated 3D modules provide three distinct advantages over flat OPV modules. The effective area of the module is reduced due to the curvature of the modules, which leads to an improved power output per unit area of roofing. There is substantial enhancement at high angles of incidence during the summer, leading to increased output during early morning and evening. Indoor characterisation showed enhancements of up to x15 for the corrugated module when compared against a flat module. There is improved performance under diffuse conditions, with the performance improvement (relative to the flat reference module)

for one corrugated module (type B) increasing from 11% under sunny conditions to 25% under cloudy conditions.

Comparison of the results from the modules on the smaller corrugations (types C and D) showed that the best performance occurred when the cell direction is across the corrugations (type D), so that shading is applied equally to each of the individual cells in a module thus avoiding mismatched performance between the cells in a module.

Outdoor measurements on larger module strips showed that the corrugated strips outperformed the flat strips by 7.5% with a 14.8% enhancement under diffuse conditions.

BIPV is seen as one of the areas where OPVs may be able to compete against mainstream PV technologies [25]–[27], [304]. This work highlights an area where the flexible and printable nature of OPVs could be used to its advantage. Geographically these advantages appear to suit countries at higher latitudes with a predominance of diffuse conditions. At higher latitudes there will be a large change in pitch between morning/evening and midday, which will allow maximum benefit from the early morning/evening enhancements that were seen. This is beneficial in countries with high penetrations of PV on the electricity network, so that the PV generation correlates better with electricity consumption and reduces the need for storage. The lifetime of best reported OPVs outdoors is approaching that of PVC corrugated roofing, which is typically guaranteed for 10 years, so they would be well matched [311]–[313]. Whilst this work has focused on laminating OPVs to standard corrugated substrates, PVC, being a mouldable thermoplastic, is an ideal material for optimising BIPV structures when used in conjunction with OPVs (either printed directly or laminated onto the substrate).

Chapter 7. Increasing Stability and Performance of OPVs using a Luminescent Downshifting Layer

In Chapter 6 the use of 3D structuring to improve outdoor performance of OPVs was investigated. This chapter examines an alternative strategy to optically enhance the performance of OPVs by the application of LDS layers. This can be achieved in two ways: improving performance under AM1.5G solar irradiation and extending operational lifetime. For the former, the range of wavelengths where light can be harvested is extended leading to a performance increase. For the latter, a UV filter is often employed to prevent extrinsic degradation of the active layers caused by photo-oxidation, but this also prevents any UV light propagation. This UV filter can be replaced by an LDS layer which not only prevents UV light from reaching the active layers of the solar cell but also down shifts the UV light into the visible region where it can be absorbed and used to generate a photocurrent.

7.1 Introduction

This work was completed in two stages. Initial studies were made in the laboratory of two discrete dyes in collaboration with a post-doctorate researcher (Dr. Omar Moudam). These were followed by outdoor stability studies using larger modules (supplied by DTU) at Bangor and then in collaboration with Ben Gurion University in Israel at their outdoor test facility in the Negev Desert.

Based upon the success of the first stage, a second phase of work was undertaken which investigated a wider range of LDS dyes with more detailed analysis. The aim was to identify single dyes and multiple-dye blends that would improve on the earlier work. This work was performed with the help of Ricardo Fernandes, an exchange student from Londrina State University, Brazil.

7.2 Single Dye LDS Layers for OPVs

7.2.1 Effect of LDS on OPV Performance and Stability

Two dyes were selected for this initial study: an organic-metal complex of europium ($Eu(dbm)_3(phen)$) (hereinafter referred to as Europium Complex) and an organic naphthalimide dye, Kremer Blue (see Section 3.3.4 for full details). They were selected as they have high absorption over the UV region (300-400 nm), where P3HT:$PC_{61}BM$ has lower EQE response and is prone to degradation due to photo-oxidation activated by UV.

The dyes were each dissolved with PMMA powder in anisole (20 mg/ml of PMMA/anisole) at a variety of concentrations between 2% and 15% by weight (LDS:PMMA). Single cell, normal geometry OPV cells were prepared using P3HT:$PC_{61}BM$ as the active layer. The LDS blends were doctor bladed onto the glass front surface of the cells at thicknesses of ~3 μm. Electrical characterisations were carried out on the cells, both before and after LDS coating.

Table 7.1 and Figure 7.1 show electrical characterisation results at various concentrations of Europium Complex in PMMA. At the higher concentrations (≥5%) there is a reduction in performance, but at 2% there is a moderate improvement, with relative PCE increasing by 8.4% and J_{SC} by 5.1%. The EQE curves show a filtering effect at wavelengths below 400nm for all concentrations and an enhancement for 2% concentration at wavelengths between 550 and 650 nm.

Table 7.1: Performance of small OPV devices (coated with various concentrations of Europium Complex), measured under AM1.5G irradiance.

Sample	PCE (%)	J_{SC} (mA/cm²)	V_{OC} (V)	FF	Relative PCE change	Relative J_{SC} change
Control	2.79	10.01	0.598	0.466	-	-
2% Eu:PMMA	3.04	10.54	0.604	0.475	+8.4%	+5.1%
5% Eu:PMMA	2.82	9.84	0.607	0.472	+1.1%	-1.7%
8% Eu:PMMA	2.31	8.24	0.604	0.464	-16.8%	-16.7%

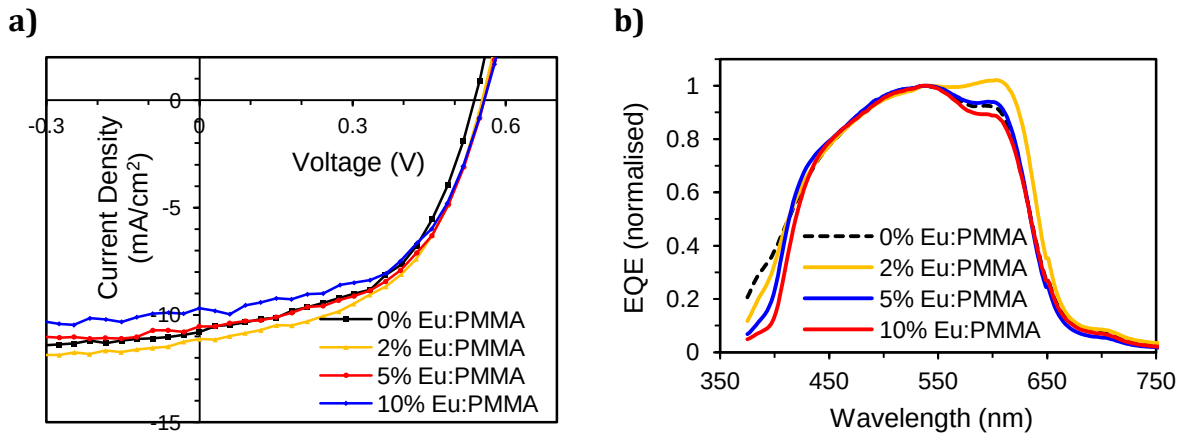

Figure 7.1: Electrical characterisation of OPV devices (coated with various concentrations of Europium Complex): a) current density vs. voltage under AM1.5G; b) normalised EQE.

The effectiveness of LDS layers for protecting OPV devices against photo-degradation was tested by indoor light soaking under AM1.5G (ISOS-L-1 protocol [119]). Tests were carried out for 550 hours on non-encapsulated devices with and without LDS coatings (Europium Complex and Kremer Blue dye, both at 2% concentration in PMMA) and the results are shown in Figure 7.2.

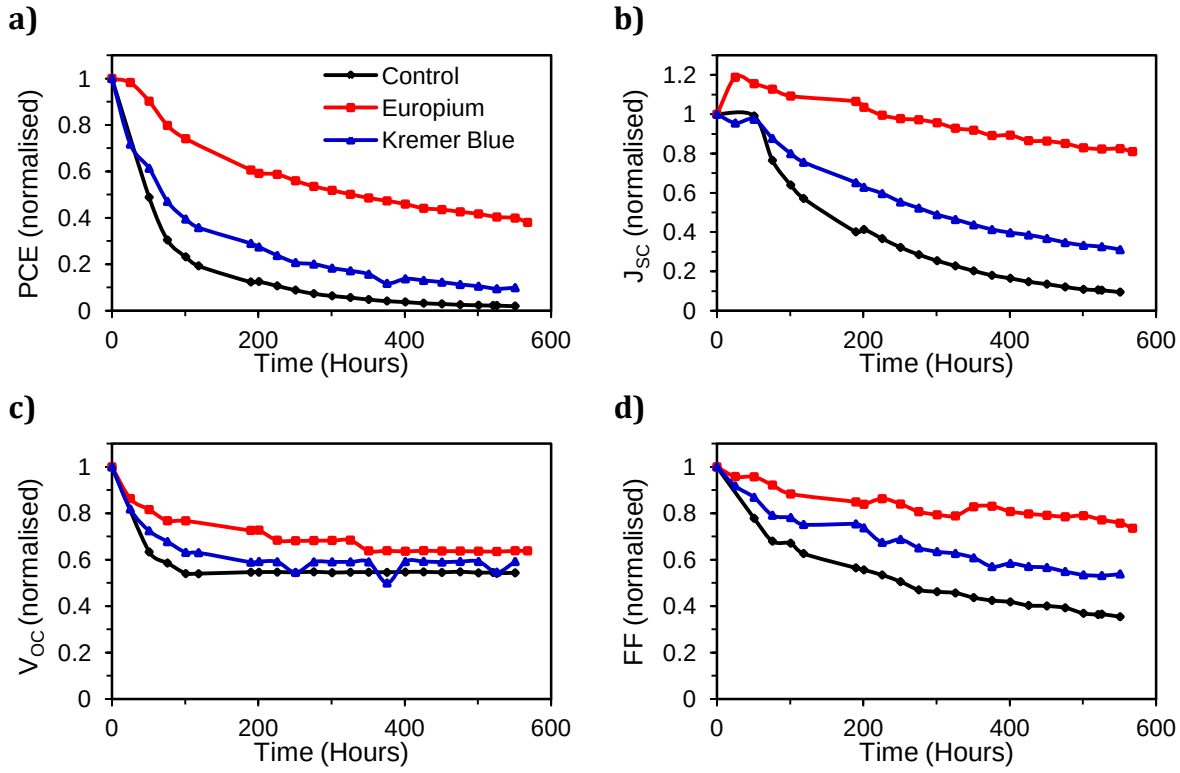

Figure 7.2: Indoor lifetime testing under AM1.5G of three OPV cells (P3HT:$PC_{61}BM$): one control, one with Europium and one with Kremer Blue. a) PCE; b) J_{SC}; c) V_{OC}; and d) FF.

All of the devices showed rapid deterioration, consistent with their lack of encapsulation, exhibiting exponential decay of their key performance parameters [67], [312]. The control device shows a rapid decrease in V_{OC} initially ($\Delta V_{OC} \approx$ -0.27 V) before the rate of degradation reduces. This trend is consistent with severe photo-oxidation of the active layer [314]. This reduction in V_{OC} is smaller in the LDS devices, due to the UV filtering effect. Both of the LDS dyes have improved the lifetime of the cells with Europium Complex outperforming Kremer Blue. All of the performance parameters are improved, especially J_{SC} and FF, leading to the improvement in PCE. Assessment of the degradation parameters (T_{50}) gives a measure of the long term stability of the devices. Europium Complex (T_{50} = 328 hours) has a greater than 6x advantage over the control device (T_{50} = 50 hours). Kremer Blue (T_{50} = 70 hours) is only marginally better than the control device.

7.2.2 Outdoor Stability Tests at Bangor University

Based on the success of the indoor stability test, outdoor stability tests were conducted at Bangor University, using Kremer Blue as the LDS material and DTU(AgGrid) modules. The LDS layers were printed by the Welsh Centre for Printing and Coating (WCPC) in Swansea (Section 4.6.1). Kremer Blue was used because WCPC had already formulated the Kremer Blue ink and the Europium Complex ink was more challenging to prepare, although it would have been preferable. It is important to note that work had to proceed quickly at this stage, as the outdoor tests needed to be conducted during summer, when light levels are at their highest and therefore for these trials Europium Complex was ignored.

Three modules were prepared for outdoor testing (Section 4.6.2):

A. **Control:** PMMA (with no LDS) printed onto PET and laminated onto the module using PDMS.

B. **LDS (on PET):** LDS printed onto PET and laminated onto the module using PDMS.

C. **LDS (printed):** LDS printed directly onto the module. The contacts were removed first to allow the module to pass through the printer and re-attached after printing was complete.

The modules were tested outdoors on the inclined OPV rack from 01/07/2014 till 09/09/2014. Figure 7.3 shows how the performance parameters changed over the

duration of the test. The data is a daily average for each parameter, where the data is only selected when the in-plane irradiance is 600±15 W/m². This ensures that only data from sunny days is included (excluding diffuse measurements) and that all measurements are when the sun is close to normal incidence (near midday) and the spectrum closely approximates AM1.5G. The figures have been normalised to their initial values. All the modules exhibited an exponential decay to their PCE with a fast rate of degradation initially, followed by a reduction in the rate of degradation.

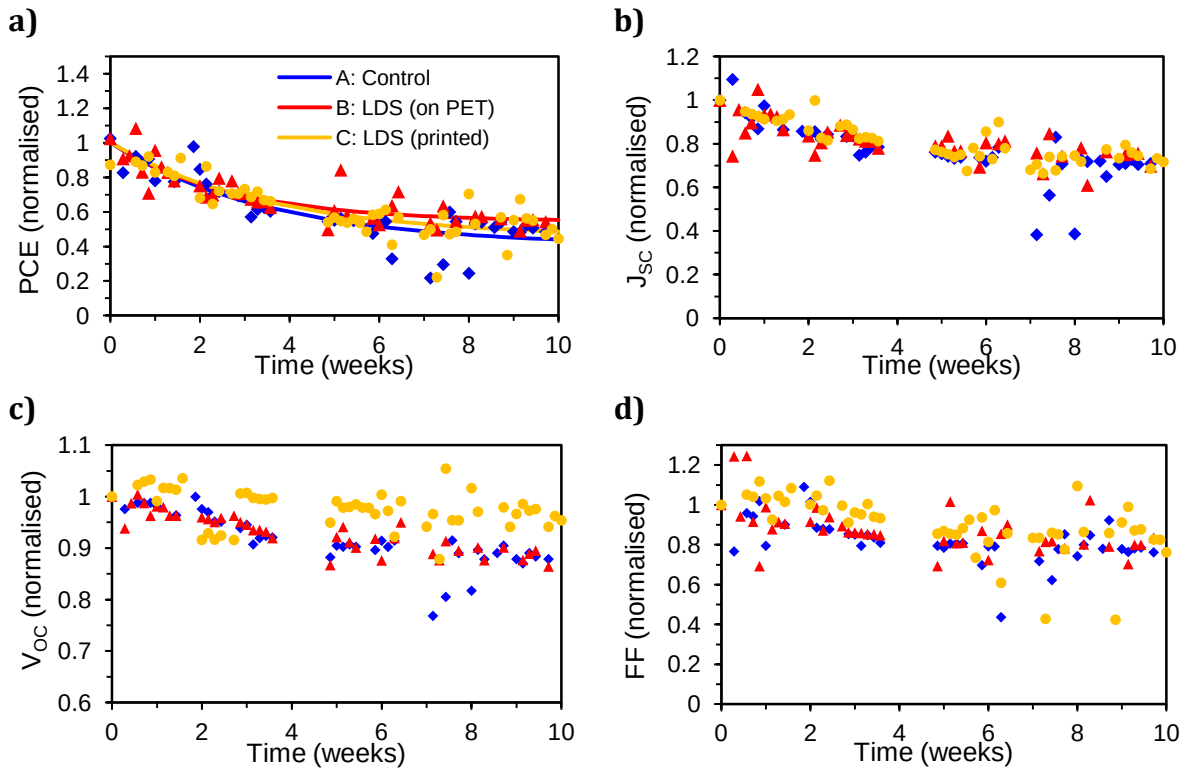

Figure 7.3: Outdoor stability tests at Bangor University: a) PCE; b) J_{SC}; c) V_{OC}; and d) FF (all normalised). The graphs were based on daily averages where the irradiance was 600±15 W/m². The data is normalised to initial values.

Table 7.2 shows the T_{80} and T_{50} lifetimes, as well as the final normalised PCE. Module A reaches T_{80} in 10 days, followed by module C (11 days) and finally module B (12 days). Only two of the modules drop to 50% of their initial performance over the 10 week testing period so, rather than use T_{50}, a better comparison is to compare their final relative efficiencies: the best performing module is module B which has dropped to 55%, whereas the worst performing module is module A which has dropped to 40%. Module B is in between at 45%. Most of this drop in PCE is due to a reduction in J_{SC}, with both V_{OC} and FF only dropping slightly over the ten weeks of measurements. Module C showed a slight improvement in V_{OC} and FF in the first week, before a gradual

degradation. Based upon this data, it is clear that the application of Kremer Blue has provided a moderate improvement to the stability of these modules under outdoor conditions.

Table 7.2: T_{80} and T_{50} lifetimes and final normalised PCEs from stability tests at Bangor University.

Sample	T_{80} Lifetime	T_{50} Lifetime	Normalised final PCE (after 10 weeks)
A: Control	10 days	46 days	40%
B: LDS (on PET)	12 days	-	55%
C: LDS (printed)	11 days	62 days	45%

7.2.3 Outdoor Stability Tests at Ben Gurion University, Israel

After the promising results from the outdoor tests at Bangor, which were conducted during the late summer, collaboration was sought with Professor Frederic Krebs at DTU and Professor Eugene Katz at Ben Gurion University, Israel. This allowed a larger number of modules to be tested at Sede Boker in Israel, under much higher UV levels than were experienced at Bangor. WCPC supplied separate PET sheets printed with: Europium Complex; Kremer Blue; and plain PMMA with no LDS for use as control samples (see Section 4.6.1).

New modules were characterised at DTU (IV under AM1.5G), before being sent to Bangor where they were prepared for outdoor testing with two different LDS dyes (see Section 4.6.3). Five different configurations were fabricated (all modules were encapsulated in PDMS on a glass backing sheet); four modules of each type to provide better statistical evidence of stability enhancements:

A. **Reference:** uncoated module.

B. **Europium Complex:** LDS (Europium complex) printed on PET and laminated onto a module.

C. **Kremer Blue:** LDS (Kremer Blue) printed on PET and laminated onto a module.

D. **PMMA Only:** PMMA (with no LDS) printed on PET and laminated onto a module.

E. **UV Filter:** a commercial self-adhesive UV filter (Solaronix SA #49132) was applied to the DTU module.

Once fabricated they were sent to DTU for further characterisation, before being shipped to Israel for outdoor testing. The outdoor testing was performed at Jacob Blaustein Institutes for Desert Research, at Sede Boker in the Negev Desert (Lat: 30.8°N, Long: 34.8°E, Alt: 475 m). On a cloudless day the spectrum at Sede Boker at noon ±2 hours closely matches AM1.5G, providing a vigorous test of LDS layers under UV light [128]. The modules were mounted on a rack inclined at 30°, facing south and with an in-plane thermopile pyranometer. IV measurements were taken once an hour (from 10am till 3pm) along with in-plane irradiance and module temperature in accordance with ISOS-O-2 test protocols. The modules were kept outside throughout the 80 day measurement period. Data analysis was performed by the author at Bangor.

A comparison of the IV measurements before and after processing and encapsulation is shown in Table 7.3. Values for each of the performance parameters have been averaged across the four modules of each type and the values shown are after processing.

Table 7.3: Performance parameters for the modules used for lifetime testing: Europium Complex, Kremer Blue, PMMA Only, UV Filter & Reference modules. Values are averaged across all modules of each type after lamination and encapsulation. Relative changes are based on each individual module's measurements before and after lamination and encapsulation.

Sample Active Area: 30 cm^2	PCE (%)	J_{SC} (mA/cm^2)	V_{OC} (V)	FF	Relative PCE change	Relative J_{SC} change
Reference	2.40 ±0.04	0.456 ±0.016	12.1 ±0.2	0.43 ±0.01	-1.79%	3.41%
Europium Complex	2.44 ±0.05	0.488 ±0.043	11.7 ±0.3	0.43 ±0.02	0.14%	4.04%
Kremer Blue	2.07 ±0.17	0.414 ±0.017	11.7 ±0.1	0.43 ±0.01	-16.01%	-9.53%
PMMA Only	2.38 ±0.12	0.480 ±0.009	11.7 ±0.0	0.42 ±0.03	-2.29%	1.17%
UV Filter	1.97 ±0.02	0.353 ±0.002	11.9 ±0.2	0.47 ±0.01	-18.87%	-18.19%

The changes in PCE and J_{SC} were obtained by comparing the relative changes experienced by each individual module and then calculating the average. The reference modules and the modules treated with plain PMMA both show a slight drop in PCE and a slight rise in J_{SC}. The modules treated with Europium Complex show a very slight increase in PCE (0.14%) and the highest increase in J_{SC} (4.04%). The Kremer Blue modules show quite a large relative drop in both PCE (-16%) and I_{SC} (-9.5%). The

modules treated with the UV filter show the largest drops, -19% in PCE and -18% in J_{SC}, due to the filtering of all light below 400 nm. Figure 7.4 shows the transmittance spectra for Quartz, PDMS, PET, PMMA and the UV filter, highlighting the different performance over the UV region.

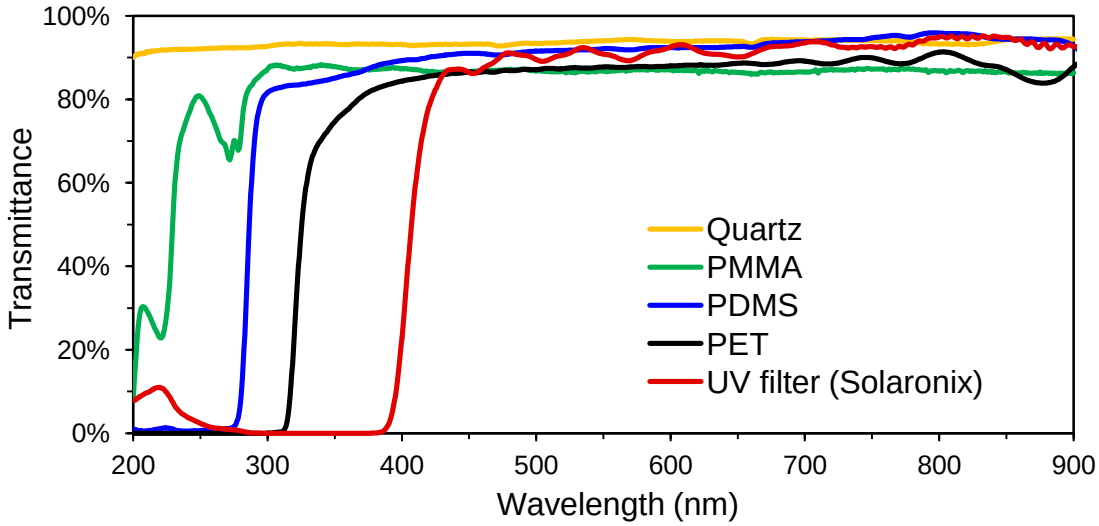

Figure 7.4: Transmittance spectra for Quartz, PMMA, PET, PDMS and UV Filter. The UV filter has a sharp cut off at 400nm, the PET is transmitting down to ~325nm, the PDMS is transmitting all the way down to ~280nm and the PMMA starts to drop off at 300nm, before cutting off at ~240nm. The quartz has greater than 90% transmission across the whole of the UV and visible spectrum.

Figure 7.5 shows the results from the lifetime testing at Ben Gurion University. These values were obtained by taking the measurements at maximum efficiency each day. In order to compensate for changes in irradiance and module temperature the values for J_{SC} and V_{OC} are adjusted to a standard irradiance of 1000 W/m^2 and temperature of 25°C. J_{SC} is adjusted by assuming a linear increase in J_{SC} with light intensity [153]. V_{OC} is adjusted to 25°C, assuming a linear decrease in V_{OC} with increasing temperature [151]. The temperature compensation factor was calculated from V_{OC} and module temperature values extracted from the first four weeks' worth of data (before any significant decrease in V_{OC} had occurred) where irradiance was 900±25 W/m^2 and produced a value of -0.022±0.003 V/°C. The values for each parameter were then normalised to their initial value. All of the modules show a non exponential decline in PCE, J_{SC} and FF over the course of the test, whereas V_{OC} remains constant for the first 50 days, after which it starts to decrease.

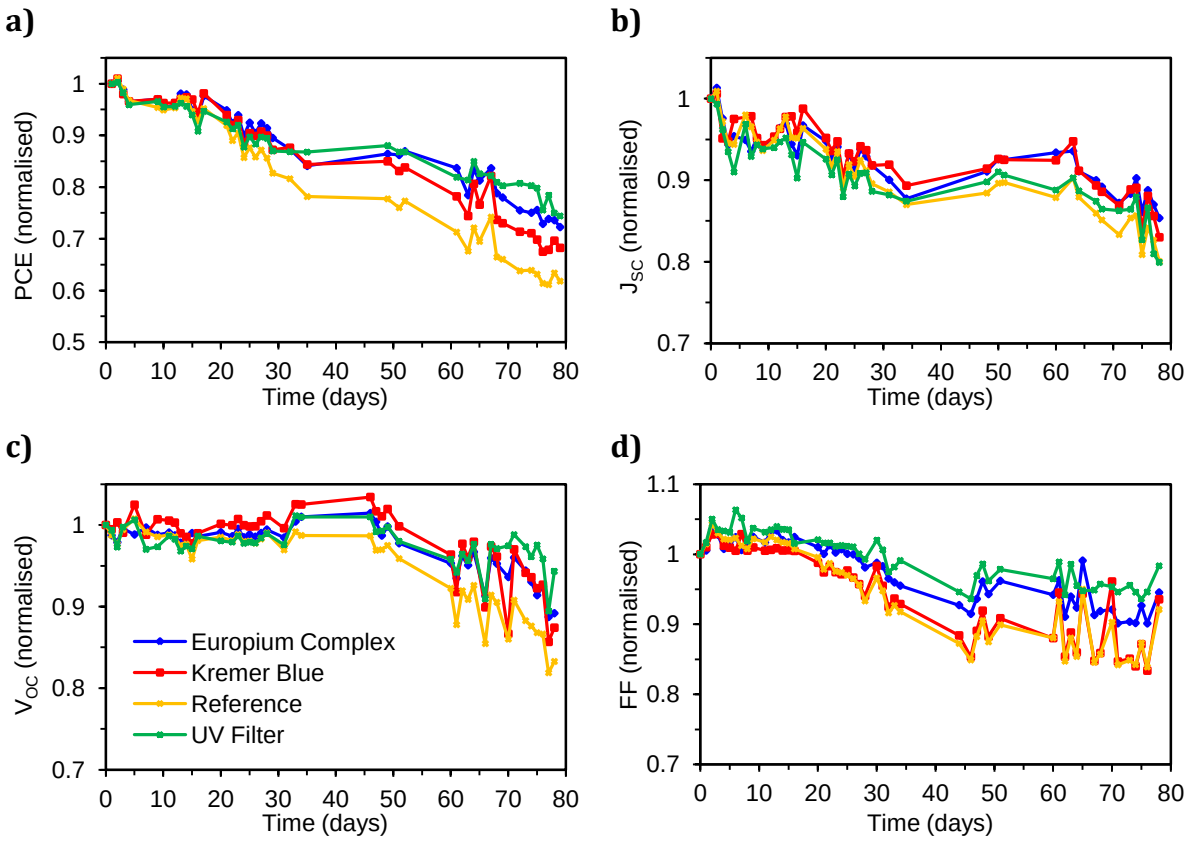

Figure 7.5: Outdoor lifetime results from testing in the Negev Desert (Ben Gurion University): a) PCE; b) J_{SC}; c) V_{OC}; and d) FF. Performance parameters were averaged across data from all modules of each type.

These results show that the modules without any UV filters (Reference modules) showed the biggest decrease in performance, with the worst performing module dropping to below 50% by the end of the test. In comparison the modules with the UV filter and the Europium Complex showed the least decrease in performance, with the best performing module only dropping to 78% of its initial value after 80 days.

Table 7.4 shows the average T_{80} lifetimes and average normalised PCE after 80 days. Average T_{80} for the Reference modules was just 34 days, which is less than half that for the modules with the UV filter (T_{80} = 75 days). The average T_{80} lifetimes for the modules with LDS coatings were 53 days for the Kremer Blue and 63 days for Europium Complex.

Table 7.4: Average T_{80} lifetimes and final normalised PCEs from stability testing in Negev Desert (Ben Gurion University).

Sample	Average T_{80} Lifetime	Average Normalised Final PCE (at 80 days)
Reference	34 days	62%
Europium Complex	63 days	72%
Kremer Blue	53 days	68%
UV Filter	75 days	74%

The different degradation rates in PCE are driven by changes in FF, with the Reference modules having the biggest drop in FF. Degradation in FF is largely driven by: decreases in shunt resistance due to the presence of shorts and shunts, which are often linked to imperfections introduced in production; increases in series resistance, which are caused by degradation of the active layer, interfaces and electrodes[93].

These results show that having a UV filter reduces degradation rates. However, it is important to note that modules with Europium Complex have a PCE advantage over the modules with the UV filter; application of the UV filter led to a relative drop in PCE of 18%, whereas no significant change was observed with the modules with Europium Complex.

7.3 Alternative Dyes for LDS Layers for OPVs

Having proved the viability of LDS layers in improving the lifetime and performance of OPV solar cells, further research was undertaken by considering a wider range of LDS materials. The aim was to better understand the optical characteristics to enable the selection of dyes for blending. Electrical performance testing was undertaken using IV and EQE characterisation, as well as indoor lifetime testing under solar simulator. Due to time constraints it was not possible to undergo long term outdoor tests.

Thirteen different dyes were selected; all of them either organic or organo-metallic complexes (Section 3.3.4). Quantum Dots were not examined as they have a history of low PLQY, high radiative overlap and are expensive [219].

7.3.1 Optical Characterisation

All thirteen LDS materials were initially prepared at a concentration of 8 mg/ml with MicroChem A8 solution (8% by weight PMMA in anisole) and then spin coated onto quartz substrates at 2000 rpm for 60 seconds to give a film thickness of 830 nm. Figure

7.4 shows the transmittance spectra for the quartz substrates. Two of the dyes (Kremer blue and Lumogen red) were also prepared at 16 mg/ml, in order to check the effect of changes in concentration. Each substrate was tested for absorption (referenced to a quartz sample spin coated with a film of pure PMMA), photoluminescence (PL) (excitation wavelength was set at the wavelength of maximum absorption for each material) and PLQY. The optical characterisation results are shown in Figure 7.6, Figure 7.7 and Figure 7.8.

Based on the optical characterisation results (Figure 7.6) and their toxicity, ease of use in fabrication being an important issue, the following materials were excluded from further testing:

Disperse Blue 3: absorption was at the wrong range of wavelengths (500-700 nm); this is where the PL emission would ideally be to match P3HT:$PC_{61}BM$. It also had no measurable PL (a low excitation wavelength was tried in order to see if there could be any useful downshifting effect).

Alizarin: this had very low absorption across most of the AM1.5G spectrum and very low PL. The majority of the PL that was observed appeared to be re-emission at similar wavelengths to the excitation wavelength, along with some re-emission at very long wavelengths.

Rhodamine B: although this had a usable PL peak (550-600 nm) the absorption levels were relatively high across the entire spectrum. Microscopy showed that the material had not dissolved in the anisole.

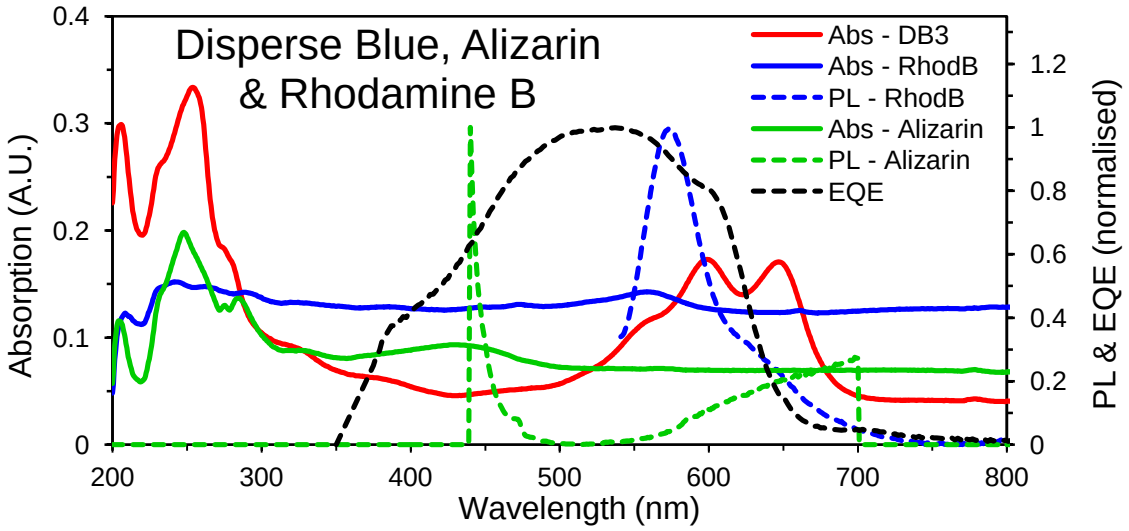

Figure 7.6: Optical characterisation results (absorption and photo-luminescence) for Disperse Blue 3 (DB3), Alizarin and Rhodamine B (RhodB) (all at 8mg/ml). The EQE curve is for P3HT:PC61BM.

7.3.2 Comparison of LDS Materials using Figures of Merit

In order to analyse and compare the different LDS materials a number of figures of merit have been used (Section 3.3.6): radiative overlap (RO); UV coverage (UVC); photoluminescent quantum yield (PLQY); absorption spectral matching (ASM); parasitic absorption (PA); and emission spectral matching (ESM). To improve upon the usefulness of these figures of merit the author has derived a weighted sum, *WS*, which was used to quickly assess and compare the relative figures of merit for a range of LDS materials:

$$\boldsymbol{WS} = \begin{bmatrix} \boldsymbol{W_{RO}}(\boldsymbol{1}-\boldsymbol{RO}) + \boldsymbol{W_{UV}UV} + \boldsymbol{W_{PLQY}PLQY} \\ +\boldsymbol{W_{ESM}ESM} + \boldsymbol{W_{PA}}(\boldsymbol{1}-\boldsymbol{PA}) + \boldsymbol{W_{ASM}ASM} \end{bmatrix} \boldsymbol{/6} \qquad 7.1$$

The weighting parameters used were: W_{RO}=1, W_{UV}=3, W_{PLQY}=2, W_{ASM}=2, W_{PA}=3, W_{ESM}=1. The most important factors were considered to be UV coverage and parasitic absorption, and the least important were radiative overlap and emission spectral matching. Tests are expected to use LDS films with fairly high absorption (in order to provide the UV filtering that is required) and it is important to allow the solar cell to make the best use of the incident irradiation. These weighting parameters are subjective and the weighted sum should be seen as qualitative rather than quantitative.

Table 7.5 shows the figures of merit and Figure 7.7 and Figure 7.8 have the optical characterisation results for the following discrete LDS dyes.

Coumarin Dyes: These both show good results with Coumarin 7 having the better PLQY and Coumarin 153 having the better values for UV coverage and parasitic absorption. Coumarin 153 had the highest weighted sum of all the dyes (95.7%). Coumarin 153 has an absorption profile that better matches P3HT:$PC_{61}BM$.

Kremer Dyes: These three dyes naturally split into two groups: the blue dye (naphthalimide) has high UV coverage and a PL emission in the 400-500nm region, whereas the orange and green dyes (perylenes) both have similar absorption profiles over the 400-500 nm range and very similar PL emissions (500-700 nm, peaking at about 560 nm). However Kremer Green has absorption across the whole spectrum and this gives it poor radiative overlap and parasitic absorption levels, whereas Kremer Orange has higher absorption than Kremer Green over the 400-500 nm range but lower absorption at higher wavelengths. Kremer Orange has the best PLQY (it has the highest PLQY of all the samples). Of these three dyes Kremer Blue has the highest weighted sum.

Lumogen Dyes: Neither of these dyes shows very good results for use as UV filters for OPVs. Both of the dyes have high parasitic absorption and the orange dye has very high radiative overlap. The red dye has very low UV coverage and low emission spectral matching. They had the two lowest weighted sums of all the dyes.

AlQ_3: Although AlQ_3 has low absorption, it has moderate PLQY and very good emission spectral matching, along with very low parasitic absorption.

Europium Complex: This dye has very good UV coverage and no radiative overlap or parasitic absorption. Although it has relatively low emission spectral matching, its sharply defined emission peak is at wavelengths which match the EQE of P3HT:PC_{61}BM.

DCM: Although DCM has very good UV coverage it has very poor figures for parasitic absorption, emission spectral matching and PLQY, which lead to a low weighted sum.

Table 7.5: Figures of Merit for discrete LDS materials with reference to P3HT:PC_{61}BM as the OPV active material[8].

LDS Material	RO	UVC	PLQY	ASM	PA	ESM	Weighted Sum
Coumarin 7	3.4%	15.7%	16.0%	8.6%	14.0%	88.0%	89.8%
Coumarin 153	2.6%	27.5%	8.4%	6.1%	6.9%	86.4%	95.7%
Kremer blue	5.4%	33.0%	5.7%	5.5%	5.4%	68.9%	94.8%
Kremer green	16.9%	30.2%	11.3%	20.0%	24.3%	72.0%	89.2%
Kremer orange	4.9%	13.5%	22.3%	9.7%	19.8%	73.7%	85.7%
Lumogen red	8.6%	9.9%	5.8%	10.4%	28.3%	39.8%	68.1%
Lumogen orange	29.7%	27.0%	8.7%	22.0%	34.3%	63.8%	78.9%
AlQ_3	0.1%	7.4%	12.5%	0.9%	0.7%	84.1%	88.5%
Europium Complex	0.1%	30.5%	6.3%	2.5%	0.8%	59.9%	94.4%
DCM	1.4%	54.8%	1.6%	22.0%	47.2%	37.9%	84.4%

[8] Figures of Merit: RO=Radiative Overlap; UVC=UV Coverage; PLQY=Photoluminescent Quantum Yield; ASM=Absorption Spectral Matching; PA=Parasitic Absorption; ESM=Emission Spectral Matching.

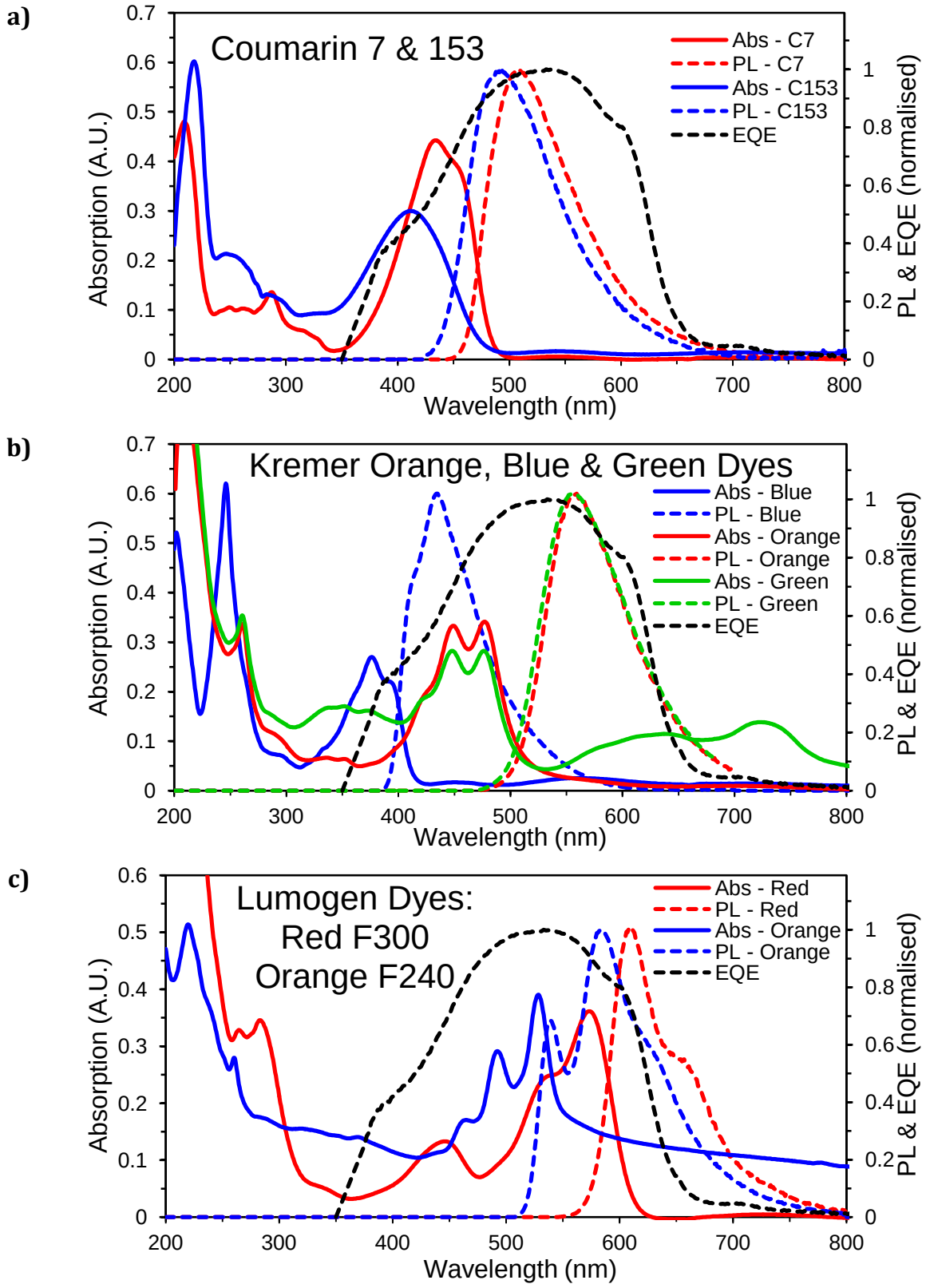

Figure 7.7: Optical characterisation results (absorption and photo-luminescence): a) Coumarin7 and Coumarin153; b) Kremer orange, blue and green dyes; and c) Lumogen red and orange dyes. All at a concentration of 8mg/ml. All of these are organic dyes. EQE curve is for P3HT:$PC_{61}BM$.

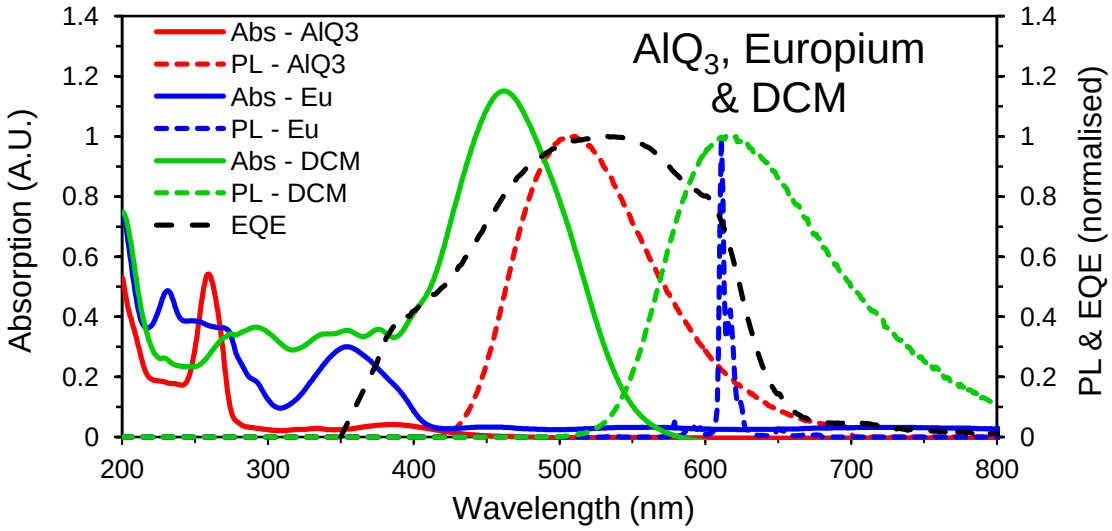

Figure 7.8: Optical characterisation results (absorption and photo-luminescence) for AlQ_3, DCM and Europium complex. AlQ_3 and Europium complex are organo-metallic dyes and DCM is an organic dye. All at a concentration of 8mg/ml. EQE curve is for P3HT:PC61BM.

7.3.3 Effect of LDS Concentration.

To compliment the PLQY measurements shown in Table 7.5, different concentrations of selected dyes were examined to see the effect of LDS concentration on PLQY (see Table D.1 in Appendix D.1). These showed that PLQY decreases as the LDS concentration increases. Therefore a set of blends of Kremer Orange in MicroChem A8 were prepared at different LDS concentrations (from 0.3 to 15 mg/ml). These were spin coated onto quartz substrates and optically characterised in order to see the effect that LDS concentration has on absorption, photoluminescence and PLQY. The results are shown in Figure 7.9.

Figure 7.9a shows how absorbance increases linearly relative to the LDS concentration. The PL measurements in Figure 7.9b all show a similar shaped curve but the peak emission is red-shifted as the concentration increases. The peak PL at the lower concentrations is at wavelengths approaching maximum EQE (for P3HT:PC_{61}BM), so increasing the concentration leads to a shift away from the EQE peak. Figure 7.9c shows how PLQY responds to changes in LDS concentration, with an exponential increase in PLQY as concentration reduces. The inset graph shows PLQY vs. [LDS concentration]$^{-1}$ plotted on a log scale and shows a linear dependence. These results show that lower concentrations exhibit better properties; the PL peak overlaps the EQE maximum for P3HT:PC_{61}BM and PLQY is at its highest. However these benefits must be balanced by the reduction in absorption as the concentration reduces which leads to fewer photons

being absorbed, leading to less UV filtering. As concentration increases it leads to lower PLQY caused by quenching, and a red-shift in the PL peak caused by radiative reabsorption (which only occurs where there is an overlap between absorption and emission spectra) [315].

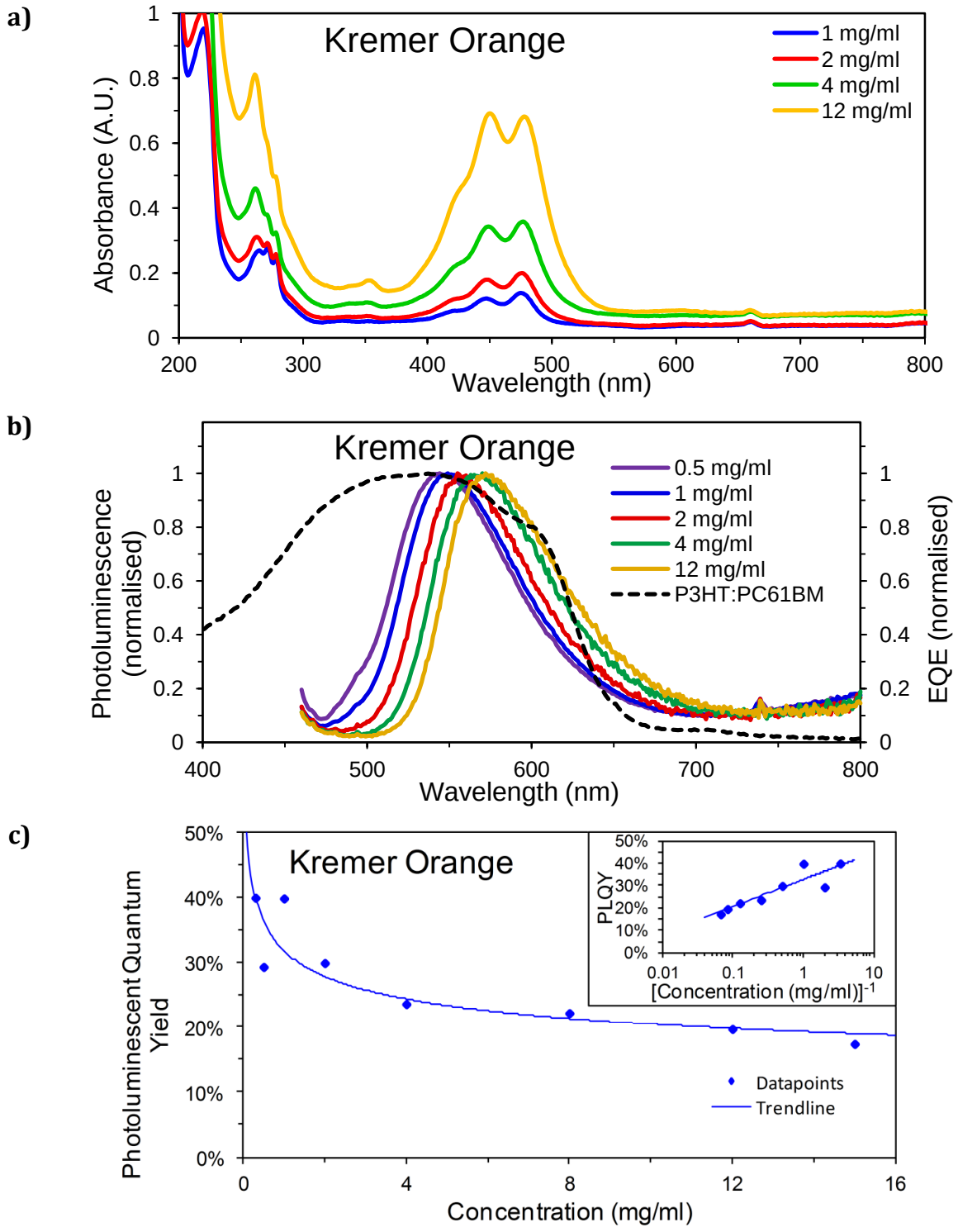

Figure 7.9: Effect of changes in LDS concentration for Kremer Orange in PMMA (MicroChem A8): a) shows the effect on absorption (measured relative to air); b) shows the effect on photoluminescence ($\lambda_{EXCITATION}$ = 450 nm), alongside the EQE curve for P3HT:$PC_{61}BM$; and c) shows the effect on PLQY (inset is PLQY vs. concentration^{-1} plotted on a log scale, which has a linear trend).

7.4 Multiple-Dye LDS Blends for OPVs

Based on the results of the discrete LDS material analysis multiple-dye blends were considered for UV filters for OPVs. The dyes were split into two groups based on their principal absorption ranges:

- 300-400 nm – Europium, Kremer Blue, Coumarin 153
- 400-500 nm – Kremer Orange, AlQ_3

Kremer Green, Coumarin 7 and both Lumogen dyes were rejected based on their optical characterisation results. Although DCM blended with AlQ_3 has been reported on before [246], it was rejected from this study, as its optical characteristics did not suit the EQE spectrum of P3HT:PC_{61}BM.

The blend solutions were prepared by weighing out the two LDS materials into a small vial, adding the requisite volume of MicroChem A8 (8% PMMA in anisole) and leaving them on a hotplate stirrer at 60°C for 24 hours. Application was by spin coating as described in Section 4.6.1. Each film was subjected to optical characterisation. Finally the blends were spin coated onto OPV test cells and tested under AM1.5G for performance and lifetime assessment.

The following blends were prepared: Kremer Orange & Coumarin 153 (KO:Co), Kremer Orange & Europium Complex (KO:Eu), Kremer Orange & Kremer Blue (KO:KB), Kremer Blue & AlQ_3 (KB:AlQ_3), Kremer Blue & Europium Complex (KB:Eu), and Europium Complex & AlQ_3 (Eu:AlQ_3).

7.4.1 Optical Characterisation of Multiple-Dye LDS Layers

The absorption results are shown in Figure 7.10 and Figure 7.11, and the photoluminescence results are shown in Figure 7.12 and Figure 7.13.

In the majority of cases the absorption of the multiple-dye is closely related to that of both discrete dyes with the effects of each discrete dye combining additively (relative to their respective concentration). This is to be expected from the Beer Lambert law and has been observed previously [194], [316], [317]. The multiple-dye blends which contain Europium Complex combined with a purely organic dye (i.e. KO:Eu and KB:Eu) have absorption spectra which do not appear to show much influence from the Europium Complex, whereas Eu:AlQ_3 has distinct peaks matching both constituents. Some studies have suggested that when two different dyes are mixed they can form

complexes that have different absorption spectra due to static or contact quenching [318].

Considering the PL spectra, the multiple-dye blends where both discrete dyes are purely organic (i.e. KO:Co and KO:KB) all show a PL peak which closely matches the PL peak of the lower energy dye. For example for the KO:Co blend the PL peak closely matches that for Kremer Orange. In this instance the emission from the Coumarin 153 has transferred to the Kremer Orange, due to Förster resonant energy transfer (FRET), where the energy is transferred directly from a donor molecule to a lower energy acceptor molecule [317]. It is unlikely to be from radiative recombination, where photons emitted by one dye are absorbed by the other dye before being re-emitted at a lower energy, as the emission peak from Coumarin153 occurs at 500 nm which is at the tail end of the absorption curve for Kremer Orange and there is no emission corresponding to Coumarin 153 at all. The PL spectra for the multiple-dye blends containing organo-metallic dyes (i.e. KB:AlQ_3, KB:Eu and Eu:AlQ_3) show different characteristics. KB:AlQ_3 and KB:Eu both show PL spectra corresponding to both discrete dyes. Eu:AlQ_3 shows a peak at 400-450 nm, which does not correspond to the AlQ_3 emission peak (500-550 nm) and a sharply defined peak at 620 nm, which corresponds to the Europium Complex. It should be noted that this last blend had a very low PLQY (2.7%). It is thought that FRET is not possible from the organo-metallic dyes, as internal transfer from the organic ligands to the metallic core dominates.

The PLQY results (see Table D.2 in Appendix D.1) had a range from 30.9% for KO:Eu, all the way down to 2.7% for Eu:AlQ_3. Apart from Eu:AlQ_3, all of the dyes with a concentration of 1mg:1mg /ml have PLQYs of 13.5% and higher.

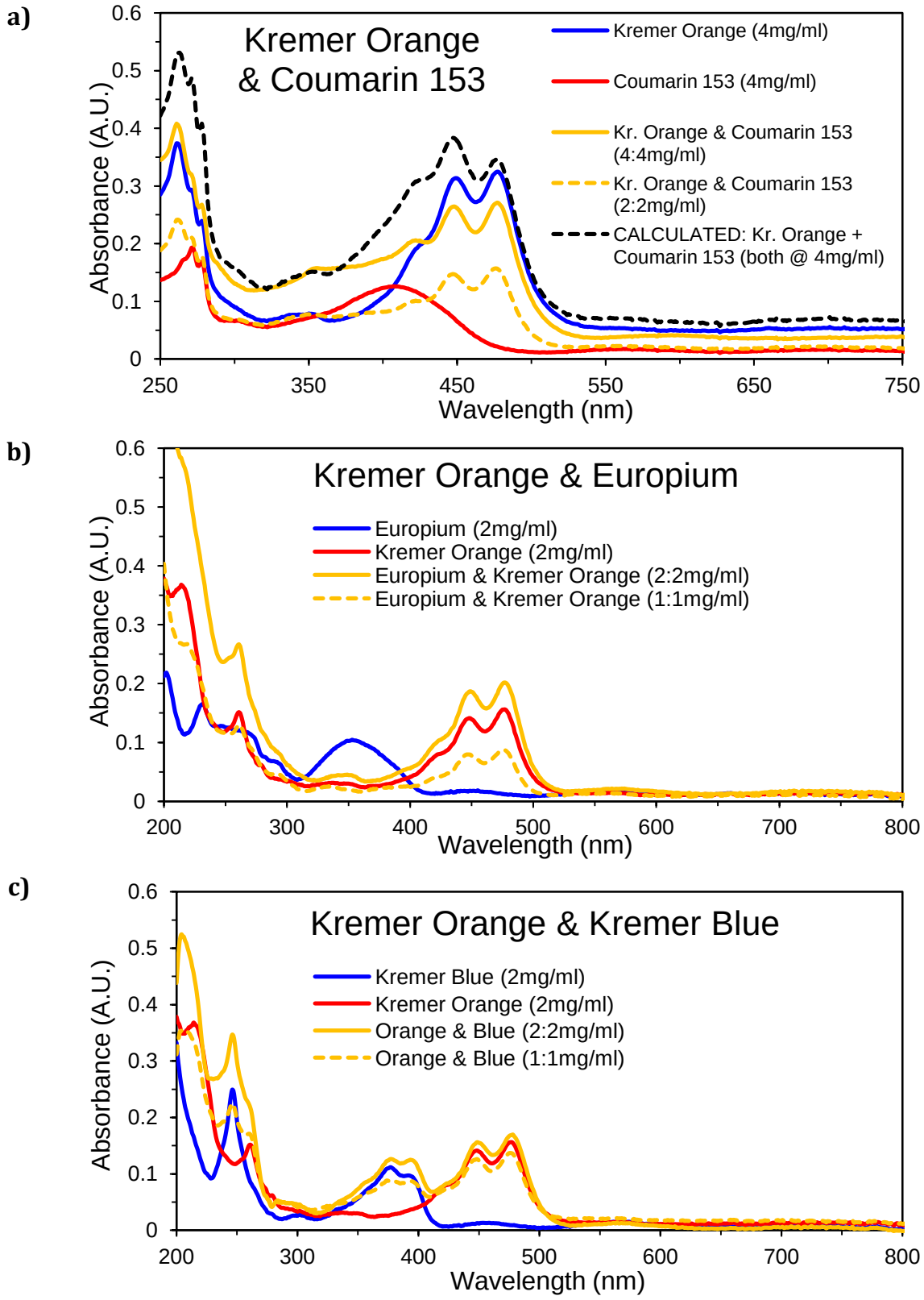

Figure 7.10: Absorption spectra for multiple-dye LDS blends and their discrete component dyes: a) Kremer Orange and Coumarin 153; b) Kremer Orange and Europium complex; and c) Kremer Orange and Kremer Blue.

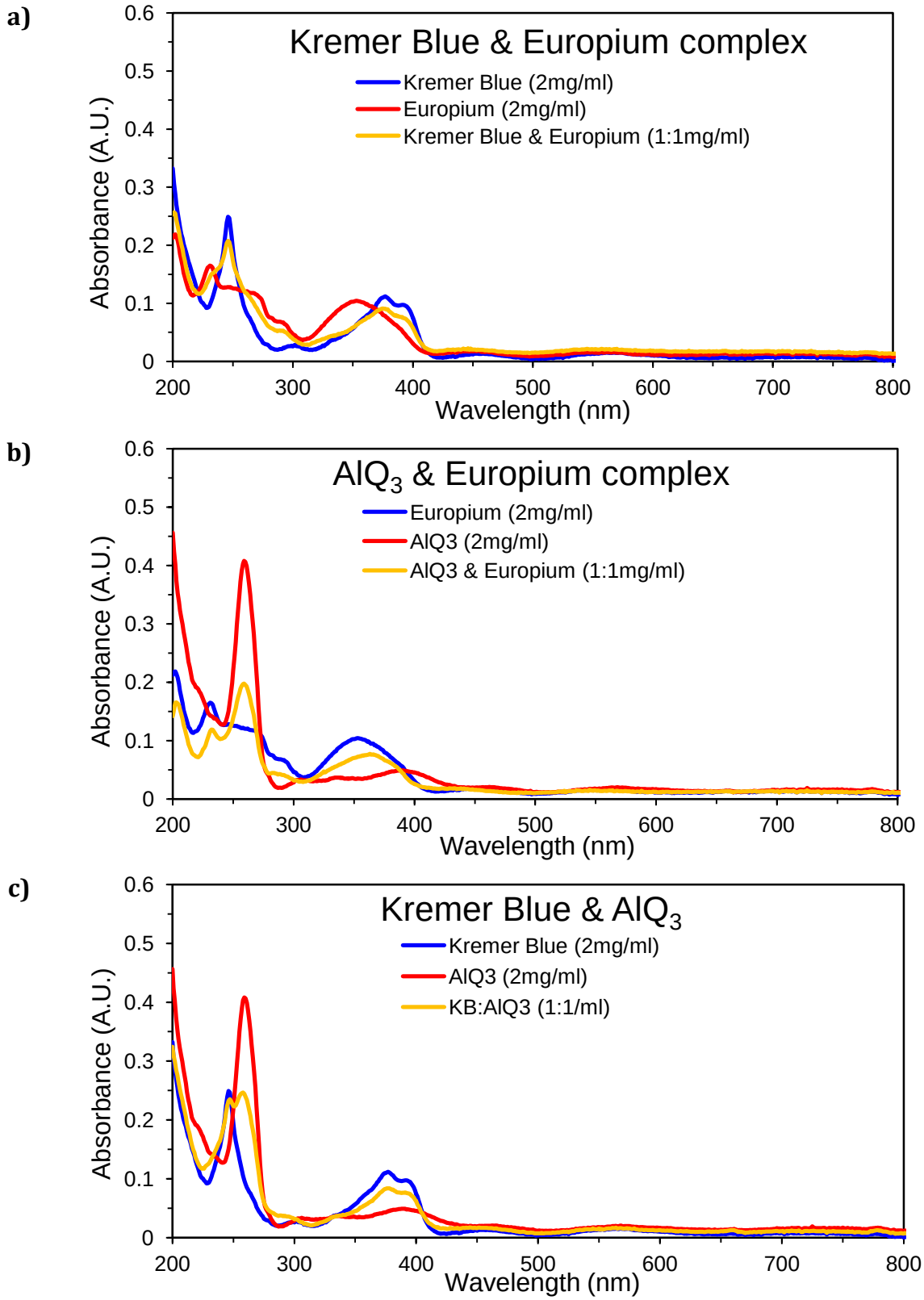

Figure 7.11: Absorption spectra for multiple-dye LDS blends and their discrete component dyes: a) Kremer Blue and Europium complex; b) AlQ_3 and Europium complex; and c) Kremer Blue and AlQ_3.

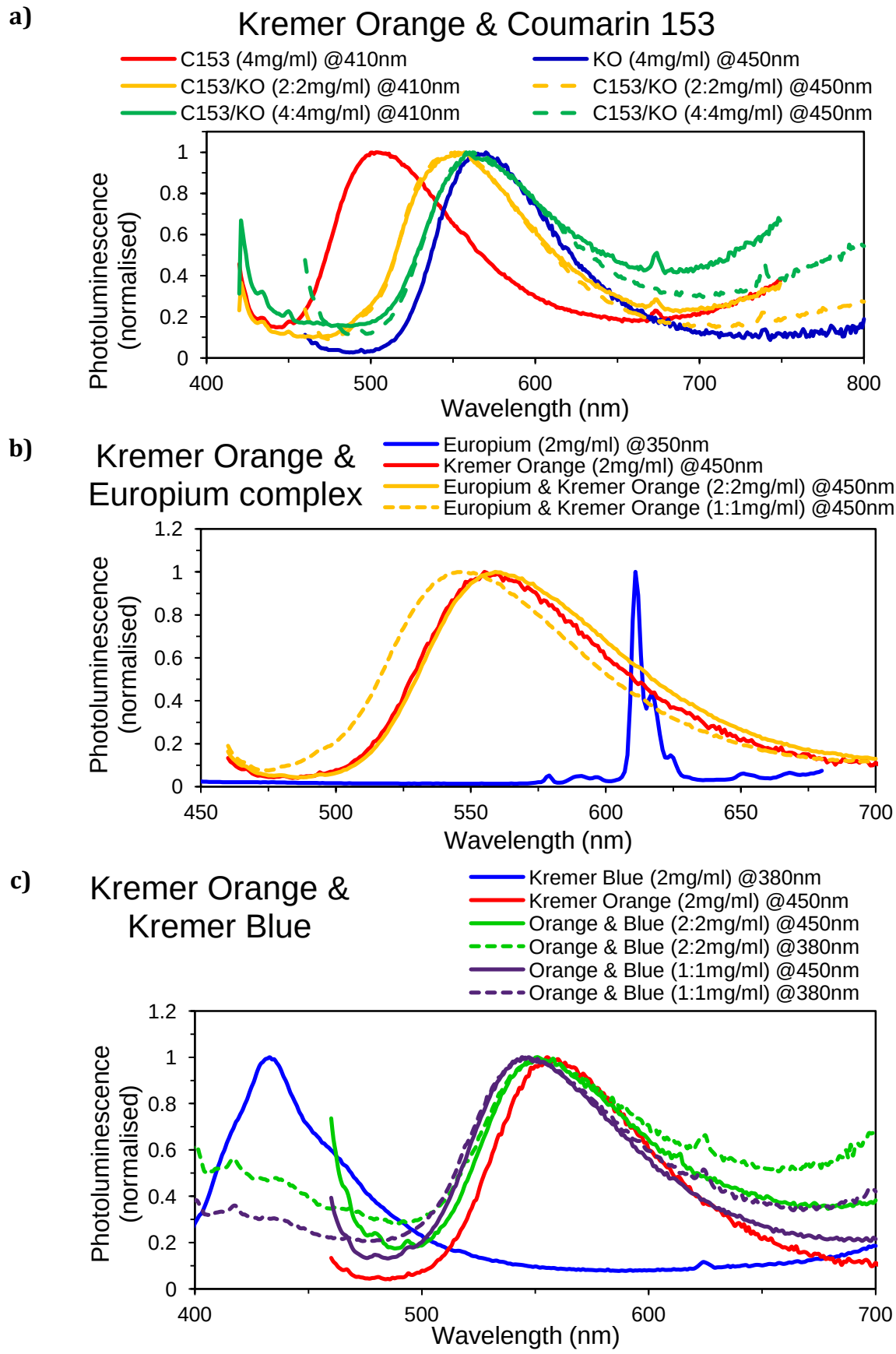

Figure 7.12: Photoluminescent spectra for multiple-dye LDS blends and their discrete component dyes: a) Kremer Orange and Coumarin 153; b) Kremer Orange and Europium complex; and c) Kremer Orange and Kremer Blue. The blends have been excited at two different wavelengths.

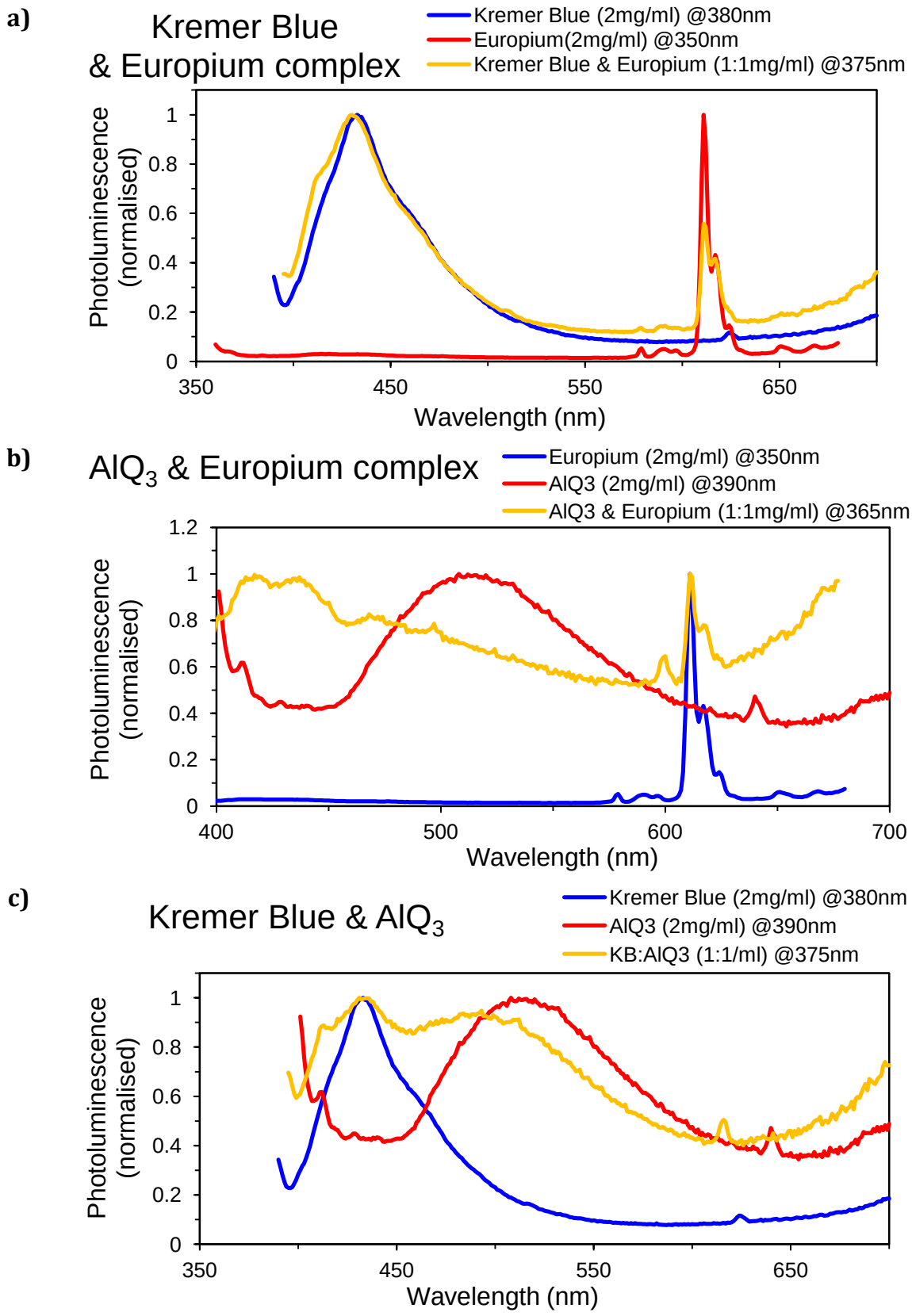

Figure 7.13: Photoluminescent spectra for multiple-dye LDS blends and their discrete component dyes: a) Kremer Blue and Europium complex; b) AlQ_3 and Europium complex; and c) Kremer Blue and AlQ_3.

7.4.2 Effect of LDS Concentration with Multiple-Dye LDS Layers

In Section 0 it was shown that varying the LDS concentration effected absorption, PL and PLQY and this was also studied for multiple-dye LDS layers, specifically Kremer Orange & Coumarin 153. Two blends of Kremer Orange & Coumarin 153 were prepared in MicroChem A8, one at 2mg:2mg /ml and the other at 4mg:4mg /ml. The absorption spectrum of the combined blend corresponds to the two discrete dyes although at a slightly lower level than the sum of the individual spectra (Figure 7.10a). The absorption of the 2mg:2mg /ml dye is about half that of the 4mg:4mg /ml dye. In Figure 7.14 PL spectra for the combined dyes and the discrete dyes are plotted, showing relative intensities (measurements were taken under the same excitation power and slit width). The PLQY of the 2mg:2mg /ml blend is 20.2% (measured when excited at both 410 nm and 450 nm) compared to 6.3% for the 4mg:4mg /ml blend. The lower concentration (2mg:2mg /ml) gave the better overall results. This corroborates the previous finding that as the LDS concentration reduces it leads to a blue-shift in the PL peak, an increase in PLQY and a decrease in absorbance.

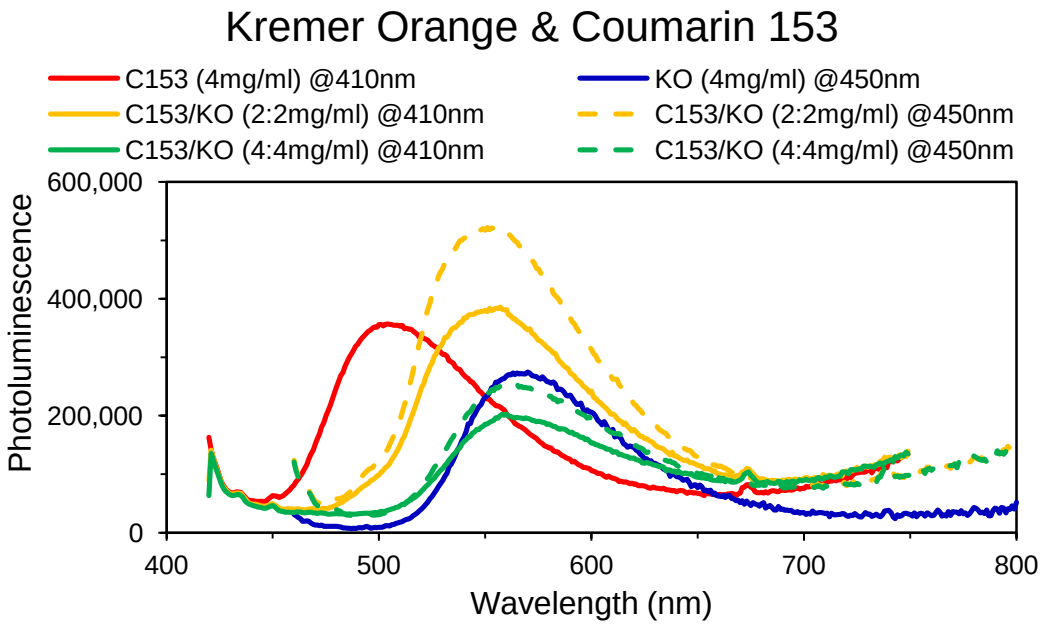

Figure 7.14: Relative photoluminescence for Kremer Orange and Coumarin 153, both as discrete and multi-dye blends.

7.4.3 Comparison of Multiple-Dye LDS Blends using Figures of Merit

Table 7.6 shows the figures of merit and weighted sums for the multiple-dye LDS blends, based on P3HT:$PC_{61}BM$ as the OPV active layer.

Table 7.6: Figures of Merit for Multi Dye LDS Layers (based on EQE for P3HT:$PC_{61}BM$)[9].

LDS Material	RO	UV	PLQY	ASM	PA	ESM	Weighted Sum
Kr. Orange/Coumarin 153 (KO:Co) (2mg:2mg /1ml)	5.4%	15.8%	20.3%	7.5%	11.5%	78.8%	90.3%
Kr. Orange/Europium (KO:Eu) (1mg:1mg /1ml)	5.0%	6.2%	30.9%	5.3%	8.1%	81.8%	90.6%
Kr. Orange/Kr. Blue (KO:KB) (1mg:1mg /1ml)	6.8%	16.0%	13.5%	8.1%	12.2%	77.7%	87.6%
Kremer Blue/AlQ_3 (KB:AlQ_3) (1mg:1mg /1ml)	15.6%	23.4%	15.9%	13.2%	15.7%	80.7%	91.0%
Kremer Blue/Europium (KB:Eu) (1mg:1mg /1ml)	6.8%	15.5%	25.3%	5.8%	6.6%	69.2%	91.9%
Europium/AlQ_3 (Eu:AlQ_3) (1mg:1mg /1ml)	3.4%	11.6%	2.7%	3.1%	3.2%	75.7%	84.9%

Kremer Orange & Coumarin 153 (KO:Co): This blend has reasonable UV coverage, low radiative overlap and good PLQY. However it has significant parasitic absorption and fairly low absorption spectral matching.

Kremer Orange & Europium Complex (KO:Eu): This blend has low radiative overlap, but low UV coverage. However it has the highest figures for PLQY and emission spectral matching.

Kremer Orange & Kremer Blue (KO:KB): This blend has good UV coverage and radiative overlap, but relatively poor PLQY, parasitic absorption and emission spectral matching.

Kremer Blue & AlQ_3 (KB:AlQ_3): This blend has the worst radiative overlap and a low PLQY. However it has the highest UV coverage and absorption spectral matching.

Kremer Blue & Europium Complex (KB:Eu): This blend has a reasonable UV coverage, radiative overlap and parasitic absorption. However it has the worst absorption spectral matching and emission spectral matching. It has the highest weighted sum.

[9] Figures of Merit: RO=Radiative Overlap; UVC=UV Coverage; PLQY=Photoluminescent Quantum Yield; ASM=Absorption Spectral Matching; PA=Parasitic Absorption; and ESM=Emission Spectral Matching.

Europium Complex & AlQ_3 (Eu:AlQ_3): This blend had the best figures for radiative overlap and parasitic absorption, but the worst PLQY and absorption spectral matching. It has the lowest weighted sum.

Apart from the KB:AlQ_3 blend all the other blends had low radiative overlap. This blend also produced the best UV coverage. The highest PLQY was for KO:Eu. KB:AlQ_3 had the best absorption spectral matching and Eu:AlQ_3 had the worst. There was not much spread across all the dyes for emission spectral matching (69%-82 %). Overall this implies that for a particular optical property a specific dye combination can be selected. For instance, to obtain a high initial PCE a blend with a high PLQY is needed (e.g. Kremer Orange & Europium). However for better stability a blend with a high UV coverage should be selected (e.g. Kremer Blue & AlQ_3).

Based on this data the Kremer Orange & Kremer Blue (KO:KB) and Europium Complex & AlQ3 (Eu:AlQ3) blends were omitted from further tests. They scored the lowest in the weighted sum, mainly due to their low PLQY figures.

7.4.4 OPV Performance with Multiple-Dye LDS Layers

Performance tests were conducted using inverted geometry cells based on P3HT:$PC_{61}BM$ with no encapsulation. IV measurements were taken of the fresh cells and then various treatments were applied to separate cells before they were retested. Three configurations were tested: 1) control device with no UV filter; 2) LDS blends (KB:AlQ_3, KB:Eu, KO:Eu and KO:Co) were spin coated onto the light facing surface; 3) an adhesive UV filter (Solaronix #49132) was applied to the top surface.

Each cell was measured under AM1.5G before and after the LDS coating was applied. Table 7.7 shows the changes in performance parameters when the LDS coatings were applied to the OPV devices.

Table 7.7: Performance parameters for the devices used for stability testing. Values are averaged across all 6 pixels. Values in brackets are relative changes (Δs) and are based on each individual device's measurements before and after coating with LDS.

Sample	PCE (%)	J_{SC} (mA/cm²)	V_{OC} (V)	FF
Reference (control)	3.5±0.1	9.8±0.3	0.57	0.63
Kremer Blue / AlQ_3	3.3±0.1 (Δ= 7.4%)	8.9±0.2 (Δ= -3.7%)	0.57 (Δ= 2.2%)	0.65 (Δ= 9.5%)
Kremer Blue / Europium	3.2±0.2 (Δ= -1.7%)	9.4±0.7 (Δ= -2.2%)	0.57 (Δ= 0.9%)	0.60 (Δ= -0.6%)
Kremer Orange / Europium	2.9±0.2 (Δ= -5.0%)	8.1±0.4 (Δ= -6.8%)	0.59 (Δ= 2.9%)	0.61 (Δ= -1.0%)
Kremer Orange / Coumarin153	2.8±0.2 (Δ=-12.5%)	7.2±0.1 (Δ=-13.7%)	0.61 (Δ= -0.4%)	0.65 (Δ= 1.2%)
UV Filter (Solaronix SA #49132)	3.0±0.3 (Δ= -5.6%)	8.9±0.6 (Δ= -6.0%)	0.57 (Δ= 0.8%)	0.59 (Δ= -0.5%)

The device with Kremer Blue & AlQ_3 (KB:AlQ_3) showed a relative improvement in PCE of 7.4%, despite a drop in J_{SC} of -3.7%, due to a large improvement of nearly 10% in FF. All of the other devices showed a drop in both PCE and J_{SC} after application of the LDS layers, with the worst device being Kremer Orange & Coumarin 153 (KO:Co) which showed a relative drop of -12.5% for PCE and -13.7% for J_{SC}. The device with the UV filter showed a drop of nearly -6%, which is actually quite good; other works have shown relative losses of over 15% when UV filters are applied, caused by increased absorption and internal reflection [213].

7.4.5 Lifetime Stability Tests for OPVs with Multiple-Dye LDS Layers

For the lifetime testing, the devices were mounted under the solar simulator (AM1.5G) and IV testing was conducted at regular intervals from which PCE, I_{SC}, V_{OC} and FF were extracted (ISOS-L-1 protocol [119]). Figure 7.15 shows the evolution of the performance parameters over the course of the lifetime testing under AM1.5G.

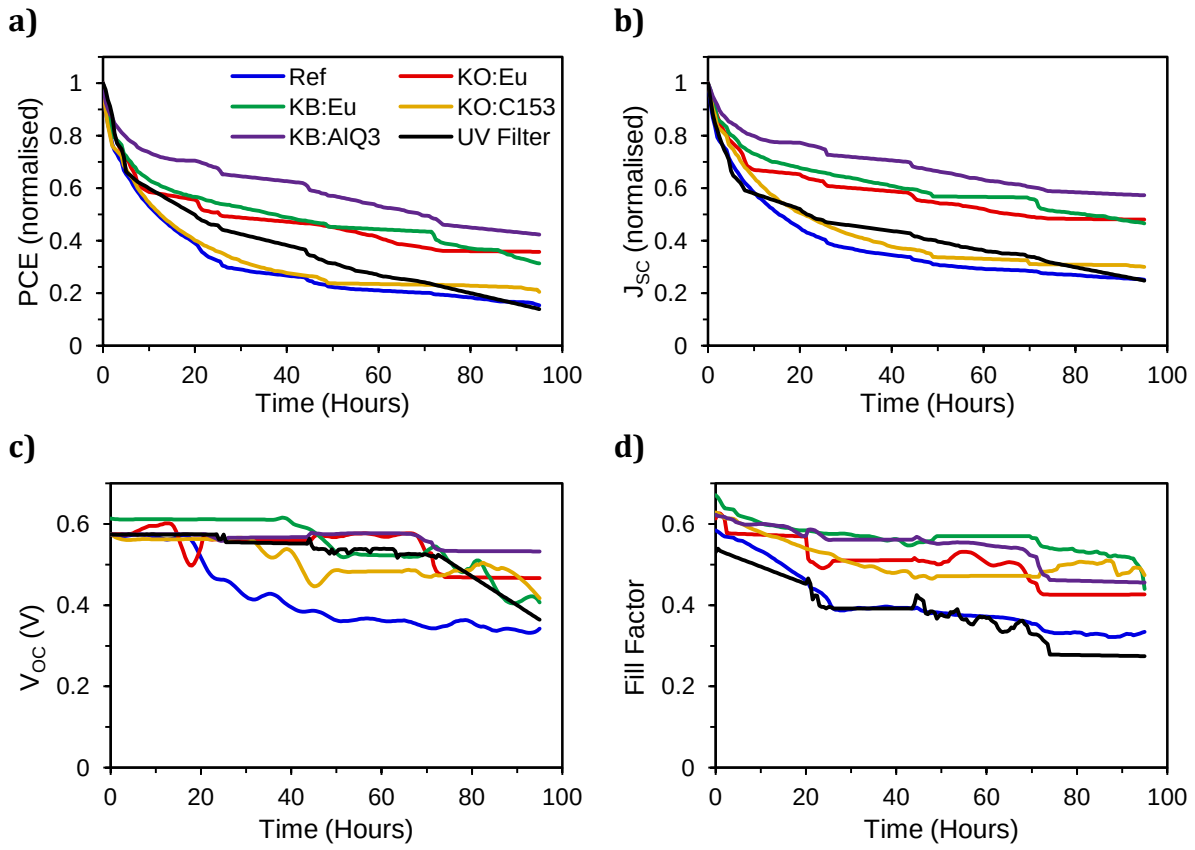

Figure 7.15: Indoor stability testing under AM1.5G on inverted geometry P3HT:$PC_{61}BM$ non-encapsulated OPVs: a) PCE (normalised); b) J_{SC} (normalised); c) V_{OC}; and d) FF.

All the devices showed rapid initial deterioration, as would be expected from non-encapsulated devices. PCE and J_{SC} both show exponential decay. All of the devices with LDS coatings performed better than the reference device, with KB:AlQ_3 having the best overall stability and KO:Co degrading almost as quickly as the reference device. After the initial drop in performance the UV filter device degraded at a slower rate than the reference and KO:Co devices, but by the end of the test it had degraded as much as the reference device as it failed to reach a steady state. The reference device showed a sharp decrease in V_{OC} after just 20 hours, the KO:Co device showed a drop in V_{OC} at 30 hours, whereas V_{OC} stayed relatively constant for all the other devices until ~70 hours. A drop in V_{OC} is indicative of photo-oxidation of the active layer causing a change in the HOMO level in the polymer [314]. Both the reference and UV filter devices showed a steady decline in FF from the start of the test, whereas the other devices showed a slower decline in FF. Reduction in FF is indicative of degradation in the PAL/electrode interfaces, usually by oxygen and water [92], [93].

Table 7.8 shows the degradation factors (T_{80} & T_{50}) from the stability tests. All of the devices showed a rapid initial degradation, which is reflected in the T_{80} figures of between 1.6 and 4.7 hours. However the values for T_{50} show how the KB:AlQ_3 device has outperformed all the other devices with an average value of 70 hours, whereas the other devices range from 12 to 38 hours. The poor performance by the KO:Co device shows that it is the UV filtering effect that is of most importance: this LDS blend has low absorption over the UV region.

Table 7.8: Degradation factors (T_{80} and T_{50}) derived from the stability tests.

Sample	T_{80} (hours)	T_{50} (hours)
Reference	1.6	11.6
Kremer Blue / AlQ_3	4.7	69.2
Kremer Blue / Europium	2.1	37.6
Kremer Orange / Europium	2.5	25.4
Kremer Orange / Coumarin153	1.5	12.4
UV filter (Solaronix)	2.6	19.9

These results confirm that incidence of UV light in the presence of atmospheric oxygen leads to the photo-oxidation of the active layer, which may lead to the formation of traps and recombination centres for photo-generated excitons [319]. Over time the concentration of these defects increase, leading to deterioration of the device performance parameters. The application of UV barrier layers is able to slow this degradation. The use of commercial UV filters usually leads to a significant drop in efficiency, due to the increased absorption by the filter, whereas the use of LDS coatings can reduce this loss and in some cases can actually increase the efficiency of the device as well as providing the UV protection required for long term device stability.

7.5 Conclusion

Initial experiments were conducted on single LDS layers and showed that these layers could provide significant improvements to OPVs, both in terms of performance (over 8% gain in PCE) and stability indoors (x6 for T_{50}). Outdoor stability studies in Bangor showed that modules with a Kremer Blue coating outperformed control modules. Similar studies in Israel showed that modules with a Europium Complex coating had similar degradation rates as those with a commercial UV filter and both outperformed control modules without a UV filter. When considering PCE, application of the Europium Complex led to no change whereas application of the UV filter reduced

PCE by 18% providing clear evidence that LDS layers can operate as an alternative to commercial UV filters, but without the drop in performance.

More in depth investigation of a larger number of LDS dyes was then conducted, which were sourced from previous papers in the field. Optical characterisations were performed and the dyes were compared using calculated figures of merit. Optical characterisation showed that as the LDS concentration was reduced it led to an exponential increase in PLQY and a linear decrease in the absorbance. The photoluminescent emission peak was also observed to blue shift as the LDS concentration reduced.

A number of two dye blends were investigated with the component dyes selected based on their figures of merit and optical properties. Optical characterisations of the blends were performed which showed that absorption of the blend was a little below the sum of the spectra of the discrete dyes. The photoluminescent emission peaks of purely organic dye blends were seen to shift to the lower energy dye by FRET but the organo-metallic dyes behaved differently with emissions corresponding to both dyes being present. Examination of the effect of concentration for blended dyes showed similar results to that of the discrete dyes.

Electrical characterisation of OPV devices coated with different dyes, both discrete and blended, showed that a gain in PCE was only possible with low LDS concentrations with a gain of over 7% for the Kremer Blue & AlQ_3 blend. Indoor stability tests showed that this blend worked well giving an improvement at T_{50} of six times the lifetime of an untreated cell. This dye blend consists of discrete dyes which both have good absorption in the UV region, but little absorption over regions where the cell had a high EQE.

Chapter 8. Conclusions and Suggestions for Further Research

A review of the most important findings of this thesis, including: -

- *Benchmarking of OPV modules against other PV technologies at the same test site.*
- *Demonstration of improved yield using three-dimensional structured OPV modules.*
- *Demonstration of improved yield and stability of OPVs using LDS coatings consisting of both single and multiple-dye blends.*

This thesis focused on the outdoor monitoring of OPVs with the aim of improving the stability and performance of OPV cells and modules under real world conditions. This is important as in order for OPVs to become commercially viable they must make the transition from small laboratory cells to larger modules that can be of real use.

Suggestions for further research are also given.

8.1 Outdoor Monitoring of OPVs

An in-depth literature review of OPVs used outdoors highlighted that one of the main problems facing OPVs when they are used outdoors is degradation caused by the ingress of oxygen and water and subsequent photo-oxidation. Although good quality barrier layers are being used, failure at the edges and where connecting wires exit were identified as the primary routes for oxygen and water to gain access. The important role that UV radiation plays in photo-oxidation was highlighted.

Before the research could start an outdoor monitoring system was setup, conforming to the ISOS-O-2 protocol. This allowed many different monitoring campaigns to be performed, looking at various aspects of OPV performance. The first campaign was on untreated R2R modules which were monitored during the summer. These were found to degrade quite quickly and close examination of the modules showed that the encapsulation had failed at the edges.

Detailed module temperature analysis was performed on both OPV and polycrystalline silicon modules, showing that both have a linear relationship between

irradiance and module temperature above ambient temperature. Further analysis was performed on the relationship between module temperature and PCE, I_{SC}, V_{OC} and FF for OPV modules. It was shown that V_{OC} has a negative temperature coefficient, but that I_{SC}, PCE and FF have positive temperature coefficients.

A second outdoor campaign was performed, this time over winter, using untreated modules, apart from one module with a UV filter. In comparison with the summer results all of these modules were shown to degrade much more slowly due to the lower levels of irradiance and UV experienced. The module with the UV filter was shown to be particularly stable and outperformed the best control module by 62% (based on normalised yields).

A different type of OPV module, DTU(AgNW), with a composite AgNW/ZnO front electrode was monitored outdoors and found to degrade much more slowly than the DTU(AgGrid) modules used in the earlier outdoor tests. This is attributed to the UV filtering effect of the ZnO in the front electrode.

Several different PV technologies have been compared to examine the effect of irradiance on PCE, I_{SC}, V_{OC} and FF. These included poly-Si, CIS, DSSC and two different types of R2R fabricated OPV modules. It was shown that R2R OPV modules, when compared to traditional PV (poly-Si and CIS), have similar J_{SC} performance, but that V_{OC} and FF performance was much worse.

Overall these outdoor results show that OPV modules perform well under high levels of irradiance, aided by positive temperature coefficients. It was shown that degradation was driven by photo-oxidation and physical ingress of water and oxygen, and that UV filtering slowed these degradation rates.

8.2 Improvement of Yield using 3D Structured Modules

To improve the yield of OPVs outdoors, the use of 3D structuring for modules was investigated. The literature review revealed that very little research had been undertaken on macroscopic structured PV. This is partly due to the rigidity of traditional PV and this is one area where OPV and other flexible thin film technologies have a great advantage.

Indoor characterisation and outdoor monitoring (during winter and summer) was performed on OPV modules laminated onto corrugated roofing in various designs. It was shown that corrugated 3D modules provide three distinct advantages over flat OPV

modules. 1) The effective area of the module is reduced, due to the curvature of the module, which leads to an improved power output per unit area of roofing. 2) There is substantial enhancement at high angles of incidence during the summer, leading to increased output during early morning and evening. Indoor characterisation showed enhancements of up to x15 for the corrugated module when compared against a flat module. 3) There is improved performance under diffuse conditions, with the performance improvement (relative to the flat reference module) increasing from 11% under sunny conditions to 25% under cloudy conditions. Outdoor measurements on larger module strips showed that the corrugated strips outperformed the flat strips by 7.5% with a 14.8% enhancement under diffuse conditions.

These results highlight the contribution OPVs could make in BIPV, especially in countries with high penetrations of PV on the electricity network, so that the PV generation correlates better with electricity consumption and reduces the need for storage.

8.3 Improvement of Lifetime using LDS Coatings

The last phase of research looked at the use of LDS coatings to improve performance and stability of OPVs. The literature review highlighted the performance improvements that were possible using LDS coatings and the wide range of different LDS materials that are available.

Results from the initial experiments on single dye LDS coatings showed that application of LDS coatings can provide significant improvements to OPVs, both in terms of performance (over 8% gain in PCE) and stability indoors (x6 for T_{50}). Outdoor stability studies in Bangor and Israel showed that modules with an LDS coating outperformed control modules and had a similar lifetime to modules with a commercial UV filter, but without the 18% drop in performance.

Detailed optical characterisations of a larger number of discrete dyes were performed. The dyes were selected based on previous studies and on their compatibility with the EQE of P3HT:$PC_{61}BM$. A figure of merit based on a weighted sum was devised in order to allow the comparison of LDS materials. A number of two-dye blends were investigated with the component dyes being selected based on these figures of merit and their optical properties. Optical characterisations of these dye blends were performed. The photoluminescent emission peaks of purely organic dye blends were seen to shift to

the lower energy dye by FRET, but the organo-metallic dyes behaved differently with emissions corresponding to both dyes being present. Examination of the effect of concentration for blended dyes showed similar results to that of the discrete dyes.

The results of electrical characterisations of OPV cells coated with these LDS blends showed that a relative gain in PCE of 7% could be achieved using a blend of Kremer Blue & AlQ_3. Indoor stability tests showed that this blend gave an improvement at T_{50} of six times the lifetime of an untreated cell.

These results show that LDS coatings can provide suitable UV filtering to improve the stability of OPV devices without any significant drop in performance. The use of different dyes allows the tuning of a blend to match the performance of OPV devices with different EQE characteristics.

8.4 Future Work

OPVs are close to becoming a viable commercial technology, as the obstacles of efficiency, stability and cost are being overcome. As active layer materials become more stable and achieve higher efficiencies, the importance of preventing the ingress of water and oxygen by the use of effective encapsulation and the utilisation of UV filters to reduce photo-oxidation come to the fore. Although this project was not directly focused on encapsulation it was an issue that had to be addressed in order to carry out the experiments and is an important area of research.

Given further time, an analysis of outdoor spectral performance of OPVs would have been attempted, to examine if there are ideal conditions for OPVs to operate under.

The next phase of research on the 3D structured modules would be to build larger structures, similar to the larger modules described in Section 6.4, and monitor them for longer periods of time. An analysis of corrugated modules by ray tracing would complement the work in Section 6.3 and enable better designs to be made.

The LDS work showed that blended dyes can provide improvements. The work on blended dyes is at an early stage and would merit further work, including outdoor monitoring. It was shown that reducing LDS concentration led to increased PLQY, but at the cost of reduced absorption. The effect of varying the thickness of the coating should be investigated in order to optimise the concentration and thickness. Further work is required to fine-tune the weighted figures of merit and improve accuracy.

REFERENCES

[1] Intergovernmental Panel on Climate Change, "Future Global and Regional Climate Change - AR5 WG1 Summary for Policymakers," *IPCC books online*, 2013.

[2] U.S. Energy Information Administration (EIA), "International Energy Outlook 2016," *Energy Inf. Adm. books online*, 2016.

[3] International Energy Agency, "World Energy Outlook 2015," *Int. Energy Agency books online*, 2015.

[4] Renewable Energy Policy Network for the 21st Century, "Renewables 2016 Global Status Report," 2016. [Online]. Available: http://www.ren21.net/wp-content/uploads/2016/06/GSR_2016_Full_Report_REN21.pdf.

[5] J. Tsao, N. Lewis, and G. Crabtree, "Solar FAQs," *US Dep. Energy*, pp. 1–24, 2006.

[6] International Energy Agency, "World Energy Statistics 2016," *Int. Energy Agency books online*, 2016.

[7] International Energy Agency, "Energy Policies of IEA Countries: The United Kingdom 2012 Review," *Int. Energy Agency books online*, 2012.

[8] UK Government, "Digest of UK Energy Statistics (DUKES)." [Online]. Available: https://www.gov.uk/government/collections/digest-of-uk-energy-statistics-dukes.

[9] International Energy Agency, "Tracking Clean Energy Progress 2016," *Int. Energy Agency books online*, 2016.

[10] International Energy Agency, "Next Generation Wind and Solar Power," *Int. Energy Agency books online*, 2016.

[11] International Energy Agency, "Snapshot of Global Photovoltaic Markets 2015," *Int. Energy Agency books online*, 2016.

[12] Fraunhofer Institute for Solar Energy Systems, "Photovoltaics Report," 2016. [Online]. Available: https://www.ise.fraunhofer.de/en/downloads-englisch/pdf-files-englisch/photovoltaics-report-slides.pdf.

[13] G. F. Brown and J. Wu, "Third generation photovoltaics," *Laser Photonics Rev.*, vol. 3, no. 4, pp. 394–405, 2009.

[14] M. A. Green, "Third generation photovoltaics: Assessment of progress over the last decade," *34th IEEE Photovolt. Spec. Conf.*, pp. 000146–000149, 2009.

[15] H. Spanggaard and F. C. Krebs, "A brief history of the development of organic and polymeric photovoltaics," *Sol. Energy Mater. Sol. Cells*, vol. 83, no. 2, pp. 125–146, Jun. 2004.

[16] G. A. Chamberlain, "Organic solar cells: A review," *Sol. Cells*, vol. 8, no. 1, pp. 47–83, 1983.

[17] C. W. Tang, "Two-layer organic photovoltaic cell," *Appl. Phys. Lett.*, vol. 48, no. 2, pp. 183–185, 1986.

[18] N. S. Sariciftci, L. Smilowitz, A. J. Heeger, and F. Wudl, "Photoinduced Electron Transfer from a Conducting Polymer to Buckminsterfullerene," *Science*, vol. 258, no. 5087, pp. 1474–1476, 1992.

[19] G. Yu, J. Gao, J. C. Hummelen, F. Wudl, and A. J. Heeger, "Polymer Photovoltaic Cells: Enhanced Efficiencies via a Network of Internal Donor-Acceptor Heterojunctions," *Science*, vol. 270, no. 5243, pp. 1789–1791, 1995.

[20] M. Jørgensen *et al.*, “The state of organic solar cells — A meta analysis,” *Sol. Energy Mater. Sol. Cells*, vol. 119, pp. 84–93, 2013.

[21] M. A. Green, K. Emery, Y. Hishikawa, W. Warta, and E. D. Dunlop, “Solar cell efficiency tables (version 48),” *Prog. Photovolt. Res. Appl.*, vol. 24, pp. 905–913, 2016.

[22] Heliatek Gmbh, “Heliatek sets new OPV world record efficiency of 13.2%,” 2016. [Online]. Available: http://www.heliatek.com/en/press/press-releases/details/heliatek-sets-new-organic-photovoltaic-world-record-efficiency-of-13-2. [Accessed: 25-Jun-2016].

[23] National Renewable Energy Laboratory (NREL), “Best Research Cell Efficiencies Chart.” [Online]. Available: http://www.nrel.gov/pv/assets/images/efficiency_chart.jpg. [Accessed: 19-Oct-2016].

[24] A. K. Shukla, K. Sudhakar, and P. Baredar, “A comprehensive review on design of building integrated photovoltaic system,” *Energy Build.*, vol. 128, pp. 99–110, 2016.

[25] P. Heinstein, C. Ballif, and L. E. Perret-Aebi, “Building integrated photovoltaics (BIPV): Review, potentials, barriers and myths,” *Green*, vol. 3, no. 2, pp. 125–156, 2013.

[26] B. van der Wiel, H. J. Egelhaaf, H. Issa, M. Roos, and N. Henze, “Market Readiness of Organic Photovoltaics for Building Integration,” *MRS Proceedings*, vol. 1639, 2014.

[27] S. B. Darling and F. You, “The case for organic photovoltaics,” *RSC Adv.*, vol. 3, no. 39, pp. 17633–17648, 2013.

[28] C. J. Brabec, N. S. Sariciftci, and J. C. Hummelen, “Plastic Solar Cells,” *Adv. Funct. Mater.*, vol. 11, no. 1, pp. 15–26, 2001.

[29] “Polysolar Ltd.” [Online]. Available: http://www.polysolar.co.uk/. [Accessed: 30-Nov-2016].

[30] Heliatek Gmbh, “HeliaFilm® Flyer.” [Online]. Available: http://www.heliatek.com/files/content/downloads/broschure/Heliatek_Flyer_online_2016.pdf. [Accessed: 01-Dec-2016].

[31] S. Berny *et al.*, “Solar Trees: First Large-Scale Demonstration of Fully Solution Coated, Semitransparent, Flexible Organic Photovoltaic Modules,” *Adv. Sci.*, vol. 3, no. 5, pp. 1–7, 2016.

[32] S. R. Wenham, M. A. Green, M. E. Watt, and R. Corkish, *Applied Photovoltaics*, 2nd ed. Earthscan, 2007.

[33] C. Hu and R. M. White, *Solar Cells: From Basic to Advanced Systems*. New York: McGraw-Hill, 1983.

[34] D. L. King, J. A. Kratochvil, and W. E. Boyson, “Measuring Solar Spectral and Angle-of-Incidence Effects on Photovoltaic Modules and Solar Irradiance Sensors,” *26th IEEE Photovolt. Spec. Conf.*, no. September, pp. 1113–1116, 1997.

[35] S. Nann and C. Riordan, “Solar spectral irradiance under clear and cloudy skies: Measurements and a semiempirical model,” *J. Appl. Meteorol.*, vol. 30, no. 4, pp. 447–462, 1991.

[36] American Society for Testing and Materials (ASTM) Terrestrial Reference Spectra, “ASTM G173-03 Tables,” 2012. [Online]. Available: http://rredc.nrel.gov/solar/spectra/am1.5/.

[37] Å. Skaaland, M. Ricke, K. Wallevik, and R. Strandberg, “Potential and Challenges for

Building Integrated Photovoltaics in the Agder Region," *Agderforsking, Tech. Rep.*, no. 6, pp. 1–120, 2011.

[38] J. A. Duffie and W. A. Beckman, *Solar Engineering of Thermal Processes*, 4th ed. Wiley, 1980.

[39] P. Blanc *et al.*, "Direct normal irradiance related definitions and applications: The circumsolar issue," *Sol. Energy*, vol. 110, pp. 561–577, 2014.

[40] S. Ransome, "Modelling inaccuracies of PV energy yield simulations," *33rd IEEE Photovolt. Spec. Conf.*, 2008.

[41] D. R. Myers, K. Emery, and C. Gueymard, "Proposed reference spectral irradiance standards to improve concentrating photovoltaic system design and performance evaluation," *29th IEEE Photovolt. Spec. Conf.*, 2002.

[42] A. M. Noorian, I. Moradi, and G. A. Kamali, "Evaluation of 12 models to estimate hourly diffuse irradiation on inclined surfaces," *Renew. Energy*, vol. 33, no. 6, pp. 1406–1412, 2008.

[43] B. Liu and R. Jordan, "The interrelationship and characteristics distribution of direct, diffuse and total solar radiation," *Sol. Energy*, vol. 4, no. 3, pp. 1–19, 1960.

[44] R. Perez, R. Seals, P. Ineichen, R. Stewart, and D. Menicucci, "A New Simplified Version of the Perez Diffuse Irradiance Model for Tilted Surfaces," *Sol. Energy*, vol. 39, no. 3, pp. 221–231, 1987.

[45] R. Perez, P. Ineichen, R. Seals, J. Michalsky, and R. Stewart, "Modeling daylight availability and irradiance components from direct and global irradiance," *Sol. Energy*, vol. 44, no. 5, pp. 271–289, 1990.

[46] R. E. Bird and R. L. Hulstrom, "A simplified clear sky model for direct and diffuse insolation on horizontal surfaces," *Tech. Rep. SERI/TR-642-761. Solar Energy Research Inst., Golden, CO(USA)*, 1981.

[47] G. Pelletier, "Solrad.xls (NOAA)." Washington Department of Ecology.

[48] H. J. Snaith, "How should you measure your excitonic solar cells?," *Energy Environ. Sci.*, vol. 5, no. 4, p. 6513, 2012.

[49] B. Qi and J. Wang, "Fill factor in organic solar cells," *Phys. Chem. Chem. Phys.*, vol. 15, no. 23, pp. 8972–8982, Jun. 2013.

[50] J. Nelson, *The physics of solar cells*. London: Imperial College Press, 2003.

[51] J. H. Burroughes *et al.*, "Light-emitting diodes based on conjugated polymers," *Nature*, vol. 347, no. 6293, pp. 539–541, 1990.

[52] Y.-L. Loo and I. McCulloch, "Progress and Challenges for Commercialization of Organic Electronics," *MRS Bulletin*, vol. 33, no. 7, pp. 653–662, 2008.

[53] S. R. Forrest, "The path to ubiquitous and low-cost organic electronic appliances on plastic.," *Nature*, vol. 428, no. 6986, pp. 911–918, 2004.

[54] X. Zhang, P. Bäuerle, T. Aida, P. Skabara, and C. Kagan, "Organic Electronics for a Better Tomorrow : Innovation, Accessibility, Sustainability," *Chem. Sci. Soc. Summit (CS3)*, 2012.

[55] J.-M. Nunzi, "Organic photovoltaic materials and devices," *Comptes Rendus Phys.*, vol. 3, no. 4, pp. 523–542, 2002.

[56] L. Dou *et al.*, "25th Anniversary Article: a Decade of Organic/Polymeric Photovoltaic Research.," *Adv. Mater.*, vol. 25, no. 46, pp. 6642–71, Dec. 2013.

[57] J. Nelson, S. A. Choulis, and J. R. Durrant, "Charge recombination in polymer/fullerene photovoltaic devices," *Thin Solid Films*, vol. 451, pp. 508–514, Mar. 2004.

[58] C. M. Proctor, M. Kuik, and T.-Q. Nguyen, "Charge carrier recombination in organic solar cells," *Prog. Polym. Sci.*, vol. 38, no. 12, pp. 1941–1960, 2013.

[59] A. Moliton and J. Nunzi, "How to model the behaviour of organic photovoltaic cells," *Polym. Int.*, vol. 55, no. 6, pp. 583–600, 2006.

[60] J. M. Shaw and P. F. Seidler, "Organic Electronics: Introduction," *IBM J. Res. Dev.*, vol. 45, no. 1, pp. 3–9, 2001.

[61] C. J. Brabec *et al.*, "Tracing photoinduced electron transfer process in conjugated polymer/fullerene bulk heterojunctions in real time," *Chem. Phys. Lett.*, vol. 340, no. 3, pp. 232–236, 2001.

[62] J. Nelson, "Organic photovoltaic films," *Curr. Opin. Solid State Mater. Sci.*, vol. 6, no. 1, pp. 87–95, 2002.

[63] D. Wohrle and D. Meissner, "Organic Solar Cells," *Adv. Mater.*, vol. 3, no. 3, pp. 129–138, 1991.

[64] J. A. Bartelt *et al.*, "The importance of fullerene percolation in the mixed regions of polymer-fullerene bulk heterojunction solar cells," *Adv. Energy Mater.*, vol. 3, no. 3, pp. 364–374, 2013.

[65] H. Hoppe and N. S. Sariciftci, "Morphology of polymer/fullerene bulk heterojunction solar cells," *J. Mater. Chem.*, vol. 16, no. 1, pp. 45–61, 2006.

[66] G. J. Hedley *et al.*, "Determining the optimum morphology in high-performance polymer-fullerene organic photovoltaic cells.," *Nat. Commun.*, vol. 4, 2013.

[67] H. Waters *et al.*, "Effect of processing additive 1,8-octanedithiol on the lifetime of PCPDTBT based Organic Photovoltaics," *Org. Electron.*, vol. 15, no. 10, pp. 2433–2438, Jul. 2014.

[68] A. C. Mayer, S. R. Scully, B. E. Hardin, M. W. Rowell, and M. D. McGehee, "Polymer-based solar cells," *Mater. Today*, vol. 10, no. 11, pp. 28–33, 2007.

[69] J. E. Slota, X. He, and W. T. S. Huck, "Controlling nanoscale morphology in polymer photovoltaic devices," *Nano Today*, vol. 5, no. 3, pp. 231–242, 2010.

[70] Y. Yang, K. Mielczarek, M. Aryal, A. Zakhidov, and W. Hu, "Nanoimprinted polymer solar cell," *ACS Nano*, vol. 6, no. 4, pp. 2877–2892, 2012.

[71] A. J. Mozer and N. S. Sariciftci, "Conjugated polymer photovoltaic devices and materials," *Comptes Rendus Chim.*, vol. 9, no. 5, pp. 568–577, May 2006.

[72] A. M. Ramos, M. T. Rispens, J. K. J. Van Duren, J. C. Hummelen, and R. A. J. Janssen, "Photoinduced electron transfer and photovoltaic devices of a conjugated polymer with pendant fullerenes," *J. Am. Chem. Soc.*, vol. 123, no. 27, pp. 6714–6715, 2001.

[73] A. Cravino *et al.*, "A Soluble Donor-Acceptor Double-Cable Polymer: Polythiophene with Pendant Fullerenes," *Monatshefte für Chemie/Chemical Mon.*, vol. 134, no. 4, pp. 519–527, 2003.

[74] P. Boland, K. Lee, and G. Namkoong, "Device optimization in PCPDTBT:PCBM plastic solar cells," *Sol. Energy Mater. Sol. Cells*, vol. 94, no. 5, pp. 915–920, May 2010.

[75] M. C. Scharber *et al.*, "Design rules for donors in bulk-heterojunction solar cells—Towards 10% energy-conversion efficiency," *Adv. Mater.*, vol. 18, no. 6, pp. 789–794, 2006.

[76] E. Bundgaard and F. C. Krebs, "Low band gap polymers for organic photovoltaics," *Sol. Energy Mater. Sol. Cells*, vol. 91, no. 11, pp. 954–985, 2007.

[77] J. Kettle, H. Waters, M. Horie, and S.-W. Chang, "Effect of hole transporting layers on the performance of PCPDTBT : PCBM organic solar cells," *J. Phys. D. Appl. Phys.*, vol. 45, no. 12, p. 125102, 2012.

[78] J. Kettle *et al.*, "Optimisation of PCPDTBT solar cells using polymer synthesis with Suzuki coupling," *Sol. Energy Mater. Sol. Cells*, vol. 95, no. 8, pp. 2186–2193, 2011.

[79] D. Mühlbacher *et al.*, "High Photovoltaic Performance of a Low-Bandgap Polymer," *Adv. Mater.*, vol. 18, no. 21, pp. 2884–2889, 2006.

[80] G. Li *et al.*, "High-efficiency solution processable polymer photovoltaic cells by self-organization of polymer blends," *Nat. Mater.*, vol. 4, no. 11, pp. 864–868, Oct. 2005.

[81] M. Campoy-Quiles *et al.*, "Morphology evolution via self-organization and lateral and vertical diffusion in polymer:fullerene solar cell blends.," *Nat. Mater.*, vol. 7, no. 2, pp. 158–164, 2008.

[82] H.-L. Yip and A. K.-Y. Jen, "Recent advances in solution-processed interfacial materials for efficient and stable polymer solar cells," *Energy Environ. Sci.*, vol. 5, no. 3, pp. 5994–6011, 2012.

[83] Y. Lin and X. Zhan, "Non-fullerene acceptors for organic photovoltaics: an emerging horizon," *Mater. Horizons*, vol. 1, no. 5, pp. 470–488, 2014.

[84] D. Angmo, N. Espinosa, and F. Krebs, "Indium Tin Oxide-Free Polymer Solar Cells: Toward Commercial Reality," in *Low-cost Nanomaterials*, Springer London, 2014, pp. 189–225.

[85] J. Fahlteich, M. Fahland, W. Schönberger, and N. Schiller, "Permeation barrier properties of thin oxide films on flexible polymer substrates," *Thin Solid Films*, vol. 517, no. 10, pp. 3075–3080, 2009.

[86] G. B. Murdoch, S. Hinds, E. H. Sargent, S. W. Tsang, L. Mordoukhovski, and Z. H. Lu, "Aluminum doped zinc oxide for organic photovoltaics," *Appl. Phys. Lett.*, vol. 94, no. 21, p. 213301, 2009.

[87] D. Angmo and F. C. Krebs, "Flexible ITO-free polymer solar cells," *J. Appl. Polym. Sci.*, vol. 129, no. 1, pp. 1–14, Jul. 2013.

[88] L. Andrés *et al.*, "Rapid synthesis of ultra-long silver nanowires for tailor-made transparent conductive electrodes: proof of concept in organic solar cells," *Nanotechnology*, vol. 26, no. 26, p. 265201, 2015.

[89] S.-I. Na, S.-S. Kim, J. Jo, and D.-Y. Kim, "Efficient and Flexible ITO-Free Organic Solar Cells Using Highly Conductive Polymer Anodes," *Adv. Mater.*, vol. 20, no. 21, pp. 4061–4067, 2008.

[90] Y. Galagan *et al.*, "ITO-free flexible organic solar cells with printed current collecting grids," *Sol. Energy Mater. Sol. Cells*, vol. 95, no. 5, pp. 1339–1343, 2011.

[91] E. Pavlopoulou, G. Fleury, D. Deribew, F. Cousin, M. Geoghegan, and G. Hadziioannou, "Phase separation-driven stratification in conventional and inverted P3HT:PCBM organic solar cells," *Org. Electron.*, vol. 14, no. 5, pp. 1249–1254, 2013.

[92] J. U. Lee, J. W. Jung, J. W. Jo, and W. H. Jo, "Degradation and stability of polymer-

based solar cells," *J. Mater. Chem.*, vol. 22, no. 46, pp. 24265–24283, 2012.

[93] N. Grossiord, J. M. Kroon, R. Andriessen, and P. W. M. Blom, "Degradation mechanisms in organic photovoltaic devices," *Org. Electron.*, vol. 13, no. 3, pp. 432–456, Mar. 2012.

[94] M. Jørgensen, K. Norrman, and F. C. Krebs, "Stability/degradation of polymer solar cells," *Sol. Energy Mater. Sol. Cells*, vol. 92, no. 7, pp. 686–714, Jul. 2008.

[95] H. Hintz, H.-J. Egelhaaf, L. Lüer, J. Hauch, H. Peisert, and T. Chassé, "Photodegradation of P3HT−A Systematic Study of Environmental Factors," *Chem. Mater.*, vol. 23, no. 2, pp. 145–154, 2011.

[96] M. Manceau, A. Rivaton, and J. L. Gardette, "Involvement of singlet oxygen in the solid-state photochemistry of P3HT," *Macromol. Rapid Commun.*, vol. 29, no. 22, pp. 1823–1827, 2008.

[97] B. Roth *et al.*, "The Critical Choice of PEDOT:PSS Additives for Long Term Stability of Roll-to-Roll Processed OPVs," *Adv. Energy Mater.*, vol. 5, no. 9, 2015.

[98] F. C. Krebs and K. Norrman, "Analysis of the Failure Mechanism for a Stable Organic Photovoltaic During 10 000 h of Testing," *Prog. Photovolt. Res. Appl.*, vol. 15, no. 8, pp. 697–712, 2007.

[99] M. Vogel, S. Doka, C. Breyer, M. C. Lux-Steiner, and K. Fostiropoulos, "On the function of a bathocuproine buffer layer in organic photovoltaic cells," *Appl. Phys. Lett.*, vol. 89, no. 16, pp. 163501–163501, 2006.

[100] M. Glatthaar *et al.*, "Efficiency limiting factors of organic bulk heterojunction solar cells identified by electrical impedance spectroscopy," *Sol. Energy Mater. Sol. Cells*, vol. 91, no. 5, pp. 390–393, Mar. 2007.

[101] L. Zuo, J. Yao, H. Li, and H. Chen, "Assessing the origin of the S-shaped I–V curve in organic solar cells: An improved equivalent circuit model," *Sol. Energy Mater. Sol. Cells*, vol. 122, pp. 88–93, Mar. 2014.

[102] G. Dennler *et al.*, "A new encapsulation solution for flexible organic solar cells," *Thin Solid Films*, vol. 511, pp. 349–353, Jul. 2006.

[103] C. Lungenschmied *et al.*, "Flexible, long-lived, large-area, organic solar cells," *Sol. Energy Mater. Sol. Cells*, vol. 91, no. 5, pp. 379–384, Mar. 2007.

[104] L. La Notte *et al.*, "Influence of encapsulation materials on the optical properties and conversion efficiency of heat-sealed flexible polymer solar cells," *Surf. Coatings Technol.*, vol. 255, pp. 69–73, 2014.

[105] F. C. Krebs, "Encapsulation of polymer photovoltaic prototypes," *Sol. Energy Mater. Sol. Cells*, vol. 90, no. 20, pp. 3633–3643, Dec. 2006.

[106] J. Ahmad, K. Bazaka, L. J. Anderson, R. D. White, and M. V. Jacob, "Materials and methods for encapsulation of OPV: A review," *Renew. Sustain. Energy Rev.*, vol. 27, pp. 104–117, 2013.

[107] A. Norris, N. Powell, B. Ketola, J. N. Cotsell, and K. R. Mcintosh, "Advanced Silicone Photovoltaic Encapsulants," *Future Photovoltaics*, no. September, pp. 1–8, 2010.

[108] M. D. Kempe, "Accelerated UV Test Methods for Encapsulants of Photovoltaic Modules," *33rd IEEE Photovolt. Spec. Conf.*, no. May, 2008.

[109] M. Kempe, "Overview of scientific issues involved in selection of polymers for PV applications," *37th IEEE Photovolt. Spec. Conf.*, no. June 19-24, 2011.

[110] S. Cros *et al.*, "Definition of encapsulation barrier requirements: A method applied to organic solar cells," *Sol. Energy Mater. Sol. Cells*, vol. 95, no. SUPPL. 1, pp. S65–S69, 2011.

[111] F. C. Krebs *et al.*, "The OE-A OPV demonstrator anno domini 2011," *Energy Environ. Sci.*, vol. 4, no. 10, pp. 4116–4123, 2011.

[112] F. C. Krebs *et al.*, "Freely available OPV - The fast way to progress," *Energy Technol.*, vol. 1, no. 7, pp. 378–381, 2013.

[113] R. R. Søndergaard *et al.*, "The use of polyurethane as encapsulating method for polymer solar cells — An inter laboratory study on outdoor stability in 8 countries," *Sol. Energy Mater. Sol. Cells*, vol. 99, pp. 292–300, 2012.

[114] W. Shockley and H. J. Queisser, "Detailed Balance Limit of Efficiency of p-n Junction Solar Cells," *J. Appl. Phys.*, vol. 32, no. 3, p. 510, 1961.

[115] S. Rühle, "Tabulated values of the Shockley–Queisser limit for single junction solar cells," *Sol. Energy*, vol. 130, pp. 139–147, 2016.

[116] R. A. J. Janssen and J. Nelson, "Factors limiting device efficiency in organic photovoltaics," *Adv. Mater.*, vol. 25, no. 13, pp. 1847–1858, 2013.

[117] "Solar spectrum," *AIP STAC Conference*, 2005. [Online]. Available: http://www.vicphysics.org/documents/events/stav2005/spectrum.JPG. [Accessed: 21-Nov-2016].

[118] J. D. Servaites, S. Yeganeh, T. J. Marks, and M. A. Ratner, "Efficiency Enhancement in Organic Photovoltaic Cells: Consequences of Optimizing Series Resistance," *Adv. Funct. Mater.*, vol. 20, no. 1, pp. 97–104, Jan. 2010.

[119] M. O. Reese *et al.*, "Consensus stability testing protocols for organic photovoltaic materials and devices," *Sol. Energy Mater. Sol. Cells*, vol. 95, no. 5, pp. 1253–1267, May 2011.

[120] L. Dunn, M. Gostein, and K. Emery, "Comparison of Pyranometers vs. PV Reference Cells for Evaluation of PV Array Performance," in *Photovoltaic Specialists Conference (PVSC) 38th IEEE*, 2012, pp. 2899–2904.

[121] British Standard, "IEC 61724:1998. Photovoltaic system performance monitoring — Guidelines for measurement , data exchange and analysis," p. 20, 1998.

[122] T. Dierauf, A. Growitz, S. Kurtz, and C. Hansen, "Weather-Corrected Performance Ratio," *NREL Tech. Rep. NREL/TP-5200-57991*, no. April, pp. 1–16, 2013.

[123] T. Ishii, T. Takashima, and K. Otani, "Long-term performance degradation of various kinds of photovoltaic modules under moderate climatic conditions," *Prog. Photovolt. Res. Appl.*, vol. 19, no. 2, pp. 170–179, Mar. 2011.

[124] F. C. Krebs, "Roll-to-roll fabrication of monolithic large-area polymer solar cells free from indium-tin-oxide," *Sol. Energy Mater. Sol. Cells*, vol. 93, no. 9, pp. 1636–1641, 2009.

[125] F. C. Krebs, R. Søndergaard, and M. Jørgensen, "Printed metal back electrodes for R2R fabricated polymer solar cells studied using the LBIC technique," *Sol. Energy Mater. Sol. Cells*, vol. 95, no. 5, pp. 1348–1353, 2011.

[126] R. R. Søndergaard, M. Hösel, and F. C. Krebs, "Roll-to-Roll fabrication of large area functional organic materials," *J. Polym. Sci. Part B Polym. Phys.*, vol. 51, no. 1, pp. 16–34, 2013.

[127] M. Hösel, H. F. Dam, and F. C. Krebs, "Development of Lab-to-Fab Production

Equipment Across Several Length Scales for Printed Energy Technologies, Including Solar Cells," *Energy Technol.*, vol. 3, no. 4, pp. 293–304, 2015.

[128] E. A. Katz, S. Gevorgyan, M. S. Orynbayev, and F. C. Krebs, "Out-door testing and long-term stability of plastic solar cells," *Eur. Phys. J. Appl. Phys.*, vol. 36, no. 3, pp. 307–311, 2006.

[129] J. A. Hauch, P. Schilinsky, S. A. Choulis, R. Childers, M. Biele, and C. J. Brabec, "Flexible organic P3HT : PCBM bulk-heterojunction modules with more than 1 year outdoor lifetime," *Sol. Energy Mater. Sol. Cells*, vol. 92, pp. 727–731, 2008.

[130] D. Angmo *et al.*, "Outdoor operational stability of indium-free flexible polymer solar modules over 1 year studied in India, Holland, and Denmark," *Adv. Eng. Mater.*, vol. 16, no. 8, pp. 976–987, 2014.

[131] D. Angmo *et al.*, "Scalability and stability of very thin, roll-to-roll processed, large area, indium-tin-oxide free polymer solar cell modules," *Org. Electron.*, vol. 14, no. 3, pp. 984–994, Mar. 2013.

[132] D. Angmo and F. C. Krebs, "Over 2 Years of Outdoor Operational and Storage Stability of ITO-Free, Fully Roll-to-Roll Fabricated Polymer Solar Cell Modules," *Energy Technol.*, vol. 3, no. 7, pp. 774–783, 2015.

[133] S. A. Gevorgyan *et al.*, "Interlaboratory indoor ageing of roll-to-roll and spin coated organic photovoltaic devices: Testing the ISOS tests," *Polym. Degrad. Stab.*, vol. 109, pp. 162–170, 2014.

[134] M. V. Madsen *et al.*, "Worldwide outdoor round robin study of organic photovoltaic devices and modules," *Sol. Energy Mater. Sol. Cells*, vol. 130, pp. 281–290, Nov. 2014.

[135] S. A. Gevorgyan *et al.*, "Round robin performance testing of organic photovoltaic devices," *Renew. Energy*, vol. 63, pp. 376–387, 2014.

[136] F. C. Krebs *et al.*, "A round robin study of flexible large-area roll-to-roll processed polymer solar cell modules," *Sol. Energy Mater. Sol. Cells*, vol. 93, no. 11, pp. 1968–1977, Nov. 2009.

[137] S. A. Gevorgyan *et al.*, "Interlaboratory outdoor stability studies of flexible roll-to-roll coated organic photovoltaic modules: Stability over 10,000h," *Sol. Energy Mater. Sol. Cells*, vol. 116, pp. 187–196, Sep. 2013.

[138] S. A. Gevorgyan *et al.*, "An inter-laboratory stability study of roll-to-roll coated flexible polymer solar modules," *Sol. Energy Mater. Sol. Cells*, vol. 95, no. 5, pp. 1398–1416, 2011.

[139] O. Haillant, "Accelerated weathering testing principles to estimate the service life of organic PV modules," *Sol. Energy Mater. Sol. Cells*, vol. 95, no. 5, pp. 1284–1292, 2011.

[140] M. Corazza, F. C. Krebs, and S. A. Gevorgyan, "Lifetime of organic photovoltaics: Linking outdoor and indoor tests," *Sol. Energy Mater. Sol. Cells*, vol. 143, pp. 467–472, 2015.

[141] C. Owens *et al.*, "Comparative Indoor and Outdoor Degradation of Organic Photovoltaic Cells via Inter-laboratory Collaboration," *Polymers*, vol. 8, no. 1, p. 1, 2015.

[142] H. C. Weerasinghe, D. Vak, B. Robotham, C. J. Fell, D. Jones, and A. D. Scully, "New barrier encapsulation and lifetime assessment of printed organic photovoltaic

modules," *Sol. Energy Mater. Sol. Cells*, vol. 155, pp. 108–116, 2016.

[143] C. J. M. Emmott *et al.*, "In-situ , long-term operational stability of organic photovoltaics for off-grid applications in Africa," *Sol. Energy Mater. Sol. Cells*, vol. 149, pp. 284–293, 2016.

[144] A. J. Medford *et al.*, "Grid-connected polymer solar panels: initial considerations of cost, lifetime, and practicality.," *Opt. Express*, vol. 18, no. 103, pp. A272-285, Sep. 2010.

[145] F. C. Krebs, N. Espinosa, M. Hösel, R. R. Søndergaard, and M. Jørgensen, "25th Anniversary Article: Rise to Power - OPV-Based Solar Parks," *Adv. Mater.*, vol. 26, no. 1, pp. 29–39, Jan. 2014.

[146] P. Sommer-Larsen, M. Jørgensen, R. R. Søndergaard, M. Hösel, and F. C. Krebs, "It is all in the Pattern-High-Efficiency Power Extraction from Polymer Solar Cells through High-Voltage Serial Connection," *Energy Technol.*, vol. 1, no. 1, pp. 15–19, Jan. 2013.

[147] D. M. Tanenbaum, H. F. Dam, R. Rösch, M. Jørgensen, H. Hoppe, and F. C. Krebs, "Edge sealing for low cost stability enhancement of roll-to-roll processed flexible polymer solar cell modules," *Sol. Energy Mater. Sol. Cells*, vol. 97, pp. 157–163, 2012.

[148] N. Espinosa, M. Hösel, D. Angmo, and F. C. Krebs, "Solar cells with one-day energy payback for the factories of the future," *Energy Environ. Sci.*, vol. 5, no. 1, p. 5117, 2012.

[149] K. A. Mazzio and C. K. Luscombe, "The future of organic photovoltaics," *Chem. Soc. Rev.*, vol. 44, no. 1, pp. 78–90, 2015.

[150] L. Lucera *et al.*, "Guidelines for Closing the Efficiency Gap between Hero Solar Cells and Roll-To-Roll Printed Modules," *Energy Technol.*, vol. 3, no. 4, pp. 373–384, 2015.

[151] E. A. Katz *et al.*, "Temperature dependence for the photovoltaic device parameters of polymer-fullerene solar cells under operating conditions," *J. Appl. Phys.*, vol. 90, no. 10, p. 5343, 2001.

[152] I. Riedel, J. Parisi, V. Dyakonov, L. Lutsen, D. Vanderzande, and J. C. Hummelen, "Effect of Temperature and Illumination on the Electrical Characteristics of Polymer–Fullerene Bulk-Heterojunction Solar Cells," *Adv. Funct. Mater.*, vol. 14, no. 1, pp. 38–44, Jan. 2004.

[153] T. Tromholt, E. A. Katz, B. Hirsch, A. Vossier, and F. C. Krebs, "Effects of concentrated sunlight on organic photovoltaics," *Appl. Phys. Lett.*, vol. 96, no. 7, p. 73501, 2010.

[154] J. Zhao and M. A. Green, "Optimized antireflection coatings for high efficiency silicon solar cells," *IEEE Trans. Electron Devices*, vol. 38, no. 8, pp. 1925–1934, 1991.

[155] N. Shibata, "Plasma-Chemical Vapor-Deposited Silicon Oxide/Silicon Oxynitride Double-Layer Antireflective Coating for Solar Cells," *Jpn. J. Appl. Phys.*, vol. 30, no. 5R, p. 997, 1991.

[156] P. Campbell and M. A. Green, "Light trapping properties of pyramidally textured surfaces," *J. Appl. Phys.*, vol. 62, no. 1, pp. 243–249, 1987.

[157] C. G. Bernhard, "Structural and functional adaptation in a visual system.," *Endeavour*, vol. 26, no. 98, pp. 79–84, 1967.

[158] A. P. Amalathas and M. M. Alkaisi, "Efficient light trapping nanopyramid structures for solar cells patterned using UV nanoimprint lithography," *Mater. Sci. Semicond. Process.*, vol. 57, pp. 54–58, 2017.

[159] F. Jiao *et al.*, "Enhanced performance for solar cells with moth-eye structure fabricated by UV nanoimprint lithography," *Microelectron. Eng.*, vol. 103, no. November, pp. 126–130, 2013.

[160] T. Lohmueller, R. Brunner, and J. P. Spatz, "Improved Properties of Optical Surfaces by Following the Example of the 'Moth Eye,'" in *Biomimetics Learning From Nature*, A. Mukherjee, Ed. InTech, 2010.

[161] P. I. Stavroulakis, S. A. Boden, T. Johnson, and D. M. Bagnall, "Suppression of backscattered diffraction from sub-wavelength 'moth-eye' arrays.," *Opt. Express*, vol. 21, no. 1, pp. 1–11, 2013.

[162] K. S. Han, H. Lee, D. Kim, and H. Lee, "Fabrication of anti-reflection structure on protective layer of solar cells by hot-embossing method," *Sol. Energy Mater. Sol. Cells*, vol. 93, no. 8, pp. 1214–1217, 2009.

[163] A. Haque, F. Sultana, M. A. Awal, and M. Rahman, "Efficiency Improvement of Bulk Heterojunction Organic Photovoltaic Solar Cell through Device Architecture Modification," *Int. J. Eng. Technol.*, vol. 4, no. 5, pp. 567–572, 2012.

[164] S.-Y. Chuang, C.-C. Yu, H.-L. Chen, W.-F. Su, and C.-W. Chen, "Exploiting optical anisotropy to increase the external quantum efficiency of flexible P3HT:PCBM blend solar cells at large incident angles," *Sol. Energy Mater. Sol. Cells*, vol. 95, no. 8, pp. 2141–2150, Aug. 2011.

[165] K. Forberich, G. Dennler, M. C. Scharber, K. Hingerl, T. Fromherz, and C. J. Brabec, "Performance improvement of organic solar cells with moth eye anti-reflection coating," *Thin Solid Films*, vol. 516, no. 20, pp. 7167–7170, 2008.

[166] J. Kettle, A. Rees, E. B. Brousseau, and M. Horie, "Low-temperature thermal nanoimprint lithography of anti-reflective structures for flexible low band gap organic solar cells," *J. Phys. D. Appl. Phys.*, vol. 46, no. 10, p. 105102, 2013.

[167] D.-H. Ko *et al.*, "Light-trapping nano-structures in organic photovoltaic cells," *J. Mater. Chem.*, vol. 21, no. 41, p. 16293, 2011.

[168] Q. Gan, F. J. Bartoli, and Z. H. Kafafi, "Plasmonic-enhanced organic photovoltaics: breaking the 10% efficiency barrier.," *Adv. Mater.*, vol. 25, no. 17, pp. 2385–96, May 2013.

[169] S. I. Na, S. S. Kim, J. Jo, S. H. Oh, J. Kim, and D. Y. Kim, "Efficient polymer solar cells with surface relief gratings fabricated by simple soft lithography," *Adv. Funct. Mater.*, vol. 18, no. 24, pp. 3956–3963, 2008.

[170] M. Peters, J. C. Goldschmidt, T. Kirchartz, and B. Bläsi, "The photonic light trap-Improved light trapping in solar cells by angularly selective filters," *Sol. Energy Mater. Sol. Cells*, vol. 93, no. 10, pp. 1721–1727, 2009.

[171] Z. Tang, W. Tress, and O. Inganas, "Light trapping in thin film organic solar cells," *Mater. Today*, vol. 17, no. 8, pp. 389–396, 2014.

[172] M. Niggemann, M. Glatthaar, A. Gombert, A. Hinsch, and V. Wittwer, "Diffraction gratings and buried nano-electrodes - Architectures for organic solar cells," *Thin Solid Films*, vol. 451–452, pp. 619–623, 2004.

[173] A. Morales-Acevedo (Ed.), *Solar Cells - Research and Application Perspectives*. InTech, 2013.

[174] M. Bernardi, N. Ferralis, J. H. Wan, R. Villalon, and J. C. Grossman, "Solar energy generation in three dimensions," *Energy Environ. Sci.*, vol. 5, no. 5, pp. 6880–6884,

2012.

[175] B. Myers, M. Bernardi, and J. C. Grossman, “Three-dimensional photovoltaics,” *Appl. Phys. Lett.*, vol. 96, no. 7, p. 71902, 2010.

[176] V. Zardetto *et al.*, “Outdoor and diurnal performance of large conformal flexible metal/plastic dye solar cells,” *Appl. Energy*, vol. 113, pp. 1155–1161, Jan. 2014.

[177] S. B. Rim, S. Zhao, S. R. Scully, M. D. McGehee, and P. Peumans, “An effective light trapping configuration for thin-film solar cells,” *Appl. Phys. Lett.*, vol. 91, no. 24, p. 243501, 2007.

[178] S. J. Kim, G. Y. Margulis, S.-B. Rim, M. L. Brongersma, M. D. McGehee, and P. Peumans, “Geometric light trapping with a V-trap for efficient organic solar cells.,” *Opt. Express*, vol. 21, no. 103, pp. A305-312, 2013.

[179] K. Tvingstedt, V. Andersson, F. Zhang, and O. Inganäs, “Folded reflective tandem polymer solar cell doubles efficiency,” *Appl. Phys. Lett.*, vol. 91, no. 12, p. 123514, 2007.

[180] N. J. Alley, S. Dias, K.-S. Liao, and S. A. Curran, “Fabrication, characterization, and optical modeling of a new architecture for organic photovoltaics: The vertically orientated stack device,” *J. Appl. Phys.*, vol. 111, no. 6, p. 64914, 2012.

[181] G. Dennler *et al.*, “Angle dependence of external and internal quantum efficiencies in bulk-heterojunction organic solar cells,” *J. Appl. Phys.*, vol. 102, no. 5, p. 54516, 2007.

[182] E. Klampaftis, D. Ross, K. R. McIntosh, and B. S. Richards, “Enhancing the performance of solar cells via luminescent down-shifting of the incident spectrum: A review,” *Sol. Energy Mater. Sol. Cells*, vol. 93, no. 8, pp. 1182–1194, Aug. 2009.

[183] B. S. Richards, “Enhancing the performance of silicon solar cells via the application of passive luminescence conversion layers,” *Sol. Energy Mater. Sol. Cells*, vol. 90, no. 15, pp. 2329–2337, Sep. 2006.

[184] B. S. Richards, “Luminescent layers for enhanced silicon solar cell performance: Down-conversion,” *Sol. Energy Mater. Sol. Cells*, vol. 90, no. 9, pp. 1189–1207, May 2006.

[185] T. Trupke, M. A. Green, and P. Würfel, “Improving solar cell efficiencies by down-conversion of high-energy photons,” *J. Appl. Phys.*, vol. 92, no. 3, pp. 1668–1674, 2002.

[186] T. Trupke, M. A. Green, and P. Würfel, “Improving solar cell efficiencies by up-conversion of sub-band-gap light,” *J. Appl. Phys.*, vol. 92, no. 7, pp. 4117–4122, 2002.

[187] G. G. Stokes, “On the Change of Refrangibility of Light,” *Philos. Trans. R. Soc. London*, vol. 142, pp. 463–562, 1852.

[188] R. Rothemund, “Optical modelling of the external quantum efficiency of solar cells with luminescent down-shifting layers,” *Sol. Energy Mater. Sol. Cells*, vol. 120, no. PART B, pp. 616–621, 2014.

[189] A. I. Lvovsky, “Fresnel Equations,” in *Encyclopedia of Optical Engineering*, Taylor and Francis: New York, Published online: 27 Feb 2013, pp. 1–6.

[190] S. McDowall, T. Butler, E. Bain, K. Scharnhorst, and D. Patrick, “Comprehensive analysis of escape-cone losses from luminescent waveguides.,” *Appl. Opt.*, vol. 52, no. 6, pp. 1230–9, 2013.

[191] W. A. Shurcliff and R. C. Jones, “The trapping of fluorescent light produced within objects of high geometrical symmetry,” *J. Opt. Soc. Am.*, vol. 39, no. 11, pp. 912–916,

1949.

[192] H. J. Hovel, R. T. Hodgson, and J. M. Woodall, “The effect of fluorescent wavelength shifting on solar cell spectral response,” *Sol. Energy Mater.*, vol. 2, no. 1, pp. 19–29, 1979.

[193] B. S. Richards and E. Klampaftis, “Luminescent Encapsulation Layers for Multicrystalline Silicon PV Modules,” *Photovoltaics Int.*, pp. 104–109, 2011.

[194] E. Klampaftis, M. Congiu, N. Robertson, and B. S. Richards, “Luminescent Ethylene Vinyl Acetate Encapsulation Layers for Enhancing the Short Wavelength Spectral Response and Efficiency of Silicon Photovoltaic Modules,” *IEEE J. Photovoltaics*, vol. 1, no. 1, pp. 29–36, 2011.

[195] E. Klampaftis and B. S. Richards, “Improvement in multi-crystalline silicon solar cell efficiency via addition of luminescent material to EVA encapsulation layer,” *Prog. Photovolt. Res. Appl.*, vol. 19, no. 3, pp. 345–351, 2011.

[196] D. Ross *et al.*, “The Impact of Luminescent Down Shifting on the Performance of CdTe Photovoltaics : Impact of the Module Vintage,” *IEEE J. Photovoltaics*, vol. 4, no. 1, pp. 457–464, 2014.

[197] E. Klampaftis, D. Ross, S. Seyrling, A. N. Tiwari, and B. S. Richards, “Increase in short-wavelength response of encapsulated CIGS devices by doping the encapsulation layer with luminescent material,” *Sol. Energy Mater. Sol. Cells*, vol. 101, pp. 62–67, Jun. 2012.

[198] K. Mcintosh, G. Lau, J. Cotsell, K. Hanton, and D. Batzner, “Increase in External Quantum Efficiency of Encapsulated Silicon Solar Cells from a Luminescent Down-Shifting layer,” *Prog. Photovolt. Res. Appl.*, vol. 17, no. 3, pp. 191–197, 2009.

[199] M. Kennedy *et al.*, “Large Stokes shift downshifting Eu(III) films as efficiency enhancing UV blocking layers for dye sensitized solar cells,” *Phys. Status Solidi Appl. Mater. Sci.*, vol. 212, no. 1, pp. 203–210, 2015.

[200] H. Ahmed *et al.*, “Characterization of Luminescent Down-Shifting Materials and Applications for PV Devices,” in *Proceedings of the 8th Photovoltaic Science Application and Technology (PVSAT-8) Conference and Exhibition.*, 2012, pp. 1–4.

[201] L. Aubouy *et al.*, “Ephocell project: smart light collecting system for the efficiency enhancement of solar cells - ray trace modeling of downshifting and upconverting systems,” *27th Eur. Photovolt. Sol. Energy Conf.*, 2012.

[202] A. Turshatov, D. Busko, Y. Avlasevich, T. Miteva, K. Landfester, and S. Baluschev, “Synergetic effect in triplet-triplet annihilation upconversion: Highly efficient multi-chromophore emitter,” *ChemPhysChem*, vol. 13, no. 13, pp. 3112–3115, 2012.

[203] M. Zahedifar, Z. Chamanzadeh, and S. M. Hosseinpoor Mashkani, “Synthesis of LaVO4: Dy3+ luminescent nanostructure and optimization of its performance as down-converter in dye-sensitized solar cells,” *J. Lumin.*, vol. 135, pp. 66–73, 2013.

[204] Z. Hosseini, W. Huang, C. Tsai, T. Chen, N. Taghavinia, and E. W. Diau, “Enhanced Light Harvesting with a Reflective Luminescent Down-Shifting Layer for Dye-Sensitized Solar Cells,” *ACS Appl. Mater. Interfaces*, vol. 5, no. 12, pp. 5397–5402, 2013.

[205] Z. Hosseini, E. W.-G. Diau, K. Mehrany, and N. Taghavinia, “Assessment of Luminescent Downshifting Layers for the Improvement of Light-Harvesting Efficiency in Dye-Sensitized Solar Cells,” *ChemPhysChem*, vol. 15, no. 17, pp. 3791–3799, 2014.

[206] Z. Hosseini, N. Taghavinia, and E. W.-G. Diau, “Application of a dual functional luminescent layer to enhance the light harvesting efficiency of dye sensitized solar cell,” *Mater. Lett.*, vol. 188, no. February, pp. 92–94, 2017.

[207] G. Ma, H. Xie, P. Cheng, Y. Li, and J. Tang, “Performance enhancement of polymer solar cells with luminescent down-shifting sensitizer,” *Appl. Phys. Lett.*, vol. 103, no. 4, p. 43302, 2013.

[208] A. J. Das and K. S. Narayan, “Retention of power conversion efficiency--from small area to large area polymer solar cells.,” *Adv. Mater.*, vol. 25, no. 15, pp. 2193–9, Apr. 2013.

[209] M. Prosa *et al.*, “Integration of a silk fibroin based film as a luminescent down-shifting layer in ITO-free organic solar cells,” *RSC Adv.*, vol. 4, no. 84, pp. 44815–44822, 2014.

[210] W. Xu *et al.*, “YVO4:Eu3+,Bi3+ UV to visible conversion nano-films used for organic photovoltaic solar cells,” *J. Mater. Chem.*, vol. 21, no. 33, pp. 12331–12336, 2011.

[211] P. G. Parejo, M. Zayat, and D. Levy, “Highly efficient UV-absorbing thin-film coatings for protection of organic materials against photodegradation,” *J. Mater. Chem.*, vol. 16, no. 22, p. 2165, 2006.

[212] M. Zayat, P. Garcia-Parejo, and D. Levy, “Preventing UV-light damage of light sensitive materials using a highly protective UV-absorbing coating.,” *Chem. Soc. Rev.*, vol. 36, no. 8, pp. 1270–1281, 2007.

[213] M. Sun Ryu, H. Jin Cha, and J. Jang, “Improvement of operation lifetime for conjugated polymer:fullerene organic solar cells by introducing a UV absorbing film,” *Sol. Energy Mater. Sol. Cells*, vol. 94, no. 2, pp. 152–156, 2010.

[214] V. Turkovic *et al.*, “Long-term stabilization of organic solar cells using UV absorbers,” *J. Phys. D Appl. Phys.*, vol. 49, no. 12, p. 125604, 2016.

[215] S. Engmann *et al.*, “Photon recycling across a ultraviolet-blocking layer by luminescence in polymer solar cells,” *J. Appl. Phys.*, vol. 112, no. 3, p. 34517, 2012.

[216] A. Goetzberger and W. Greubel, “Solar Energy Conversion with Fluorescent Collectors,” *Appl. Phys.*, vol. 14, no. 2, pp. 123–139, 1977.

[217] W. H. Weber and J. Lambe, “Luminescent greenhouse collector for solar radiation.,” *Appl. Opt.*, vol. 15, no. 10, pp. 2299–2300, 1976.

[218] M. Ayad, M. Fathi, M. Abderrazak, and A. Aissat, “Studies of the Effect of a Photons Converter (LDS) on the Characteristic Parameters of the Solar Cells,” *Int. J. Renew. Energy Res.*, vol. 2, no. 4, pp. 596–599, 2012.

[219] D. Alonso-Álvarez, D. Ross, and B. S. Richards, “Luminescent down-shifting for CdTe solar cells : A review of dyes and simulation of performance,” *38th IEEE Photovolt. Spec. Conf.*, pp. 9–14, 2012.

[220] D. Ross *et al.*, “First ever full size CdTe luminescent down-shifting module,” *38th IEEE Photovolt. Spec. Conf.*, p. 1940, 2012.

[221] G. F. de Sá *et al.*, “Spectroscopic Properties and Design of Highly Luminescent Lanthanide Coordination Complexes,” *Coord. Chem. Rev.*, vol. 196, no. 1, pp. 165–195, 2000.

[222] Y. Yang *et al.*, “Listening to lanthanide complexes: Determination of the intrinsic luminescence quantum yield by nonradiative relaxation,” *ChemPhysChem*, vol. 9, no. 4, pp. 600–606, 2008.

[223] H. A. Ahmed, J. Walshe, M. Kennedy, T. Confrey, J. Doran, and S. J. McCormack, "Enhancement in solar cell efficiency by luminescent down-shifting layers," *Adv. Energy Res.*, vol. 1, no. 2, pp. 117–126, 2013.

[224] D. Alonso-Álvarez *et al.*, "Luminescent down-shifting experiment and modelling with multiple photovoltaic technologies," *Prog. Photovolt. Res. Appl.*, vol. 23, no. 4, pp. 479–497, 2015.

[225] M. S. Su'ait, M. Y. A. Rahman, and A. Ahmad, "Review on polymer electrolyte in dye-sensitized solar cells (DSSCs)," *Sol. Energy*, vol. 115, pp. 452–470, 2015.

[226] J. Preat, D. Jacquemin, and E. A. Perp, "Towards new efficient dye-sensitised solar cells," *Energy Environ. Sci.*, vol. 3, no. 7, pp. 891–904, 2010.

[227] A. Hagfeldt, G. Boschloo, L. Sun, L. Kloo, and H. Pettersson, "Dye-sensitized solar cells," *Chem. Rev.*, vol. 110, no. 11, pp. 6595–6663, Nov. 2010.

[228] S. Ferrere and B. A. Gregg, "New perylenes for dye sensitization of TiO2," *New J. Chem.*, vol. 26, no. 9, pp. 1155–1160, 2002.

[229] J. Clayden, N. Greeves, and S. Warren, *Organic Chemistry (2nd Ed)*. Oxford University Press, 2012.

[230] S. I. Weissman, "Intramolecular energy transfer. The fluorescence of complexes of europium," *J. Chem. Phys.*, vol. 10, no. 4, pp. 214–217, 1942.

[231] O. Moudam *et al.*, "Europium complexes with high total photoluminescence quantum yields in solution and in PMMA.," *Chem. Commun.*, vol. 43, pp. 6649–6651, 2009.

[232] J.-M. Lehn, "Perspectives in Supramolecular Chemistry—From Molecular Recognition towards Molecular Information Processing and Self-Organization," *Angew. Chemie Int. Ed.*, vol. 29, no. 11, pp. 1304–1319, 1990.

[233] C. W. Tang and S.A.VanSlyke, "Organic electroluminescent diodes," *Appl. Phys. Lett.*, vol. 51, no. 12, pp. 913–915, 1987.

[234] P. E. Burrows and S. R. Forrest, "Electroluminescence from trap-limited current transport in vacuum deposited organic light emitting devices," *Appl. Phys. Lett.*, vol. 64, no. 17, pp. 2285–2287, 1994.

[235] L. Danos, T. Parel, T. Markvart, V. Barrioz, W. S. M. Brooks, and S. J. C. Irvine, "Increased efficiencies on CdTe solar cells via luminescence down-shifting with excitation energy transfer between dyes," *Sol. Energy Mater. Sol. Cells*, vol. 98, pp. 486–490, Mar. 2012.

[236] B. Basheer, D. Mathew, B. K. George, and C. P. Reghunadhan Nair, "An overview on the spectrum of sensitizers: The heart of Dye Sensitized Solar Cells," *Sol. Energy*, vol. 108, pp. 479–507, 2014.

[237] L. R. Wilson, "Luminescent Solar Concentrators; A study of optical properties, re-absorption and device optimisation," Doctoral dissertation, Heriot-Watt University, Edinburgh, 2010.

[238] E. Klampaftis, "On improving the short-wavelength response and efficiency of photovoltaic modules via luminescent down-shifting of the incident light," Doctoral dissertation, Heriot-Watt University, Edinburgh, 2013.

[239] "Kremer Fluorescent Dyes." [Online]. Available: http://shop.kremerpigments.com/en/dyes-und-vegetable-color-paints/fluorescent-colors/. [Accessed: 12-Dec-2016].

[240] K. D. Seo *et al.*, "Coumarin dyes containing low-band-gap chromophores for dye-

sensitised solar cells," *Dye. Pigment.*, vol. 90, no. 3, pp. 304–310, 2011.

[241] K. Hara *et al.*, "Molecular design of coumarin dyes for efficient dye-sensitized solar cells," *J. Phys. Chem. B*, vol. 107, no. 2, pp. 597–606, 2003.

[242] C. Würth, M. Grabolle, J. Pauli, M. Spieles, and U. Resch-Genger, "Comparison of methods and achievable uncertainties for the relative and absolute measurement of photoluminescence quantum yields.," *Anal. Chem.*, vol. 83, no. 9, pp. 3431–9, May 2011.

[243] C. Martín, M. Ziółek, and A. Douhal, "Ultrafast and Fast Charge Separation Processes in Real Dye-Sensitized Solar Cells," *J. Photochem. Photobiol. C Photochem. Rev.*, vol. 26, pp. 1–30, 2016.

[244] J. E. Moser and M. Gratzel, "Observation of temperature independent heterogeneous electron transfer reactions in the inverted Marcus region," *Chem. Phys.*, vol. 176, no. 2–3, pp. 493–500, 1993.

[245] J. M. Drake, M. L. Lesiecki, J. Sansregret, and W. R. L. Thomas, "Organic dyes in PMMA in a planar luminescent solar collector: a performance evaluation," *Appl. Opt.*, vol. 21, no. 16, pp. 2945–2952, 1982.

[246] B. Beyer and K. Leo, "Efficiency increase of organic solar cells with emissive light-in-coupling layers," *J. Mater. Chem. C*, vol. 3, no. 41, pp. 10830–10836, 2015.

[247] S. D. Hodgson, W. S. M. Brooks, A. J. Clayton, G. Kartopu, V. Barrioz, and S. J. C. Irvine, "The impact of quantum dot concentration on the optical properties of QD/PMMA luminescent down-shifting films applied to CdTe photovoltaic devices," *Nano Energy*, vol. 4, pp. 1–6, 2014.

[248] R. F. Kubin and A. N. Fletcher, "Fluorescence quantum yields of some rhodamine dyes," *J. Lumin.*, vol. 27, no. 4, pp. 455–462, 1983.

[249] B. C. Rowan, L. R. Wilson, and B. S. Richards, "Advanced Material Concepts for Luminescent Solar Concentrators," *IEEE J. Sel. Top. Quantum Electron.*, vol. 14, no. 5, pp. 1312–1322, 2008.

[250] J. Gutmann *et al.*, "Emission of Rhodamine B in PMMA opals for luminescent solar concentrators," *SPIE Photonics Eur.*, vol. 8438, 2012.

[251] G. Maggioni, A. Campagnaro, S. Carturan, and A. Quaranta, "Dye-doped parylene-based thin film materials: Application to luminescent solar concentrators," *Sol. Energy Mater. Sol. Cells*, vol. 108, pp. 27–37, 2013.

[252] A. M. Bagher, M. M. A. Vahid, and M. Mohsen, "Types of Solar Cells and Application," *Am. J. Opt. Photonics*, vol. 3, no. 5, pp. 94–113, 2015.

[253] Z. Yao, A. Apostoluk, L. Shibin, S. Daniele, and B. Masenelli, "ZnO nanoparticles as a luminescent down-shifting layer for photosensitive devices," *J. Semicond.*, vol. 34, no. 5, p. 53005, May 2013.

[254] M. C. Peel, B. L. Finlayson, and T. A. McMahon, "Updated world map of the Köppen-Geiger climate classification," *Hydrol. Earth Syst. Sci. Discuss.*, vol. 4, no. 2, pp. 439–473, 2007.

[255] "Shell ST36 PV Module Specification." [Online]. Available: http://www.atlantasolar.com/pdf/Shell/ShellST36_USv1.pdf. [Accessed: 10-Jul-2016].

[256] "Davis Vantage Pro2 Weather Station." [Online]. Available: http://www.davisweather.co.uk/product-range/9-weather-stations/56-vantage-pro-2. [Accessed: 01-Jul-2016].

[257] M. Hösel, R. R. Søndergaard, M. Jørgensen, and F. C. Krebs, “Fast Inline Roll-to-Roll Printing for Indium-Tin-Oxide-Free Polymer Solar Cells Using Automatic Registration,” *Energy Technol.*, vol. 1, no. 1, pp. 102–107, Jan. 2013.

[258] B. Roth *et al.*, “Improving the Operational Stability of PBDTTTz-4 Polymer Solar Cells Modules by Electrode Modification,” *Adv. Eng. Mater.*, vol. 18, no. 4, pp. 511–517, 2016.

[259] G. A. dos Reis Benatto *et al.*, “Carbon: The ultimate electrode choice for widely distributed polymer solar cells,” *Adv. Energy Mater.*, vol. 4, no. 15, 2014.

[260] M. Hösel *et al.*, “High-Volume Processed, ITO-Free Superstrates and Substrates for Roll-to-Roll Development of Organic Electronics,” *Adv. Sci.*, vol. 1, no. 1, 2014.

[261] G. A. dos Reis Benatto *et al.*, “Roll-to-roll printed silver nanowires for increased stability of flexible ITO-free organic solar cell modules.,” *Nanoscale*, vol. 8, no. 1, pp. 318–26, 2016.

[262] Y. Sun, J. H. Seo, C. J. Takacs, J. Seifter, and A. J. Heeger, “Inverted polymer solar cells integrated with a low-temperature-annealed sol-gel-derived ZnO film as an electron transport layer,” *Adv. Mater.*, vol. 23, no. 14, pp. 1679–1683, 2011.

[263] R. Rösch *et al.*, “Investigation of the degradation mechanisms of a variety of organic photovoltaic devices by combination of imaging techniques—the ISOS-3 inter-laboratory collaboration,” *Energy Environ. Sci.*, vol. 5, no. 4, pp. 6521–6540, 2012.

[264] *ASTM G173-03(2012), Standard Tables for Reference Solar Spectral Irradiances: Direct Normal and Hemispherical on 37° Tilted Surface*. ASTM International, West Conshohocken, PA, 2012.

[265] IEC, “IEC 60904-7 Photovoltaic Devices. Part 7: Computation of Spectral Mismatch Error Introduced in the Testing of a Photovoltaic Device.,” *Int. Electrotech. Comm. Ed. 3*, 2008.

[266] C. H. Seaman, “Calibration of solar cells by the reference cell method - The spectral mismatch problem,” *Sol. Energy*, vol. 29, no. 4, pp. 291–298, 1982.

[267] P. M. Sommeling *et al.*, “Spectral response and IV-characterization of dye-sensitized nanocrystalline TiO2 solar cells,” *Sol. Energy Mater. Sol. Cells*, vol. 62, no. 4, pp. 399–410, 2000.

[268] S. E. Shaheen, C. J. Brabec, S. N. Sariciftci, F. Padinger, T. Fromherz, and J. C. Hummelen, “2.5% Efficient Organic Plastic Solar Cells,” *Appl. Phys. Lett.*, vol. 78, no. 6, pp. 841–843, 2001.

[269] C. Palmer and E. Loewen, *Diffraction Grating Handbook (6th edition)*. Newport Corporation., 2005.

[270] F. C. Krebs and M. Jørgensen, “2D Characterization of OPV from Single and Tandem Cells to Fully Roll-to-Roll Processed Modules with and without Electrical Contact,” *Adv. Opt. Mater.*, vol. 2, no. 5, pp. 465–477, 2014.

[271] J. C. de Mello, F. Wittman, and R. H. Friend, “An Improved Experimental Determination of External Photoluminescence Quantum Efficiency,” *Adv. Mater.*, vol. 9, no. 3, pp. 230–232, 1997.

[272] “infinityOPV.” [Online]. Available: http://infinitypv.com/infinitypro/opv/foil. [Accessed: 11-Jan-2016].

[273] “PVSYST Photovoltaic Software.” [Online]. Available: http://www.pvsyst.com/en/. [Accessed: 14-Jan-2016].

[274] J. Freeman, J. Whitmore, N. Blair, and A. P. Dobos, "Validation of multiple tools for flat plate photovoltaic modeling against measured data," *40th IEEE Photovolt. Spec. Conf.*, no. August, pp. 1932–1937, 2014.

[275] N. Aste, C. Del Pero, F. Leonforte, and M. Manfren, "A simplified model for the estimation of energy production of PV systems," *Energy*, vol. 59, pp. 503–512, 2013.

[276] N. van der Borg and M. J. Jansen, "Energy loss due to shading in a BIPV application.," *Proc. 3rd World Conf. on Photovolt. Energy Convers. IEEE*, vol. 3, no. May, pp. 2220–2222, 2003.

[277] O. W. Westbrook and F. D. Collins, "Energy model validation for large-scale photovoltaic systems," *39th IEEE Photovolt. Spec. Conf.*, pp. 830–835, 2013.

[278] A. F. Souka and H. H. Safwat, "Determination of the optimum orientations for the double-exposure, flat-plate collector and its reflectors," *Sol. Energy*, vol. 10, no. 4, pp. 170–174, 1966.

[279] "MicroChem NANO^{TM}PMMA and Copolymer Data Sheet," 2016. [Online]. Available: http://microchem.com/pdf/PMMA_Data_Sheet.pdf. [Accessed: 19-Feb-2016].

[280] W. Liu, X. Tian, J. Zheng, and P. Cui, "Excitation Dependence of the Photoluminescence in Poly (ethylene terephthalate)," *Acta Polym. Sin.*, vol. 4, 2005.

[281] N. Shibata *et al.*, "Performance Validation of a Photovoltaic Inverter under Enhanced Cloud Edge Conditions," in *Future Energy Electronics Conference (IFEEC), 2015 IEEE 2nd International.*, 2015.

[282] E. Skoplaki and J. A. Palyvos, "Operating temperature of photovoltaic modules: A survey of pertinent correlations," *Renew. Energy*, vol. 34, no. 1, pp. 23–29, Jan. 2009.

[283] R. G. Ross, "Interface design considerations for terrestrial solar cell modules," *12th IEEE Photovolt. Spec. Conf.*, vol. 1, 1976.

[284] E. Skoplaki, A. G. Boudouvis, and J. A. Palyvos, "A simple correlation for the operating temperature of photovoltaic modules of arbitrary mounting," *Sol. Energy Mater. Sol. Cells*, vol. 92, no. 11, pp. 1393–1402, Nov. 2008.

[285] A. V. Shah *et al.*, "Material and solar cell research in microcrystalline silicon," *Sol. Energy Mater. Sol. Cells*, vol. 78, no. 1, pp. 469–491, Jul. 2003.

[286] W.-H. Baek, H. Yang, T.-S. Yoon, C. J. Kang, H. H. Lee, and Y.-S. Kim, "Effect of P3HT:PCBM concentration in solvent on performances of organic solar cells," *Sol. Energy Mater. Sol. Cells*, vol. 93, no. 8, pp. 1263–1267, Aug. 2009.

[287] K. Akhmad, A. Kitamura, F. Yamamoto, H. Okamoto, H. Takakura, and Y. Hamakawa, "Outdoor performance of amorphous silicon and polycrystalline silicon PV modules," *Sol. Energy Mater. Sol. Cells*, vol. 46, no. 3, pp. 209–218, Jun. 1997.

[288] G. Makrides, B. Zinsser, G. E. Georghiou, M. Schubert, and J. H. Werner, "Temperature behaviour of different photovoltaic systems installed in Cyprus and Germany," *Sol. Energy Mater. Sol. Cells*, vol. 93, no. 6, pp. 1095–1099, Jun. 2009.

[289] E. Skoplaki and J. A. Palyvos, "On the temperature dependence of photovoltaic module electrical performance: A review of efficiency/power correlations," *Sol. Energy*, vol. 83, no. 5, pp. 614–624, May 2009.

[290] M. Mattei, G. Notton, C. Cristofari, M. Muselli, and P. Poggi, "Calculation of the polycrystalline PV module temperature using a simple method of energy balance," *Renew. Energy*, vol. 31, no. 4, pp. 553–567, 2006.

[291] D. L. Evans, "Simplified method for predicting photovoltaic array output," *Sol.*

Energy, vol. 27, no. 6, pp. 555–560, 1981.

[292] G. Malliaras and R. Friend, "An Organic Electronics Primer," *Phys. Today*, vol. 58, no. 5, p. 53, 2005.

[293] R. Coehoorn, W. F. Pasveer, P. A. Bobbert, and M. A. J. Michels, "Charge-carrier concentration dependence of the hopping mobility in organic materials with Gaussian disorder," *Phys. Rev. B*, vol. 72, no. 15, p. 155206, 2005.

[294] L. A. Ribeiro, W. F. Cunha, P. H. O. Neto, R. Gargano, and G. M. Silva, "Impurity effects and temperature influence on the exciton dissociation dynamics in conjugated polymers," *Chem. Phys. Lett.*, vol. 580, pp. 108–114, 2013.

[295] S. R. Cowan, A. Roy, and A. J. Heeger, "Recombination in polymer-fullerene bulk heterojunction solar cells," *Phys. Rev. B*, vol. 82, no. 24, p. 245207, 2010.

[296] Frederik C. Krebs, *private communication*. 2014.

[297] M. Corazza, F. C. Krebs, and S. A. Gevorgyan, "Predicting, categorizing and intercomparing the lifetime of OPVs for different ageing tests," *Sol. Energy Mater. Sol. Cells*, vol. 130, pp. 99–106, Nov. 2014.

[298] T. Tromholt, A. Manor, E. A. Katz, and F. C. Krebs, "Reversible degradation of inverted organic solar cells by concentrated sunlight.," *Nanotechnology*, vol. 22, no. 22, p. 225401, Jun. 2011.

[299] B. Tripathi, P. Yadav, and M. Kumar, "Effect of varying illumination and temperature on steady-state and dynamic parameters of dye-sensitized solar cell using AC impedance modeling," *Int. J. Photoenergy*, vol. 2013, 2013.

[300] M. Grätzel, "Dye-sensitized solar cells," *J. Photochem. Photobiol. C Photochem. Rev.*, vol. 4, no. 2, pp. 145–153, 2003.

[301] A. Hauch and A. Georg, "Diffusion in the electrolyte and charge-transfer reaction at the platinum electrode in dye-sensitized solar cells," *Electrochim. Acta*, vol. 46, no. 22, pp. 3457–3466, 2001.

[302] T. Toyoda *et al.*, "Outdoor performance of large scale DSC modules," *J. Photochem. Photobiol. A Chem.*, vol. 164, no. 1, pp. 203–207, 2004.

[303] A. Asghar, M. Emziane, H. K. Pak, and S. Y. Oh, "Outdoor testing and degradation of dye-sensitized solar cells in Abu Dhabi," *Sol. Energy Mater. Sol. Cells*, vol. 128, pp. 335–342, 2014.

[304] S. Lizin, S. Van Passel, E. De Schepper, and L. Vranken, "The future of organic photovoltaic solar cells as a direct power source for consumer electronics," *Sol. Energy Mater. Sol. Cells*, vol. 103, pp. 1–10, 2012.

[305] A. J. Roscoe and G. W. Ault, "Supporting high penetrations of renewable generation via implementation of real-time electricity pricing and demand response," *IET Renew. Power Gener.*, vol. 4, no. 4, pp. 369–382, 2010.

[306] E. Tröster and J. D. Schmidt, "Evaluating the impact of PV module orientation on grid operation," in *Proceedings of the 2nd International Workshop on Integration of Solar Power into Power Systems*, 2012.

[307] D. D'Ercole, L. Dominici, T. M. Brown, F. Michelotti, A. Reale, and A. Di Carlo, "Angular response of dye solar cells to solar and spectrally resolved light," *Appl. Phys. Lett.*, vol. 99, no. 21, p. 213301, 2011.

[308] J. H. Fatehi and K. J. Sauer, "Modeling the incidence angle dependence of photovoltaic modules in PVsyst," *40th IEEE Photovolt. Spec. Conf.*, pp. 1335–1338, 2014.

[309] B. Liu and R. Jordan, “Daily insolation on surfaces tilted towards equator,” *ASHRAE J.; (United States)*, vol. 10, 1961.

[310] R. Steim, P. Schilinsky, S. A. Choulis, and C. J. Brabec, “Flexible polymer photovoltaic modules with incorporated organic bypass diodes to address module shading effects,” *Sol. Energy Mater. Sol. Cells*, vol. 93, no. 11, pp. 1963–1967, 2009.

[311] B. Andreasen *et al.*, “TOF-SIMS investigation of degradation pathways occurring in a variety of organic photovoltaic devices – the ISOS-3 inter-laboratory collaboration,” *Phys. Chem. Chem. Phys.*, vol. 14, no. 33, p. 11780, 2012.

[312] C. H. Peters, I. T. Sachs-Quintana, J. P. Kastrop, S. Beaupré, M. Leclerc, and M. D. McGehee, “High efficiency polymer solar cells with long operating lifetimes,” *Adv. Energy Mater.*, vol. 1, no. 4, pp. 491–494, 2011.

[313] J. Adams *et al.*, “Air-processed organic tandem solar cells on glass: toward competitive operating lifetimes,” *Energy Environ. Sci.*, vol. 8, no. 1, pp. 169–176, 2015.

[314] H. Hintz, H. J. Egelhaaf, H. Peisert, and T. Chassé, “Photo-oxidation and ozonization of poly(3-hexylthiophene) thin films as studied by UV/VIS and photoelectron spectroscopy,” *Polym. Degrad. Stab.*, vol. 95, no. 5, pp. 818–825, 2010.

[315] Joseph R. Lakowicz, *Principles of Fluorescence Spectroscopy*, 3rd ed. Springer., 2006.

[316] B. A. Swartz, T. Cole, and A. H. Zewail, “Photon trapping and energy transfer in multiple-dye plastic matrices: an efficient solar-energy concentrator,” *Opt. Lett.*, vol. 1, no. 2, pp. 73–5, 1977.

[317] B. Balaban, S. Doshay, M. Osborn, Y. Rodriguez, and S. A. Carter, “The role of FRET in solar concentrator efficiency and color tunability,” *J. Lumin.*, vol. 146, pp. 256–262, 2014.

[318] S. A. E. Marras, F. R. Kramer, and S. Tyagi, “Efficiencies of fluorescence resonance energy transfer and contact-mediated quenching in oligonucleotide probes.,” *Nucleic Acids Res.*, vol. 30, no. 21, p. e122, 2002.

[319] P. Cheng and X. Zhan, “Stability of organic solar cells: challenges and strategies,” *Chem. Soc. Rev.*, vol. 45, no. 9, pp. 2544–2582, 2016.

[320] S. U. Lee, W. S. Choi, and B. Hong, “A comparative study of dye-sensitized solar cells added carbon nanotubes to electrolyte and counter electrodes,” *Sol. Energy Mater. Sol. Cells*, vol. 94, no. 4, pp. 680–685, 2010.

Appendix A Collaborations and Authorship

This appendix details the research which was performed in collaboration with other universities and explains the circumstances which led to these collaborations. Clear guidance is given of the demarcation between the author's and others' contributions.

A.1 Outdoor Monitoring of OPV Modules

In summer 2013, the OPV research group at Bangor University were involved in a global round robin that was organised by Professor Frederik Krebs and his group at Technology University of Denmark (DTU), to study the reproducibility of outdoor measurements and to test the rigor of the ISOS protocols[1]. As a result of this, Bangor was one of the first laboratories to receive OPV modules sourced from the freeOPV programme at DTU[2]. Part of the agreement under which DTU supplied these modules was that users should keep them informed of any significant results and papers that arose from the use of the modules. The author was also invited to be a trial participant on a new online OPV course run by Prof. Krebs and to provide feedback and corrections; the subsequent first live course had over 8500 participants [3].

Following publication of the author's first paper on outdoor monitoring of OPVs[4] and having shown them the results from the first two batches of 3D structured modules, Prof. Krebs was keen to collaborate on the 3D structured project. DTU supplied a fresh batch of OPV modules and performed LBIC and IV characterisation, both before and after lamination onto the corrugated substrates. All other testing and analysis was performed by the author. Having twice presented a workshop and seminar on "Outdoor Performance Monitoring" for the MSc course at Cardiff School of Engineering run by Professor Nick Jenkins, the author was given access to their Lucas Nuelle solar simulator for the indoor angular characterisation measurements. A paper was published based on this collaboration on 3D structured OPV modules[5].

---

[1] M. V. Madsen et al., "Worldwide outdoor round robin study of organic photovoltaic devices and modules," *Sol. Energy Mater. Sol. Cells*, vol. 130, pp. 281–290, Nov. 2014.

[2] F. C. Krebs et al., "Freely available OPV - The fast way to progress," *Energy Technology*, vol. 1, no. 7, pp. 378–381, 2013.

[3] https://www.coursera.org/learn/solar-cell

[4] Noel Bristow, Jeff Kettle. "Outdoor performance of organic photovoltaics: Diurnal analysis, dependence on temperature, irradiance, and degradation." *J. Renew. Sustain. Energy*, 7.1 (2015): 013111.

[5] Jeff Kettle, Noel Bristow, Tracy Sweet, Nick Jenkins, Gisele A. dos Reis Benatto, Mikkel Jørgensen, Frederik C. Krebs. "Three dimension corrugated Organic Photovoltaics for building integration; improving the efficiency, oblique angle and diffuse performance of solar cells", *Energy Environ. Sci*. 8.11 (2015).

A.2 Outdoor Stability Testing of LDS Coatings on OPV Modules

The last phase of research in this thesis involved the use of LDS coatings to improve the stability and yield of OPV modules. The early work on this was performed in collaboration with Dr. Omar Moudam, who has a strong background in LDS.

After the early indoor testing on discrete dyes, the research moved on to test these dyes on OPV modules outdoors. From this point on the author assumed full control of the research. For the outdoor testing the LDS dyes were printed onto PET by the Welsh Centre for Printing and Coating (WCPC) in Swansea, under the direction of the author. WCPC were partners with Bangor University and Waterford Institute of Technology in the Wales Ireland Network for Innovative Photovoltaic Technologies (WINIPT) which funded all of the research for this thesis.

After the success of the outdoor stability tests on LDS dyes at Bangor, collaboration was again sought with DTU to provide a larger number of modules and with Professor Eugene Katz of Ben Gurion University, Israel (BGU). BGU were able to provide testing facilities in the Negev Desert, allowing the LDS coated OPV modules to be tested under conditions of very high irradiance and UV. As with the previous collaboration DTU were able to provide a large number of fresh OPV modules. The modules were tested by DTU under their solar simulator, sent to Bangor for preparation with LDS by the author, returned to DTU for post lamination tests and then sent to Israel for outdoor testing at BGU. All the data analysis on these results was performed by the author. A paper was published based on this collaboration[6].

The author would like to thank all of these collaborators, especially Professors Krebs, Katz and Jenkins, for giving him the opportunity to work with leaders in the field of OPV and PV research. It is the author's belief that it is through collaborations such as these that research can progress at a faster rate and new ideas can be brought to the fore.

[6] J. Kettle, N. Bristow, D.T. Gethin, Z. Tehrani, O. Moudam, B. Li, E.A. Katz, G.A. dos Reis Benatto, F.C. Krebs. "Luminescent down shifter for enhancing efficiency and stability of organic photovoltaics." *Solar Energy Materials and Solar Cells*, 144 (2016): 481-487.

Appendix B Outdoor Monitoring of OPVs – Extra Results

B.1 Meteorological Measurements at Bangor.

Table B.1 shows the weather statistics measured on the roof of the School of Electronics during the course of this research (2013-2015). The data is aggregated by season (Winter: December, January & February; Spring: March, April & May; Summer: June, July & August; Autumn: September, October & November).

Table B.1: Climate statistics for Bangor during the course of this research (2013-2015). Data measured by weather station on Dean Street roof. Average minimum and maximum values are averages of daily maximum and minimum figures.

Year	Season	Temperature (°C)			Humidity (%)		Wind (m/s)	Irradiance (W/m²)		UV Index		Rain (mm)
		Mean	Avg. Min	Avg. Max	Mean	Avg. Min	Mean	Mean	Avg. Max	Mean	Avg. Max	Total
2013	Spring	7.6	4.7	10.9	74.7	59.1	1.7	141	1167	0.75	3.97	148
	Summer	16.5	13.0	20.4	76.9	58.7	1.2	200	1229	1.30	6.26	135
	Autumn	12.1	9.7	14.6	81.6	68.8	1.2	62	954	0.32	2.19	247
	Winter †	7.9	5.4	10.3	75.5	64.0	1.6	35	654	0.12	0.84	189
2014	Spring	10.7	7.6	14.2	78.9	62.3	1.3	136	1359	0.74	3.90	194
	Summer	16.3	12.9	20.0	76.9	59.1	1.0	204	1338	1.30	6.26	158
	Autumn	13.0	9.8	16.0	80.7	66.6	1.0	77	1018	0.34	2.06	211
	Winter	7.3	5.1	9.3	82.2	72.4	1.8	26	519	0.08	0.71	332
2015	Spring	9.0	5.9	12.3	78.2	61.5	1.4	142	1419	0.68	3.62	164
	Summer	15.2	11.8	18.9	77.3	60.2	1.3	193	1294	1.07	5.49	122
	Autumn	12.0	8.7	15.2	81.6	68.1	1.1	74	1013	0.31	1.92	224
	Winter	7.6	5.2	9.8	82.3	71.9	1.9	24	526	0.07	0.65	325

† The weather station was not operational until the end of January 2013, so rainfall total is lower than expected – other figures are averages and are therefore not affected so much.

Appendix C Development of OPVs onto Structured Corrugated Substrates – Extra Results

C.1 LBIC Imaging Results – Full Data

LBIC testing was performed at DTU on all the flat modules before they were laminated, followed by retesting after lamination, initially with the modules positioned normal to the laser beam and then at various angles of tilt to simulate changes in pitch and yaw (Figure 6.1 & Figure C.1).

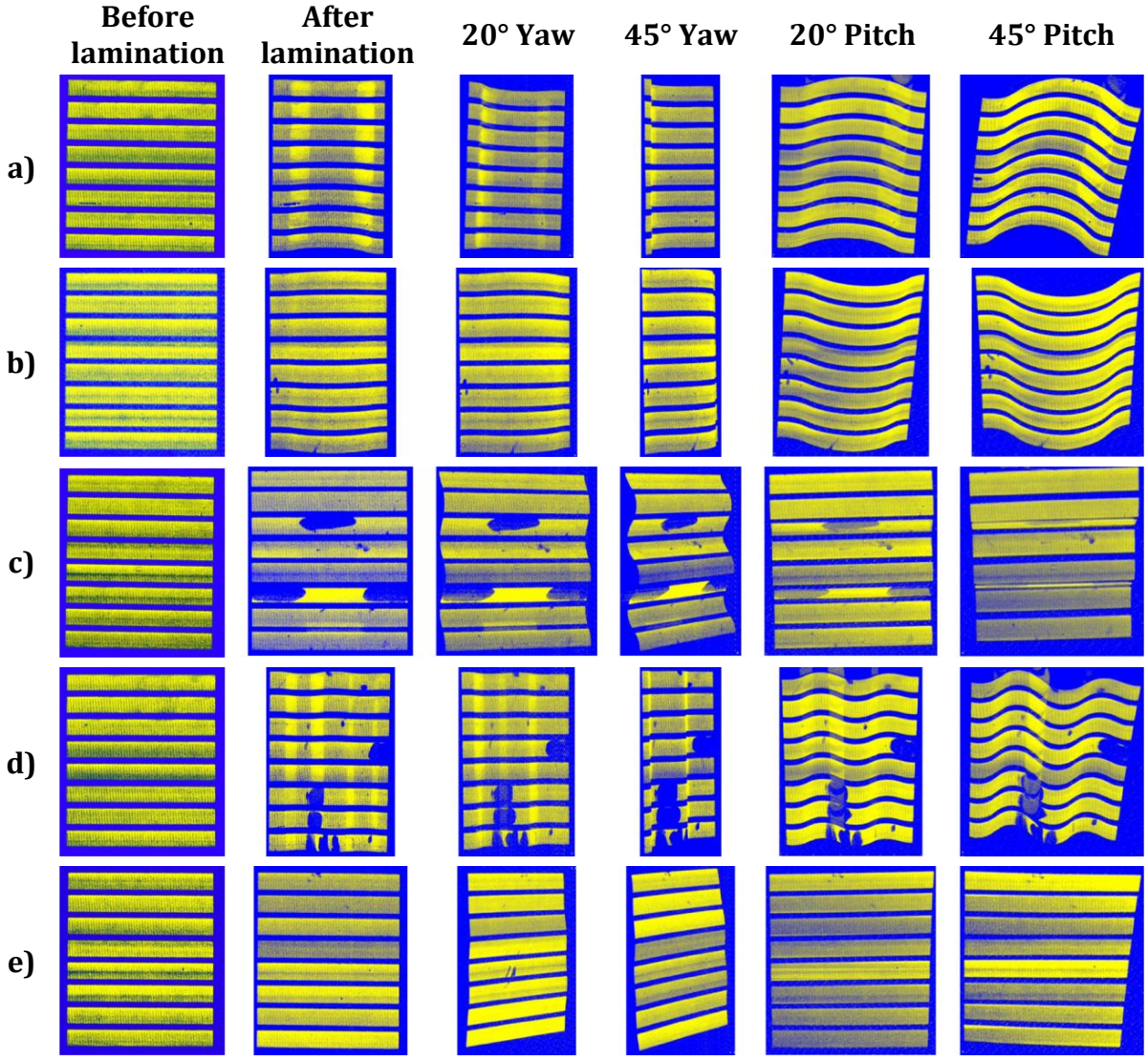

Figure C.1: LBIC images of 3D structured modules: a) type A; b) type B; c) type C; d) type D; and e) flat reference module. The first column shows the modules before lamination. The second column shows the modules after lamination. The third column shows the modules tilted at 20° and in the fourth column at 45° (in both cases the left edge is tilted up, simulating variations in yaw). The fifth column shows the modules tilted at 20° and in the sixth column at 45° (in both cases the top edge is tilted up, simulating variations in pitch).

C.2 Repeat LBIC Imaging for Failure Analysis

The LBIC measurements at normal incidence were repeated on two extra sets of laminated modules in order to confirm the reliability of the results (Figure C.2). These images confirm the main findings: reflective in-coupling effect from steep sides of type A and type D modules leads to increased photocurrent; delamination defects on smaller corrugated profiles (types C & D). These LBIC measurements were taken immediately after fabrication of the 3D modules and this is why fewer defects are found on the smaller corrugations, as delamination is exacerbated by prolonged static stress[7].

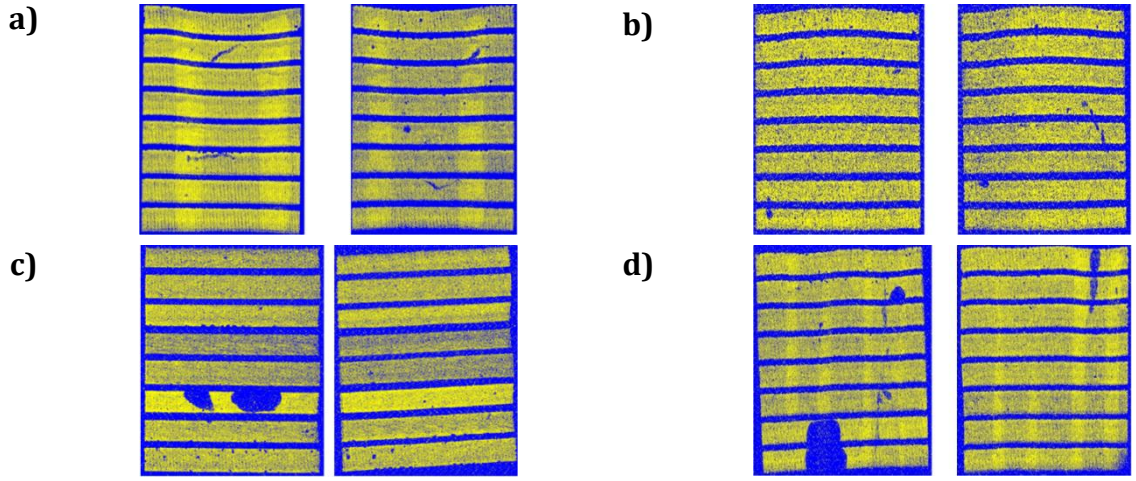

Figure C.2: Repeat LBIC measurements on 3D structured modules (laser beam normal to the module): a) type A (single concave); b) type B (single convex); c) type C (small inline); and d) type D (small transverse).

C.3 Angular Characterisation.

Angular characterisation measurements were performed on three sets of modules using the Lucas Nuelle equipment at Cardiff University. The last set is presented and discussed in detail in the main body of the thesis (see Section 6.2.2) and the results from measurements made on the first set of modules are presented here for completeness.

These modules were measured immediately before lamination and then again once they had been laminated onto the corrugated substrates. Their effective PCEs at normal incidence are shown in Table C.1. The type A module shows the largest relative

[7] M. Hösel, D. Angmo, R. R. Søndergaard, G. A. dos Reis Benatto, J. E. Carlé, M. Jørgensen, and F. C. Krebs, "High-Volume Processed, ITO-Free Superstrates and Substrates for Roll-to-Roll Development of Organic Electronics," *Adv. Sci.*, vol. 1, no. 1, 2014.

improvement in performance (15.2%) and the type D module shows a relative drop in performance of -12.9%. The other two modules show only a slight relative improvement of 5.6% (type B) and 7.7% (type C). The better results for the modules on the smaller corrugated profiles are possibly because they were measured immediately after lamination and before delamination defects had set in. This would confirm the hypothesis that delamination defects get worse over time (as suggested by the repeat LBIC measurements in Appendix C.2).

Table C.1: Module PCEs measured before and after lamination on Lucas Nuelle equipment for each structured module. Measurements shown are for normal incidence (yaw=90° and pitch=0°).

Module Type	PCE before lamination (flat)	Effective PCE after lamination	Relative change in PCE
A	1.88%	2.16%	15.2%
B	2.12%	2.24%	5.6%
C	1.40%	1.50%	7.7%
D	1.39%	1.21%	-12.9%

The results in Figure C.3 show the normalised PCE and relative enhancement in PCE experienced by all of the modules at various angles of pitch and across all angles of yaw. At low angles of incidence (yaw≈10°) the PCE of the type B module exceeds its value when the light is normal to the module (yaw=90°), leading to relative enhancements compared to the flat module of up to nearly thirty-fold (at pitch=52°). The type A module also experiences relative enhancements at low angles of yaw of up to nearly ten-fold, again at pitch=52°. Comparing the modules on the smaller corrugated profiles it can be seen that the type D module always outperforms the type C module. The type D module performs similarly to the flat reference module, except for a very slight enhancement at low angles of incidence. The type C module performs worse than the flat module at all angles of incidence except at yaw=10° and pitch=68°.

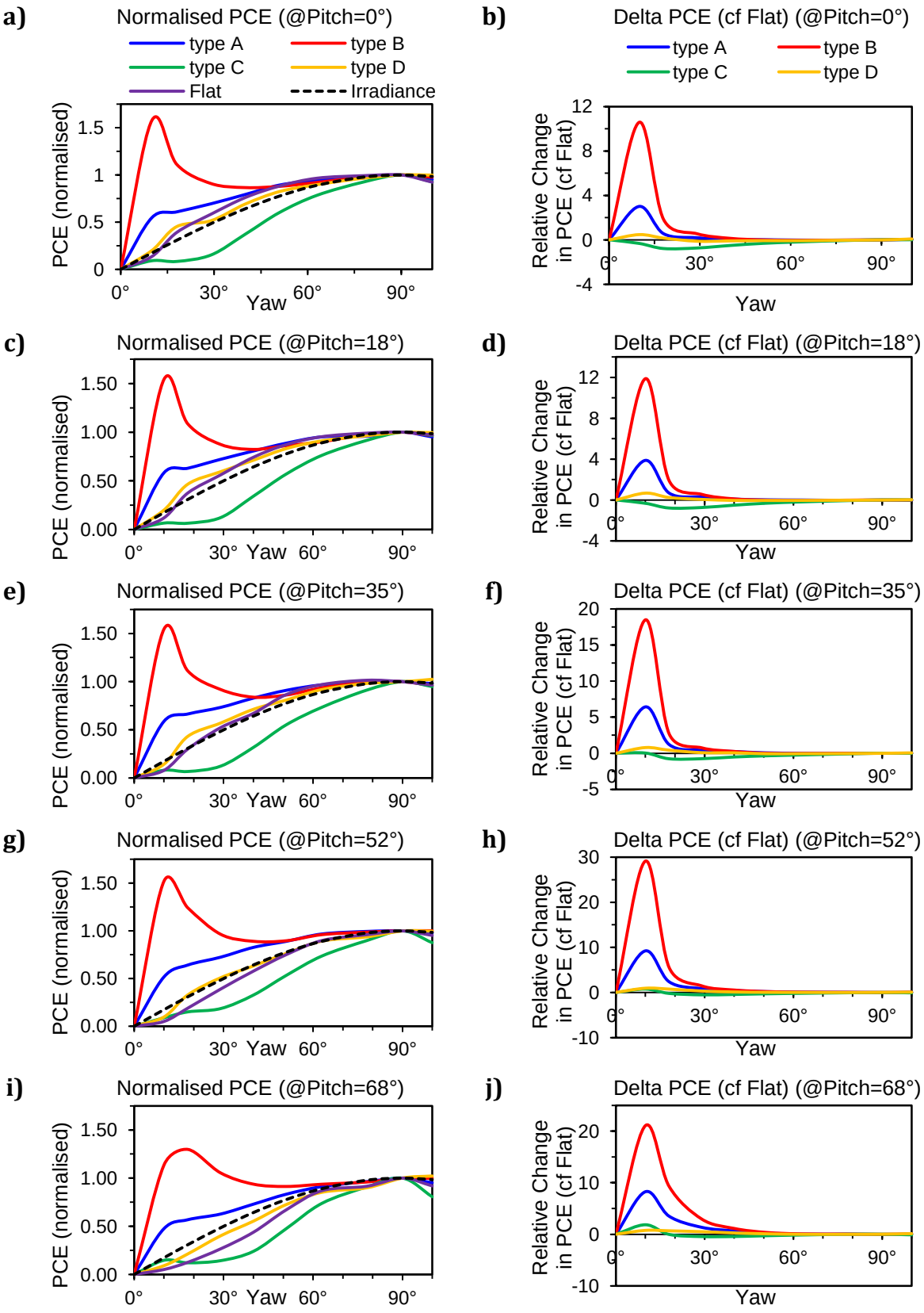

Figure C.3: Angular characterisation results at various angles of pitch: a) & b) 0°; c) & d) 18°; e) & f) 35°; g) & h) 52°; and i) & j) 68°. The left column shows effective PCE (normalised at yaw = 90°). The right column shows relative enhancement in effective PCE compared to the flat reference module.

C.4 Outdoor Measurements – Summer 2015

These results are further analysis of the data presented in the thesis (Section 6.2.4). Figure C.4 shows diurnal measurements for I_{SC}, V_{OC} and fill factor over the course of a sunny day (10/06/2015) and a cloudy day (22/05/2015). I_{SC} closely follows irradiance on both days, whereas V_{OC} is steady for the majority of the day when it is sunny, but is much more dependent on irradiance on the cloudy day. On the cloudy day V_{OC} never reaches the peak levels seen on the sunny day. Fill factor is less dependent on irradiance and is fairly steady during the course of both days, although the effect of varying irradiance can be seen on the cloudy day.

Figure C.5 shows the main performance indicators (PCE, I_{SC}, V_{OC} and FF) plotted against irradiance for the two days, one sunny (solid lines) and the other cloudy (dashed lines). The trends for the cloudy and sunny days closely match for each module type, apart from PCE and I_{SC} for the type B module, which show non-linear behaviour at low irradiances on the sunny day. This is due to the enhancement seen in early morning and late evening on the sunny day. The type A module also shows lower fill factor on the sunny day, leading to lower PCE. V_{OC} trends for the modules on the smaller corrugated profiles (types C & D) are noticeable lower than for the other module types, due to delamination defects causing faults at the electrode interfaces.

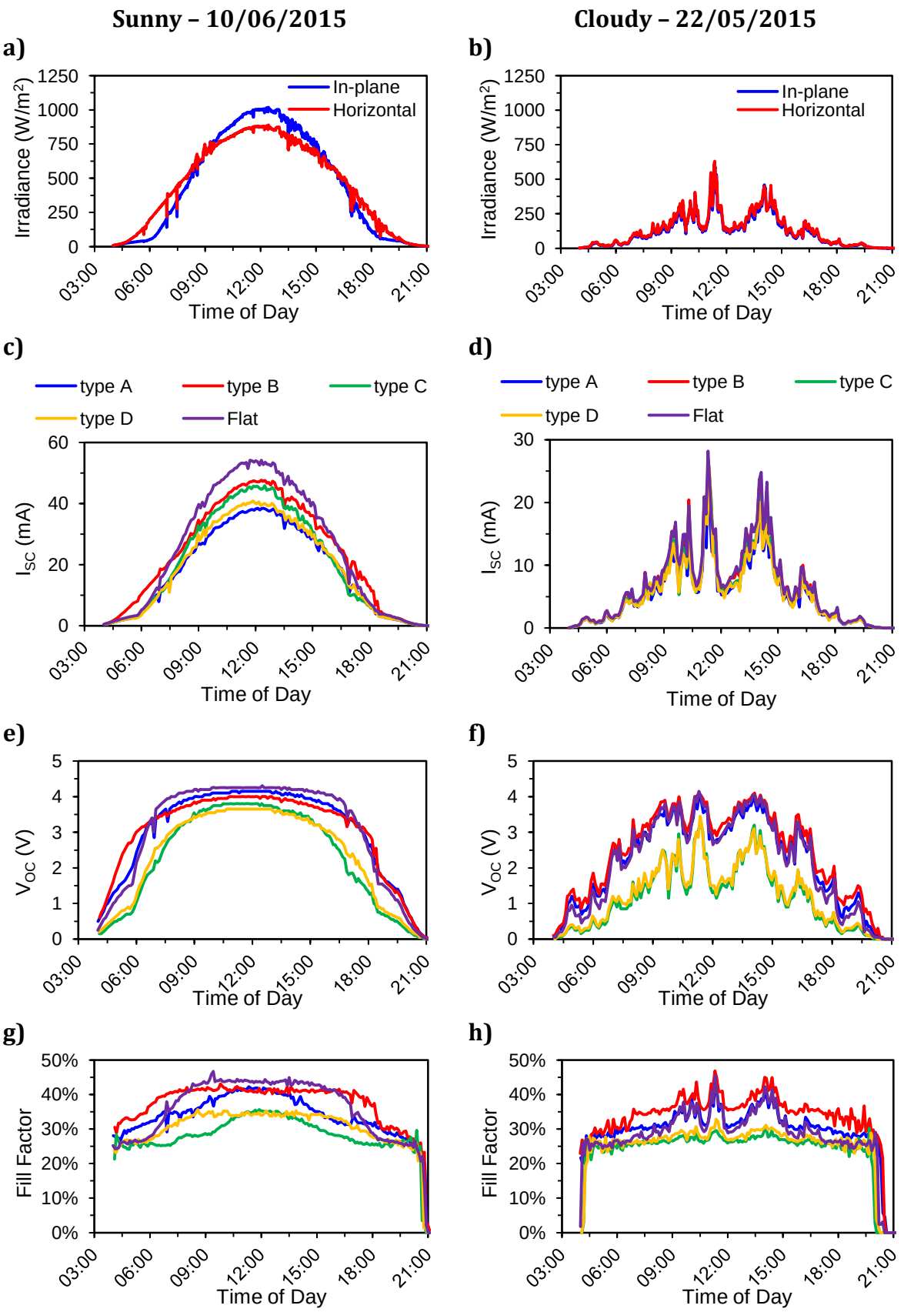

Figure C.4: Outdoor monitoring: summer 2015. The left column shows results from 10/06/2015 (sunny day), the right column shows results from 22/05/15 (cloudy day): a) & b) Irradiance; c) & d) I_{SC}; e) & f) V_{OC}; and g) & h) Fill Factor.

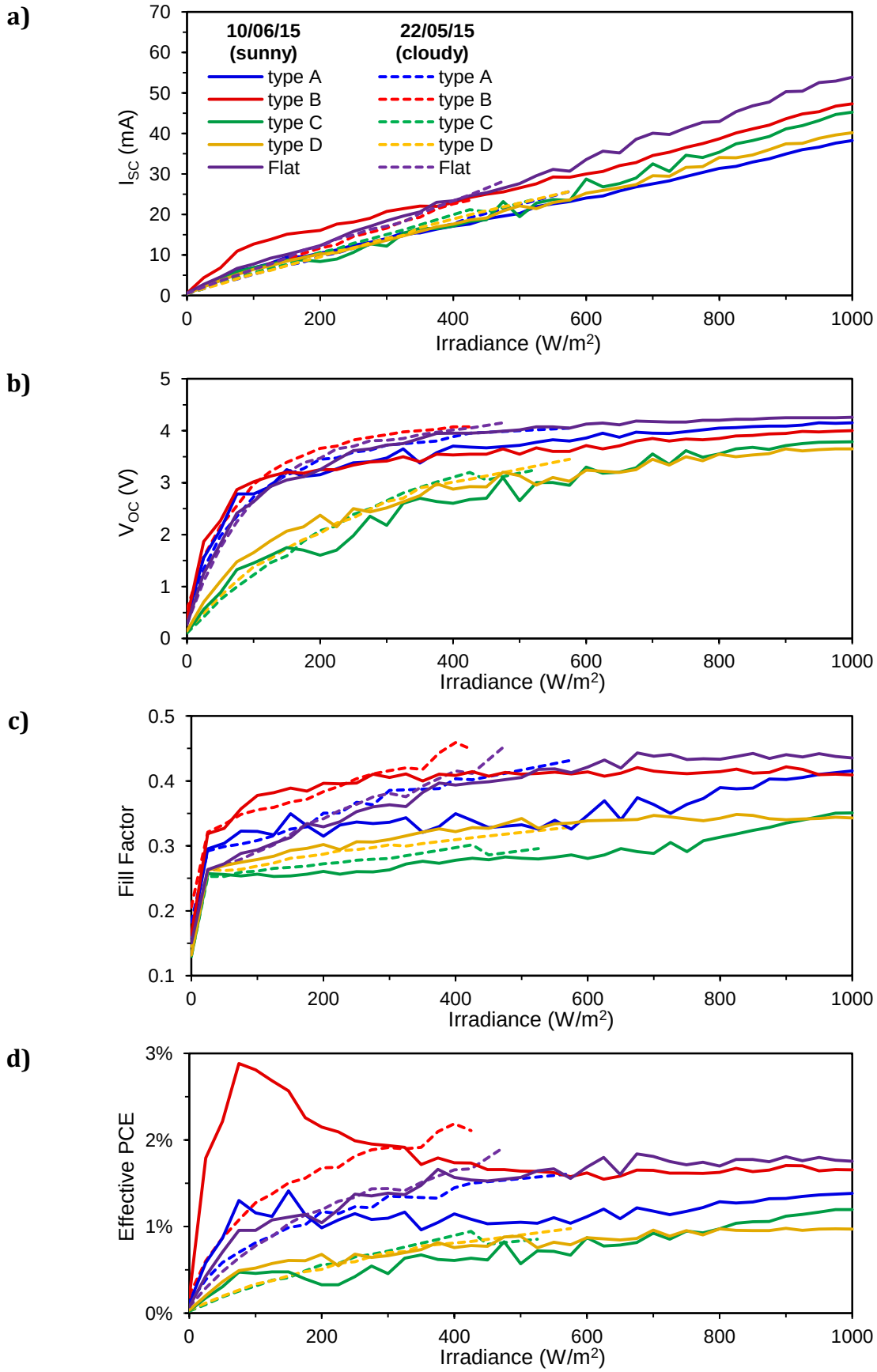

Figure C.5: Outdoor monitoring during summer 2015. Analysis of performance parameters against irradiance on sunny (10/06/2015) and cloudy (22/05/2015) days: a) I_{SC} vs. Irradiance; b) V_{OC} vs. Irradiance; c) Fill Factor vs. Irradiance; and d) Effective PCE vs. Irradiance.

Figure C.6 shows the diurnal pitch and yaw experienced by the modules on a day during the summer monitoring (22/05/2015). The sun is behind the modules for a period during the morning and evening (AOI > 90°), area shaded red on the graph. The enhancements in effective PCE in the early morning and evening are seen when the horizontal angle of incidence exceeds 70° (yaw < 20°), i.e. before 08:30 and after 15:30. This corresponds with the results seen in the angular characterisation in Section 6.2.2.

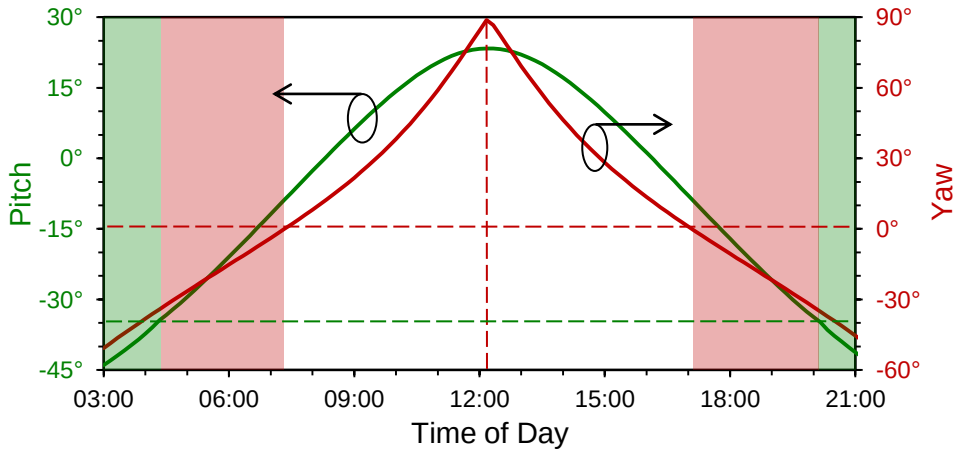

Figure C.6: Outdoor monitoring: summer 2015. Diurnal pitch and yaw experienced on 22/05/2015. Green shaded area: sun below the horizon (pitch < -35°). Red shaded area: sun behind the modules.

C.5 Outdoor Measurements – Summer 2014

Figure C.7 shows results from the outdoor monitoring that took place between 23/06/2014 and 30/06/2014. Data from two contrasting days are presented, allowing a comparison between the performance on a sunny day (with high levels of direct normal irradiation) and a cloudy day (with predominantly diffuse irradiation). The sunny day shows that the modules on the larger corrugated profiles (types A & B) both outperformed the flat reference modules. In the early morning and late afternoon the efficiencies peak, with the type B module reaching 3x its midday level. The type D module performs better than the flat modules, as its efficiency does not drop off over the course of the day. The type C module performs far worse than the flat modules. The results for the cloudy day show that all of the modules have outperformed the flat reference modules, with the type A having the highest gains, followed closely by the type B and type D, and the type C the lowest. The cumulative daily yield data shows that all of the 3D modules apart from the type C outperform the flat modules.

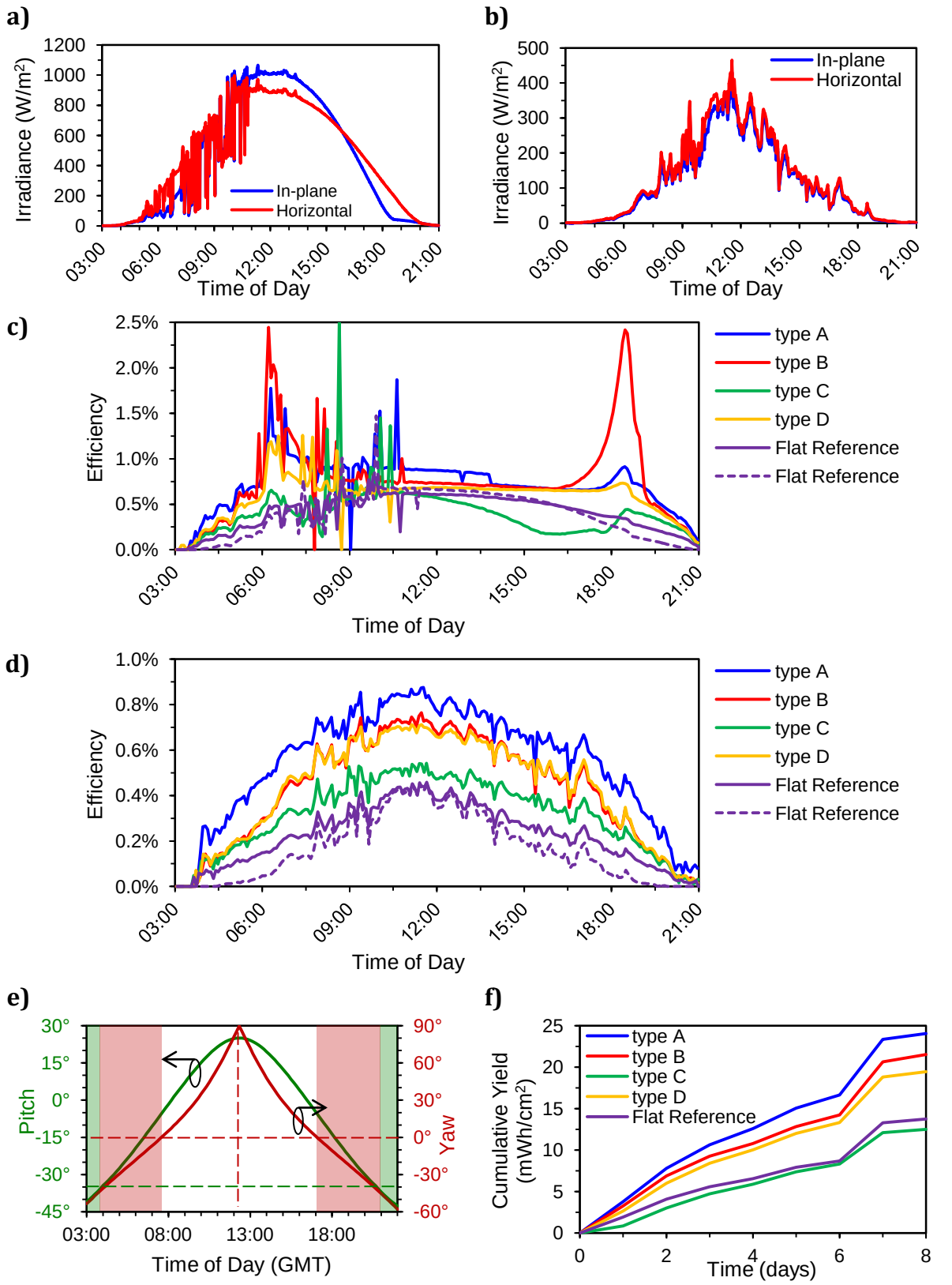

Figure C.7: Outdoor monitoring during summer 2014. Diurnal irradiance: a) Sunny day (29/06/14); b) Cloudy day (28/06/14). Diurnal Efficiency: c) Sunny day; d) Cloudy day. e) Diurnal pitch and yaw (28/06/14). Green shaded area: sun below the horizon (sunrise: 03:50, sunset: 20:50). Red shaded area: sun behind the modules. f) Cumulative yield over the period.

Table C.2 shows analysis of the daily yield data under various irradiance conditions. Comparing the overall performance of the 3D modules against the flat reference modules shows that type A outperformed them by 75%, type B outperformed them by 56% and type D by 41%. Only type C underperformed the flat modules (-9%). Comparisons of the yields under different climatic conditions show that for all of the 3D modules the most improvement is seen on diffuse days (type A: +101%), with lower gains on intermediate days and the lowest gains on sunny days (type A: +57% and type C: -30%).

Table C.2: Analysis of daily yields for the 3D modules during summer 2014 under different irradiance conditions[8]. Gain is the percentage improvement shown by the 3D modules when compared to the flat reference module.

Foil Type	Sunny		Intermediate		Cloudy		Total	
	Average Daily Yield (mWh/cm²)	Gain (cf. Flat)	Average Daily Yield (mWh/cm²)	Gain (cf. Flat)	Average Daily Yield (mWh/cm²)	Gain (cf. Flat)	Average Daily Yield (mWh/cm²)	Gain (cf. Flat)
Flat	2.38	-	1.83	-	1.00	-	1.72	-
A	3.72	57%	3.44	88%	2.00	101%	3.01	75%
B	3.52	48%	3.00	64%	1.66	66%	2.69	56%
C	1.67	-30%	1.94	6%	1.20	21%	1.56	-9%
D	2.92	23%	2.88	57%	1.64	65%	2.43	41%

C.6 Outdoor Measurements – Winter 2013

These tests were performed between 26/11/2013 and 04/12/2013 on five modules: one of each 3D type plus a flat reference. Figure C.8 shows diurnal efficiencies for a sunny day (04/12/2013) and a cloudy day (27/11/2013) during winter 2013. The sunny day had a total insolation of 0.8kWh/m², maximum irradiance of 670W/m², and ambient temperatures with a maximum of 9.9°C and an average of 7.0°C. The cloudy day had a total insolation of 0.175kWh/m², maximum irradiance of 50W/m², and ambient temperatures with a maximum of 10.7°C and an average of 9.8°C. On both days the best performing module is the type A, followed by the type D and the type C. All three outperformed the flat reference module at midday. On the cloudy day there is no

[8] Irradiance ratings are based on daily insolation figures by comparing measured insolation against theoretical maximum (based on Bird model): Sunny: >80% of maximum insolation, Diffuse: <40% of maximum insolation, otherwise Intermediate.

Bird model: R. E. Bird and R. L. Hulstrom, "A simplified clear sky model for direct and diffuse insolation on horizontal surfaces," *Tech. Rep. SERI/TR-642-761.* Solar Energy Research Inst., Golden, CO(USA), 1981.

crossover between the performance of the 3D module types and the difference in performance is more spread out, whereas on the sunny day the performances are less separated and the type C module's efficiency drops below that of the flat reference cell for the majority of the afternoon. It can be seen that the 3D modules have a better performance under diffuse conditions when compared to the flat module.

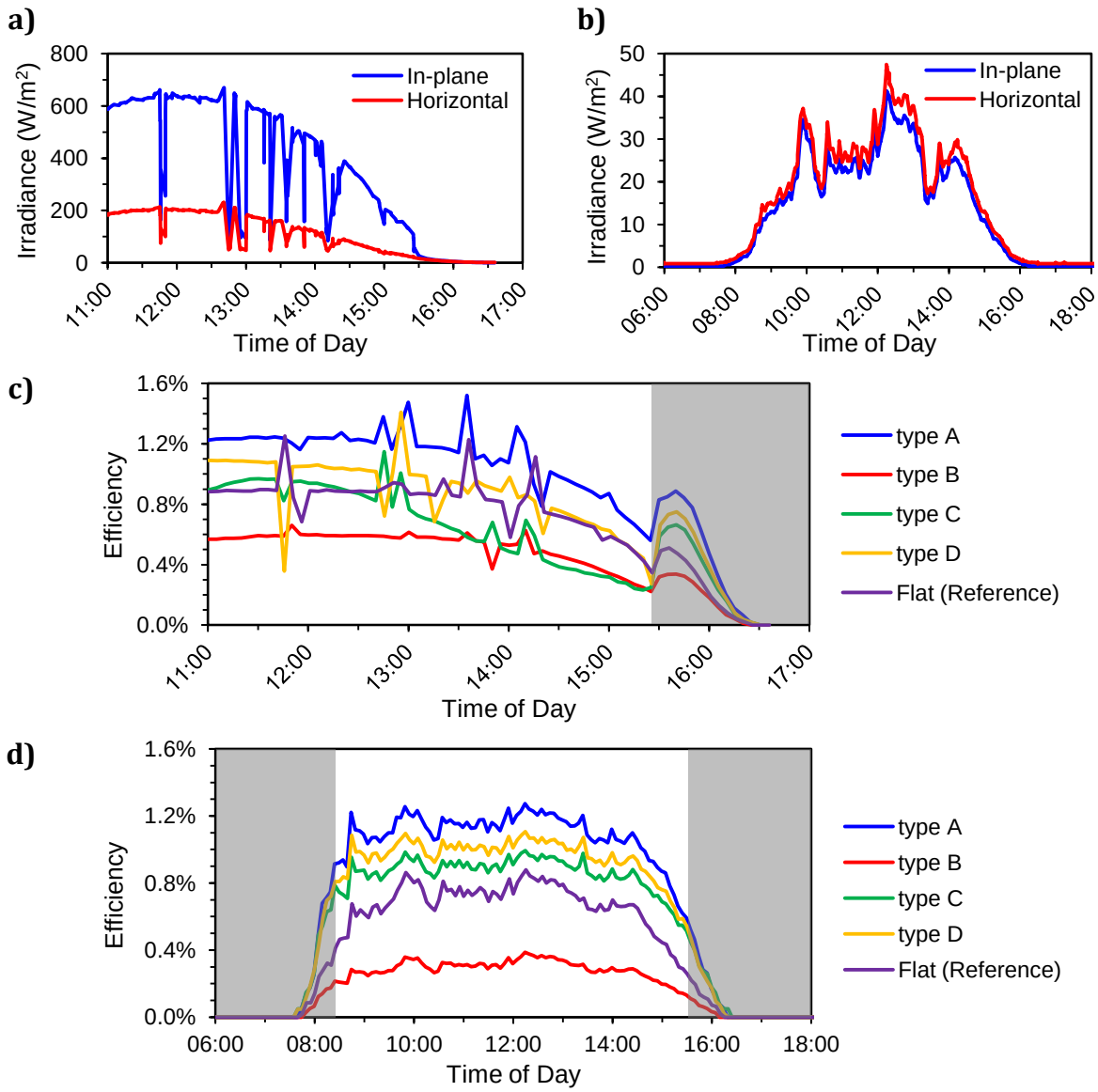

Figure C.8: Outdoor monitoring – winter 2013. Diurnal irradiance: A: Sunny (4/12/13), B: Cloudy (27/11/13). Diurnal efficiency: C: Sunny afternoon, D: Cloudy day. The greyed out areas are when the modules are subject to shading from the adjacent racks and roof structures. [sunrise: 08:10, sunset: 16:05]

The type B module has performed very badly in comparison to all of the other modules. Examination of the I_{SC} and V_{OC} vs. irradiance plots (Figure C.9) would suggest that this module is defective, probably due to delamination. The 3D modules are

expected to have different light collection capacities and this should show through differences in I_{SC} rather than V_{OC}. The type B module has a very different V_{OC} performance to all the other modules; V_{OC} rises much more slowly and does not reach a steady value. Its I_{SC} performance however is broadly similar to the other modules and has a linear relation to irradiance. These defects were not seen during the 3D angular characterisation measurements (see Appendix C.3), which were performed when these 3D modules were first laminated. During these tests the type B module had the best performance. This backs up the likelihood that these are delamination defects, as these types of defect appear to get worse over time. The delamination is likely to be at the interface between the photoactive layer and electrode, as this causes degradation of V_{OC}, but does not significantly affect I_{SC} [9]. Therefore it is reasonable to ignore the type B module in this set of outdoor measurements.

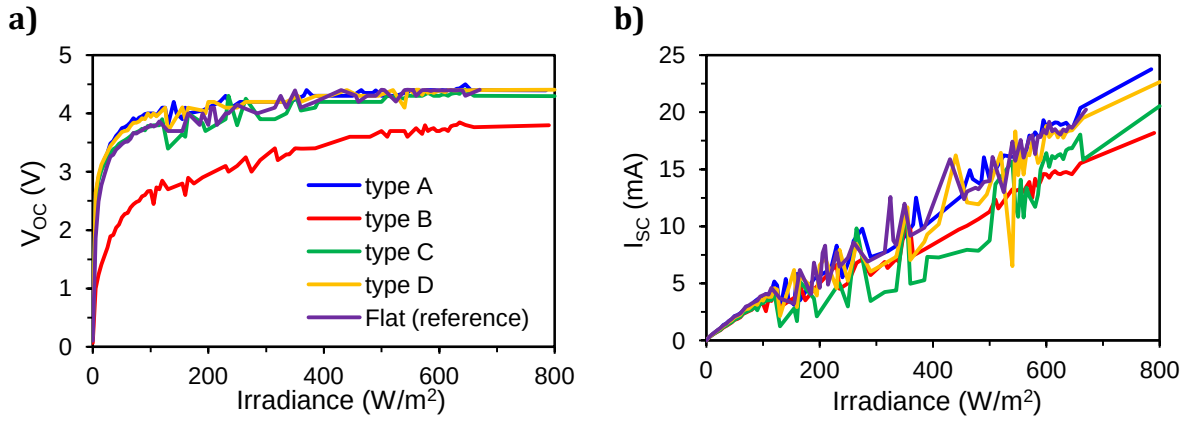

Figure C.9: V_{OC} vs. Irradiance (a) and I_{SC} vs. Irradiance (b) for the winter outdoor monitoring. It can be seen that the type B module has very different V_{OC} characteristics from the other modules.

Table C.3 shows the average daily yields for the different module types during the course of the monitoring. This shows a 55% enhancement for type A in comparison with the flat reference. The type B module shows a drop of 38%, type D a gain of 20% and type C has the same yield as the flat module. Breaking these results down by irradiance level shows that type A had the greatest enhancement during sunny conditions (sunny: 57%, cloudy: 48%), whereas all the other module types had their highest enhancement during cloudy conditions. Comparing the two module types based on smaller corrugated profiles shows that type D outperforms type C.

[9] N. Grossiord, J. M. Kroon, R. Andriessen, and P. W. M. Blom, "Degradation mechanisms in organic photovoltaic devices," *Org. Electron.*, vol. 13, no. 3, pp. 432–456, Mar. 2012.

Table C.3: Analysis of daily yields for the 3D modules during winter 2013 under different climatic conditions. Gain is the percentage improvement shown by the 3D modules when compared to the flat modules.

Module Type	Sunny		Intermediate		Cloudy		Total	
	Average Daily Yield (mWh/cm²)	Gain (cf. Flat)	Average Daily Yield (mWh/cm²)	Gain (cf. Flat)	Average Daily Yield (mWh/cm²)	Gain (cf. Flat)	Average Daily Yield (mWh/cm²)	Gain (cf. Flat)
Flat	1.61	-	0.34	-	0.14	-	0.59	-
A	2.53	57%	0.52	54%	0.21	48%	0.92	55%
B	1.03	-36%	0.21	-38%	0.07	-49%	0.37	-38%
C	1.53	-5%	0.41	22%	0.16	15%	0.59	0%
D	1.89	17%	0.45	33%	0.18	29%	0.71	20%

Figure C.10 shows the diurnal pitch and yaw experienced by the modules over the course of a day during the winter monitoring (29/11/2013). It can be seen that the maximum yaw (at sunrise and sunset) is about 40°, corresponding to a horizontal angle of incidence of 50°. This is much less than the 70° required for the oblique angle enhancements seen during the summer monitoring and explains why these are absent during the winter months.

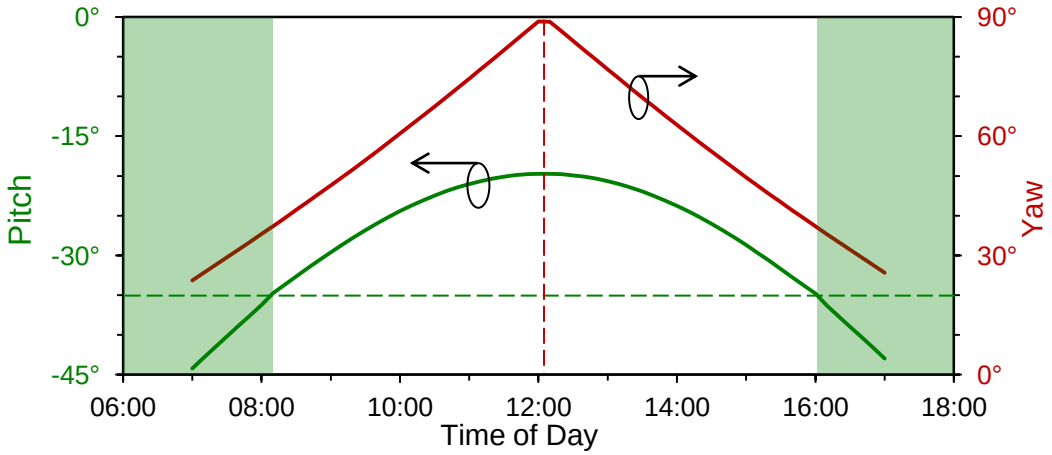

Figure C.10: Outdoor monitoring during winter 2013. Diurnal pitch and yaw experienced on 29/11/2013. Green shaded area: sun below the horizon (pitch < -35°).

Appendix D Increasing Stability and Performance of OPVs Using LDS layers – Extra Results

D.1 PLQY Results.

Table D.1: PLQY results for discrete LDS materials.

LDS Material	Concentration (wt in MicroChem A8)	Excitation Wavelength	PLQY
Coumarin 7	8 mg/ml	405 nm	16.0%
Coumarin 153	8 mg/ml	411 nm	8.4%
Kremer 94736 - blue	8 mg/ml	375 nm	5.7%
Kremer 94736 - blue	16 mg/ml	375 nm	1.9%
Kremer 94737 - green	8 mg/ml	447 nm	11.3%
Kremer 94700 - orange	8 mg/ml	450 nm	22.3%
Lumogen F red 300	8 mg/ml	445 nm	5.8%
Lumogen F red 300	16 mg/ml	445 nm	3.6%
Lumogen F orange 240	8 mg/ml	492 nm	8.7%
AlQ_3	8 mg/ml	385 nm	12.5%
Europium complex	8 mg/ml	350 nm	6.3%
DCM	8 mg/ml	462 nm	1.6%

Table D.2: PLQY results for multiple-dye LDS materials.

LDS Material	Concentration (dry weight in MicroChem A8)	PLQY
Kremer Orange & Coumarin 153	2mg:2mg/ml	20.3%
Kremer Orange & Coumarin 153	4mg:2mg/ml	6.3%
Kremer Orange & Europium complex	1mg:1mg/ml	30.9%
Kremer Orange & Europium complex	2mg:2mg/ml	23.7%
Kremer Orange & Kremer Blue	1mg:1mg/ml	13.5%
Kremer Orange & Kremer Blue	2mg:2mg/ml	5.5%
Kremer Blue & AlQ_3	1mg:1mg/ml	15.9%
Kremer Blue & Europium complex	1mg:1mg/ml	25.3%
AlQ_3 & Europium complex	1mg:1mg/ml	2.7%

D.2 Figures of Merit – Weighted Sums for Various Active Layers.

In the main thesis the weighted sum is given for P3HT:$PC_{61}BM$. For completeness weighted sums are provided for other OPV active layers which we have fabricated at Bangor (see Figure D.1, Table D.3 and Table D.4).

Table D.3: Weighted sums for discrete dyes with various OPV active layers.

LDS Material	Weighted Sums			
	P3HT:$PC_{61}BM$	PTB7:$PC_{61}BM$	PCPDTBT:$PC_{61}BM$	PCPDTBT:$PC_{71}BM$
Coumarin 7	89.8%	83.3%	79.3%	79.9%
Coumarin 153	95.7%	87.0%	84.3%	84.8%
Kremer Blue	94.8%	86.4%	87.1%	86.6%
Kremer Green	89.2%	82.6%	80.9%	81.2%
Kremer Orange	85.7%	83.7%	80.6%	79.7%
Lumogen Red	68.1%	74.4%	73.9%	70.2%
Lumogen Orange	78.9%	77.7%	76.8%	74.8%
AlQ_3	88.5%	78.1%	77.0%	77.5%
Europium complex	94.4%	89.9%	87.7%	87.1%
DCM	84.4%	99.0%	94.4%	89.7%

Table D.4: Weighted sums for blended dyes with various OPV active layers.

LDS Material	Weighted Sums			
	P3HT:$PC_{61}BM$	PTB7:$PC_{61}BM$	PCPDTBT:$PC_{61}BM$	PCPDTBT:$PC_{71}BM$
Kremer Orange/ Coumarin153 (2mg:2mg:1ml)	90.3%	84.0%	81.6%	81.5%
Kremer Orange/ Europium (1mg:1mg:1ml)	90.6%	82.4%	80.6%	80.8%
Kremer Orange/ Kremer Blue (1mg:1mg:1ml)	87.6%	81.2%	79.1%	78.9%
Kremer Blue/ AlQ_3 (1mg:1mg:1ml)	91.0%	81.0%	81.2%	81.1%
Kremer Blue/ Europium (1mg:1mg:1ml)	91.9%	83.2%	83.9%	83.5%
AlQ_3/Europium (1mg:1mg:1ml)	84.9%	75.3%	75.3%	75.3%

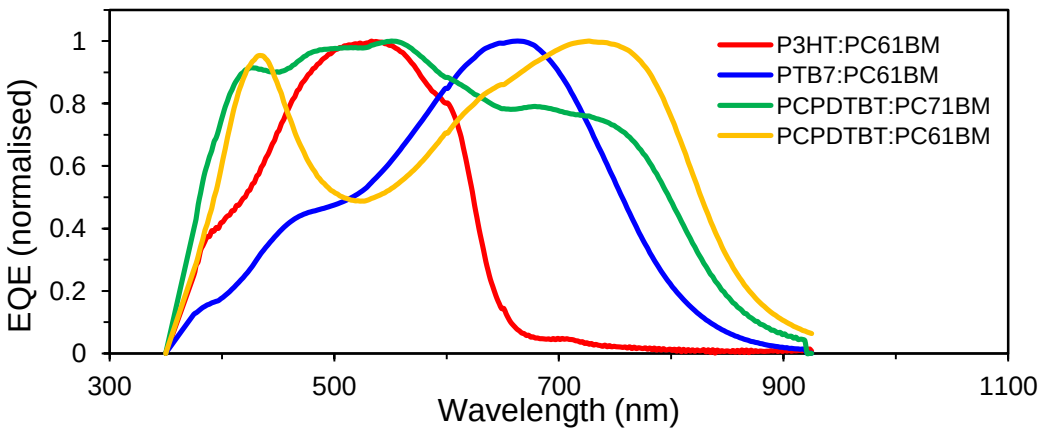

Figure D.1: Normalised EQE curves for various OPV active layers.